

ABSTRACT

Title of dissertation: QUANTUM COHERENT PHENOMENA IN
SUPERCONDUCTING CIRCUITS
AND ULTRACOLD ATOMS

Kaushik Mitra, Doctor of Philosophy, 2010

Dissertation directed by: Professor Christopher Lobb
Department of Physics

This thesis consists of theoretical studies of superconducting qubits, and trapped bosons and fermions at ultracold temperature. In superconducting qubits I analyze the resonant properties and decoherence behavior of dc SQUID phase qubits, in which one junction acts as a phase qubit and the rest of the device provides isolation from dissipation and noise in the bias lead. Typically qubit states in phase qubits are detected by tunneling it to the voltage state. I propose an alternate non-destructive readout mechanism which relies on the difference in the magnetic flux through the SQUID loop due to state of the qubit. I also study decoherence effects in a dc SQUID phase qubit caused by the isolation circuit. When the frequency of the qubit is at least two times larger than the resonance frequency of the isolation circuit, I find that the decoherence time of the qubit is two orders of magnitude larger than the typical ohmic regime, where the frequency of the qubit is much smaller than the resonance frequency of the isolation circuit. This theory is extended to other similar superconducting quantum devices and has been applied

to experiments from the group at the University of Maryland. I also demonstrate, theoretically, vacuum Rabi oscillations, analogous to circuit-QED, in superconducting qubits coupled to an environment with resonance. The result obtained gives an exact analytical expression for coherent oscillation of state between the system (the qubit) and the environment with resonance.

Next I investigate ultracold atoms in harmonically confined optical lattices. They exhibit a ‘wedding cake structure’ of alternating Mott shells with different number of bosons per site. In regions between the Mott shells, a superfluid phase emerges at low temperatures which at higher temperatures becomes a normal Bose liquid. Using finite-temperature quantum field theoretic techniques, I find analytically the properties of the superfluid, Bose liquid, and Mott insulating regions. This includes the finite temperature order parameter equation for the superfluid phase, excitation spectrum, Berezinskii-Kosterlitz-Thouless transition temperature and vortex-antivortex pair formation (in the two dimensional case), finite temperature compressibility and density - density correlation function. I also study interacting mixtures of ultracold bosonic and fermionic atoms in harmonically confined optical lattices. For a suitable choice of parameters I find emergence of superfluid and Fermi liquid (non-insulating) regions out of Bose-Mott and Fermi-band insulators, due to finite boson and fermion hopping. I also propose a possible experiment for the detection of superfluid and Fermi liquid shells through the use of Gauss-Laguerre and Gaussian beams followed by Bragg spectroscopy.

Another area I explore is ultracold heteronuclear molecules such as KRb, RbCs and NaCs. I obtain the finite and zero-temperature phase diagram of bosons in-

teracting via short range repulsive interactions and long-ranged isotropic dipolar interactions in two-dimensions. I build an analytical model for such systems that describes a first order quantum phase transition at zero temperature from a triangular crystalline phase (analogous to Wigner crystal phase of electrons) to superfluid phase. At finite temperature the crystalline phase melts, due to topological defects, to a hexatic phase where translational order is destroyed but hexagonal orientational order is preserved. Further temperature increase leads to the melting of the hexatic phase into a normal dipolar Bose liquid.

QUANTUM COHERENT PHENOMENA IN
SUPERCONDUCTING CIRCUITS AND ULTRACOLD ATOMS

by

Kaushik Mitra

Dissertation submitted to the Faculty of the Graduate School of the
University of Maryland, College Park in partial fulfillment
of the requirements for the degree of
Doctor of Philosophy
2010

Advisory Committee:
Professor Christopher Lobb, Chair
Professor Carl J Williams
Professor C. A. R. Sá de Melo
Professor Eite Tiesinga
Professor Robert Anderson
Professor Jeffrey Bub

© Copyright by
Kaushik Mitra
2010

Acknowledgments

I owe my gratitude to all the people who have made this thesis possible and because of whom my graduate experience has been one that I will cherish forever.

First I would like to thank my advisor Dr. Carl J Williams for giving me an opportunity to work in a challenging and stimulating environment. I thank him for giving me the flexibility to choose my own problems, and the independence to work in my own style and pace. Due to him I could interact and collaborate with so many post docs and professors belonging to so many different institutes and centers. He also gave me the opportunity to travel to several conferences and workshops all across US and Europe which made graduate school such a rewarding experience. Finally he was always very supportive while I was exploring my options regarding careers after PhD.

I believe that the job of an advisor is to provide the right atmosphere, and let the student learn, thrive, and prosper on his own. I am grateful to Carl for being a true advisor to me.

Next I would like to thank my co-advisor Professor Christopher Lobb. He has always been there for me whenever I needed him. A well known rule in behavioral economics is that we remember two things from an experience, its peak and its end. I am especially grateful to Chris for the interaction I had with him in the last few days during which he helped me prepare for my interviews and painstakingly proof read this dissertation.

Next I would like to thank Professor Carlos Sá de Melo. During the past

several years I had the honor of working closely with him. From him I have learned, not only quantum many body theory or essential ideas of condensed matter, but also important things about life and work beyond physics. This dissertation would not have been possible without him, but his influence goes far beyond that, and is perhaps next only to my parents.

Next I would like to thank Dr. Eite Tiesinga. I am certain that it is a privilege to be working in an office next to his. Whenever I had any question regarding any problem I was working on, I would just walk next door and bug him with my queries. And invariably he would provide an answer or at least a direction towards it. I have always been inspired by his working style and ethic, and his willingness to learn and work on new problems.

I would also like to thank Professor Robert Anderson for being very helpful with his comments and suggestions during my presentations. I would also like to thank Professor Jeffrey Bub for agreeing to serve on my thesis committee and for sparing his invaluable time reviewing the manuscript.

During the past several years I have interacted and collaborated with several people. Frederick Strauch in particular has been a tremendous influence and a mentor for the first two years. His breadth and depth of knowledge is quite awe inspiring. I have always looked forward going to my office at NIST and that is because of the fine company I had in the form of interesting office mates like Tom Hanna and Pascal Naidon. Without the intermittent conversations I had with them about several funny things, life would have been boring. Anzi Hu, Emily Townsend, Ludwig Mathey, Layla Homorazi, Stephen Maxwell, Menderes Iskin, they all made the

NIST experience memorable. I would also like to thank experimentalists at Maryland: Sudeep Dutta, Hanhee Paik, Tauno Palomaki, Vitaley Zaretsky, Hyeokshin Kwon, and others, for enduring a theorist like me, and their support.

My roommates, Prateek, Kevin, Zrinka, Yigit, Jupe, Kanu and Katie, and former ones, Sandeep and Dyan. Thanks for being such nice friends. Folks at DESI: Ashutosh, Arun, Nana, Anu, Viji, Vindo, Sravya, Sharmi, Utsav, and others. DESI has been an integral part of my life, and I cherish the time I had with DESI volunteers. Shivani for being such a nice friend, and Monika for everything she did for me.

Finally I would like to thank my parents, and my brother for their love and support.

Table of Contents

List of Tables	viii
List of Figures	ix
List of Definitions of Selected Symbols	xiv
List of Abbreviations	xviii
1 Introduction	1
1.1 Introduction	1
1.2 Macroscopic quantum phenomena in SQUIDs	2
1.3 Many body quantum coherence in Bose condensates	7
1.3.1 Spontaneous symmetry breaking and off-diagonal long range order	8
1.4 Macroscopic quantum interference in atomic BECs	13
1.4.1 Josephson effect	13
1.4.2 Josephson effect in a BEC in a double well potential	14
1.4.3 Rabi, Josephson, and Fock regimes	17
1.5 Outline of thesis	19
2 Quantum behavior of dc SQUID phase qubit	24
2.1 Introduction	24
2.2 The circuit Hamiltonian and the effective potential	30
2.3 Cubic approximation	39
2.4 Numerical simulations	43
2.5 Comparison between numerical simulations and perturbation results	46
2.6 Response of the system to low frequency noise	48
2.7 State dependent current redistribution	54
2.8 Conclusions	55
3 Decoherence in superconducting qubits: A Caldeira-Leggett approach	57
3.1 Introduction	57
3.2 Spectral densities of superconducting qubits with environmental resonances	60
3.3 Bloch-Redfield equations: decoherence properties	68
3.4 Frequency renormalization	73
3.4.1 Phase and flux qubits	74
3.4.2 Charge qubits	76
3.5 Non-Markovian behavior near resonance	77
3.5.1 Phase and flux qubits	79
3.5.2 Charge qubits	81
3.6 Conclusions	82

4	Superfluid and Mott Insulating shells of bosons in harmonically confined optical lattices	84
4.1	Introduction	84
4.2	Bose-Hubbard Hamiltonian	87
4.3	Emergence of the shell structure	89
4.3.1	Continuum approximation	92
4.3.2	Nearly degenerate perturbation theory	93
4.3.3	Non-degenerate perturbation theory	101
4.4	Excitations in Mott and superfluid regions	106
4.4.1	Quasiparticle and quasihole excitations in the Mott regions	106
4.4.2	Excitations in superfluid regions	108
4.5	Detection of superfluid shells	114
4.6	Conclusions	118
5	Superfluid and Fermi liquid phases of Bose-Fermi mixtures in optical lattices	120
5.1	Introduction	120
5.2	Bose-Fermi Hubbard Hamiltonian	123
5.3	Finite hopping: perturbative treatment	124
5.4	Order parameter and compressibility	126
5.5	Detection of superfluid and Fermi liquid shells	128
5.6	Conclusions	131
6	Hexatic, Wigner crystal, and superfluid phases of dipolar bosons	134
6.1	Introduction	134
6.2	Hamiltonian	136
6.2.1	Dipolar Wigner crystal phase	136
6.2.2	Superfluid phase	141
6.3	Melting from Wigner crystal to hexatic phase	143
6.4	Transition from hexatic to normal phase	146
6.5	The phase diagram	148
6.6	Supersolid phase	148
6.7	Experimental characterization of various phases	149
6.8	Conclusions	151
7	Quantum fluctuations, entropy removal and non-equilibrium cooling of bosons in harmonically confined optical lattices	152
7.1	Introduction	152
7.2	Mean-field local density approximation	155
7.3	Functional integral approach	159
7.3.1	Slave - fermion technique	160
7.3.2	Hubbard-Stratonovich transformation	163
7.3.3	Mean field theory	165
7.3.4	Beyond mean field theory	166
7.3.5	Equivalence with mean field LDA approach	167

7.4	Analytical results	172
7.5	Non-equilibrium cooling	175
7.6	Conclusions	178
8	Summary and future directions	181
8.1	Superconducting qubits	181
8.2	Ultracold atoms	184
	Bibliography	188

List of Tables

2.1	dc SQUID phase qubit parameters used in the calculations.	35
-----	---	----

List of Figures

1.1	A rf SQUID loop with Josephson junction J with critical current I_c , inductance L , and external flux Φ_a . The effective capacitance across the junction is C , and the current induced is I	4
2.1	Schematic of a phase qubit. I is the bias current, J is the Josephson junction, and C is the equivalent capacitance across the junction. . .	26
2.2	Tilted washboard potential U of the phase qubit (Fig. 2.1) as a function of γ	26
2.3	Schematic of dc SQUID phase qubit. The circuit contains two Josephson junctions J_1 and J_2 , with junction capacitance C_1 and C_2 , respectively. The inductances of the two arms of the SQUID are L_1 and L_2 . The current source I biases the two junctions, while an external flux Φ_a is provided by the current source I_f through the mutual inductance M . The currents flowing through the right and left arms of the SQUID are I_1 and I_2 respectively.	29
2.4	2D surface plot of the potential U for the dc SQUID phase qubit with the parameters in Table 1 and $I = 17.00mA$	34
2.5	Cross-section of U along γ_2 for $\gamma_1 = 0$ with the parameters in Table 1 and $I = 17.00mA$. The numbers label the individual wells.	36
2.6	(a) Cross-section of U along γ_1 for $\gamma_2 = 0$. (b) Cross-section of U along γ_1 for $\gamma_2 = 0$ showing a single well. Parameters are same as in Table 1 and $I = 17.00mA$	38
2.7	(a) Critical current I_c vs. well number along γ_2 . (b) Plasma frequency $\omega_2/2\pi$ vs. well number along γ_2 . For both graphs the well-numbers are from Fig. 2.5.	39
2.8	(a) Energy levels and (b) tunneling rates for different metastable states for well $k = 0$ as a function of bias current I . Symbols are from numerical calculation of the full 2D Hamiltonian using complex scaling, while the solid curves show analytical calculation where coupling between the two junctions is ignored. Dashed curves in panel b) show results from second-order perturbation theory. States are labeled by the ket $ n, m\rangle$, where the first index represents the qubit junction state and the second the isolation junction state. The dashed vertical lines in panel b) indicate avoided level crossings in the corresponding energy levels (see text).	44
2.9	(a) Energy levels and (b) tunneling rates for various metastable states for well $k = 8$ as a function of bias current I . The meaning of the symbols <i>etc.</i> is as in Fig. 2.8	45
2.10	Absolute value of the response functions r_c and r_q as a function of current for well number $k = 0$ and 8. Points are obtained by exact numerical calculation, solid lines are from perturbation theory (see Sec 2.6) and dashed line shows predictions from classical analysis. . .	53

2.11	Expectation value of the current $\langle I_2 \rangle$ flowing through the isolation junction as a function of I for well number 0. The points are numerical calculations based on the exact 2D Hamiltonian whereas the solid lines correspond to an analytical calculation with Hamiltonian \bar{H} without the coupling term (see Eq. 2.24).	55
3.1	Flux qubit measured by a dc SQUID blue line. The qubit corresponds to the inner SQUID loop with critical current I_c and capacitance C_J for both Josephson junctions denoted by the large \times symbol. The inner SQUID is shunted by a capacitance C_s , and environmental resistance R and is biased by a ramping current I_b . The outer dc-SQUID loop has junction capacitance C_0 and critical current I_{c0}	60
3.2	Circuit diagram of the Cooper-pair box. The superconducting island (large \times) is connected to a large reservoir through a Josephson junction with Josephson energy E_J and capacitance C_J . The voltage bias V_g is provided through a resonator (cavity) having environmental impedance $Z(\omega)$, which is connected to the gate capacitance C_g as shown.	62
3.3	Schematic drawing of a phase qubit with an RLC isolation circuit. The phase qubit is shown inside the solid red box, the RLC isolation circuit is shown inside the dashed box to the left, and the internal admittance circuit is shown inside the dashed box to the right.	64
3.4	T_1 (in seconds) as a function of qubit frequency ω_{01} . The solid red curves describe the phase qubit with RLC isolation network (Fig. 3.3) with parameters $R = 50$ ohms, $L_1 = 3.9$ nH, $L = 2.25$ pH, $C = 2.22$ pF, and qubit parameters $C_0 = 4.44$ pF, $R_0 = \infty$ and $L_0 = 0$. The dashed curves correspond to an RL isolation network with the same parameters, except that $C = 0$. Main figure ($T = 0$), inset ($T = 50$ mK) with $\Omega = 141 \times 10^9$ rad/sec.	71
3.5	T_1 (in nanoseconds) as a function of qubit frequency ω_{01} . The solid red curves describe a phase qubit with RLC isolation network (Fig. 3.3) with same parameters of Fig. 3.2 except that $R_0 = 5000$ ohms. The dashed curves correspond to an RL isolation network with the same parameters of the RLC network, except that $C = 0$. Main figure ($T = 0$), inset ($T = 50$ mK) with $\Omega = 141 \times 10^9$ rad/sec.	72
3.6	Renormalization of energy splitting for the phase qubit with RLC isolation network (Fig. 3.3) for the parameters $R = 50$ ohms, $L_1 = 3.9$ nH, $L = 2.25$ pH, $C = 2.22$ pF, and qubit parameters $C_0 = 4.44$ pF, $R_0 = 5000$ ohms and $L_0 = 0$, $T = 0$, and $\Omega = 141 \times 10^9$ rad/sec. Parameters are same as in Ref. [54].	76
3.7	Population of the excited state of the dc SQUID phase qubit (Fig. 3.3) as a function of time $\rho_{11}(t)$, with $\rho_{11}(t = 0) = 1$ for $R = 50$ ohms (solid black curve), 350 ohms (dotted blue curve), and $R = 550$ ohms (dashed red curve), and $L_1 = 3.9$ nH, $L = 2.25$ pH, $C = 2.22$ pF, $C_0 = 4.44$ pF, $R_0 = \infty$ and $L_0 = 0$	81

4.1	Phase diagram of the homogeneous Bose Hubbard model. For the inhomogeneous Bose Hubbard system, the dashed red line indicates the values of the local chemical potential $\mu_{\mathbf{r}}$ that the system exhibits from $\mu_{\mathbf{r}} = 2.5U$ (Fig 4.4) or $\mu_{\mathbf{r}} = 2.2U$ (Fig 4.5) at the center of the trap to $\mu_{\mathbf{r}} = 0$ at the edge of the trap for $t = 1.25 \times 10^{-2}U$. This figure indicates how the system exhibits an alternating structure of Mott and superfluid shells	90
4.2	Schematic plot of local energies $E_{0,n}(\mathbf{r})$ and $E_{0,n+1}(\mathbf{r})$ showing the degenerate radius $R_{c,n}$. This local energy degeneracy is lifted by the the presence of a finite hopping t , which leads to an avoided level crossing shown as dashed red curve, and to the emergence of a superfluid region with inner radius $R_{n,-}$ and outer radius $R_{n,+}$	95
4.3	Schematic plot of superfluid regions, shown in red, and the Mott regions, shown in white. The radius $R_{c,n}$ separates Mott shells with filling factor n and $n + 1$ for $t = 0$. The superfluid regions have inner radius $R_{n,-}$ and outer radius $R_{n,+}$ and emerge between Mott shells n and $n + 1$ for non-zero t	97
4.4	a) Shell structure of Mott and superfluids regions in a 2D square optical lattice with harmonic envelope as a function of radius r/a for $t \neq 0$. The superfluid regions are shown in red whereas the Mott regions are shown in white. The black circles indicate the Mott boundaries $R_{c,n}$ at $t = 0$. b) The local filling factor $n(\mathbf{r})$ is shown in solid lines for $t \neq 0$ and in dashed lined for ($t = 0$). The red curve shows the local superfluid order parameter $ \psi(\mathbf{r}) ^2$. The parameters are $\Omega = 6 \times 10^{-6}U$, $t = 1.25 \times 10^{-2}U$ and $\mu = 2.5U$	98
4.5	a) Shell structure of Mott and superfluids regions in a 2D square optical lattice with harmonic envelope as a function of radius r/a for $t \neq 0$. The superfluid regions are shown in red whereas the Mott regions are shown in white. The black circles indicate the Mott boundaries $R_{c,n}$ at $t = 0$. b) The local filling factor $n(\mathbf{r})$ is shown in solid lines for $t \neq 0$ and in dashed lined for ($t = 0$). The red curve shows the local superfluid order parameter $ \psi(\mathbf{r}) ^2$. The parameters are $\Omega = 6 \times 10^{-6}U$, $t = 1.25 \times 10^{-2}U$ and $\mu = 2.2U$	100
4.6	The squared amplitude of the superfluid order parameter $ \psi(\mathbf{r}) ^2$ is shown as a solid line (red) for the nearly degenerate case, and as a dashed line (gray) for the non-degenerate case. Notice that near the boundaries where $\psi(\mathbf{r}) \approx 0$, both methods agree and describe the superfluid accurately. However, at the center of the superfluid shell, the non-degenerate method breaks down. The parameters are same as in Fig. 4.4, and we show the order parameter for the inner most superfluid shell, between $n = 2$ and $n = 3$ Mott shells.	105
4.7	a) Quasiparticle E_{qp} (solid line), quasihole E_{qh} (dashed line),and Mott gap E_g (red) energies for $\mathbf{k} = 0$ versus r/a . b) Sound velocity for the outermost superfluid ring versus r/a . Same parameters as in Fig. 4.4	107

4.8	Three-dimensional view of a vortex-antivortex pair in 2D superfluid shell separating two 3D Mott regions.	114
4.9	Schematic plot for the detection of superfluid shells using Bragg spectroscopy. The angles θ_1 and θ_2 indicate the locations of strongest momentum transfer from the Bragg beams (large green arrows) to the rotating superfluid shells of radii R_1 and R_2 . The gray arrows indicate the sense of rotation of the superfluid shells.	117
5.1	(a) Shell structure of Bose-Fermi mixtures in harmonically confined optical lattices showing a coexisting Bose-Mott and Fermi-band insulator region at the center ($n_B = 1, n_F = 1$), a coexisting Bose-Mott insulator and Fermi liquid region (in blue), a Bose-Mott insulator region ($n_B = 1, n_F = 0$), and Bose-Superfluid region at the edge (in red). (b) filling factors for fermions shown as the solid dark blue curve and for bosons shown as the dashed red curve. The solid parabolic curve in light blue shows the order parameter in the superfluid region. The parameters used are $t_F = t_B = 0.0325U_{BB}$, $U_{BF} = 0.1U_{BB}$, $\mu_B = 0.8U_{BB}$, $\mu_F = 0.4U_{BB}$ and $\Omega_F = \Omega_B = 8 \times 10^{-6}U_{BB}$, which are representative of Bose-Fermi mixtures with nearly the same mass such as ${}^6\text{Li}$ and ${}^7\text{Li}$, ${}^{39}\text{K}$ and ${}^{40}\text{K}$, or ${}^{172}\text{Yb}$ and ${}^{173}\text{Yb}$. For the parameters chosen, the widths of the superfluid and FL shells are several times larger than the lattice spacing a	132
5.2	Schematic plot for the detection of outer red superfluid and inner blue Fermi liquid shells using Bragg spectroscopy. The angles θ_1 and θ_2 indicate the locations of strongest momentum transfer from the Bragg beams (large green arrows) to the rotating superfluid and Fermi liquid shells of radii R_1 and R_2 . The gray arrows indicate the sense of rotation of the conducting shells.	133
6.1	Plots of the dipolar Wigner crystal energy E_{DWC} in units of the dipolar energy E_D versus the inverse of the variational parameter α for $r_D = 10$ (blue dot-dashed line), $r_D = 13.1$ (red dotted line), $r_D = 17$ (green solid line). The horizontal (black dot-dashed line) is the energy E_{DSF} for a uniform superfluid.	142
6.2	Finite temperature phase diagram of T/E_D versus r_D showing the dipolar superfluid (DSS), dipolar Wigner crystal (DWC), dipolar hexatic (DHF) and dipolar normal fluid (DNF) phases.	147
6.3	Bragg scattering patterns near the first reciprocal vectors for a) the dipolar Wigner crystal phase and for b) the dipolar hexatic fluid phase.	150
7.1	The number density of atoms per site in 2D between $n = 2$ and $n = 0$ Mott states. The parameters used are $t = 0.0125U$, $U = 1$, and temperature $T = 0.05U$ much higher than the critical temperature.	157

7.2	The local entropy in 2D between $n = 2$ and $n = 0$ Mott states. The parameters used are the same as in Fig. 7.1.	159
7.3	The local critical temperature in 2D between $n = 2$ and $n = 0$ Mott shells calculated using slave fermion (black solid), slave fermion with gaussian fluctuations (black dashed), and mean field LDA method (blue). The parameters used are $t = 0.0125U$ and $U = 1$	168
7.4	The order parameter in 2D between $n = 2$ and $n = 1$ Mott shells. The parameters used are $t = 0.0125U$, $U = 1$, and temperature $T = 0.015U$. The black solid curve is calculated using slave fermionic theory, the black dashed curve using slave fermion with gaussian fluctuations, and blue curve using mean field LDA theory.	170
7.5	The local entropy in 2D between $n = 2$ and $n = 1$ Mott state using the slave fermion approach upto fourth order gaussian correction in $\phi_{\mathbf{q}}$ (dashed) and spin wave spectrum (solid). The parameters used are $t = 0.0125U$, $U = 1$, and temperature $T = 0.02U$	173
7.6	The energy levels of the $F = 1$ trapped atoms for different m levels as a function of site index. The cooling technique employs RF knives that selectively takes the atoms in normal phase, shown as dashed (red) curve, to antitrapped $m = -1$ state.	177
7.7	The number density of atoms per site in 3D between $n = 2$ and $n = 0$ Mott states using the slave fermion approach with Gaussian corrections. The parameters used are $t = 0.0125U$, and $U = 1$. The harmonic trap potential is $1/2\Omega r^2$ where $\Omega = 10^{-5}U$. The temperature $T = 0.1U$ and $\mu = 1.4$ for dashed curve. After entropy removal which kicks out atoms in the normal phase between $n = 0.8$ and $n = 0.2$ and atoms between $n = 1.2$ and $n = 1.8$, the new temperature is $T = 0.03U$ and $\mu = 1.23$. The new density distribution is shown in red.	179

List of Definitions of Selected Symbols

- h : Planck's constant
- \mathcal{L} : Lagrangian
- H : Hamiltonian
- $\delta(x)$: delta function of variable x

Chapter 1:

- n : number density of a gas of free bosons
- n_0 : condensate density
- μ : chemical potential
- V : total volume
- $n_{\mathbf{p}}^{reg}$: the expected number of particles in momentum state \mathbf{p} for Bose-Einstein statistics
- λ : two particle scattering amplitude in the Born approximation
- a : s-wave scattering length
- N : total number of bosons
- $|\Phi_\lambda\rangle$: ground state of the weakly interacting Bose gas
- ω_p : Josephson plasma frequency
- E_J : Josephson energy
- E_c : capacitance energy in superconductors
- E'_c : charging energy in the BEC double well potential
- N_0 : number of bosons present in the left and right well
- \bar{N} : number of transferred particles across the weak link of the superconductor or across the barrier of the BEC double well potential
- ω_R : Rabi oscillation frequency between the two modes of the BEC in a double well potential

Chapter 2:

- r_c : classical response function
- r_q : quantum response function

Chapter 3:

- ω_{01} : transition frequency between $|0\rangle$ and $|1\rangle$ qubits states
- $J(\omega)$: generic spectral density
- $J_1(\omega)$: spectral density of flux and phase qubits
- $J_2(\omega)$: spectral density of charge qubits
- Ω : environmental resonance frequency of phase qubits
- Γ : resonance width of phase qubits
- Ω_1 : environmental resonance frequency for flux qubits
- Γ_1 : resonance width of flux qubits
- Ω_2 : environmental resonance frequency for charge qubits
- Γ_2 : resonance width of charge qubits
- T_1 : relaxation time
- T_2 : decoherence time
- δE : energy shift of the qubit due to the environment
- Ω_{Ra} : frequency of the environmentally generated Rabi oscillation for phase and flux qubits
- Δ : frequency of the environmentally generated Rabi oscillation for charge qubits

Chapter 4:

- t : tunneling energy in the Bose-Hubbard Hamiltonian
- μ : chemical potential
- $V(\mathbf{r})$: harmonically confined trapping potential
- $\mu(\mathbf{r})$: local chemical potential $\mu - V(\mathbf{r})$
- U : on-site interaction energy in the Bose-Hubbard Hamiltonian
- n : number of atoms per site in the Mott phase
- z : number of nearest neighbors for each site in the optical lattice
- a : separation between lattice sites
- $R_{n,+}$: outer radius of the superfluid shell between n and $n + 1$ Mott shells

- $R_{n,-}$: inner radius of the superfluid shell between n and $n + 1$ Mott shells
- $\kappa(\mathbf{r})$: local compressibility of the superfluid regions
- $c(\mathbf{r})$: local sound velocity in the superfluid regions
- $\rho_s(\mathbf{r})$: local superfluid density
- T_{BKT} : BKT transition temperature for the superfluid regions
- $\epsilon_{i,f}$: internal initial and final state of the bosons in the superfluid regions

Chapter 5:

- K_B : kinetic energy of bosons
- K_F : kinetic energy of fermions
- μ_B : chemical potential of bosons
- μ_F : chemical potential of fermions
- t_B : hopping energy of bosons
- t_F : hopping energy of fermions
- U_{BB} : on site interaction energy of bosons
- U_{BF} : on site Bose-Fermi interaction energy
- $V_B(\mathbf{r})$: harmonic trap potential for bosons
- $V_F(\mathbf{r})$: harmonic trap potential for fermions
- n_B : number of bosons per site in the Bose-Mott phase
- n_F : number of fermions per site in the Fermi-Mott phase
- R_{B,n_B,n_F} : radius of the boundary between shells (n_B, n_F) and $(n_B + 1, n_F)$
- R_{F,n_B} : radius of the boundary between shells $(n_B, 0)$ and $(n_B, 1)$

Chapter 6:

- a : separation between bosons in DWC phase
- ρ : number density of bosons
- D : dipolar interaction strength
- U : local interaction strength
- E_D : characteristic dipolar energy $D\rho^{3/2}$

- E_U : characteristic local energy $U\rho$
- K : characteristic kinetic energy $\hbar^2\rho/2m$
- r_D : ratio between E_D and K
- r_U : ratio between E_U and K
- N : total number of bosons
- σ : width of the local Gaussian wave functions
- α : dimensionless variational parameter σ/a
- r_0 : screening length of the dipolar potential
- T_h : critical temperature for the phase transition from DSF to DHF
- T_n : critical temperature for the phase transition from DHF to DNF

Chapter 7:

- \mathcal{Z} : grand-canonical partition function
- Ω : thermodynamic potential
- $S(\mathbf{r})$: local entropy
- $n(\mathbf{r})$: local number density
- $\chi(\mathbf{r})$: local compressibility
- $T_c(\mathbf{r})$: local critical temperature for onset of superfluidity
- $E_{\pm}(\mathbf{r})$: local energies describing the superfluid region between p and $p + 1$ Mott phase
- \hat{b}_i^{α} : slave boson operator that creates bosons of type α at the site i
- \hat{f}_i^{α} : slave fermion operator that creates fermions of type α at the site i
- N_s : number of lattice sites for a given local chemical potential
- w : waist of the laser beam that creates the optical lattice
- ω_0 : frequency of the magnetic trap

List of Abbreviations

BEC	Bose Einstein Condensate
SQUID	Superconducting Quantum Interference Device
MQC	Macroscopic Quantum Coherence
BKT	Berezinsky-Kosterlitz-Thouless
WKB	Wentzel-Kramers-Brillouin
LDA	Local Density Approximation
DWC	Dipolar Wigner Crystal
DSF	Dipolar Superfluid
DHF	Dipolar Hexatic Fluid
DSS	Dipolar Supersolid
DNF	Dipolar Normal Fluid
KTNHY	Kosterlitz-Thouless-Nelson-Halperin-Young

Chapter 1

Introduction

1.1 Introduction

Ever since its discovery, quantum mechanics has been used to describe a wide range of physical systems and has become the foundation of different branches of physics including condensed matter, atomic-molecular-optical and particle physics. However, until recently, our ability to control and exploit quantum phenomena in matter was at a very primitive stage. Two seminal experiments which heralded an era of systematic study and control of coherent quantum phenomena are: realization of the first Bose Einstein condensates by Cornell, Wieman and Ketterle in 1995 [1, 2], and the demonstration of the first superconducting qubit by Nakamura and co-workers in 1999 [3]. The former led to the exciting field of ultracold atoms where quantum many-body physics of interacting bosonic and fermionic systems can be experimentally studied. The later gave rise to the field of superconducting qubits where macroscopic electrical circuits can be viewed as artificial atoms which can be controlled and manipulated quantum mechanically. In this thesis I will present my research in these two different areas of quantum physics. My first area will be the study of theoretical models of ultracold atoms which are relevant to condensed matter systems. Second is the study of quantum decoherence in superconducting qubits.

In this introductory chapter I will review certain aspects of Superconducting QUantum Interference Devices (SQUIDs) and atomic Bose-Einstein Condensates (BECs). In Sec. 1.1 I will review why SQUIDs are very well suited to study superposition of macroscopically distinct quantum states. This makes them a very good candidate for a qubit in a quantum computer [4]. In Sec. 1.2 I will describe two key features of Bose-Einstein condensates viz. symmetry breaking and off-diagonal long range order. These two properties are manifested as superfluidity and macroscopic quantum coherence. In Sec 1.3 I will try to connect these two systems (SQUIDs and BECs) and describe how the Josephson effect, which is the central phenomenon that governs the dynamics of SQUIDs, can be observed in BECs. In particular I will discuss how one can study an interference of two different macroscopic BEC wave functions. Finally I will conclude in Sec 1.4 with a layout for the rest of the thesis.

1.2 Macroscopic quantum phenomena in SQUIDs

The goal of preparing a macroscopic object in a quantum mechanical superposition of macroscopically-distinct states is one which has been consciously pursued for the last twenty years. In fact, experiments directly or indirectly related to this question have been carried out on quantum optics [5], magnetic systems [6], mesoscopic grains [3], dislocations [7] and other systems. However, the area in which this program has been most systematically pursued is that of electronic devices incorporating the Josephson effect, and recently a milestone in this area has been

passed with a couple of experiments [8, 9] which give a very strong evidence that macroscopic quantum coherence (MQC) has indeed been obtained in such systems.

What distinguishes SQUIDS from these other candidate systems for macroscopic quantum coherence? First, Josephson device experiments are on a single physical system subjected to repeated trials under the same conditions; by contrast, in an experiment to look for MQC in (e.g.) biomolecules, one typically measures the summed response of a large number of independent and equivalent systems. While it is certainly possible to look for the effects of (e.g.) quantum tunneling out of a metastable well at the single-grain or single molecular level, any evidence of MQC as such has not been claimed at this level. Although this ‘time ensemble’ aspect is of no special relevance so long as one is interested only in verifying that the predictions of quantum mechanics continue to work at the relevant level of ‘macroscopicness’, it becomes crucial both in the context of quantum computing and testing the limits of quantum theory.

The second feature which distinguishes the SQUID system is simply that the physics of the relevant degree of freedom (in this case the trapped flux or circulating current) is believed to be extremely well understood at the classical level, to the extent that all the parameters relevant to MQC can be independently measured in experiments which stay within the (quasi-) classical regime. By contrast, in most other candidate systems there are a number of parameters and/or effects which can affect the MQC behavior quantitatively, and which have to be guessed at since independent measurement is not usually possible.

For the purposes of illustration I shall consider the very simplest system rele-

vant to the observation of MQC, namely a single ring closed with a single Josephson junction (“a SQUID”) and subject to an external flux Φ_a which for present purpose I treat as a classical control parameter. A schematic for such a device is shown in Fig. 1.1. For such a system the dynamical variable is the trapped flux Φ (or equivalently the circulating current I) and the macroscopically distinct states whose quantum superposition we seek to produce correspond to the values of Φ which differ by a flux quanta $\phi_0 = h/2e$, where e is the charge of an electron.

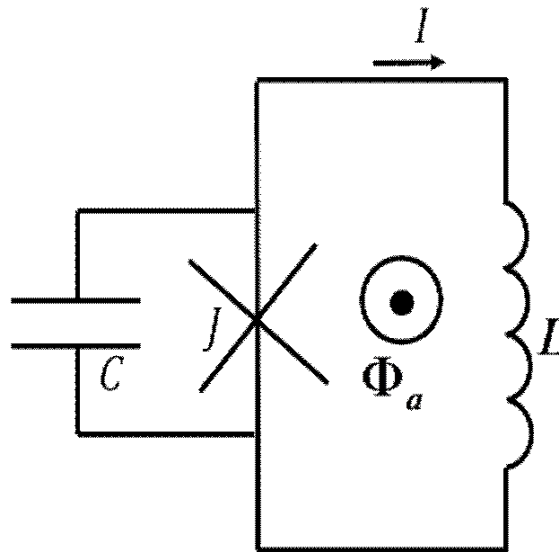


Figure 1.1: A rf SQUID loop with Josephson junction J with critical current I_c , inductance L , and external flux Φ_a . The effective capacitance across the junction is C , and the current induced is I .

Let me first provide a classical description for this system [10]. In this description, one can treat Φ as completely analogous to the position variable x of a particle moving in one dimensional potential. In this picture the role of particle mass is played by the effective capacitance C of the junction and the potential $U(\Phi)$

in which it moves is a sum of the self inductance term of the form $(\Phi - \Phi_a)^2/2L$ (L = self inductance of the ring) and a coupling term of the form $I_c\phi_0/2\pi\Phi$ due to the Josephson junction. This simple model appears to describe rather well the dynamics of the flux in the classical regime, that is the regime where we expect the effects of treating Φ as a quantum mechanical operator to be unimportant.

To extend the description to the quantum regime, the standard procedure is to impose a canonical commutation relation between the dynamical coordinate Φ and its conjugate momentum $p_\Phi \equiv \partial\mathcal{L}/\partial\dot{\Phi}$ (where \mathcal{L} is the Lagrangian). For the observation of MQC, we need to adjust the parameters L , I_c , and Φ_a so that $U(\Phi)$ has two nearly degenerate minima. The crucial step in this argument is of course the interpretation of the commutation relation $[\hat{p}_\Phi, \hat{\Phi}] = i\hbar$. One can ask the following two questions as posed by Leggett [10]. First, exactly what is it about the classical equation of motion which assures us that it is legitimate to quantize it at all? Can one quantize the equations of mathematical economics? If not, why not? Second, does it matter that the form of $U(\Phi)$ which enters is itself a consequence of considerations which are essentially quantum mechanical in nature? Is one somehow in the danger of quantizing the same thing twice?

In response to the first question, Leggett argues that if we believe quantum mechanics at all, we believe that there is a set of coordinates $\{x_i\}$ such that their canonically conjugate momentum can be defined, and that for this set of coordinates, at least, the quantization procedure implicit in the requirement $p_i \rightarrow -i\hbar(\partial/\partial x_i)$ is legitimate. At the same time, it is well known that this canonical quantization procedure is invariant under any (nonsingular) transformation to a new set of

coordinates, and we regard Φ , together with a large set of other unspecified coordinates, as forming just such a new coordinate set. Consequently the interpretation of $p_\phi \equiv \partial\mathcal{L}/\partial\dot{\Phi}$, is legitimate. At what level of ‘macroscopicness’ does the quantizing of an Hamiltonian becomes illegitimate is still a matter of extensive debate [11].

In response to the second question, Leggett draws an analogy between the procedure one is implicitly following here and the familiar procedure used in the case of diatomic molecules. In the latter case, typically, one first holds the relative position \mathbf{R} of the nuclei fixed and solves the Schrödinger equation for the electrons, obtaining thereby some electronic energy $E(\mathbf{R})$ which contains all the effects of quantum mechanics as applied to the electrons. One then treats the quantity $E(\mathbf{R})$ as a part of the effective potential for the nuclear motion, and solves for the classical vibrational motion in this potential. Finally one quantizes this classical motion to obtain the familiar quantized vibrational levels. The procedure that one follows in quantizing the motion of a SQUID is essentially the same.

So far, the discussion has proceeded by analogy with the description of a single isolated one-particle system. However, an important property which distinguishes the ‘macroscopic’ coordinates characteristic of condensed matter systems from the simple one-particle coordinates is that the former are inevitably coupled strongly to other degrees of freedom. Thus it is necessary to build into the description from the start some account of the interaction of the flux with all the other relevant degrees of freedom. From general notions concerning the effects of system environment interaction, one would expect that in the quantum regime, one important effect of the latter would be to ‘decohere’ superpositions of states corresponding to appreciably

different values of Φ , and thereby to tend to wash out the phenomenon of MQC. This issue will be discussed in great detail later on in this thesis.

1.3 Many body quantum coherence in Bose condensates

Bose Einstein Condensation (BEC) represents the classic example of many body quantum coherence, and a genuinely quantum-statistical phase transition in that it occurs without the help of interaction (Einstein called it “condensation without attraction” [12]). Long range order, symmetry breaking, and order parameter are key concepts underlying the phenomenon of BEC [13]. To understand these concepts let me first consider an ideal Bose gas. In an ideal Bose gas at sufficiently low temperature, we get a Bose-Einstein condensate in which the lowest energy state with momentum $p = 0$ becomes occupied by a macroscopic number of particles. This macroscopic occupation suggests an expression of the total atom density n in terms of an integral over the momenta \mathbf{p} of the number of particles occupying the corresponding momentum state where the zero-momentum state is explicitly retained. That is

$$n = \int (n_0 \delta(\mathbf{p}) + (2\pi\hbar)^{-3} n_{\mathbf{p}}^{(reg)}) d^3 p, \quad (1.1)$$

$$n_{\mathbf{p}}^{(reg)} = \frac{1}{e^{\beta(p^2/2m - \mu)} - 1} \quad (1.2)$$

where n_0 is the density of particles in the condensate state with $\mathbf{p} = 0$, and $n_{\mathbf{p}}^{(reg)}$ is the occupation number of particles in the momentum states with $\mathbf{p} \neq 0$. Finally, $\beta = 1/kT$, T is the temperature, k is Boltzmann constant, m is the particle mass, and μ is the chemical potential, .

There exists a critical temperature T_{BEC} below which an ideal Bose gas exhibits BEC and when the chemical potential $\mu = 0$. At such temperatures, the condensate density n_0 is given by

$$n_0 = n \left(1 - (T/T_{BEC})^{3/2}\right). \quad (1.3)$$

The critical temperature

$$T_{BEC} = \alpha \frac{\hbar^2}{m} n^{2/3} \quad (1.4)$$

where¹

$$\alpha = \frac{2\pi}{\zeta^{2/3}(3/2)} = 3.3142\dots \quad (1.5)$$

At high temperature $T > T_{BEC}$ there is no condensate which means $n_0 = 0$. The question we shall discuss below is how this behavior is modified by the presence of weak interatomic interactions. This problem, due to the existence of a simple analytical method, serves well to illustrate the new features of Bose condensation of interacting particles: spontaneous symmetry breaking and the off-diagonal long-range order.

1.3.1 Spontaneous symmetry breaking and off-diagonal long range order

The Hamiltonian for a weakly interacting Bose gas with a short-range interaction is given by [13]

$$\mathcal{H} = \int d\mathbf{r} \left(-\hat{\phi}^\dagger(\mathbf{r}) \frac{\hbar^2}{2m} \nabla^2 \hat{\phi}(\mathbf{r}) + \frac{\lambda}{2} \hat{\phi}^\dagger(\mathbf{r}) \hat{\phi}^\dagger(\mathbf{r}) \hat{\phi}(\mathbf{r}) \hat{\phi}(\mathbf{r}) \right) \quad (1.6)$$

¹ $\zeta(x)$ is the Riemann zeta function.

in dimension $D = 3$. The operator $\hat{\phi}^\dagger(\mathbf{r})$ is the Bose field operator which creates a particle at position \mathbf{r} , and $\hat{\phi}(\mathbf{r})$ is the Bose field operator which destroys a particle at position \mathbf{r} . The coupling constant λ is the two particle scattering amplitude in the Born approximation and is equal to $4\pi\hbar^2 a/m$ where a is the s-wave scattering length.

Let N be the total number of particles. At zero temperature, the BEC state is characterized by occupation of the zero momentum state where $\mathbf{p} = \hbar\mathbf{k} = 0$ by all N particles. Such a state is denoted by $|BEC\rangle_N = (a_{\mathbf{k}=0}^\dagger)^N |vac\rangle$ where the operator $a_{\mathbf{k}}^\dagger$ creates a particle in momentum state \mathbf{k} and $|vac\rangle$ is the vacuum state. The operator $a_{\mathbf{k}}$ destroys a particle in momentum state \mathbf{k} . We thus get

$$a_{\mathbf{k}=0}|BEC\rangle_N = \sqrt{N}|BEC\rangle_{N-1}. \quad (1.7)$$

The formula given above, at large N , suggests replacing the number state $|BEC\rangle_N$ by a coherent state $|BEC\rangle$ such that $a_{\mathbf{k}=0}|BEC\rangle = \sqrt{N}|BEC\rangle$. This can be achieved if the BEC state is understood as a coherent state, and the Hamiltonian given by Eq. (1.6) is considered in the Fock space [16] where all particle numbers are allowed. Such an approach gives results equivalent to that of the problem with fixed particle number N in the limit $N \rightarrow \infty$ since for a coherent state the quantum uncertainty in the number of particles $\delta N = \sqrt{N} \ll N$. Upon such a replacement, the field operator $\hat{\phi}(\mathbf{r}) = V^{-1/2} \sum_{\mathbf{k}} a_{\mathbf{k}} e^{i\mathbf{k}\cdot\mathbf{r}}$ turns into a classical field $\phi = \sqrt{N/V} = \sqrt{n}$, where V is the system volume and n is the number density of particles.

To describe the BEC state we are thus led to consider the coherent states,

$$|\phi\rangle = \exp\left(\sqrt{V}\left(\phi\hat{a}_0^\dagger - \phi^*\hat{a}_0\right)\right)|0\rangle \quad (1.8)$$

which have the desired property $\hat{\phi}|\phi\rangle = \phi|\phi\rangle$. These states do not correspond to any specific number of particles, in fact they are characterized by a distribution of particle numbers. Accordingly, the states $|\phi\rangle$ are not invariant under the number operator $\hat{N} = \sum_{\mathbf{k}} a_{\mathbf{k}}^\dagger a_{\mathbf{k}}$, while the Hamiltonian given by Eq. (1.6) commutes with \hat{N} . One has to understand why the BEC state apparently does not respect the particle number conservation.

We start by noting that

$$e^{i\gamma\hat{N}}|\phi\rangle = |e^{i\gamma}\phi\rangle \quad (1.9)$$

and

$$e^{i\gamma\hat{N}}\mathcal{H}e^{-i\gamma\hat{N}} = \mathcal{H} \quad (1.10)$$

i.e. the operator $e^{i\gamma\hat{N}}$, applied to $|\phi\rangle$, produces a state of the same energy as that of $|\phi\rangle$ but with a phase shifted by γ . Since the overlap of coherent states obeys $|\langle\phi'|\phi\rangle|^2 = e^{-V|\phi'-\phi|^2}$, any two different states $|\phi\rangle, |\phi'\rangle$ are orthogonal in the limit $V \rightarrow \infty$. Thus the states with different phase factors, $|\phi\rangle, |e^{i\gamma}\phi\rangle$, are macroscopically distinct. This observation demonstrates that the BEC states form a degenerate manifold parameterized by a phase variable $0 < \gamma < 2\pi$.

To clarify the origin of this degeneracy let us find the state $|\phi\rangle$ that provides minimum energy given the Hamiltonian given by Eq. (1.6). Taking a minimum at fixed particle density can be done by adding to \mathcal{H} a term proportional to \hat{N} , $\mathcal{H} \rightarrow \mathcal{H} - \mu\hat{N}$. Taking the expectation value, we obtain

$$U(\phi) = \langle\phi|\mathcal{H} - \mu\hat{N}|\phi\rangle = \frac{\lambda}{2}|\phi|^4 - \mu|\phi|^2 \quad (1.11)$$

- the so called Mexican hat potential. The energy minima are found on the circle $|\phi|^2 = \mu/\lambda$ i.e. the phase of ϕ is arbitrary, while the modulus $|\phi|$ is fixed, thereby giving a relation between the density and the chemical potential $\mu = \lambda n$.

The macroscopic Hamiltonian given by Eq. (1.6) has global $U(1)$ symmetry, since it is invariant under adding a constant phase factor to the wavefunction of the system, $\hat{\phi} \rightarrow e^{i\gamma}\hat{\phi}$. The ground states, however, do not possess this symmetry: adding a phase factor to the state $|\phi\rangle$ produces a different ground state. This phenomenon, called *spontaneous symmetry breaking*, is absent in the non-interacting ideal Bose gas. In the interacting system, the $U(1)$ symmetry breaking has a very fundamental consequence: it leads to *superfluidity* [13].

A system whose gauge symmetry has been spontaneously broken can be described by an order parameter that behaves in many aspects like a macroscopic wave function $\Psi(\mathbf{r})$. In the simplest cases, the order parameter reduces to a complex scalar, $\Psi(\mathbf{r}) = \sqrt{n(\mathbf{r})}e^{i\gamma(\mathbf{r})}$, where $n(\mathbf{r})$ is the “superfluid density” and $\gamma(\mathbf{r})$ is the phase. For Bose-Einstein condensates of dilute alkali gases, $\Psi(\mathbf{r})$ is the wave function of the macroscopically occupied one-atom state.

There is yet another way to understand the phenomenon of $U(1)$ symmetry breaking, due to Penrose and Onsager [14], that does not require consideration of the states with fluctuating particle number. Given the ground state $|\Phi_\lambda\rangle$ of the weakly interacting Bose gas described by Eq. (1.6), we can get the reduced density matrix

$$R(x, x') = \langle \Phi_\lambda | \hat{\phi}^\dagger(x') \hat{\phi}(x) | \Phi_\lambda \rangle. \quad (1.12)$$

Using the translational invariance, one expects that the quantity $R(x, x')$ will depend only on the distance $x - x'$ between the two points. By going to Fourier representation, one can transform Eq. (1.12) to the form

$$R(x, x') = \frac{1}{(2\pi)^3} \int d^3k e^{-i\mathbf{k}(\mathbf{x}-\mathbf{x}')} n_{\mathbf{k}}, \quad (1.13)$$

where

$$n_{\mathbf{k}} = \langle \Phi_\lambda | \hat{a}_{\mathbf{k}}^\dagger \hat{a}_{\mathbf{k}} | \Phi_\lambda \rangle \quad (1.14)$$

In a Bose condensate, the particle distribution $n_{\mathbf{k}}$ has singularity at $\mathbf{k} = \mathbf{0}$,

$$n_{\mathbf{k}} = n_0 (2\pi)^3 \delta(\mathbf{k}) + f(\mathbf{k}) \quad (1.15)$$

where $f(\mathbf{k})$ is a smooth function. Accordingly the density matrix in Eq. (1.12) has two terms,

$$R(x, x') = n_0 + \tilde{f}(x - x'), \quad (1.16)$$

with

$$\tilde{f}(x - x') = \frac{1}{(2\pi)^2} \int d^3k e^{-i\mathbf{k}(\mathbf{x}-\mathbf{x}')} f_{\mathbf{k}} \quad (1.17)$$

The constant n_0 is independent of point of separation, and the second part, $\tilde{f}(x - x')$, vanishes at large $|x - x'|$.

In ordinary liquids all correlations vanish at several interatomic distance. Thus a density matrix that does not vanish at large point separation represents an anomaly. The finite limit $n_0 = \lim_{|x-x'| \rightarrow \infty} \langle \Phi_\lambda | \hat{\phi}^\dagger(x') \hat{\phi}(x) | \Phi_\lambda \rangle$ suggests that the quantities $\hat{\phi}(x)$, $\hat{\phi}^\dagger(x')$ in some sense have finite expectation values $\langle \hat{\phi}(x) \rangle = e^{i\gamma} \sqrt{n_0}$ with fixed modulus, but an undetermined phase. The name *off diagonal long range*

order or ODLRO, associated with this phenomenon, expresses the fact that in the density matrix the ordering is revealed by the behavior of the off-diagonal component $R(x, x')|_{|x-x'|\rightarrow\infty}$.

1.4 Macroscopic quantum interference in atomic BECs

Bose Einstein condensates, along with other exotic quantum many body phenomena like superconductivity, superfluidity, the Josephson effects, and the integer quantum Hall effects are examples of macroscopic quantum phenomena. However, they cannot be viewed as direct examples of superposition of macroscopically distinct states. I will now review certain aspects of macroscopic quantum interference in BECs. The essential idea is borrowed from the Josephson effect in superconductors which governs the dynamics of SQUIDS.

1.4.1 Josephson effect

Josephson predicted [15] that, between two weakly linked superconductors of phases γ_1 and γ_2 , a non-dissipative particle (Cooper pair) current flows between them whose value is $I(\gamma) = I_c \sin \gamma$, where I_c is the critical current and

$$\gamma = \gamma_2 - \gamma_1 \equiv \int_1^2 d\mathbf{r} \cdot \nabla \gamma(\mathbf{r}) \quad (1.18)$$

is the relative phase. He also predicted that in presence of non-zero chemical potential difference $\mu = \mu_2 - \mu_1$, the relative phase rotates as $\dot{\gamma} = -\mu/\hbar$. The Josephson relations can be obtained from very general considerations and can be applied to any macroscopic wave functions, like the Gross-Pitaevskii [13] wave function of BECs.

They can be obtained as the equations of motion of the “pendulum Hamiltonian”

$$H(\gamma, \bar{N}) = E_J(1 - \cos \gamma) + \frac{1}{2}E_c\bar{N}^2, \quad (1.19)$$

where $E_J = \hbar I_c$ is the Josephson coupling energy, \bar{N} is the number of transferred particles across the weak link, and $E_c \equiv \partial\mu/\partial\bar{N}$ is the capacitive energy due to interactions. In the absence of external constraints, $\mu = E_c\bar{N}$. For trapped BECs, E_c can be obtained to a good accuracy from the Thomas-Fermi (TF) calculation of the chemical potential.

When both E_c and $k_B T$ are $\ll E_J$, the Josephson pendulum Hamiltonian given by Eq. (1.19) can be approximated as a harmonic oscillator whose frequency

$$\omega_p = \frac{1}{\hbar} \sqrt{E_J E_c} \quad (1.20)$$

is the Josephson plasma frequency.

1.4.2 Josephson effect in a BEC in a double well potential

It is possible to create two Bose condensates which are spatially separated by a double well potential. The barrier in between the two wells can be viewed as a weak link between the two condensates and one can study Josephson effect in such systems. Furthermore high-contrast matter-wave interference can be observed after switching off the potential and letting the condensates expand and overlap. Such an experiment was performed [17] by evaporatively cooling sodium atoms in a double-well potential formed by magnetic and optical forces.

To model such a system let me consider a symmetric double-well single particle potential $V(\mathbf{r})$ with minima at \mathbf{r}_1 and \mathbf{r}_2 , and with no loss of generality I set $V(\mathbf{r}_1) =$

$V(\mathbf{r}_2) = 0$. I assume the potential is such that the two lowest states are closely spaced and well separated from higher levels of the potential, and that many particle interactions do not significantly change this situation. This assumption permits a two-mode approximation to the many-body description of the system. To proceed I expand the potential around each minimum as

$$V(\mathbf{r}) = \tilde{V}^2(\mathbf{r} - \mathbf{r}_j) + \dots \quad (1.21)$$

where j assumes values 1, 2, and $\tilde{V}^2(\mathbf{r} - \mathbf{r}_j)$ is the parabolic approximation to the potential in the vicinity of each minimum. I now define the state $u_0(\mathbf{r})$ as the normalized single-particle ground-state mode of the local potential $\tilde{V}(\mathbf{r})$, with energy E_0 , and define the local mode solutions of the individual wells $u_{1,2}(\mathbf{r}) = u_0(\mathbf{r} - \mathbf{r}_{1,2})$. These local modes are not exactly orthogonal, but we may write

$$\int d^3\mathbf{r} u_j^*(\mathbf{r}) u_k(\mathbf{r}) = \delta_{jk} + \epsilon(1 - \delta_{jk}), \quad (1.22)$$

where j and k assume values 1, 2. Here ϵ is the overlap between the modes of opposite wells. If the position uncertainty in the state $u_0(\mathbf{r})$ is much less than the separation of the minima of the global potential $V(\mathbf{r})$, then $\epsilon \ll 1$, and first-order perturbation theory, with ϵ as an expansion parameter, will suffice. In first-order perturbation theory the modes are determined to order ϵ^0 , which ignores inter-well coupling, in which case the local modes may be treated as orthogonal. The energy eigenstates of the global double-well potential may then be approximated as the symmetric (+) and asymmetric (-) combinations

$$u_{\pm}(\mathbf{r}) \approx \frac{1}{\sqrt{2}} [u_1(\mathbf{r}) \pm u_2(\mathbf{r})], \quad (1.23)$$

with corresponding eigenvalues $E_{\pm} = E_0 \pm \mathcal{R}$, and

$$\mathcal{R} = \int d^3\mathbf{r} u_1^*(\mathbf{r}) \left[V(\mathbf{r}) - \tilde{V}^{(2)}(\mathbf{r} - \mathbf{r}_1) \right] u_2(\mathbf{r}). \quad (1.24)$$

The tunneling frequency ω_R between the two minima is then given by the energy level splitting of these two lowest states, $\omega_R = 2\mathcal{R}/\hbar$. The matrix element \mathcal{R} , which is of order ϵ , describes the coupling between the local modes.

The many-body Hamiltonian describing atomic BEC in a potential is given by

$$\mathcal{H}_V = \int dx \left(-\hat{\phi}^\dagger(x) \frac{\hbar^2}{2m} \nabla_x^2 \hat{\phi}(x) + \frac{\lambda}{2} \hat{\phi}^\dagger(x) \hat{\phi}^\dagger(x) \hat{\phi}(x) \hat{\phi}(x) + V(\mathbf{r}) \right) \quad (1.25)$$

where m , λ , and $\hat{\phi}$ are defined below Eq. (1.6). In the two-mode approximation we expand the field operators in terms of the local modes and introduce the Heisenberg picture annihilation and creation operators

$$c_j(t) = \int d^3\mathbf{r} u_j^*(\mathbf{r}) \hat{\phi}(\mathbf{r}, t) \quad (1.26)$$

so that $[c_j, c_k^\dagger] = \delta_{jk}$ to order ϵ^0 . Then retaining terms up to order ϵ , the many-body Hamiltonian reduces to the following two-mode approximation [18]:

$$H' = -\frac{\hbar\omega_R}{2} (c_1^\dagger c_2 + c_2^\dagger c_1) + \frac{E'_c}{4} \left[(c_1^\dagger c_1)^2 + (c_2^\dagger c_2)^2 \right], \quad (1.27)$$

where $E'_c = 2\lambda/V_{eff}$, and $V_{eff}^{-1} = \int d^3\mathbf{r} |u_0(\mathbf{r})|^4$ is the effective mode volume of each well. Here we have retained only self-phase modulation arising from self-interaction within each well since the cross-interaction terms involve matrix elements such as $(\lambda/2) \int d^3\mathbf{r} |u_1\mathbf{r}|^2 |u_2(\mathbf{r})|^2$, which are of order ϵ^2 compared to the self-phase modulation matrix elements E'_c , and should therefore be consistently neglected to first order. Particle number conservation requires $c_1^\dagger c_1 + c_2^\dagger c_2 = N = 2N_0$, where N is

the sum of the number of atoms in each mode. We also define N_1 as the number of atoms in mode 1 and N_2 as the number of atoms in mode 2. Also $N_{1,2} = N_0 \pm \bar{N}$, where \bar{N} is the number of transferred particles from one mode to another,

To establish the connection with the pendulum Hamiltonian given by Eq. (1.19), we define the number eigenstates $|\bar{N}\rangle \equiv |N_1 N_2\rangle$ where \bar{N} can be viewed as the number of transferred particles across the barrier. Using this definition we get

$$\langle \bar{N} + 1 | H' | \bar{N} \rangle = \frac{E_J}{2} = -\frac{\hbar\omega_R}{2} \sqrt{N_0(N_0 + 1) - \bar{N}(\bar{N} + 1)}. \quad (1.28)$$

In the limit $1 \ll \bar{N} \ll N_0$, $E_J = \hbar\omega_R \sqrt{(N_0^2 - \bar{N}^2)}$. Noting that the particle number eigenstates admit a phase representation

$$|\gamma\rangle = -\frac{1}{\sqrt{2\pi}} \sum_{\bar{N}} e^{-i\bar{N}\gamma} |\bar{N}\rangle, \quad (1.29)$$

we get the non-rigid pendulum Hamiltonian,

$$H' \approx -N_0 \hbar\omega_R \sqrt{1 - \bar{N}^2/N_0^2} \cos \gamma + \frac{1}{2} E'_c \bar{N}^2. \quad (1.30)$$

In the limit of $\gamma \ll 1$ and $n \ll N_0$, Eq. (1.30) also acquires a harmonic form with natural oscillation frequency

$$\omega^2 = \frac{N_0 E'_c}{\hbar} \omega_R + \omega_R^2. \quad (1.31)$$

1.4.3 Rabi, Josephson, and Fock regimes

A clear limitation of the standard pendulum Hamiltonian given by Eq. (1.19) is that, in the non-interacting limit $E_c \rightarrow 0$, the dynamics are suppressed and the Josephson plasma frequency for small collective oscillations vanishes. However, this

contradicts our physical notion that non-interacting atoms should indeed exhibit some dynamics. For instance, under the effect of the Hamiltonian given by Eq. (1.27), an atom initially prepared in state $|1\rangle = c_1^\dagger|0\rangle$ will undergo Rabi oscillations between states $|1\rangle$ and $|2\rangle = c_2^\dagger|0\rangle$ with frequency ω_R . Thus Eq. (1.27) provides a more unified description which views collective Josephson behavior and single atom Rabi oscillations as particular cases of more general dynamics [19]. It is thus clear that, for a given interaction strength, the double BEC system can be driven continuously from the Josephson to the Rabi regime by varying ω_R , something feasible experimentally [20]. This is analogous to how Gross-Pitaevskii equation of a many boson system reduces for zero interaction to the Schrödinger equation. The crossover between collective Josephson and individual Rabi dynamics cannot be studied in a single sample of a superconductor or a superfluid, because the interactions cannot be tuned experimentally. It is a nice feature of a BEC that it allows us to study the crossover between these two qualitatively different dynamical regimes in an elegant fashion.

In the limit of very strong interactions, quantum fluctuations of the phase dominate, the Josephson coupling becomes a small perturbation, and the relative particle number is approximately a good quantum number. This is the Fock regime, where the particle number eigenstates (Fock states) are stationary states.

In summary, the magnitude of the ‘charging’ energy E'_c distinguishes three regimes:

1. $E'_c \ll \hbar\omega_R/N_0$ (Rabi)

2. $\hbar\omega_R/N_0 \ll E'_c \ll N_o\hbar\omega_R$ (Josephson)

3. $N_0\hbar\omega_R \ll E'_c$ (Fock)

To a reader familiar with superconducting qubits, one might identify these three regimes as the BEC analogue of phase, flux, and charge qubit in the same order as above. However, in case of superconducting qubits, the crossover from one regime to another cannot be studied in the same sample.

1.5 Outline of thesis

In rest of the thesis I will present my results on six different problems on which I have been working. The chapters are entirely independent of each other and the reader might feel free to flip over to the chapters of interest. The essential theme remains exploring, theoretically, quantum coherent features in superconducting circuits, and trapped bosons and fermions at ultracold temperature.

In chapter 2 I analyze the behavior of a dc superconducting quantum interference device phase qubit in which one junction acts as a phase qubit and the rest of the device provides isolation from dissipation and noise in the bias leads. Ignoring dissipation, I find the two-dimensional Hamiltonian of the system and use numerical methods and a cubic approximation to solve the Schrödinger's equation for the eigenstates, energy levels, tunneling rates, and expectation value of the currents in the junctions. Using these results, I investigate how well this design provides isolation while preserving the characteristics of a phase qubit. In addition, I show that the expectation value of current flowing through the isolation junction depends on

the state of the qubit and can be used for nondestructive read out of the qubit state.

In chapter 3 I study decoherence effects in qubits coupled to environments that exhibit resonant frequencies in their spectral function. I model the coupling of the qubit to its environment via the Caldeira-Leggett formulation of quantum dissipation/decoherence, and study the simplest example of decoherence effects in circuits with resonances such as a dc SQUID phase qubit in the presence of an isolation circuit which is designed to enhance the coherence time. I emphasize that the spectral density of the environment is strongly dependent on the circuit design, and can be engineered to produce longer decoherence times. I begin with a general discussion of superconducting qubits such as the flux qubit, the Cooper pair box and the phase qubit and show that in these kinds of systems appropriate circuit design can greatly modify the spectral density of the environment and lead to enhancement of decoherence times. In the particular case of the phase qubit, for instance, I show that when the frequency of the qubit is at least two times larger than the resonance frequency of the environmental spectral density, the decoherence time of the qubit is a few orders of magnitude larger than that of the typical ohmic regime, where the frequency of the qubit is much smaller than the resonance frequency of the spectral density. In addition, I demonstrate that the environment does not only affect the decoherence time, but also the frequency of the transition itself, which is shifted from its environment-free value. Second, I show that when the qubit frequency is nearly the same as the resonant frequency of the environmental spectral density, an oscillatory non-Markovian decay emerges, as the qubit and its environment self-generate Rabi oscillations of characteristic time scales shorter than the decoherence

time.

In chapter 4 I study weakly interacting atomic or molecular bosons in quantum degenerate regime and trapped in harmonically confined optical lattices, that exhibit a wedding cake structure consisting of insulating (Mott) shells. I find that superfluid regions emerge between Mott shells as a result of fluctuations due to finite hopping. I find that the order parameter equation in the superfluid regions is not of the Gross-Pitaevskii type except near the insulator to superfluid boundaries. I obtain the excitation spectra in the Mott and superfluid regions, and I show that the superfluid shells possess low energy sound modes with spatially dependent sound velocity described by a local index of refraction directly related to the local superfluid density. Lastly, I discuss the Berezinskii-Kosterlitz-Thouless transition and vortex-antivortex pairs in thin (wide) superfluid shells (rings) limited by three (two) dimensional Mott regions.

In chapter 5 I describe interacting mixtures of ultracold bosonic and fermionic atoms in harmonically confined optical lattices. For a suitable choice of parameters I study the emergence of superfluid and Fermi liquid (non-insulating) regions out of Bose-Mott and Fermi-band insulators, due to finite boson and fermion hopping. I obtain the shell structure for the system and show that angular momentum can be transferred to the non-insulating regions from Laguerre-Gaussian beams, which combined with Bragg spectroscopy can reveal all superfluid and Fermi liquid shells.

In chapter 6 I discuss the finite temperature phase diagram of two-dimensional dipolar bosons as a function of the interaction strength. I identify the stable phases as dipolar superfluid (DSF), dipolar Wigner crystal (DWC), dipolar hexatic fluid

(DHF), and dipolar normal fluid (DNF). I also show that other interesting phases like dipolar supersolid (DSS) and dipolar hexatic superfluid (DHSF) are at least metastable, and can potentially be reached by thermal quenching. In particular, for large densities or strong dipolar interactions, I find that the DWC exists at low temperatures, but melts into a DHF at higher temperatures, where translational crystalline order is destroyed but orientational order is preserved. Upon further increase in temperature the DHF phase melts into the DNF, where both orientational and translational lattice order are absent. Lastly, I discuss the static structure factor for some of the stable phases and show that they can be identified via optical Bragg scattering measurements.

In chapter 7 I extend the work presented in chapter 4 to a finite temperature theory. I calculate the finite temperature order parameter and the critical temperature of the superfluid regions, as well as the local entropy (within the local density approximation) for the entire system using two different approaches. First, I use a mean field local density approximation where the superfluid regions are considered as a two level system. Next, I use a more accurate ‘slave fermion’ method which I explain in detail. The results of the later indicate that the mean-field local density approximation alone overestimates the critical temperature for superfluidity, and that when quantum fluctuations are included, the critical temperature drops typically by a factor of three. In current experiments, the temperature is much greater than the critical temperature of the superfluid regions. I propose an experiment to reduce the temperature lower than the critical temperature of the superfluid regions by removing the high entropy atoms analogous to evaporation cooling.

Finally, in chapter 8, I present my conclusions and future directions.

Chapter 2

Quantum behavior of dc SQUID phase qubit

2.1 Introduction

There are currently several types of superconducting devices that are being actively investigated for use as quantum bits (see references [21] to [38]). These devices can be grouped into three broad classes: charge, flux and phase qubits, according to which dynamical variable is most sharply defined and which basis states are used. In this chapter I will examine the quantum behavior of the dc Superconducting Quantum Interference Device (SQUID) phase qubit, investigate the optimization of the device and discuss how well this design provides isolation while preserving the characteristics of a phase qubit. This type of phase qubit [21, 22, 29, 30] was first proposed by Martinis *et al.* [22] and has two junctions in a superconducting loop, just as in a conventional dc SQUID [31, 32].

The quantum behavior of dc SQUIDs has been of interest for nearly three decades. Much early research was driven by the desire to construct quantum limited amplifiers and magnetic sensors [33] as well as understanding intrinsic quantum mechanical effects in the SQUID [34]. However, most of this prior work on amplifiers and sensors involved SQUIDs that were shunted with resistors and biased into a finite-voltage power-dissipating state to achieve a non-hysteretic response. In contrast, for use as a qubit, one needs to understand the behavior of SQUID's that are

in the low-dissipation limit (no resistive shunt across the junctions) and the device is biased in the zero-voltage state. In particular, we need to understand how to choose the device parameters and arrange the bias so that the device is well-isolated from its leads.

The dc SQUID phase qubit is one type of phase qubit. The archetypal or ideal phase qubit is just a single Josephson tunnel junction connected to a current bias source (see Fig. 2.1) [21]. The behavior of an ideal phase qubit is analogous to that of a ball trapped in a tilted washboard potential [see Fig. 2.2], where the position is proportional to the phase difference across the junction, the size of the ripples in the potential is proportional to the junction's critical current, the tilt is proportional to the applied current, and the mass of the ball is proportional to the junction's capacitance [10]. Quantization of the system yields discrete metastable energy levels as well as a continuum of levels [10]. If the junction capacitance and critical current are sufficiently large, and the tilt not too large, the metastable levels have classically a well-defined phase (hence the name "phase qubit"), corresponding to the ball being trapped in one well of the potential and the lossless flow of supercurrent through the tunnel junction. The two lowest meta-stable energy levels in a well can be used as qubit states ($|0\rangle$ and $|1\rangle$) and their separation in energy can be tuned by changing the bias current. The continuum states correspond to the ball rolling down the potential and a voltage being developed across the junction. The qubit states can decay via quantum tunneling to the continuum, with $|1\rangle$ escaping two or three orders of magnitude faster than $|0\rangle$, thus monitoring the decay rate allows sensitive detection of the state.

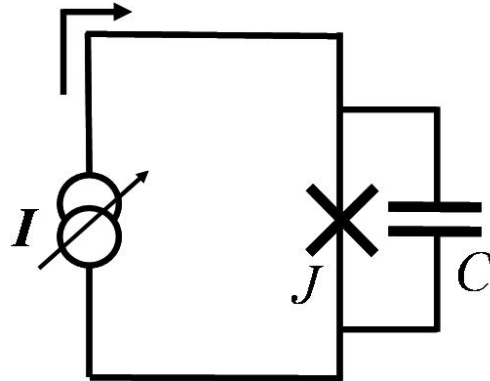


Figure 2.1: Schematic of a phase qubit. I is the bias current, J is the Josephson junction, and C is the equivalent capacitance across the junction.

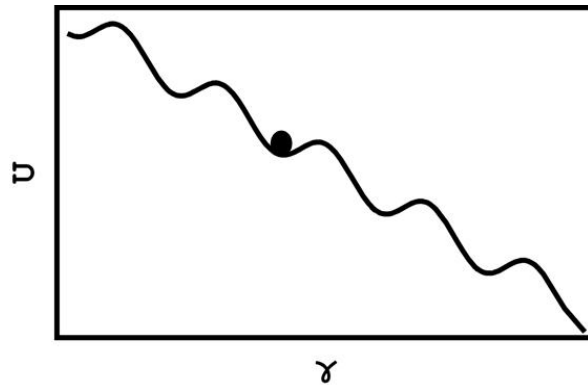


Figure 2.2: Tilted washboard potential U of the phase qubit (Fig. 2.1) as a function of γ .

The phase qubit has some potentially significant advantages, including simplicity, the ability to tune the transition frequency and a fast built-in read-out capability. However, there are also significant problems with this simple design.

1. While the ability to tune the transition frequency by applying a bias current is very useful, fluctuations in the bias current will cause fluctuations in the transition frequency, leading to dephasing and inhomogeneous broadening.
2. Wire leads are needed to connect the bias current source, which is typically at room temperature, to the junction, which must be cooled to milli-kelvin temperatures. These leads will present a dissipative impedance to the junction, decreasing the excited state lifetime T_1 and producing a short coherence time.
3. While tunneling to the voltage state can provide a fast, high-fidelity readout of the state, it is a highly intrusive measurement that not only causes the qubit state to leave the computational basis, but also causes the dissipation of relatively large amounts of energy at the junction.
4. Dielectric loss and two-level charge fluctuators in the tunnel barrier, the substrate or nearby insulation layers, or critical current fluctuators in the tunnel junction barrier, can all lead to significant dissipation and dephasing, limiting the coherence time of the device [35].

The main idea behind the design of the dc SQUID phase qubit [22] is to overcome the first two problems by inserting a broad-band inductive isolation network between the qubit junction and the bias leads. Overcoming the third problem re-

quires implementing a state readout technique, such as microwave reflectometry, that does not require tunneling to the voltage state. Here we will examine another possible approach to non-destructive read-out in this device. Overcoming the fourth problem will require the use of low-loss materials with a low density of defects, especially in the tunnel barrier [35].

Other approaches are possible. One example is operating at a “sweet spot”, i.e. at a bias current where the first derivative of the potential with respect to the bias current is zero. At such values the transition frequency is independent of current to first order, and one can minimize decoherence from current fluctuations. In the phase qubit this requires biasing the device at zero current and choosing the device parameters to maintain sufficient anharmonicity. This is the approach taken in the transmon [36]. Such an approach could be used in conjunction with broad-band isolation. However, since removing the ability to apply bias current will sacrifice tunability, one needs to consider the trade-off involved.

Figure 2.3 shows a circuit schematic of the dc SQUID phase qubit. In this device, junction J_1 is assumed to behave like a phase qubit and the rest of the circuit is used to provide isolation from dissipation and low-frequency bias-current noise. The lowest two energy levels of junction J_1 , labeled $|0\rangle$ and $|1\rangle$, are used as the qubit states. An external current source provides a bias current I to the circuit and a second current source supplies current I_f to mutual inductance M in order to apply a flux $\Phi_a = MI_f$ to the SQUID loop. The mutual inductance M must be small enough to ensure that too much noise does not couple to the SQUID via this coil. The second junction J_2 is called the isolation junction and is used to provide

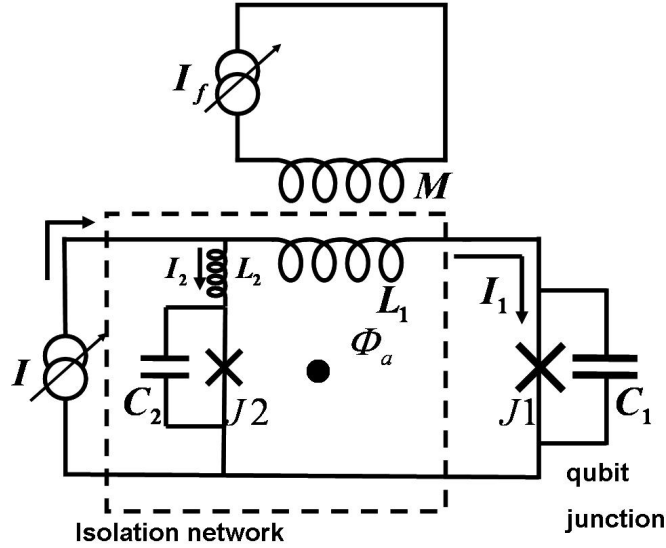


Figure 2.3: Schematic of dc SQUID phase qubit. The circuit contains two Josephson junctions J_1 and J_2 , with junction capacitance C_1 and C_2 , respectively. The inductances of the two arms of the SQUID are L_1 and L_2 . The current source I biases the two junctions, while an external flux Φ_a is provided by the current source I_f through the mutual inductance M . The currents flowing through the right and left arms of the SQUID are I_1 and I_2 respectively.

a state readout capability, for example via tunneling to the voltage state.

To protect junction J_1 from fluctuations in the bias current I , the inductances L_1 and L_2 are chosen so that $L_1 \gg L_2$; L_1 and L_2 act like an inductive current divider. To bias J_1 and set the spacing between energy levels, both currents I and I_f are applied. Since $L_1 \gg L_2$, when I is applied most of the current goes through junction J_2 , leaving J_1 unbiased. If positive flux Φ_a is then applied to the SQUID, a circulating current is induced that opposes the initial applied flux. If just the right magnitude of flux is applied, this produces a current flow through J_2 that exactly

cancels the current due to the bias current I , and leaves current flowing just in J_1 . In this situation, the effective current flowing through the qubit junction J_1 is I while any fluctuation in the bias current mainly flows through the isolation junction J_2 .

In the next section, I will discuss the SQUID Hamiltonian and potential energy for typical bias conditions. In contrast to earlier work, my analysis treats both junctions quantum mechanically. In Section 2.3, I will develop a cubic approximation for the potential and in Section 2.4 I will discuss numerical solutions of Schrödinger's equation for the exact Hamiltonian. In Section 2.5 I will compare the energy levels found using these two approaches and conclude that the results are very nearly the same under typical bias conditions. In Section 2.6, I will analyze how well the qubit junction is isolated from current noise and compare my results to classical analysis of the circuit. In Section 2.7, I will identify novel features in the coupling between the state of the qubit and the circulating current, and discuss the implications of this for non-destructive state readout. Finally, I conclude with a brief summary. The work presented in this chapter is a longer version of Ref. [54].

2.2 The circuit Hamiltonian and the effective potential

Consider the dc SQUID circuit shown in Fig. 2.3. Its dynamics are described by the Lagrangian

$$\mathcal{L}(\gamma_1, \dot{\gamma}_1, \gamma_2, \dot{\gamma}_2) = \frac{1}{2}m_1\dot{\gamma}_1^2 + \frac{1}{2}m_2\dot{\gamma}_2^2 - U(\gamma_1, \gamma_2) \quad (2.1)$$

where $m_i = (\Phi_0/2\pi)^2 C_i$ is the effective mass of the i -th junction, $\Phi_0 = h/2e$ is the flux quantum, C_i is the capacitance of the i -th junction, and γ_1 and γ_2 are the gauge invariant phase differences across junctions J_1 and J_2 . The potential energy term U is

$$U(\gamma_1, \gamma_2) = -E_{J1} \cos \gamma_1 - \frac{\Phi_0}{2\pi} I \frac{L_2}{L} \gamma_1 - E_{J2} \cos \gamma_2 - \frac{\Phi_0}{2\pi} I \frac{L_1}{L} \gamma_2 + \left(\frac{\Phi_0}{2\pi}\right)^2 \left(\frac{1}{2L}\right) \left(\gamma_1 - \gamma_2 - 2\pi \frac{\Phi_a}{\Phi_0}\right)^2 \quad (2.2)$$

where $E_{ji} = I_{0i} \Phi_0 / 2\pi$ is the Josephson energy for the i -th junction, and I_{0i} is the critical current of the i -th junction. Note that in this expression, we have assumed for simplicity that the mutual inductance between the arms of the SQUID can be neglected, so that the total inductance of the SQUID loop is $L = L_1 + L_2$ [31]. The first two terms in the Lagrangian are just the energy stored in the two junction capacitances. To see this, note that the ac Josephson relations give

$$V_1 = \frac{\Phi_0}{2\pi} \dot{\gamma}_1, \quad (2.3)$$

$$V_2 = \frac{\Phi_0}{2\pi} \dot{\gamma}_2, \quad (2.4)$$

where V_1 and V_2 are the voltages across junctions J_1 and J_2 respectively.

Given the Lagrangian, we can now use Euler-Lagrange equation to find the equation of motion for γ_1

$$0 = \frac{\partial}{\partial t} \frac{\partial \mathcal{L}}{\partial \dot{\gamma}_1} - \frac{\partial \mathcal{L}}{\partial \gamma_1} = m_1 \ddot{\gamma}_1 + \frac{\partial}{\partial \gamma_1} U(\gamma_1, \gamma_2). \quad (2.5)$$

Substituting Eq. (2.2) for U and using the definition of m_1 , we can write this in the form

$$I \frac{L_2}{L} - \left(\frac{\Phi_0}{2\pi L} \right) \left(\gamma_1 - \gamma_2 - 2\pi \frac{\Phi_a}{\Phi_0} \right) = I_{01} \sin \gamma_1 + C_1 \frac{\Phi_0}{2\pi} \ddot{\gamma}_1 \quad (2.6)$$

The left hand side of Eq. (2.6) can be simplified by using the flux-phase relation for the SQUID loop [31],

$$\gamma_1 = \gamma_2 + \frac{2\pi}{\Phi_0} (-L_1 I_1 + L_2 I_2 + \Phi_a). \quad (2.7)$$

where I_1 and I_2 are the currents flowing through the J_1 and J_2 arms of the SQUID loop, respectively (see Fig. 2.3). From current conservation, the bias current must divide between the two arms of the SQUID, so $I = I_1 + I_2$. Using this and the flux phase relation, we find

$$I_1 = I \frac{L_2}{L} - \left(\frac{\Phi_0}{2\pi L} \right) \left(\gamma_1 - \gamma_2 - 2\pi \frac{\Phi_a}{\Phi_0} \right) \quad (2.8)$$

and Eq. (2.6) can then be put in the simple form-

$$I_1 = I_{01} \sin \gamma_1 + C_1 \frac{\Phi_0}{2\pi} \ddot{\gamma}_1. \quad (2.9)$$

This is just what one would expect when current conservation is applied to the J_1 arm of the SQUID; *i.e.* the current in the J_1 arm of the SQUID is the sum of the supercurrent current through junction J_1 (from the dc Josephson relation this is just $I_{01} \sin \gamma_1$) and the displacement current $C_1 \dot{V}_1$ through the capacitor C_1 .

Similarly, using Euler's equation we can find the equation of motion for γ_2

$$I \frac{L_1}{L} + \left(\frac{\Phi_0}{2\pi L} \right) \left(\gamma_1 - \gamma_2 - 2\pi \frac{\Phi_a}{\Phi_0} \right) = I_{02} \sin \gamma_2 + C_2 \frac{\Phi_0}{2\pi} \ddot{\gamma}_2. \quad (2.10)$$

Again applying $I = I_1 + I_2$ and the flux-phase relation, we find

$$I_2 = I \frac{L_1}{L} + \left(\frac{\Phi_0}{2\pi L} \right) \left(\gamma_1 - \gamma_2 - 2\pi \frac{\Phi_a}{\Phi_0} \right) \quad (2.11)$$

and we can write Eq. (2.10) as

$$I_2 = I_{02} \sin \gamma_2 + C_2 \frac{\Phi_0}{2\pi} \ddot{\gamma}_2. \quad (2.12)$$

Again, this is just what one would expect when current conservation is applied to the J_2 arm of the SQUID. Thus, the Lagrangian given by Eq. (2.1) yields equations of motion (2.6) and (2.10), and these are just the expected coupled equations of motion for the junction phases γ_1 and γ_2 in a dc SQUID.

The Hamiltonian of the dc SQUID can now be written as

$$\mathcal{H} = p_1 \dot{\gamma}_1 + p_2 \dot{\gamma}_2 - \mathcal{L} = \frac{p_1^2}{2m_1} + \frac{p_2^2}{2m_2} + U(\gamma_1, \gamma_2), \quad (2.13)$$

where the canonical momenta are found from $p_i = \partial \mathcal{L} / \partial \dot{\gamma}_i = m_i \dot{\gamma}_i$. Using the standard prescription of quantum mechanics, we identify $p_i = -i\hbar \partial / \partial \gamma_i$ and γ_i as operators.

To proceed, we now assume that the external flux Φ_a and the bias current I are changed simultaneously such that $\Phi_a = L_1 I$. This simultaneous ramping of the applied flux and the current is done in experiments so that the static applied current mainly flows through J_1 while leaving J_2 unbiased, as discussed above. In this case,

the Josephson inductance [37] of the isolation junction J_2 is a minimum and one obtains the highest isolation of the qubit junction J_1 from current noise in the bias leads. With this assumption the terms in the potential U that are proportional to just γ_2 cancel and we find

$$U(\gamma_1, \gamma_2) = -E_{J1} \cos \gamma_1 - E_{J1} \frac{I}{I_{01}} \gamma_1 - E_{J2} \cos \gamma_2 + E_L (\gamma_1 - \gamma_2)^2, \quad (2.14)$$

where $E_L = (\Phi_0/2\pi)^2 / 2L$ sets the scale for the inductive coupling energy between the two junctions and we have ignored an offset term that does not depend on γ_1 and γ_2 . Of course if there are fluctuations in the current I that are independent of fluctuations in Φ_a , then Eq. (2.14) would not be appropriate. We consider this situation below in Section 2.6.

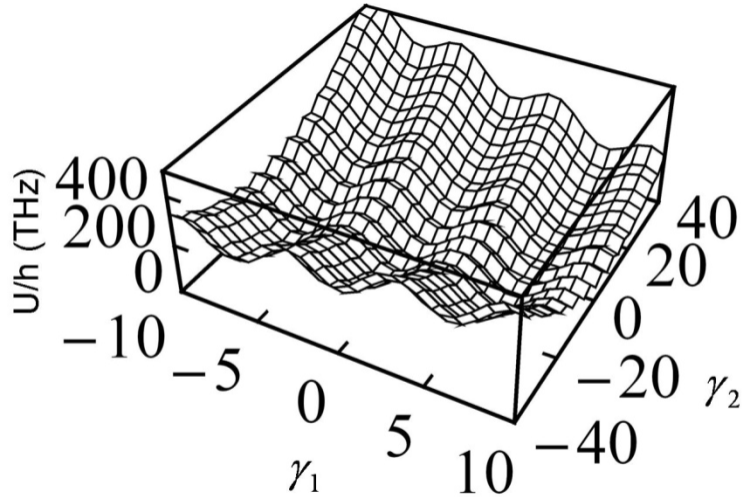


Figure 2.4: 2D surface plot of the potential U for the dc SQUID phase qubit with the parameters in Table 1 and $I = 17.00mA$.

Figures 2.4, 2.5, and 2.6 show different views of the two-dimensional potential U given by Eq. (2.14). The parameters for the simulation are listed in Table 1, and

I_{01} (mA)	17.75	I_{02} (mA)	6.40
C_1 (pF)	4.44	C_2 (pF)	2.22
L_1 (nH)	3.39	L_2 (pH)	20.0
E_{J1}/h (THz)	8.82	E_{J2}/h (THz)	3.17
E_{C1}/h (MHz)	3.82	E_{C2}/h (MHz)	8.73
β	39.83	κ_0	0.0040
f_{p1} (GHz)	16.42	f_{p2} (GHz)	14.88
E_L/h (GHz)	24.22	g_{12} (GHz)	24.22
r_I	7182	M (pH)	16.0

Table 2.1: dc SQUID phase qubit parameters used in the calculations.

they correspond to typical values used in experiments. In particular, the device is biased with $I/I_{01} = 0.95$ and simultaneously biased with external flux as described above. For the region of γ_1 and γ_2 shown in the figure the potential is dominated by a washboard potential along γ_1 [see Fig 2.6], just as in the ideal phase qubit and a parabolic potential along γ_2 [see Fig. 2.5]. The depths of the local minima are very different along the two directions. For these conditions, wells are 25 times shallower along the γ_1 direction than along the γ_2 direction. Along γ_1 the potential near a local minimum behaves like a harmonic potential with a significant additional cubic term, while along γ_2 it acts as a simple harmonic potential with a much smaller anharmonic component. The potential U also contains coupling between γ_1 and γ_2

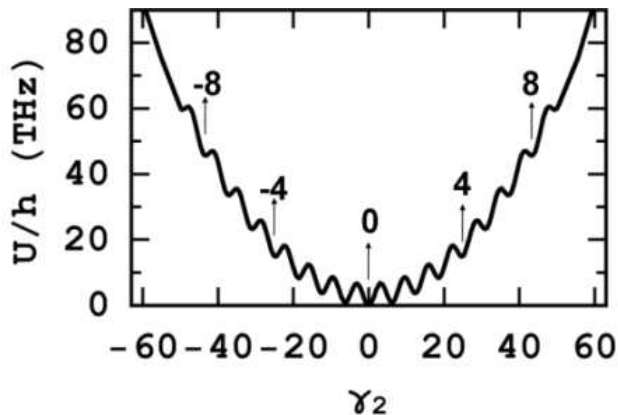


Figure 2.5: Cross-section of U along γ_2 for $\gamma_1 = 0$ with the parameters in Table 1 and $I = 17.00mA$. The numbers label the individual wells.

that is proportional to E_L . Since the overall energy scale of the Hamiltonian is set by E_{j1} and E_{j2} , we can construct a dimensionless coupling constant [38]

$$\kappa_0 = \frac{E_L}{(E_{j1} + E_{j2})/2} = \frac{1}{2\pi\beta} \quad (2.15)$$

where $\beta = L(I_{01} + I_{02})$ is the SQUID modulation parameter. Thus we see that increasing the loop inductance L and critical currents of the junctions causes the coupling between the junctions to decrease and that the weakest coupling is achieved for $\beta \gg 1$. In this limit, if the critical currents are not too different, the loop will be able to trap a persistent circulating current and a corresponding trapped flux. There will be a maximum number of such persistent current states equal to the number of wells in the potential U , depending on L and the smaller of the two critical currents, with the trapped flux in different states differing by approximately $n_w \Phi_0$, where n_w is an integer equal to the difference in well index. For example in Fig. 2.5 the difference in trapped flux between well 1 and 8 would be $7\Phi_0$. We note that for the best isolation from the bias leads, the device would be run with no circulating current, corresponding to $n_w = 0$ in Fig 2.5 and no current through the isolation junction J_2 . High flux states, up to $n_w = \pm 8$ in the case of Fig. 2.5, correspond to loading J_2 with current which increases its Josephson inductance and reduces the isolation. For phase qubits we are mainly interested in the limit $E_{j1} \approx E_{j2} \gg e^2/2C_1 \approx e^2/2C_2$. In this limit the junction phases are typically well-localized in a given well. Experimentally, the system can be initialized in any of the local minima [38, 39] and the behavior depends on which well is chosen. The position and depth of each minimum depends on the bias current. For a particular well, the minimum disappears at a critical bias current I_c . In general, this bias critical current is not equal to either the critical current I_{01} or I_{02} of the individual junctions. In Fig. 2.7(a) we show the critical bias current I_c for different wells along the γ_2 direction, while remaining in the well closest to $\gamma_1 = 0$. It is the value of

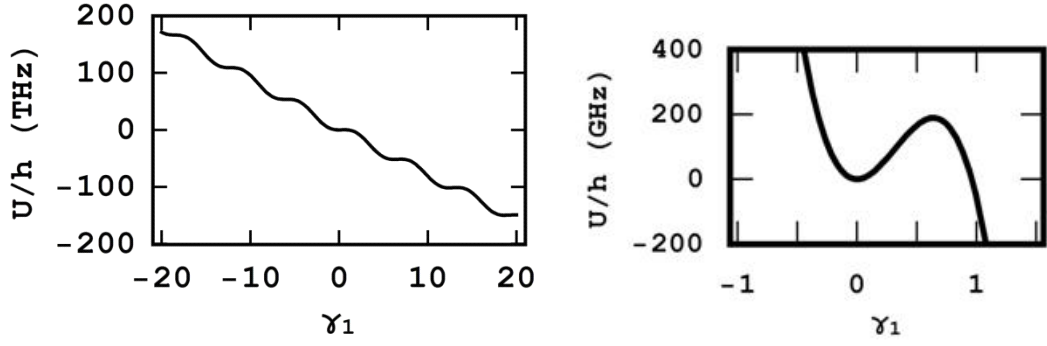


Figure 2.6: (a) Cross-section of U along γ_1 for $\gamma_2 = 0$. (b) Cross-section of U along γ_1 for $\gamma_2 = 0$ showing a single well. Parameters are same as in Table 1 and $I = 17.00mA$

I_c where a particular minimum of the potential U reduces to a saddle point and is calculated numerically. The nearly linear dependence of the critical current with well number is a consequence of the large loop inductance, which gives an effective small coupling between γ_1 and γ_2 ; the different minima correspond to circulating currents in the SQUID loop that differ by about Φ_0/L .

In Fig. 2.7(b) we show the plasma frequency ω_2 of the isolation junction as a function of well number along γ_2 , where $m_2\omega_2^2 = d^2U(\gamma_1, \gamma_2)/d\gamma_2^2$ at the minima. In the absence of the small coupling term $E_L(\gamma_1 - \gamma_2)^2$, the minima along γ_2 would be spaced by 2π and the plasma frequency ω_2 would be independent of the well index. The coupling term causes the distance between the minima to decrease, producing a quadratic decrease of ω_2 with increase in well index number.

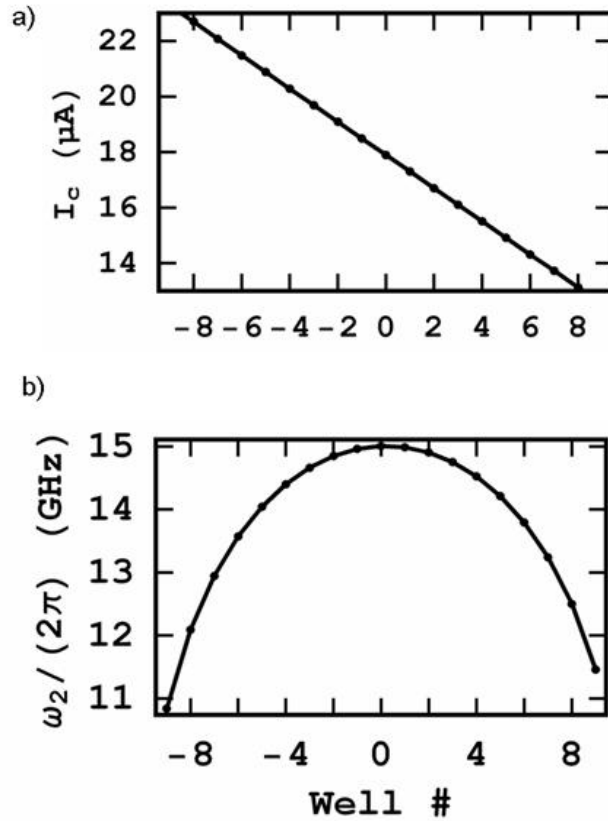


Figure 2.7: (a) Critical current I_c vs. well number along γ_2 . (b) Plasma frequency $\omega_2/2\pi$ vs. well number along γ_2 . For both graphs the well-numbers are from Fig. 2.5.

2.3 Cubic approximation

It is not possible to obtain exact analytical solutions to the Schrödinger's equation for the Hamiltonian given by Eq. (2.13). However, since phase qubits are in the limit $E_{j1} \approx E_{j2} \gg e^2/2C_1 \approx e^2/2C_2$, the junction phases can be relatively well-localized in a given well. Useful approximate results can then be found by making an expansion of the potential near a local minimum (γ_1^m, γ_2^m) of the well and truncating at the cubic terms [44]. For I near the critical current I_c of this well, the Hamiltonian can be approximated as

$$\begin{aligned}\bar{\mathcal{H}} \cong & \frac{p_1^2}{2m_1} + \frac{1}{2}m_1\omega_1^2(\gamma_1 - \gamma_1^m)^2 - g_1(\gamma_1 - \gamma_1^m)^3 + \frac{p_2^2}{2m_2} + \frac{1}{2}m_2\omega_2^2(\gamma_2 - \gamma_2^m)^2 \\ & g_{12}(\gamma_1 - \gamma_1^m)(\gamma_2 - \gamma_2^m) + U(\gamma_1^m, \gamma_2^m),\end{aligned}\quad (2.16)$$

where

$$\begin{aligned}m_1\omega_1^2 &= E_{J1}\cos\gamma_1^m + 2E_L \\ &\approx E_{J1}\sqrt{1 - \left(\frac{I - I_c}{I_{01}} + \sin\gamma_1^*\right)^2} + 2E_L\end{aligned}\quad (2.17)$$

$$m_2\omega_2^2 = E_{J2}\cos\gamma_2^m + 2E_L, \quad (2.18)$$

$$g_1 = \frac{1}{6}E_{J1}\sin\gamma_1^*, \quad (2.19)$$

$$g_{12} = -2E_L, \quad (2.20)$$

$$\gamma_1^* = \arccos(-2E_L/E_{J1}), \quad (2.21)$$

$$\gamma_2^m \approx 2\pi k + 2E_L(\gamma_1^* - 2\pi k)/E_{J2}, \quad (2.22)$$

$$I_c = I_{01}\sin\gamma_1^* + \frac{2E_L}{\Phi_0/(2\pi)}(\gamma_1^* - \gamma_2^m). \quad (2.23)$$

where the integer k is the well index, and I_c is the critical bias current. The cubic term in $(\gamma_1 - \gamma_1^m)$ is proportional to γ_1 while the coupling between $\gamma_1\gamma_2$ is proportional to g_{12} . Since $E_L \ll E_{J1}$, Eq. 2.21 implies under typical bias condition that γ_1^* , which is the critical value of γ_1 at which the washboard minima turns into a saddle point, is close to $\pi/2$ and $\sin\gamma_1^* \approx 1$. We note that in this truncated Hamiltonian, the $(\gamma_1 - \gamma_2)$ coupling term has been retained exactly, and the higher order terms in $(\gamma_1 - \gamma_1^m)$ and $(\gamma_2 - \gamma_2^m)$ that have been dropped are about 3 orders of magnitude smaller than the coupling term.

Equations (2.16) to (2.23) reproduce the nearly linear dependence of the numerically-determined critical current with well index along γ_2 , as seen in Fig. 2.2(a), as well as the quadratic dependence of the plasma frequency shown in Fig. 2.2(b). Deviations from the quadratic behavior, however, are significant for larger well-number index. Also, the expression for ω_1 given in Eq. (2.17) has some similarities to the single qubit case [30], but in fact has a different form and differs quantitatively.

The eigenvalues and eigenfunctions of the Hamiltonian $\bar{\mathcal{H}}$ can be found by treating the cubic and linear coupling terms as small perturbations to the rest of the Hamiltonian, and then applying second-order time-independent perturbation theory [44]. Tunneling rates can then be determined using the WKB (Wentzel-Kramers-Brillouin) approximation.

I will now summarize perturbation theory results for the Hamiltonian $\bar{\mathcal{H}}$.

$$\begin{aligned} \bar{\mathcal{H}} \cong & \frac{p_1^2}{2m_1} + \frac{1}{2}m_1\omega_1^2(\gamma_1 - \gamma_1^m)^2 - g_1(\gamma_1 - \gamma_1^m)^3 + \frac{p_2^2}{2m_2} + \frac{1}{2}m_2\omega_2^2(\gamma_2 - \gamma_2^m)^2 \\ & + g_{12}(\gamma_1 - \gamma_1^m)(\gamma_2 - \gamma_2^m) + U(\gamma_1^m, \gamma_2^m), \end{aligned} \quad (2.24)$$

as in Eq. (2.16), where for notational convenience we set $\gamma_1^m = \gamma_2^m = 0$. For a typical dc SQUID phase qubit, the g_{12} term is a small perturbation to the rest of the Hamiltonian; this term couples the phases γ_1 and γ_2 together. If we neglect this term the Hamiltonian separates. The motion along the γ_2 direction is harmonic, whereas that along γ_1 also has a cubic term proportional to g_1 . The eigenstates of this uncoupled Hamiltonian up to second order in g_1 are denoted by $|n, m\rangle = |n\rangle|m\rangle$ where n is the excitation in the qubit junction and m is the excitation in the isolation junction.

The corresponding eigenenergies of this uncoupled Hamiltonian up to second order in g_1 are

$$E_{n,m} = \left(\left(n + \frac{1}{2} \right) - \frac{30}{8} \lambda^2 \left[\left(n + \frac{1}{2} \right)^2 + \frac{7}{60} \right] \right) \hbar \omega_1 + \left(m + \frac{1}{2} \right) \hbar \omega_2 \quad (2.25)$$

where $n, m = 0, 1, \text{ etc.}$ and

$$\lambda = \frac{g_1}{\left[\left(\frac{m\omega_1}{\hbar} \right)^{3/2} \hbar \omega_1 \right]}. \quad (2.26)$$

The tunneling rates of the metastable energy levels of the cubic Hamiltonian can be found using a WKB (Wentzel-Kramers-Brillouin) approximation, and one finds [44]

$$\Gamma_{n,m} = \frac{\omega_1}{\sqrt{2\pi n!}} (432N_s)^{n+1/2} \exp\left(-\frac{36}{5}N_s\right), \quad (2.27)$$

where $N_s = 1/(54\lambda^2)$ is approximately the number of harmonic oscillator states with energy below the barrier of the cubic potential. The tunneling rate is independent of the state in the γ_2 direction. The above expression can be improved upon when N_s is less than 2. We find empirically that a more accurate expression is given by

$$\Gamma_{n,m} = \frac{\omega_1}{\sqrt{2\pi n!}} (432N_s)^{n+1/2} \frac{1}{1 + A \exp(36N_s/5)} \quad (2.28)$$

where the fitting parameter A turns out to be independent of n and m and can be determined from the exact numerical tunneling rates. Thus, the complex eigenenergies of the Hamiltonian \bar{H} with the coupling κ set to zero are $E_{n,m} - i\hbar\Gamma_{n,m}/2$.

For non-zero κ , we can compute corrections to the uncoupled eigenenergies using second order perturbation theory. We find the perturbative energy shift is

$$\Delta \left(E_{mn} - i\hbar \frac{\Gamma_{mn}}{2} \right) = \sum_{n'm'} g_{12}^2 \frac{|\langle nm | \gamma_1 \gamma_2 | n'm' \rangle|^2}{E_{nm} - i\hbar \frac{\Gamma_{nm}}{2} - E_{n'm'} + i\hbar \frac{\Gamma_{n'm'}}{2}}, \quad (2.29)$$

where the sum excludes $n'm' = nm$. The matrix elements in Eq. 2.29 reduce to simple products such as $\langle n|\gamma_1|n'\rangle\langle m|\gamma_2|m'\rangle$, where the matrix elements of γ_2 are determined by the properties of harmonic oscillator solutions. Up to second order in λ , the matrix elements $\gamma_{nn'} = \langle n|\gamma_1|n'\rangle$ are given by $\gamma_{0,0} = 3\lambda/2$, $\gamma_{0,1} = 1/\sqrt{2} + 11\sqrt{2}\lambda^2/8$, $\gamma_{0,2} = -\lambda/\sqrt{2}$, $\gamma_{0,3} = 3\sqrt{3}\lambda^2/8$, $\gamma_{1,1} = 9\lambda/2$, $\gamma_{1,2} = 1 + 11\lambda^2/2$, and $\gamma_{2,2} = 15\lambda/2$, for example [44].

2.4 Numerical simulations

For comparison, we also numerically solved Schrödinger's equation for the Hamiltonian H given by Eqs. (2.13-2.14) and obtained the energy levels, tunneling rates, and the wave function of the various resonant states. For this numerical simulation, we used the method of complex scaling [40]. In this method we make the substitutions $\gamma \rightarrow \gamma e^{i\theta}$ and $p_\gamma \rightarrow p_\gamma e^{-i\theta}$ for both γ_1 and γ_2 , using the same angle θ in the Hamiltonian, and find the complex eigenvalues and eigenvectors of the resulting non-Hermitian Hamiltonian. This transformation allows Gamow–Siegert states [41] (subject to outgoing boundary wave conditions) to be calculated in a finite basis set. The complex eigenvalues are of the form $E - i\hbar\Gamma/2$, where the real part is the energy of the metastable state and the imaginary part gives the tunneling rate Γ . To discretize the Hamiltonian we use a two dimensional harmonic oscillator basis localized about the relevant potential minimum with frequencies equal to the plasma frequencies along γ_1 and γ_2 . We find convergence up to 0.1% is reached for a basis set of 30×30 harmonic oscillator states.

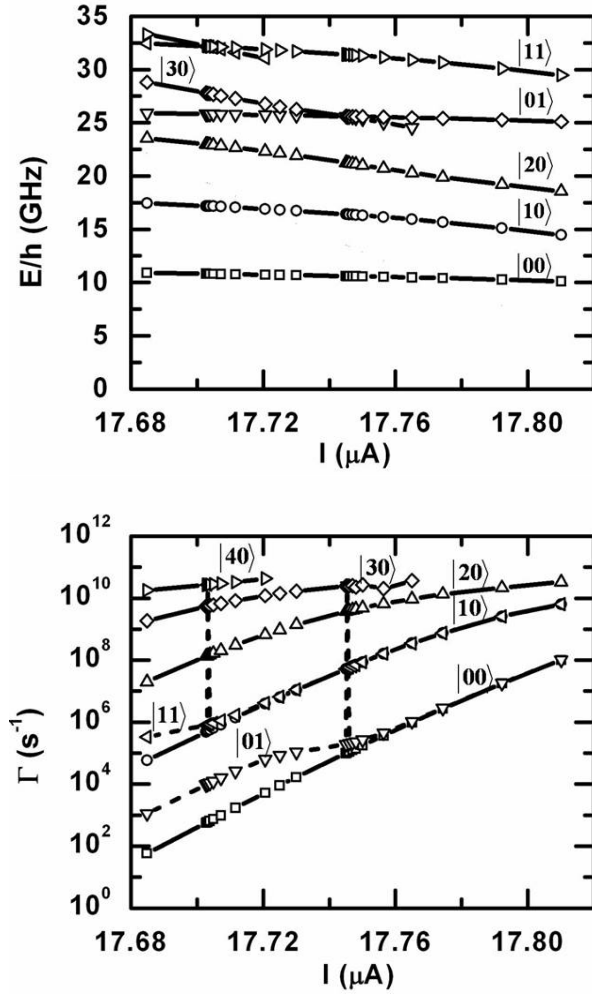


Figure 2.8: (a) Energy levels and (b) tunneling rates for different metastable states for well $k = 0$ as a function of bias current I . Symbols are from numerical calculation of the full 2D Hamiltonian using complex scaling, while the solid curves show analytical calculation where coupling between the two junctions is ignored. Dashed curves in panel b) show results from second-order perturbation theory. States are labeled by the ket $|n, m\rangle$, where the first index represents the qubit junction state and the second the isolation junction state. The dashed vertical lines in panel b) indicate avoided level crossings in the corresponding energy levels (see text).

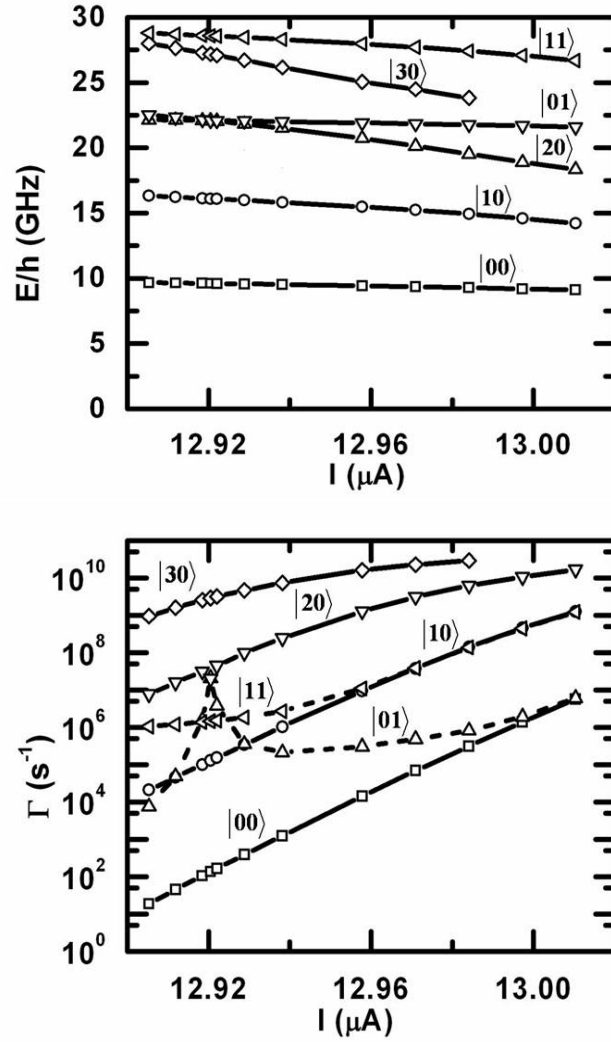


Figure 2.9: (a) Energy levels and (b) tunneling rates for various metastable states for well $k = 8$ as a function of bias current I . The meaning of the symbols *etc.* is as in Fig. 2.8

2.5 Comparison between numerical simulations and perturbation results

The symbols in Fig. 2.8(a) show calculated energy levels vs. bias current I for the $k = 0$ well, as found from the numerical simulation using complex scaling. In this case, we have set the coupling between the junctions to $\kappa_0 = 0.004$ (see Table 1 for the rest of the device parameters) and assumed simultaneous flux and current ramping. For comparison, the solid curves show results for the energy levels when $\kappa_0 = 0$, calculated from the analytical results for single junctions. As expected since the numerical simulations were done for quite weak coupling, the results from these two calculations are virtually identical on this scale.

In Fig. 2.8, the bias current runs from $I = 0.90I_c$ to $0.97I_c$, *i.e.* close to the critical current of $17.82 \mu A$ of the $k = 0$ well. These currents correspond to reasonable conditions for reading out the state by a tunneling measurement, such as the experiments in ref. [22]. We note that this critical current exceeds $I_{01} = 17.75 \mu A$ because some of the applied current is diverted through junction J_2 ; even with a simultaneous flux and current ramp, the change in Josephson inductance with current causes some imbalance. The eigenstates are labeled by state $|n, m\rangle$ where n is the excitation in the qubit junction and m is the excitation in the isolation junction.

In Fig. 2.8(a) only the states $|00\rangle$ and $|10\rangle$ lie below the top of the saddle point of the two-dimensional potential, which might suggest that only these state have a lifetime that is long compared to the oscillation period of the harmonic trap.

This, however, is not true. States with one excitation in the isolation junction, *i.e.* $|01\rangle$ and $|11\rangle$, are also long lived against tunneling. This is because the isolation junction is well described by a harmonic potential and the coupling between the two junctions is small. The state $|20\rangle$ also lives relatively long, but only because it lies just slightly above the barrier.

Figure 2.8(a) also shows two examples of crossings in the energy level diagram. These are actually avoided crossings, although the splitting is too small to be seen on this scale. At each crossing, an excited state of the qubit junction ($n = 3$ or 4) is in resonance with a state with one excitation ($m = 1$) in the isolation junction. Since the coupling constant κ_0 is small, the mixing is small and the resulting splittings are very small (approximately $6MHz$). As a result, in an experiment where the current is being swept, it will be relatively easy to be nonadiabatic with respect to the crossings.

The symbols in Fig. 2.8(b) show the corresponding tunneling rate versus current for the different states, as found from the numerical simulations using complex scaling. Again, the solid curves show results when the coupling $\kappa_0 = 0$, found using the analytical results for single junctions given in Sec. 2.3. We note that there is no discernible difference between the coupled and uncoupled results, except for states $|01\rangle$ and $|11\rangle$ where the isolation junction is excited. For these excited states of the isolation junction, the perturbative effects of the coupling term are needed because the tunneling rates are sensitive to even small mixings with highly-excited levels of the qubit junction. Here the $|01\rangle$ state mixes with $|30\rangle$ while the $|11\rangle$ state mixes with $|40\rangle$ [see Fig. 2.8(a)]. For comparison, the dashed curves show the results when

the coupling term is included using second order perturbation theory; we find excellent agreement with complex scaling. From these results, we conclude that as long as we stay away from the very narrow avoided crossings, the dc SQUID phase qubit behaves much like a single phase qubit and the coupling can be safely ignored.

Figure 2.9 shows energy levels and tunneling rates for well $k = 8$ along the γ_2 direction. The critical current is reduced from the $k = 0$ value of 17.82 mA to just 13.02 μA . As shown in Fig. 2.7 the plasma frequency along the γ_2 direction decreases with well number, hence, avoided crossing between energy levels occur at smaller energies. In fact, the $|01\rangle$ state now avoids the $|20\rangle$ state and the $|11\rangle$ avoids $|30\rangle$. The effects of coupling are stronger than they were for $k = 0$ and this is reflected in the more gradual changes in the tunneling rates with current I near the avoided crossings. Consequently, as well number k increases, the circuit behaves less and less like an ideal phase qubit.

2.6 Response of the system to low frequency noise

Low frequency bias current noise can be a significant source of spectral resonance broadening and decoherence in phase qubits [22, 29, 30]. In addition, the bias leads present a dissipative impedance to the junction that decreases the lifetime of excited states. The main idea behind the design of the dc SQUID phase qubit is to use L_1 and L_2 as an inductive isolation network that steps up the lead impedance and prevent current noise from reaching the qubit. Here we examine how well this design works and what effects it produces on the qubit junction.

To understand how well the qubit junction is isolated from current noise, we first consider the classical description. When a small change ΔI is made in the bias current I , the external flux is held fixed at $L_1 I$. Provided the fluctuations are slow enough that the displacement current in the junction capacitors can be neglected, the change ΔI_1 in the current through the qubit junction can be found by treating the circuit as an inductive current divider. We find

$$\Delta I_1 = \frac{(L_2 + L_{J2})\Delta I}{L + L_{J1} + L_{J2}} \quad (2.30)$$

where $L_{Ji} = \Phi_0/2\pi I_{0i} \cos \gamma_i^m$ is the Josephson inductance of i -th junction. From Eq. (2.30), it is useful to define the current noise power isolation factor

$$r_I = \left(\frac{\Delta I}{\Delta I_1} \right)^2 = \left(\frac{L + L_{J1} + L_{J2}}{L_2 + L_{J2}} \right)^2. \quad (2.31)$$

For large r_I , the qubit junction is well-isolated from current noise in the leads. For the parameters shown in Table 1, $L + L_{J1} + L_{J2} \approx 3.4nH \gg L_2 + L_{J2} \approx 40pH$, so that $r_I \approx 7000$, and the network is quite effective at filtering out current fluctuations.

To understand the effect of the network on dissipation, we now assume that the current bias leads have a real impedance $Z_0 \approx 50\Omega$. The network steps up this impedance so that the effective parallel impedance Z_{eff} that shunts the qubit junction is found to be

$$\frac{1}{Z_{eff}} = \frac{1}{R_{eff}} + \frac{1}{i\omega L_{eff}}. \quad (2.32)$$

Here R_{eff} is the effective shunting resistance

$$R_{eff} = \left(\frac{L_1 + L_2 + L_{J2}}{L_2 + L_{J2}} \right)^2 Z_0 + \frac{\omega^2 L_1^2}{Z_0} \cong \left(\frac{L_1 + L_2 + L_{J2}}{L_2 + L_{J2}} \right)^2 Z_0 = r_I Z_0 \quad (2.33)$$

and L_{eff} is the effective parallel shunting inductance

$$L_{eff} = \frac{(L_1 + L_2 + L_{J2})^2 + \left(\frac{\omega(L_1 + L_2 + L_{J2})}{Z_0} \right)^2}{L_1 + L_2 + L_{J2} + \left(\frac{\omega(L_2 + L_{J2})}{Z_0} \right)^2 L_1} \cong L_1 + L_2 + L_{J2}. \quad (2.34)$$

For typical parameters and the low frequencies of interest, the frequency dependent terms can be neglected, as indicated. The lifetime of the excited state of the qubit then becomes

$$T_1 = \left(\frac{1}{R_{eff}} + \frac{1}{R_1} \right)^{-1} C_1 \quad (2.35)$$

where R_1 accounts for any resistance shunting the junction that is from sources other than the leads.

Finally, if we ignore the inductive network, the frequency at which the phase of the qubit junction executes small oscillations is given by [22]

$$\omega_1 = \frac{1}{\sqrt{L_{j1} C_1}} = \omega_{p1} \left(1 - \left(\frac{I_1}{I_{01}} \right)^2 \right)^{1/4}, \quad (2.36)$$

where I_1 is the current flowing through the qubit junction and

$$\omega_{p1} = \sqrt{\frac{8E_{C1}E_{J1}}{\hbar^2}} = \sqrt{\frac{2\pi I_{01}}{C_1 \Phi_0}}. \quad (2.37)$$

is the plasma frequency of the isolated junction when it is not biased. Including the rest of the circuit produces a small shift in the plasma frequency due to the shunting inductance L_{eff} , and we find a perturbed resonance frequency ω' given by

$$\omega' = \sqrt{\left(\frac{1}{L_{j1}} + \frac{1}{L_{eff}} \right) \frac{1}{C_1}} \approx \omega_1 + \frac{1}{2\omega_1 (L_1 + L_2 + L_{J2}) C_1}. \quad (2.38)$$

Given a change ΔI in the bias current, the change in the plasma frequency is then

$$\Delta\omega'_1 = \frac{d\omega'_1}{dI_1} \frac{(L_2 + L_{J_2})}{(L + L_{J_1} + L_{J_2})} \Delta I \approx -\frac{1}{2} \frac{(I/I_c)^2}{(1 - (I/I_c)^2)^{3/4}} \frac{L_2 + L_{J_2}}{L + L_{J_1} + L_{J_2}} \frac{\Delta I}{I} \quad (2.39)$$

where in the last approximation we neglected the contribution of the small correction term in Eq. (2.38). We can now define the classical response function r_c through the relationship

$$\Delta\omega'_1 = \omega_1 \frac{\Delta I}{I} r_c$$

From Eq. (2.39) we find

$$r_c \approx -\frac{1}{2} \frac{(I/I_c)^2}{(1 - (I/I_c)^2)^{3/4}} \frac{L_2 + L_{J_2}}{L + L_{J_1} + L_{J_2}}$$

To perform a quantum analysis of this situation, we now assume that the fluctuations ΔI are slow enough that time-independent perturbation theory can be used. We are interested in the situation where the current noise is not accompanied by a simultaneous fluctuation in the external flux. In this case, the Hamiltonian picks up an additional term

$$\Delta H = -\frac{\Phi_0}{2\pi} \Delta I(t) \left(\frac{L_2}{L} \gamma_1 + \frac{L_1}{L} \gamma_2 \right). \quad (2.40)$$

As we have seen in Sec 2.2, the SQUID's Hamiltonian is well approximated by a cubic potential along γ_1 and a simple harmonic potential along γ_2 with a small coupling proportional to κ_0 . With this Hamiltonian and the matrix elements listed in Sec 2.3, we can find analytical expressions for level shifts due to the perturbation ΔH . The corrections to the energy of the ground and first excited state of the qubit

up to second order are

$$\begin{aligned} \Delta_{n0} = & -\frac{\Phi_0}{2\pi}\Delta I(t)\frac{L_2}{L}\langle n0|\gamma_1 - \gamma_1^m|n0\rangle + \\ & \frac{\Phi_0}{2\pi}\Delta I(t)\left(+2\frac{L_1}{L}\langle n1|\gamma_2 - \gamma_2^m|n0\rangle\frac{\langle n0|\kappa(\gamma_1 - \gamma_1^m)(\gamma_2 - \gamma_2^m)|n1\rangle}{E_{n0} - E_{n1}}\right) \end{aligned} \quad (2.41)$$

for $n = 0$ and 1 , respectively. In this equation we have only retained terms proportional to ΔI . After some algebra we find,

$$\begin{aligned} \Delta\omega_1 &= \frac{\Delta_{10} - \Delta_{00}}{\hbar} = -\left(\frac{\Phi_0}{2\pi\hbar}\right)\frac{L_2 + L_{J2}}{L + L_{J2}}\left(\frac{1}{2}\left(\frac{2\pi}{\Phi_0}\right)^2\frac{I_{01}\sin\gamma_1^*\sqrt{\hbar}}{C_1^{3/2}\omega_1^{5/2}}\right)\Delta I \\ &\approx -\left(\frac{\Phi_0}{2\pi\hbar}\right)\frac{L_2 + L_{J2}}{L + L_{J2}}\left(\frac{1}{2}\left(\frac{2\pi}{\Phi_0}\right)^2\frac{I_{01}\sqrt{\hbar}}{C_1^{3/2}\omega_1^{5/2}}\right)\Delta I. \end{aligned} \quad (2.42)$$

We note that Eq. (2.42) is also valid for uncompensated low-frequency changes in the flux $\Delta\Phi_a$ if ΔI is replaced by $\Delta\Phi_a/L_2 = M\Delta I_f/L_2$. The typical experimental value of M is given in Table 1 which is of the same order of magnitude as L_2 . It is chosen to be sufficiently small to ensure that flux noise does not couple to the SQUID via this coil. For values we have chosen $\Delta\Phi_a/L_2 = 0.8\Delta I_f$. Thus the effect of flux noise is of the same order of magnitude as the current noise.

We can now define the quantum mechanical response function r_q through $\Delta\omega_1 = (E_{10} - E_{00})/\hbar r_q \Delta I/I$. In Fig. 2.10 we compare the classical and quantum mechanical response functions for well number 0 and 8 as a function of I/I_c . We see that the classical and quantum responses are nearly the same for currents $I/I_c < 0.97$. For smaller well index, the two curves agree over an even wider range of I/I_c . Both functions increase with current and are on the order of 1 for $I/I_c \approx 0.990$. Hence only for currents less than $0.990I_c$ does the isolation scheme work well. Furthermore in higher wells, the isolation becomes worse for the same value of I/I_c .

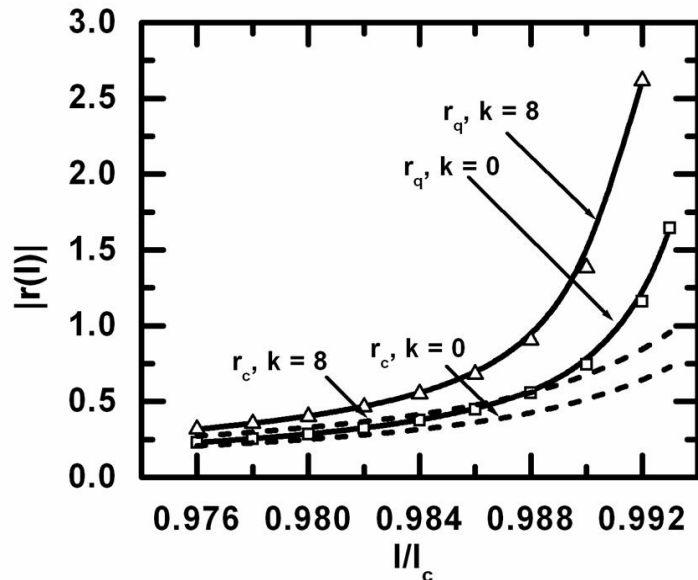


Figure 2.10: Absolute value of the response functions r_c and r_q as a function of current for well number $k = 0$ and 8 . Points are obtained by exact numerical calculation, solid lines are from perturbation theory (see Sec 2.6) and dashed line shows predictions from classical analysis.

Thus, the best isolation is achieved in the lowest well number; this is just what is expected from the classical analysis since this minimizes the Josephson inductance of the isolation junction. It is worth noting that by preparing the system in different wells, we can control the sensitivity of the system to bias current noise, and this is of considerable practical value in determining whether noise is entering the system through the leads [42].

2.7 State dependent current redistribution

In this section we examine how the state of the qubit determines the current flowing through both arms of the SQUID. Figure 7 shows the expectation value of the current flowing through the isolation junction $\langle I_2 \rangle$ as a function of I for well number 0 for four eigenstates of the Hamiltonian, *i.e.* $|00\rangle$, $|10\rangle$, $|01\rangle$ and $|11\rangle$. We find that the current changes on the order of a few nA when the qubit junction is in an excited state, while it is virtually independent of the excitation in the isolation junction. The current $\langle I_2 \rangle$ increases with bias current for all states. We have also studied the dependence of $\langle I_2 \rangle$ on the well number along the γ_2 direction. The results are qualitatively the same except that the actual current is offset or shifted by $\Phi_0/L \approx 1\mu A$ as we go from one well to the next.

As evident from fig. 2.11, the difference in $\langle I_2 \rangle$ between the ground state and the first excited state persists even when I is very small, *i.e.* in a regime where $1/\Gamma \approx \infty$. So if we can measure this small change in $\langle I_2 \rangle$ which is of the order of few nA, in that regime, the measurement will be non - destructive in so far as the qubit remains in its well or within the Hilbert space. This is in stark contrast to current schemes of measurement in phase qubits by tunneling the qubit through the barrier thereby destroying it completely. For the parameters used for the simulation, a very sensitive detector would be needed; the current only changes by a few nA in going from the ground state to the excited state, and one typically would like to read out the state in a few ns. The natural choice would be to use a second SQUID to detect the flux generated by this current. Another way is to use the so called Josephson

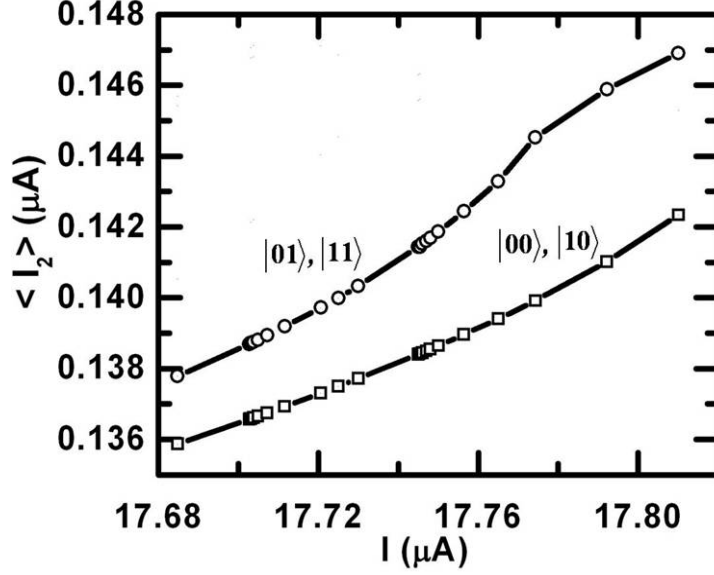


Figure 2.11: Expectation value of the current $\langle I_2 \rangle$ flowing through the isolation junction as a function of I for well number 0. The points are numerical calculations based on the exact 2D Hamiltonian whereas the solid lines correspond to an analytical calculation with Hamiltonian \bar{H} without the coupling term (see Eq. 2.24). Bifurcation Amplifier [43] device to detect small changes in $\langle I_2 \rangle$.

2.8 Conclusions

In conclusion, I analyzed the behavior of a dc SQUID phase qubit in which one junction acts as a phase qubit and the rest of the device provides isolation from dissipation and noise in the bias leads. I found the two-dimensional Hamiltonian of the system and used numerical methods and a cubic approximation to solve Schrödinger's equation for the eigenstates, energy levels, and tunneling rates. Using these results, I found that the dc SQUID phase qubit is well isolated from low

frequency bias current noise and behaves as a single phase qubit when the parameters and the bias current are chosen correctly. I also examined the state-dependent redistribution of current between the two arms of the SQUID and noted that in principle this can be used for non-destructive readout.

Chapter 3

Decoherence in superconducting qubits: A Caldeira-Leggett approach

3.1 Introduction

The possibility of using quantum mechanics to manipulate information efficiently has led, through advances in technology, to the plausibility of building a quantum computer using two-level systems, also called quantum bits or qubits. Several schemes have been proposed as attempts to manipulate qubits in atomic, molecular and optical physics (AMO), and condensed matter physics (CMP), however it is still very difficult to implement a scheme that gives both long decoherence times and is scalable.

In AMO, the most promising schemes are trapped ion systems [45], and ultracold atoms in optical lattices [46]. On the CMP side, the pursuit of solid state qubits has been quite promising in spin systems [47, 48] and superconducting devices [24, 21, 49]. While the manipulation of qubits in AMO has relied on the existence of qubits in a lattice of ions or ultra-cold atoms and the use of lasers, the manipulation of qubits in CMP has relied on the NMR techniques (spin qubits) and the Josephson effect (superconducting qubits). Integrating qubits into a full quantum computer requires a deeper understanding of decoherence effects in a single

qubit and how different qubits couple.

In AMO systems Rabi oscillations in single qubits have been observed over time scales of milliseconds since each qubit can be made quite isolated from its environment [45], however it has been very difficult to implement multi-qubit states as the coupling between different qubits is not yet fully controllable. On the other hand, in superconducting qubits Rabi oscillations have been observed [24, 35] over shorter time scales (500ns), since these qubits are coupled to many environmental degrees of freedom, and require very careful circuit design. For superconducting qubits, it has been shown experimentally [35] that sources of decoherence from two-level states within the insulating barrier of a Josephson junction can be significantly reduced by using better dielectrics and fabricating junctions of small area ($\lesssim 10 \mu\text{m}^2$).

In this chapter, I will use the Caldeira-Leggett formulation of quantum dissipation to analyze decoherence effects of superconducting qubits coupled to environments that exhibit a resonance in their spectral density. Here, I will show first how the characteristic spontaneous emission (relaxation) lifetimes T_1 for flux [9, 51], phase [22] and charge [36] qubits can be substantially enhanced, when each of them is coupled to an environment with a resonance, provided that the frequency of operation of the qubit is about twice as large as the frequency of the environmental resonance. Second, I will show that the coupling to the environment does not only cause decoherence, but also changes the qubit frequency. Lastly, I will show that when the qubit frequency is nearly the same as the resonant frequency of the environmental spectral density, an oscillatory non-Markovian decay emerges, as the qubit and its environment self-generate Rabi oscillations of characteristic time scales

shorter than the decoherence time. This chapter is a longer version of the work presented in Ref. [52, 53].

The chapter is organized as follows. In Sec. 3.2, I will derive the environmental spectral density for flux, phase, and charge qubits when each of them is coupled to an environment with a resonance. In Sec. 3.3, I will use the Caldeira-Leggett formulation of quantum dissipation to derive the Bloch-Redfield equations and to calculate the decoherence and relaxation times of these qubits. There, for the particular case of the phase qubit, I will show that when the frequency of the qubit is at least two times larger than the resonance frequency of the environmental spectral density, the decoherence time of the qubit is a few orders of magnitude larger than that of the typical ohmic regime, where the frequency of the qubit is much smaller than the resonance frequency of the spectral density. In Sec. 3.4, I will calculate the renormalization of the qubit frequency due to dressing of the two-level system with environmental degrees of freedom. In Sec. 3.5, I will derive an essentially exact non-perturbative master equation, when these systems are near resonance and where the rotating wave approximation can be applied. My results indicate that when the qubit frequency is nearly the same as the resonant frequency of the environmental spectral density, an oscillatory non-Markovian decay emerges, as the qubit and its environment self-generate Rabi oscillations of characteristic time scales shorter than the decoherence time. Finally, I will present my conclusions in Sec. 3.6.

3.2 Spectral densities of superconducting qubits with environmental resonances

In this section, we discuss three examples of superconducting qubits coupled to environments (circuits) which have resonances in their spectral functions. We begin our discussion with a simple flux qubit, then move to a charge qubit and finally to a phase qubit.

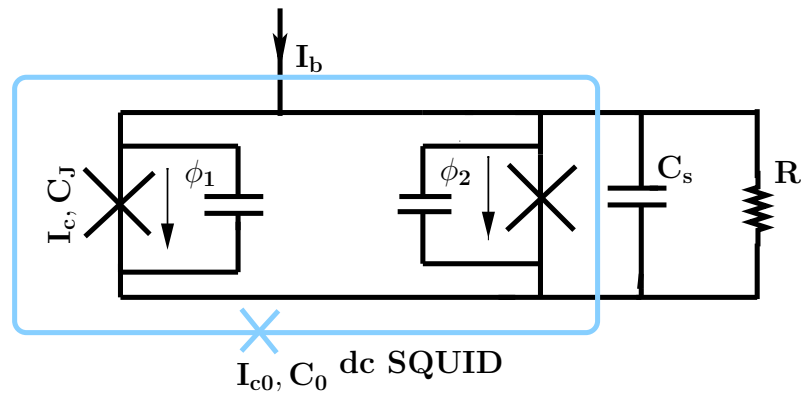


Figure 3.1: Flux qubit measured by a dc SQUID blue line. The qubit corresponds to the inner SQUID loop with critical current I_c and capacitance C_J for both Josephson junctions denoted by the large \times symbol. The inner SQUID is shunted by a capacitance C_s , and environmental resistance R and is biased by a ramping current I_b . The outer dc-SQUID loop has junction capacitance C_0 and critical current I_{c0} .

In Fig. 3.1, we show a flux qubit (inner-loop), which is measured by a dc SQUID (outer loop). To study the decoherence and relaxation time scales in such a system it is necessary to understand how noise is transferred from from the outer dc-SQUID to the qubit.

For the circuit displayed in Fig. 3.1, the classical equation of motion for the dc SQUID (outer-loop) is

$$C_0\ddot{\phi} + \frac{2\pi}{\Phi_0}I_{c0}\sin\phi - \frac{2\pi}{\Phi_0}I + \int_0^t dt'Y(t-t')\dot{\phi}(t') = 0 \quad (3.1)$$

where ϕ is the gauge invariant phase across the Josephson junction of the dc SQUID, I_{c0} is the critical current of its junction, $\Phi_0 = h/2e$ is the flux quantum, and I is the total induced current. The last term in Eq. (3.1) is the dissipation term due to effective admittance $Y(\omega)$ felt by the outer dc-SQUID [55]. In this case the total induced current in the dc SQUID (outer loop) is [56]

$$I = \left(\frac{\Phi_0}{2\pi}\right)\frac{4}{L_{dc}}\langle\delta\phi_0\sigma_z\rangle + \left(\frac{\Phi_0}{2\pi}\right)\frac{4}{L_{dc}}\langle\phi_m\rangle + \left(\frac{2\pi}{\Phi_0}\right)J_1\langle\phi_p\rangle. \quad (3.2)$$

Here $\phi_p = (\phi_1 + \phi_2)$ and $\phi_m = (\phi_2 - \phi_1)$ are the sum and difference of the gauge invariant phases ϕ_1 and ϕ_2 across the junctions of the inner SQUID, L_{dc} is the self-inductance of the inner SQUID, and J_1 is the bilinear coupling between ϕ_m and ϕ_p at the potential energy minimum. The term $\delta\phi_0 = \pi M_q I_{cir}/\Phi_0$, where I_{cir} is the circulating current of the localized states of the qubit (described in terms of Pauli matrix σ_z), and M_q is the mutual inductance between the qubit and the outer dc-SQUID.

For the charge qubit coupled to a transmission line resonator [57, 36] shown in Fig. 3.2, the classical equation of motion for the charge Q is

$$V_g(\omega) = \left(-\frac{\omega^2 L_J(\omega)}{1 - \omega^2 L_J(\omega) C_J} + \frac{1}{C_g} + i\omega Z(\omega)\right) Q(\omega) \quad (3.3)$$

Here, V_g is the gate voltage, C_g is the gate capacitance, L_J and C_J are the Josephson inductance and capacitance respectively, $Z(\omega)$ is the effective impedance seen by the

charge qubit due to a transmission line resonator (cavity), and Q is the charge across C_g .

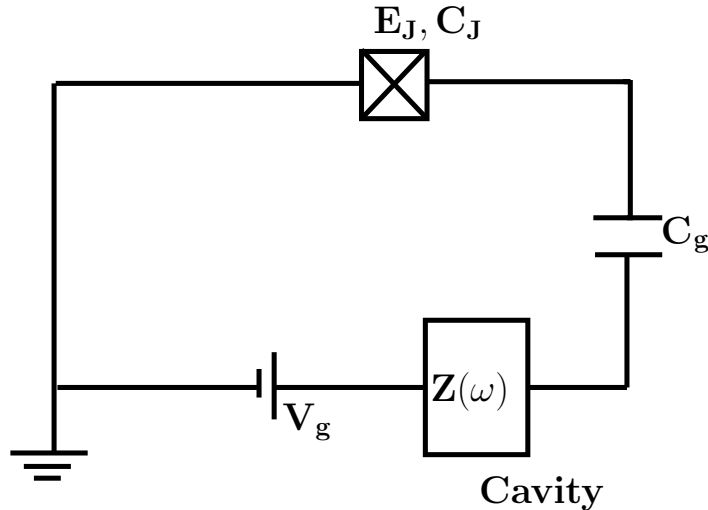


Figure 3.2: Circuit diagram of the Cooper-pair box. The superconducting island (large \times) is connected to a large reservoir through a Josephson junction with Josephson energy E_J and capacitance C_J . The voltage bias V_g is provided through a resonator (cavity) having environmental impedance $Z(\omega)$, which is connected to the gate capacitance C_g as shown.

In Fig. 3.3, we show the circuit for a phase qubit corresponding to an asymmetric dc-SQUID [22, 29]. The circuit elements inside the dashed box form an isolation network which serves two purposes: a) it prevents current noise from reaching the qubit junction; b) it is used as a measurement tool.

The classical equation of motion for the phase qubit shown in Fig. 3.3 is

$$C_0 \ddot{\gamma} + \frac{2\pi}{\Phi_0} I_{c0} \sin \gamma - \frac{2\pi}{\Phi_0} I + \int_0^t dt' Y(t-t') \dot{\gamma}(t') = 0, \quad (3.4)$$

where C_0 is the capacitance, I_{c0} is the critical current, and γ is the phase difference

across the Josephson junction J (large \times in Fig. 3.3), while I is the bias current, and $\Phi_0 = h/2e$ is the flux quantum. The last term of Eq. (3.4) can be written as $i\omega Y(\omega)\gamma(\omega)$ in Fourier space. The admittance function $Y(\omega)$ can be modeled as two additive terms $Y(\omega) = Y_{iso}(\omega) + Y_{int}(\omega)$. The first contribution $Y_{iso}(\omega)$ is the admittance that results when a transmission line of characteristic impedance R is attached to the isolation junction (here represented by a capacitance C and a Josephson inductance L) and an isolation inductance L_1 . Thus, $Y_{iso}(\omega) = Z_{iso}^{-1}(\omega)$ where $Z_{iso}(\omega) = (i\omega L_1) + [R^{-1} + i\omega C + (i\omega L)^{-1}]^{-1}$ is the impedance of the isolation network shown in Fig. 3.3. The replacement of the isolation junction by an LC circuit is justified because under standard operating conditions the external flux Φ_a varies to cancel the current flowing through the isolation junction making it zero biased [22]. Thus, the isolation junction behaves as a harmonic oscillator with inductance L which is chosen to be much smaller than L_1 . The second contribution $Y_{int}(\omega)$ is an internal admittance representing the local environment of the qubit junction, such as defects in the oxide barrier, quasiparticle tunneling, or the substrate, and can be modeled by $Y_{int}(\omega) = (R_0 + i\omega L_0)^{-1}$, where R_0 is the resistance and L_0 is the inductance of the qubit as shown in Fig. 3.3.

The equations of motion described in Eqs. (3.1), (3.3), and (3.4), can be all approximately described by the effective spin-boson Hamiltonian

$$\tilde{H} = \frac{\hbar\omega_{01}}{2}\sigma_z + \sum_k \hbar\omega_k b_k^\dagger b_k + H_{SB}, \quad (3.5)$$

written in terms of Pauli matrices σ_i (with $i = x, y, z$) and boson operators b_k and b_k^\dagger . The first term in Eq. (3.5) represents a two-level approximation for the qubit

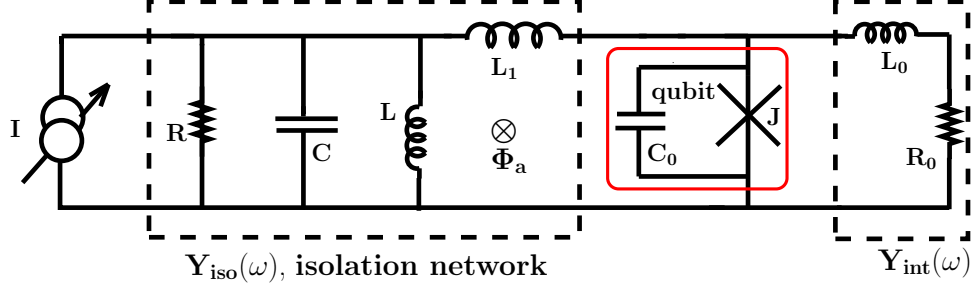


Figure 3.3: Schematic drawing of a phase qubit with an RLC isolation circuit. The phase qubit is shown inside the solid red box, the RLC isolation circuit is shown inside the dashed box to the left, and the internal admittance circuit is shown inside the dashed box to the right.

(system) described by states $|0\rangle$ and $|1\rangle$ with energy difference $\hbar\omega_{01}$. The second term corresponds to the isolation network (bath) represented by a bath of bosons, where b_k and b_k^\dagger are the annihilation and creation operator of the k -th bath mode with frequency ω_k . The third term is the system-bath (SB) Hamiltonian which corresponds to the coupling between the environment and the qubit.

At the charge degeneracy point for the charge qubit (gate charge $N_g = 0$), at the flux degeneracy point (external flux $\Phi_{\text{ext}} = \pi\Phi_0$) for the flux qubit, and at the suitable flux bias condition for the phase qubit (external flux $\Phi_a = L_1\phi_0$) H_{SB} reduces to

$$H_{SB} = \frac{1}{2}\sigma_x\hbar\langle 1|v|0\rangle \sum_k \lambda_{k1} (b_k^\dagger + b_k) \quad (3.6)$$

where $v = \phi$ for the flux qubit, $v = Q$ for the charge qubit, and $v = \gamma$ for the phase

qubit. The spectral density of the bath modes

$$J(\omega) = \hbar \sum_k \lambda_k^2 \delta(\omega - \omega_k) \quad (3.7)$$

has dimensions of energy and can be written as

$$J(\omega) = \omega \text{Re}Y(\omega) \left(\frac{\Phi_0}{2\pi} \right)^2 \quad (3.8)$$

for flux and phase qubits or as

$$J(\omega) = 2\hbar\omega \text{Re}Z(\omega) \frac{e^2}{\hbar} \quad (3.9)$$

for charge qubits.

For the flux qubit circuit shown in Fig. 3.1, the shunt capacitance C_s is used to control the environment, while the Ohmic resistance of the circuit is modelled by R . In this case, the environmental spectral density is [56]

$$J_1(\omega) = \frac{\alpha_1 \omega}{(1 - \omega^2/\Omega_1^2)^2 + 4\omega^2 \Gamma_1^2/\Omega_1^4}. \quad (3.10)$$

when $\omega_m \gg \max(\Omega_1, \omega_{01})$, and when the dc SQUID is far away from the switching point to be modelled by an ideal inductance L_J . The inner oscillator frequency $\omega_m = \sqrt{2/L_{dc}C_J}$ and the qubit frequency is ω_{01} . The external oscillator frequency

$$\Omega_1 = \sqrt{2\pi I_c^{\text{eff}}/C_s \Phi_0 [1 - (I_b/I_c^{\text{eff}})^2]^{1/4}}, \quad (3.11)$$

and plays the role of the resonant frequency, where I_c is the critical current for each of two Josephson junctions. Also, $\Gamma_1 = 1/(C_s R)$ corresponds to the resonance width, and

$$\alpha_1 = \frac{2(eI_{cir}I_bM_q)^2}{C_s^2 \hbar^2 R \Omega_1^4} \quad (3.12)$$

reflects the low frequency behavior. The coupling between the flux qubit and the outer dc SQUID emerges from the interaction of the persistent current I_{cir} of the qubit and the bias current I_b of the dc SQUID via their mutual inductance M_q .

The spectral density for the charge qubit shown in Fig. 3.2 is obtained via Eq. (3.9) by determining the real part of the impedance $Z(\omega)$. In this case, we need to solve for the normal modes of the resonator and transmission lines, including an input impedance R at each end of the resonator. This procedure results in the spectral density [57]

$$J_2(\omega) = \frac{e^2 \Omega_2}{\ell c} \frac{\Gamma_2}{(\omega - \Omega_2)^2 + (\Gamma_2/2)^2}, \quad (3.13)$$

where Ω_2 is the resonator frequency, ℓ is resonator length, c is the capacitance per unit length of the transmission line. The quantity $\Gamma_2 = \Omega_2/Q$ where Q is the quality factor of the cavity.

For the phase qubit shown in Fig. 3.3, the spectral density $J(\omega)$ is given by Eq. (3.8), and can be written in the compact form $J(\omega) = J_{iso}(\omega) + J_{int}(\omega)$. The spectral density of the isolation network is

$$J_{iso}(\omega) = \left(\frac{\Phi_0}{2\pi}\right)^2 \frac{\alpha\omega}{(1 - \omega^2/\Omega^2)^2 + 4\omega^2\Gamma^2/\Omega^4}, \quad (3.14)$$

where $\alpha = L^2/[(L + L_1)^2 R] \approx (L/L_1)^2/R$ is the leading order term in the low frequency ohmic regime,

$$\Omega = \sqrt{\frac{(L + L_1)}{LL_1 C}} \approx \frac{1}{\sqrt{LC}} \quad (3.15)$$

is essentially the resonance frequency, and $\Gamma = 1/(2CR)$ plays the role of resonance width. Here, we used $L_1 \gg L$ corresponding to the relevant experimental regime.

Notice that $J_{iso}(\omega)$ has Ohmic behavior at low frequencies since

$$\lim_{\omega \rightarrow 0} \frac{J_{iso}(\omega)}{\omega} = \left(\frac{\Phi_0}{2\pi}\right)^2 \left(\frac{L}{L_1}\right)^2 \frac{1}{R}, \quad (3.16)$$

but has a peak at frequency Ω with broadening controlled by Γ . In addition, notice that the parameter

$$\frac{\Gamma}{\Omega^2} = \frac{LL_1}{(2R(L_1 + L))} \approx \frac{L}{R} \quad (3.17)$$

is independent of C . Therefore, when there is no capacitor ($C \rightarrow 0$), the resonance disappears and

$$J_{iso}(\omega) = \left(\frac{\Phi_0}{2\pi}\right)^2 \frac{\alpha\omega}{1 + 4\omega^2\Gamma^2/\Omega^4}, \quad (3.18)$$

reduces to a Drude term with characteristic frequency $\Omega^2/2\Gamma \approx R/L$. The internal spectral density of the qubit

$$J_{int}(\omega) = \left(\frac{\Phi_0}{2\pi}\right)^2 \frac{(\omega/R_0)}{1 + \omega^2 L_0^2/R_0^2} \quad (3.19)$$

is a Drude term with characteristic frequency R_0/L_0 . Notice that $J_{int}(\omega)$ also has Ohmic behavior at low frequencies since

$$\lim_{\omega \rightarrow 0} \frac{J_{int}(\omega)}{\omega} = \left(\frac{\Phi_0}{2\pi}\right)^2 \frac{1}{R_0}. \quad (3.20)$$

Having discussed the spectral functions of the environment of three different types of superconducting qubits and their corresponding circuits, we move next to the discussion of the decoherence properties within the Bloch-Redfield description of the time evolution of the density matrix.

3.3 Bloch-Redfield equations: decoherence properties

In this section, we investigate the relaxation T_1 and decoherence T_2 times, for the three types of superconducting qubits (flux, charge and phase) described in section 3.2. In order to obtain T_1 and T_2 , we write the Bloch-Redfield equations [55]

$$\dot{\rho}_{nm} = -i\omega_{nm}\rho_{nm} + \sum_{kl} R_{nmkl}\rho_{kl} \quad (3.21)$$

for the density matrix ρ_{nm} of the spin-boson Hamiltonian in Eq. (3.5) and (3.6) derived in the Born-Markov limit [55]. Here all indices take the values 0 and 1 corresponding to the ground and excited states of the qubit, respectively, while $\omega_{nm} = (E_n - E_m)/\hbar$ is the frequency difference between states n and m . The Redfield rate tensor is

$$R_{nmkl} = -\Gamma_{lmnk}^{(1)} - \Gamma_{lmnk}^{(2)} + \delta_{nk}\Gamma_{lrrm}^{(1)} + \delta_{lm}\Gamma_{nrrk}^{(2)}, \quad (3.22)$$

where repeated indices indicate summation, and

$$\Gamma_{lmnk}^{(1)} = \hbar^{-2} \int_0^\infty dt e^{-i\omega_{nk}t} \langle H_{SB,lm}(t) H_{SB,nk}(0) \rangle, \quad (3.23)$$

$$\Gamma_{lmnk}^{(2)} = \hbar^{-2} \int_0^\infty dt e^{-i\omega_{lm}t} \langle H_{SB,lm}(0) H_{SB,nk}(t) \rangle. \quad (3.24)$$

Under these conditions, the relaxation rate becomes

$$\frac{1}{T_1} = - \sum_n R_{nnnn} = \frac{J(\omega_{01})}{M\omega_{01}} \coth\left(\frac{\hbar\omega_{01}}{k_B T}\right), \quad (3.25)$$

where we used the transition probability $|\langle 0|\nu|1\rangle|^2 = [M\omega_{01}]^{-1}$ to define the variable M , which has dimensions of mass \times area (or energy \times squared-time) and is referred to as the *mass* of the qubit. For the flux and phase qubits, the *mass* is $M \equiv$

$(\Phi_0/2\pi)^2 C_0$, where C_0 is the capacitance of the qubit. For the charge qubit, the mass is $M \equiv \hbar e/I_0$, where I_0 is the critical current. The frequency ω_{01} is the qubit frequency.

The physical interpretation of T_1^{-1} is as follows. For the system to make a transition it needs to exchange energy $E = \hbar\omega_{01}$ with the environment using a single boson. The factor $\coth(\hbar\omega_{01}/k_B T) = n(\omega_{01}) + 1 + n(\omega_{01})$ captures the sum of the rates for emission (proportional to $n(\omega_{01}) + 1$) and absorption (proportional to $n(\omega_{01})$ of a boson), where $n(\omega_{01}) = [\exp(\hbar\omega_{01}/k_B T) - 1]^{-1}$ is the Bose function.

Similarly, the decoherence rate given by the *off-diagonal* elements of the reduced density matrix ρ is

$$\frac{1}{T_2} = \text{Re}(R_{nmnm}) = \frac{1}{2T_1} + \frac{1}{T_\phi}, \quad (3.26)$$

where the dephasing rate

$$\frac{1}{T_\phi} = |\langle 0|\nu|0\rangle - \langle 1|\nu|1\rangle|^2 \lim_{\omega \rightarrow 0} \frac{J(\omega)}{\omega} 2k_B T \quad (3.27)$$

This contribution originates from dephasing processes which randomize the phases while keeping energy constant, i.e., transitions from a state into itself. Hence, they exchange zero energy with the environment and $J(0)$ enters. The prefactor measures which fraction of the total environmental noise leads to fluctuations of the energy splitting, such that only the components of noise which are *diagonal* in the basis of energy eigenstates leads to pure dephasing [59]. This effect, is thus complementary to that of the *off-diagonal* transition matrix element $\langle 0|\nu|1\rangle$ which appears in T_1 . The zero frequency argument is a consequence of the Markov approximation. Typically, $T_\phi \gg T_1$. This can be seen for example, in the Hamiltonian of the phase qubit,

where $\langle 0|\gamma|0\rangle \sim \langle 1|\gamma|1\rangle \sim \partial^3 U/\partial\gamma^3$ is the cubic correction to the potential of the phase qubit.

In Fig. 3.4, T_1 is plotted for the phase qubit as a function of the qubit frequency ω_{01} in the case of spectral densities describing an RLC [Eq. (3.14)] or Drude [Eq. (3.18)] isolation network at fixed temperatures $T = 0$ (main figure) and $T = 50\text{mK}$ (inset), with $J_{int}(\omega) = 0$ corresponding to $R_0 \rightarrow \infty$. In the limit of low temperatures ($k_B T/\hbar\omega_{01} \ll 1$), the relaxation time becomes

$$T_1(\omega_{01}) = \frac{M\omega_{01}}{J(\omega_{01})}. \quad (3.28)$$

From the main plot of Fig. 3.4 several important points can be extracted. First, in the low frequency regime ($\omega_{01} \ll \Omega$) the RL (Drude) and RLC environments produce essentially the same relaxation time $T_{1,RLC}(0) = T_{1,RL}(0) = T_{1,0} \approx (L_1/L)^2 RC_0$, because both systems are ohmic. Second, near resonance ($\omega_{01} \approx \Omega$), $T_{1,RLC}$ is substantially reduced because the qubit is resonantly coupled to its environment producing a distinct non-ohmic behavior. Third, for ($\omega_{01} > \Omega$), T_1 grows very rapidly in the RLC case. Notice that for $\omega_{01} > \sqrt{2}\Omega$, the RLC relaxation time $T_{1,RLC}$ is always larger than $T_{1,RL}$. Furthermore, in the limit of $\omega_{01} \gg \max\{\Omega, 2\Gamma\}$, $T_{1,RLC}$ grows with the fourth power of ω_{01} behaving as

$$T_{1,RLC} \approx T_{1,0} \frac{\omega_{01}^4}{\Omega^4}, \quad (3.29)$$

while for $\omega_{01} \gg \Omega^2/2\Gamma$, $T_{1,RL}$ grows only with second power of ω_{01} behaving as

$$T_{1,RL} \approx 4T_{1,0} \frac{\Gamma^2 \omega_{01}^2}{\Omega^4}. \quad (3.30)$$

Thus, $T_{1,RLC}$ is always much larger than $T_{1,RL}$ for sufficiently large ω_{01} . For param-

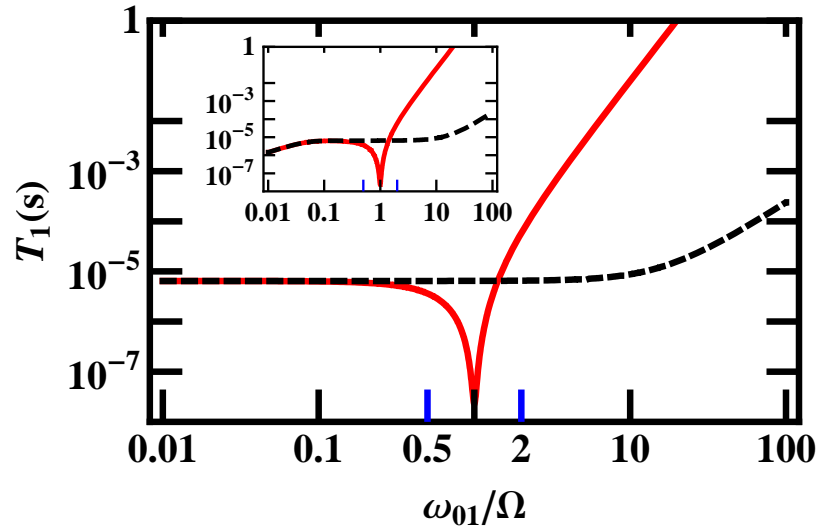


Figure 3.4: T_1 (in seconds) as a function of qubit frequency ω_{01} . The solid red curves describe the phase qubit with RLC isolation network (Fig. 3.3) with parameters $R = 50$ ohms, $L_1 = 3.9\text{nH}$, $L = 2.25\text{pH}$, $C = 2.22\text{pF}$, and qubit parameters $C_0 = 4.44\text{pF}$, $R_0 = \infty$ and $L_0 = 0$. The dashed curves correspond to an RL isolation network with the same parameters, except that $C = 0$. Main figure ($T = 0$), inset ($T = 50\text{mK}$) with $\Omega = 141 \times 10^9$ rad/sec.

eters in the experimental range (Fig. 3.4), $T_{1,RLC}$ is two orders of magnitude larger than $T_{1,RL}$, indicating a clear advantage of the RLC environment shown in Fig 3.1 over the standard ohmic RL environment. Thermal effects are shown in the inset of Fig. 3.4, where $T = 50\text{mK}$ is a characteristic experimental temperature [61]. Typical values of T_1 at low frequencies vary from 10^{-5}s at $T = 0$ to 10^{-6}s at $T = 50\text{mK}$, while the high frequency values remain essentially unchanged as thermal effects are not important for $\hbar\omega_{01} \gg k_B T$.

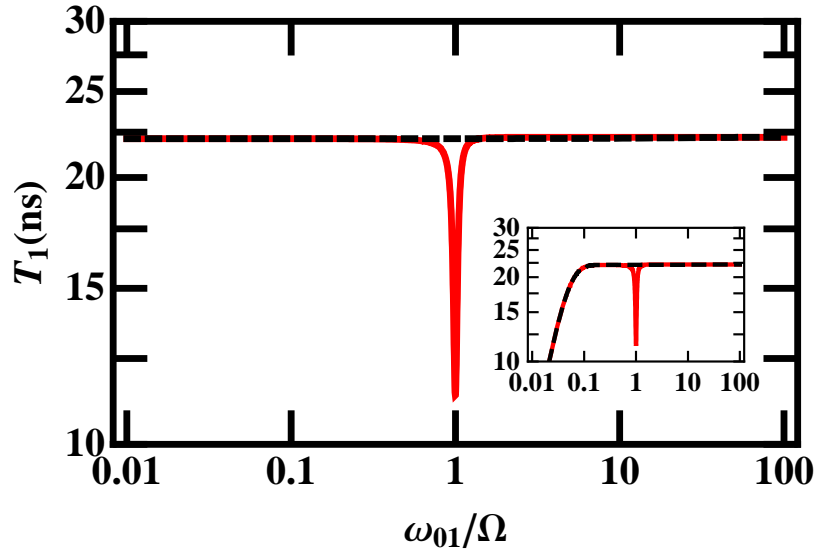


Figure 3.5: T_1 (in nanoseconds) as a function of qubit frequency ω_{01} . The solid red curves describe a phase qubit with RLC isolation network (Fig. 3.3) with same parameters of Fig. 3.2 except that $R_0 = 5000$ ohms. The dashed curves correspond to an RL isolation network with the same parameters of the RLC network, except that $C = 0$. Main figure ($T = 0$), inset ($T = 50\text{mK}$) with $\Omega = 141 \times 10^9$ rad/sec.

In the preceding analysis we neglected the effect of the local environment by setting $Y_{int}(\omega) = 0$. As a result, the low-frequency value of T_1 is substantially

larger than obtained in experiment [22, 61]. By modeling the local environment with $R_0 = 5000$ ohms and $L_0 = 0$, we obtain the T_1 versus ω_{01} plot shown in Fig. 3.5. Notice that this value of R_0 brings T_1 to values close to 20ns at $T = 0$. The message to extract from Figs. 3.4 and 3.5 is that increasing R_0 as much as possible and increasing the qubit frequency ω_{01} from 0.1Ω to 2Ω at fixed low temperature can produce a large increase in T_1 .

Having discussed the decoherence properties caused by environments with resonances for the case of superconducting qubits, we discuss next how the environment shifts (renormalizes) the qubit frequency for the same systems.

3.4 Frequency renormalization

In this section, we discuss another effect of the environment on qubit properties, in addition to dephasing and relaxation. The environment also renormalizes (shifts) the qubit frequency ω_{01} by dressing the two-state system with environmental degrees of freedom. This is similar to the physics of the Lamb shift or the Franck Condon effect. In our case, the transition frequency $E = \omega_{01}$ is renormalized according to $E_R = E + \delta E$, where $\delta E = -\text{Im}R_{1010}$ in terms of the Redfield rate tensor. The energy shift can be explicitly written as

$$\delta E = \frac{1}{4\pi} \mathcal{P} \int_0^\infty d\omega \frac{J(\omega)}{E^2 - \omega^2} [E \coth(\beta\omega/2) - \omega], \quad (3.31)$$

where \mathcal{P} denotes the Cauchy principal value, and $\beta = 1/k_B T$. Notice that δE is analogous to the energy shift obtained in second order perturbation theory, which collects all processes in which a virtual boson is emitted and reabsorbed, such that

no trace is left in the environment. The integral in Eq. (3.31) can be calculated by extending the integration to the complete real axis, closing the contour in the upper complex plane, and applying the residue theorem.

3.4.1 Phase and flux qubits

For phase and flux qubit discussed above, upon summation over all residues of the relevant poles of the spectral density, we arrive to [60]

$$\delta E = \frac{K \Omega^3 E}{2\pi 2i\Gamma} \sum_{\sigma=\pm} \frac{\sigma}{E^2 - (\sigma\Omega + i\Gamma)^2} \times \left[G(\Gamma - i\sigma) - \text{Re}G(iE) - \pi \frac{\Gamma - i\sigma\Omega}{E} \right] \quad (3.32)$$

where $G(x) = \psi(1 + \beta x/2\pi) + \psi(\beta x/2\pi)$ involves the digamma function ψ , and $K = \alpha(\Phi_0/2\pi)^2$ for phase qubit [see Eq. (3.14)], and $K = \alpha_1$ [see Eq. (3.10)] for the flux qubit. Although, we use a compact notation involving complex functions, the energy correction δE is real. Notice that δE changes sign at $\omega \simeq E$, leading to an upward shift (renormalization) of E if most of the spectral weight of $J(\omega)$ is above E (corresponding to $E < \Omega$) whereas E shifts downward in the opposite case. Physically, this corresponds to level repulsion between the spin and the oscillators in the environment. This result is consistent with usual second-order perturbation theory for energies. If the spectral weight $J(\omega)$ is concentrated at frequency $\omega = \Omega$, then the sign changes of δE happens at $E \simeq \Omega$, leading to a rather sharp structure in $\delta E(\Omega)$, and in $E_R(\Omega)$.

In the limit of low temperatures ($T \rightarrow 0$), we can replace the function G

appearing in Eq. (3.32) by an appropriate logarithm to find

$$\delta E = \frac{K}{2\pi} \frac{i\Omega^3 E}{\Gamma} \sum_{\sigma=\pm} \frac{\sigma}{E^2 - (\sigma\Omega + i\Gamma)^2} \log \left(\frac{\Gamma - i\sigma\tilde{\Omega}}{iE} \right), \quad (3.33)$$

where $\tilde{\Omega} = \Omega - \Gamma^2/\Omega$. In the underdamped limit $\Omega \gg \Gamma$, one approximates the logarithm by $\log |\Omega/E| - i\sigma\pi/2$ and rewrite the result as $E_R = E + \delta E$, with $\delta E = \delta E_\Omega + \delta E_{\text{res}}$. The first term of δE contains a logarithmic contribution which resembles the scaling in the Ohmic case (with cutoff frequency $\tilde{\Omega}$),

$$\delta E_\Omega = \frac{2}{\pi} J(E) \log \left| \frac{E}{\tilde{\Omega}} \right|. \quad (3.34)$$

where $\tilde{\Omega} \approx \Omega$. This contribution changes sign from an upward shift at $E > \tilde{\Omega}$ to a downward shift at $E < \tilde{\Omega}$ as expected from the general arguments described above.

The other contribution to δE takes into account the enormous spectral weight of the resonance, and can be written as

$$\delta E_{\text{res}} = J(E) \frac{E^2 - \tilde{\Omega}^2}{\Omega\Gamma}. \quad (3.35)$$

A term of this kind persists even in the absence of damping of the external oscillator. This term vanishes linearly with E at low energies, but undergoes the expected sign change near resonance $E \approx \Omega$, in which vicinity, a substantial renormalization also occurs.

As an illustration of the qualitative results discussed in this section, we show in Fig. 3.6 the frequency shift (renormalization) of the phase qubit with RLC isolation network described in Fig. 3.3. We make the identification $E = \omega_{01}$ and $\delta E = \delta\omega_{01}$. Near resonance $\omega_{01} \approx \Omega$, we find a frequency renormalization of about 2% which is due to the term δE_{res} .

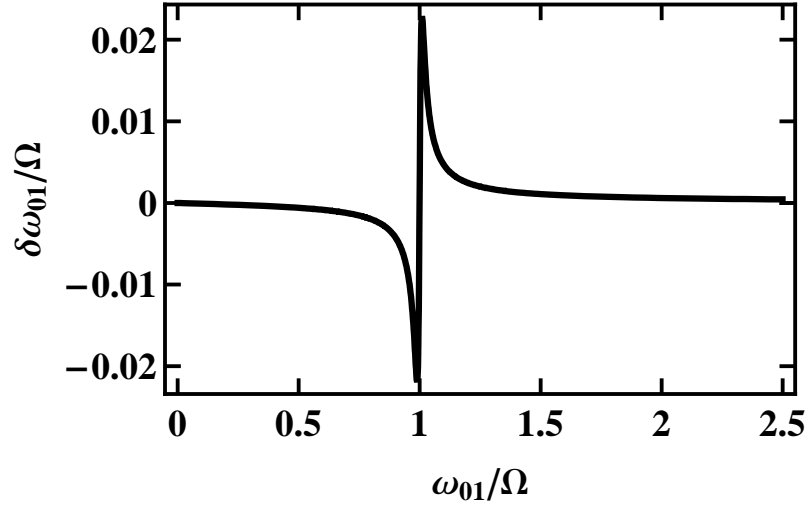


Figure 3.6: Renormalization of energy splitting for the phase qubit with RLC isolation network (Fig. 3.3) for the parameters $R = 50$ ohms, $L_1 = 3.9$ nH, $L = 2.25$ pH, $C = 2.22$ pF, and qubit parameters $C_0 = 4.44$ pF, $R_0 = 5000$ ohms and $L_0 = 0$, $T = 0$, and $\Omega = 141 \times 10^9$ rad/sec. Parameters are same as in Ref. [54].

Next, we discuss briefly the frequency renormalization of charge qubits due to environmental effects.

3.4.2 Charge qubits

For charge qubits with spectral density given by Eq. (3.13), the energy renormalization δE obtained in Eq. (3.31) can be also calculated using complex integration techniques. In the low temperature limit ($T \rightarrow 0$) there are two contributions to

$$\delta E = \delta E_\Omega + \delta E_{res}. \quad (3.36)$$

The first one is a resonant contribution

$$\delta E_{res} = e^2 \frac{\Omega_2^2}{lc} \frac{\Lambda_2 [\pi + 2 \arctan(2\Omega_2/\Gamma_2)]}{(\Lambda_2^2 + \Gamma_2^2 \Omega_2^2)}, \quad (3.37)$$

where the function

$$\Lambda_2 = E^2 - \Omega_2^2 + \left(\frac{\Gamma_2}{2}\right)^2 \quad (3.38)$$

and the second one is a non-resonant contribution

$$\delta E_\Omega = e^2 \frac{\Omega_2^2 \Gamma_2 \Omega_2 \log [E^2 / (\Gamma_2^2/4 + \Omega_2^2)]}{lc (\Lambda_2^2 + \Gamma_2^2 \Omega_2^2)}. \quad (3.39)$$

Just like the phase and flux qubit, the frequency renormalization term due to the spectral weight of the resonance δE_{res} is much larger than the logarithmic contribution δE_Ω . While δE_{res} undergoes a sign change from negative to positive at $E = \sqrt{\Omega_2^2 - (\Gamma_2/2)^2}$, δE_Ω undergoes a sign change at $\sqrt{\Omega_2^2 + (\Gamma_2/2)^2}$.

Having concluded the discussion of the frequency renormalization (shift) of superconducting qubits due to coupling to environments with resonant frequency Ω , we discuss next the behavior of superconducting qubits coupled to the same environments, when the qubit frequency ω_{01} is close to Ω , where essentially exact solutions are possible.

3.5 Non-Markovian behavior near resonance

The Bloch-Redfield equations described in Eq. (3.21) capture the long time behavior of the density matrix, but can not describe the short time behavior of the system in particular near a resonance condition $\omega_{01} \approx \Omega$, where the environmental spectral density $J(\omega \approx \Omega)$ is very large. In this case, only the environmental modes

with $\omega_k = \Omega$ couple strongly to the two-level system, like a two-level atom interacting with an electromagnetic field cavity mode that has a finite lifetime. Thus, next we derive the time evolution of the state of the flux, phase and charge qubits when the qubit frequency is close to an environmental resonance.

First, we restrict the Hamiltonian described in Eqs. (3.5) and (3.6) only to boson modes with $\omega_k \approx \Omega \approx \omega_{01}$. When $\omega_k \approx \Omega \approx \omega_{01}$, the Hamiltonian shown in Eqs. (3.5) and (3.6) can be solved in the rotating wave approximation using the complete basis set of system-bath product states $|\psi_0\rangle = |0\rangle_S \otimes |0\rangle_B$; $|\psi_1\rangle = |1\rangle_S \otimes |0\rangle_B$; $|\psi_k\rangle = |0\rangle_S \otimes |k\rangle_B$, where $|0\rangle_S$ and $|1\rangle_S$ are the states of the qubit, $|k\rangle_B$ are the states of the bath, and \otimes means tensor product. Notice that the states $|1\rangle_S \otimes |k\rangle_B$ are absent in the basis set within the rotating wave approximation and that the state of the total system at any time is

$$\phi(t) = c_0\psi_0 + c_1(t)\psi_1 + \sum_{k \neq 0,1} c_k(t)\psi_k, \quad (3.40)$$

with probability amplitudes c_0 , $c_1(t)$, and $c_k(t)$. The amplitude c_0 is constant, while the amplitudes $c_1(t)$ and $c_k(t)$ are time dependent. Assuming that there are no excited bath modes at $t = 0$, we impose the initial condition $c_k(0) = 0$, and use the normalization $|\phi(t)|^2 = 1$ to obtain the closed integro-differential equation

$$\dot{c}_1(t) = - \int_0^t dt_1 f(t-t_1) c_1(t_1), \quad (3.41)$$

where the kernel is the correlation function

$$f(\tau) = \int_0^\infty d\omega J(\omega) \exp[i(\omega_{01} - \omega)\tau]$$

directly related to the spectral density $J(\omega)$. The reduced density matrix

$$\rho(t) = \begin{pmatrix} |c_1(t)|^2 & c_1(t)c_0^* \\ c_1^*(t)c_0 & |c_0|^2 + \sum_k |c_k(t)|^2 \end{pmatrix} \quad (3.42)$$

is subject to the condition $\text{Tr}\rho(t) = 1$, or more explicitly $|c_0|^2 + \sum_k |c_k(t)|^2 = 1 - |c_1(t)|^2$, which shows that the time dynamics of $\rho(t)$ is fully determined by $c_1(t)$ for a specified value of c_0 .

3.5.1 Phase and flux qubits

For phase and flux qubits with spectral densities given by Eq. (3.14) and Eq. (3.10) respectively, we can rewrite the spectral density as

$$J_{\text{res}}(\omega) = \frac{K\Omega^3}{4i\Gamma} \sum_{\sigma=\pm 1} \frac{\sigma\omega}{\omega^2 - (\sigma\tilde{\Omega} + i\Gamma)^2}, \quad (3.43)$$

where $K = \alpha(\Phi_0/2\pi)^2$ for phase qubit [see Eq. (3.14), and $K = \alpha_1$ [see Eq. (3.10)] for the flux qubit. This reveals a resonance at $\omega = \tilde{\Omega}$ with linewidth Γ , implying that any internal off-resonance contribution to $J(\omega)$, such as $J_{\text{int}}(\omega = \tilde{\Omega})$ in the case of the phase qubit coupled to an RLC environment, can be neglected for any non-zero value of the resistance R_0 . In this case, the spectral density $J(\omega)$ dominated by the resonant contribution $J(\omega) \approx J_{\text{iso}}(\omega) \approx J_{\text{res}}(\omega)$. It is very important to emphasize, that even though $J_{\text{res}}(\omega)$ is rewritten explicitly in terms of its poles in the complex plane, a simple inspection of Eq. (3.43) shows that $J_{\text{res}}(\omega)$ is real.

For this spectral density, we can now solve for $c_1(t)$ exactly and obtain the closed form

$$c_1(t) = \mathcal{L}^{-1} \left\{ \frac{(s + \Gamma - i\omega_{01})^2 + \Omega^2 - \Gamma^2}{s [(s + \Gamma - i\omega_{01})^2 + \Omega^2 - \Gamma^2] - \kappa\Omega^4\pi i/\Gamma} \right\}$$

where $\mathcal{L}^{-1}\{F(s)\}$ is the inverse Laplace transform of $F(s)$, and $\kappa = K \times (\Phi_0/2\pi)^2 \approx 1/(\omega_{01}T_{1,0})$.

In Fig. 3.7, we plot the density matrix element $\rho_{11} = |c_1(t)|^2$ as a function of time for the dc SQUID phase qubit described in Fig 3.3. The plot contains curves for three different values of resistance, assuming that the qubit is initially (time $t = 0$) in its excited state where $\rho_{11}(0) = 1$. We consider the experimentally relevant weak dissipation limit of $\Gamma \ll \omega_{01} \approx \Omega$. Since $\Gamma = 1/(2CR)$ the width of the resonance in the spectral density shown in Eq. (3.43) is smaller for larger values of R . Thus, for large R , the RLC environment transfers energy resonantly back and forth to the qubit and induces Rabi-oscillations with an effective time dependent decay rate $\gamma(t) = -2\mathcal{R}\{\dot{c}_1(t)/c_1(t)\}$ ¹.

These environmentally-induced Rabi oscillations are a clear signature of the non-Markovian behavior [55] produced by the RLC environment, and are completely absent in the RL environment because the energy from the qubits is quickly dissipated without being temporarily stored. In the RL environment the decay in time of $\rho_{11}(t)$ has the characteristic non-oscillatory Markovian behavior. These environmentally-induced Rabi oscillations are generic features of circuits with resonances in the real part of the admittance. The frequency of the Rabi oscillations $\Omega_{Ra} = \sqrt{\pi\kappa\Omega^3/2\Gamma}$ is independent of the resistance since $\Omega_{Ra} \approx \Omega\sqrt{\pi L^2 C/L_1^2 C_0}$, and has the value of $\Omega_{Ra} = 2\pi f_{Ra} \approx 360 \times 10^6$ rad/sec in Fig. 3.7. This effect is similar to the so-called circuit quantum electrodynamics which has been of great experimental interest recently [27, 62, 63]

¹ $\mathcal{R}(z)$ is the real part of the complex variable z .

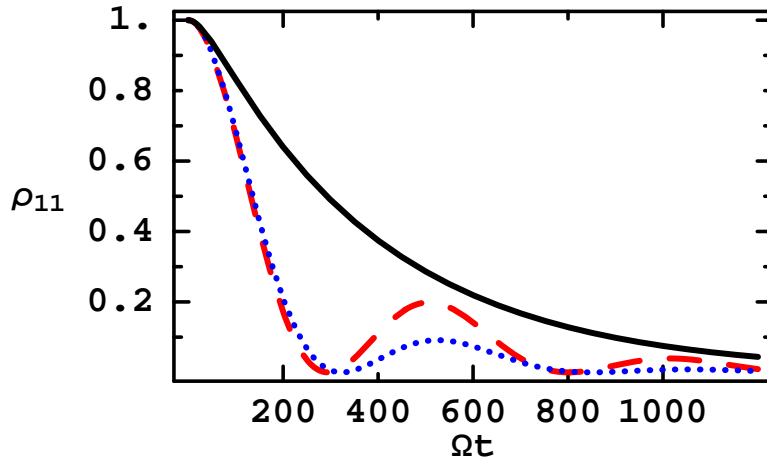


Figure 3.7: Population of the excited state of the dc SQUID phase qubit (Fig. 3.3) as a function of time $\rho_{11}(t)$, with $\rho_{11}(t = 0) = 1$ for $R = 50$ ohms (solid black curve), 350 ohms (dotted blue curve), and $R = 550$ ohms (dashed red curve), and $L_1 = 3.9\text{nH}$, $L = 2.25\text{pH}$, $C = 2.22\text{pF}$, $C_0 = 4.44\text{pF}$, $R_0 = \infty$ and $L_0 = 0$.

Next, we discuss briefly the non-Markovian dynamics for charged qubits.

3.5.2 Charge qubits

For charge qubits, the spectral density in Eq. (3.13) can be rewritten in terms of its poles in the complex plane as

$$J(\omega) = \frac{e^2 \Omega_2}{i l c} \sum_{\sigma=\pm 1} \frac{\sigma}{\omega - \Omega_2 + \sigma i \Gamma_2 / 2}. \quad (3.44)$$

Again, we can solve for $c_1(t)$ exactly, which is now given by

$$c_1(t) = c_1(0) e^{-\Gamma_2 t / 4} \left(\cosh \frac{\Delta t}{2} + \frac{\Gamma_2}{2\Delta} \sinh \frac{\Delta t}{2} \right) \quad (3.45)$$

where $\Delta = \sqrt{\Gamma_2^2/4 - 8\pi e^2 \Omega_2 / \ell c}$. Notice that the frequency Δ can be complex, so it is convenient to rewrite it as

$$\Delta = \frac{\Gamma_2}{2} \sqrt{1 - \left(\frac{2\Omega_c}{\Gamma_2}\right) \left(\frac{2\Omega_2}{\Gamma_2}\right)}, \quad (3.46)$$

where $\Omega_c = 8\pi e^2 / \ell c$. In the underdamped case where $\Omega_2 \gg \Gamma_2/2$, provided that $2\Omega_c/\Gamma_2$ is not too small, Δ becomes purely imaginary:

$$\Delta \approx i\sqrt{\Omega_c \Omega_2}. \quad (3.47)$$

Since $\cosh(i\theta) = \cos(\theta)$ and $\sinh(i\theta) = i\sin(\theta)$, where $\theta = (\sqrt{\Omega_c \Omega_2})t/2$ in the present case, it becomes clear that an oscillatory decay of the state emerges in the underdamped regime. In this regime, the period of oscillation is just $\tau = 4\pi/\sqrt{\Omega_c \Omega_2}$.

Having completed our discussion of environmentally-induced Rabi oscillations and its markedly non-markovian characteristic, we are ready to conclude.

3.6 Conclusions

In conclusion, I analyzed decoherence effects in qubits coupled to environments containing resonances in their spectral function, and I identified a crucial role played by the design of isolation circuits on decoherence properties. Furthermore, I found that the decoherence time of qubits can be two orders of magnitude larger than their typical low-frequency ohmic-regime, provided that the frequency of the qubit is about two times larger than the resonance frequency of the environmental resonance (isolation circuit in the phase qubit case). I also studied the frequency renormalization (shift) of the qubit described by a two-level system due to dressing

of the energy levels by the environmental degrees of freedom. I found that the frequency shift changes sign across the resonance frequency and is largest at resonance (about 2%). Lastly, I showed that when the qubit frequency is close to a resonance of the environment, the non-oscillatory Markovian decay of the excited state population of the qubit, gives in to an oscillatory non-Markovian decay, as the qubit and its environment self-generate Rabi oscillations of characteristic time scales shorter than the decoherence time. In particular, I discussed as a concrete example the decoherence properties of a dc SQUID phase qubit coupled with an environmental RLC circuit possessing a resonance in its spectral function, where numbers compatible with current experiments were used to estimate the environmental effects on decoherence properties [54, 61].

Chapter 4

Superfluid and Mott Insulating shells of bosons in harmonically confined optical lattices

4.1 Introduction

The recent experimental discovery of Bose-Mott insulating phases in optical lattices has generated an explosion of research in the ultra-cold atom community (see [64] for a recent review), and has helped to merge two major branches of physics: atomic-molecular-optical and condensed matter physics. Most experiments thus far have relied on measuring the momentum distribution of the atoms after switching off the trap confining the atoms to infer the existence of a superfluid to insulator transition [65, 66, 67]. However, very recently, two experimental groups [68, 69] have used spatially selective microwave spectroscopy to probe *in situ* the superfluid-to-insulator transition of ^{87}Rb in a three dimensional (3D) optical lattice with a harmonic envelope. In these experiments, the shell structure of the Bose-Mott insulating states was revealed for very deep lattices [70]. Regions of filling fraction $n = 1$ through $n = 5$ ($n = 1$ through $n = 3$) were mapped in the experimental work of Ref. [68] (Ref. [69]). Their observations in three-dimensional optical lattices lead to the confirmation of the Mott-insulating shell structure consisting of “Mott plateaus” with abrupt transitions between any two successive shells as proposed in

two dimensional (2D) [70] optical lattices.

One of the next frontiers for ultra-cold bosons in optical lattices is the search for superfluid regions separating Mott-insulating shells. Even though the Mott shell structure was determined recently using microwave spectroscopy [68, 69], any evidence of superfluid shells has remained elusive, and awaits an experimental breakthrough. Thus, my main motivation is to describe the most important signatures of superfluid shells with the hope that they will be detected experimentally, and for this purpose, I determine the existence of superfluid regions, their sizes, their excitation spectra and I propose a specific detection scheme for them. This chapter is a longer version of the work presented in Ref. [71].

To study the emergence of superfluid shells and their properties, I will describe 2D and 3D optical lattices of atomic or molecular bosons in harmonically confining potentials, and treat the boson hopping perturbatively by starting from Mott insulating states. My main results are as follows. Between Mott regions of filling fraction n and $n + 1$, superfluid shells emerge as a result of fluctuations due to finite hopping. However, standard perturbation theory [73] breaks down in the presence of a harmonic potential since superfluid shells emerge at the boundary between two locally degenerate Mott regions. Because of this local degeneracy, I will use a nearly-degenerate perturbation approach developed here. The finite hopping breaks the local energy degeneracy of neighboring Mott shells, determines the size of the superfluid regions and is responsible for the quasiparticle, sound and vortex excitations. In addition, because superfluid shells emerge between two locally degenerate insulating regions, the local energy is non-analytic in the hopping (or order param-

eter), and the equation of motion for the superfluid is not of the Gross-Pitaevskii type. This situation is therefore quite distinct from the non-degenerate perturbation theory discussed in the context of lattices without a harmonic potential [73], and from trapped bosons without a lattice [74], where the superfluid phase can be described by a Gross-Pitaevskii equation, since it emerges from a non-degenerate insulating or normal ground state, respectively.

Furthermore, I will describe quasiparticle, sound and vortex excitations in the superfluid regions. I will show that the energy cost to add a boson in superfluid shells is much smaller than to add a boson in the filled Mott regions. In addition, I will show that the superfluid shells possess low energy sound modes with spatially dependent sound velocity described by a local index of refraction directly related to the local superfluid density. Since the order parameter must vanish at the boundaries of the superfluid shells, both the superfluid density and sound velocity also vanish. For 3D optical lattices, when superfluid regions are thin (nearly 2D) spherical or ellipsoidal shells, I will also obtain bound vortex-antivortex excitations below the Berezinski-Kosterlitz-Thouless (BKT) transition temperature [75, 76] and show that the BKT temperature is different for each superfluid region. Finally, I propose the use of Laguerre-Gaussian beams and Bragg spectroscopy techniques for the detection of superfluid shells. Since Laguerre-Gaussian beams can transfer angular momentum to the superfluid regions and generate stable supercurrents, subsequent use of Bragg spectroscopy can selectively identify superfluid shell regions which are rotating with resonant velocities.

The remainder of the chapter is organized as follows. In Sec. 4.2, I present

the Bose-Hubbard Hamiltonian in a harmonic trap. In Sec. 4.3, I analyze the emergence of an alternating superfluid and Mott shell structure, comparing two different approaches involving non-degenerate and nearly-degenerate perturbation theory. I show that degenerate perturbation theory breaks down, since the superfluid regions emerge between two locally degenerate Mott shells. I also obtain the order parameter equation, the characteristic sizes of the superfluid and Mott regions, the local filling fraction and the local compressibility. In the same section, I also find that the superfluid order parameter that emerges between two Mott shells is not of the Gross-Pitaevskii type, except very close to the insulating boundaries. In Sec. 4.4, I describe quasiparticle, sound and vortex excitations in the superfluid regions, and quasiparticle and quasihole excitations in the Mott regions for completeness. In Sec. 4.5, I propose an experiment using Laguerre-Gaussian beams and Bragg spectroscopy, which can be performed in order to visualize the existence of superfluid shells. Lastly, I state my conclusions in Sec. 4.6.

4.2 Bose-Hubbard Hamiltonian

To describe the physics of alternating insulating and superfluid shells of atomic or molecular bosons in optical lattices, we use the lattice Bose-Hubbard Hamiltonian with a harmonic potential described by

$$H = -t \sum_{\mathbf{r}, \mathbf{a}} c_{\mathbf{r}}^{\dagger} c_{\mathbf{r}+\mathbf{a}} + \frac{U}{2} \sum_{\mathbf{r}} c_{\mathbf{r}}^{\dagger} c_{\mathbf{r}}^{\dagger} c_{\mathbf{r}} c_{\mathbf{r}} - \sum_{\mathbf{r}} \mu_{\mathbf{r}} c_{\mathbf{r}}^{\dagger} c_{\mathbf{r}} \quad (4.1)$$

where $\mu_{\mathbf{r}} = \mu - V(\mathbf{r})$ is the local chemical potential,

$$V(\mathbf{r}) = \frac{\Omega_{\rho} \rho^2}{2a^2} + \frac{\Omega_z z^2}{2a^2} \quad (4.2)$$

is the harmonically confining potential, a is the lattice spacing, and $c_{\mathbf{r}}^{\dagger}$ is the creation operator for a boson at site \mathbf{r} . Here, the vector $\mathbf{r} = (x, y, z)$, and the distance $\rho = \sqrt{x^2 + y^2}$. The anisotropic confining potential $V(\mathbf{r})$ becomes isotropic when $\Omega_{\rho} = \Omega_z$. Furthermore, t is the hopping parameter and U is the interaction strength, which we assume to be repulsive (positive). The sum in the first term on the right hand side of Eq. 4.1 is restricted to nearest neighbors. The harmonic trap makes the system inhomogeneous and introduces interesting properties which are absent in homogeneous Bose-Hubbard systems [77, 73].

For bosons in a homogeneous optical lattice, the Bose-Hubbard model without the harmonic confining potential can be used. In this case, it is well known that an integer number of particles on each site describes an insulating state for sufficiently large U ($U \gg t$). This is because the on-site interaction U makes it energetically unfavorable for a particle to move from one site to another. In this situation the system is in what is known as the Mott insulator phase [78]. However, if the quantum expectation of the number of bosons per site is non-integer, the extra bosons can move more easily, at a small energy cost, because their interaction energy is essentially the same on every site. For this reason, a system with non-integer number of bosons on each site is a superfluid at zero temperature [77].

Recently, several Mott-insulator shells of bosons were detected in optical lattices [68, 69], which are inevitably inhomogeneous, and thus require a model that includes the effects of the harmonic part of the confining potential. This can be modeled by the inhomogeneous Bose-Hubbard hamiltonian described in Eq. (4.1). In this case, one can either be in a regime where the entire system is superfluid or

in a regime where the system exhibits a shell structure of alternating Mott-insulator and superfluid regions. The existence of this shell structure has been shown numerically [70], but the lack of analytical progress has hindered a true understanding of the emergence and properties of these shells.

A simple argument for the emergence of the shell structure can be made by inspection of the standard phase diagram of the homogenous Bose-Hubbard model shown in Fig. 4.1 upon the substitution of $\mu \rightarrow \mu_{\mathbf{r}}$. In an inhomogenous system, the effective local chemical potential $\mu_{\mathbf{r}}$ is spatially varying. Thus, in the regions where the number density $n(\mathbf{r})$ is not an integer, a superfluid shell emerges, and in the regions where $n(\mathbf{r})$ is an integer, a Mott-insulator shell appears.

Even though a simple argument for the existence of the shell structure can be made, many questions need to be seriously addressed. For instance, what are the characteristic order parameter, dimensions and excitations of each superfluid shell? Thus, we begin our presentation by discussing next the emergence of the Mott-insulator and superfluid shell structure.

4.3 Emergence of the shell structure

A standard approach to analyse such bosonic systems is to use the Bogoliubov mean field approximation. However, as shown in [73], this approximation fails to predict the expected phase transition since it treats the interactions only approximately. Hence, instead of using the Bogoliubov approximation, we generalize a method found in the literature [77, 73], by introducing a local mean field theory that

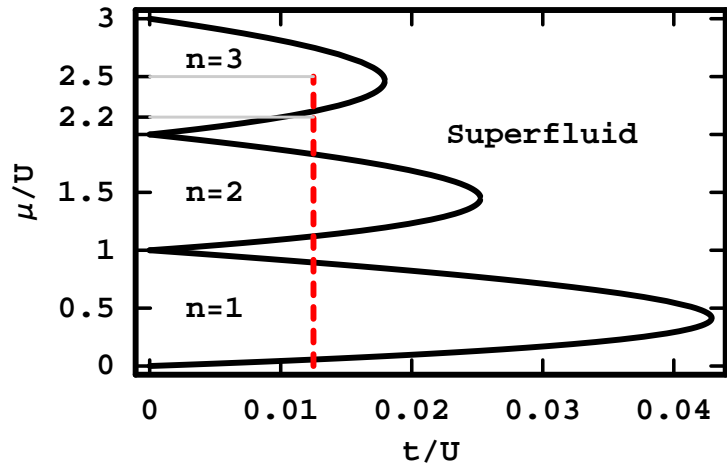


Figure 4.1: Phase diagram of the homogeneous Bose Hubbard model. For the inhomogeneous Bose Hubbard system, the dashed red line indicates the values of the local chemical potential μ_r that the system exhibits from $\mu_r = 2.5U$ (Fig 4.4) or $\mu_r = 2.2U$ (Fig 4.5) at the center of the trap to $\mu_r = 0$ at the edge of the trap for $t = 1.25 \times 10^{-2}U$. This figure indicates how the system exhibits an alternating structure of Mott and superfluid shells

treats the interactions exactly and approximates the kinetic energy of the atoms in the optical lattice. We introduce the local superfluid order parameter $\psi_{\mathbf{r}} = \langle c_{\mathbf{r}} \rangle$. We can now construct a consistent local mean field theory by substituting the operator $c_{\mathbf{r}}^\dagger c_{\mathbf{r}+\mathbf{a}} \rightarrow \langle c_{\mathbf{r}}^\dagger \rangle c_{\mathbf{r}+\mathbf{a}} + c_{\mathbf{r}}^\dagger \langle c_{\mathbf{r}+\mathbf{a}} \rangle - \langle c_{\mathbf{r}}^\dagger \rangle \langle c_{\mathbf{r}+\mathbf{a}} \rangle$, leading to an effective local Hamiltonian

$$H_{\mathbf{r}}^{\text{eff}} = H_{0,n}(\mathbf{r}) - t \sum_{\mathbf{a}} (c_{\mathbf{r}} \psi_{\mathbf{r}+\mathbf{a}}^* + c_{\mathbf{r}}^\dagger \psi_{\mathbf{r}+\mathbf{a}} - \psi_{\mathbf{r}}^* \psi_{\mathbf{r}+\mathbf{a}}), \quad (4.3)$$

which is diagonal in the site index \mathbf{r} with

$$H_{0,n}(\mathbf{r}) = \frac{U}{2} \hat{n}_{\mathbf{r}} (\hat{n}_{\mathbf{r}} - 1) - \mu_{\mathbf{r}} \hat{n}_{\mathbf{r}}, \quad (4.4)$$

where $\hat{n}_{\mathbf{r}} = c_{\mathbf{r}}^\dagger c_{\mathbf{r}}$ is the number operator. For $t = 0$, the shell structure for Mott-insulating phases is revealed by fixing $\hat{n}_{\mathbf{r}} = n$, to obtain the local energy

$$E_{0,n}(\mathbf{r}) = \frac{U}{2} n(n-1) - \mu_{\mathbf{r}} n, \quad (4.5)$$

when $(n-1)U < \mu_{\mathbf{r}} < nU$. Since $E_{0,n+1}(\mathbf{r}) - E_{0,n}(\mathbf{r}) = nU - \mu_{\mathbf{r}}$, the change from a Mott shell with filling fraction n to $n+1$ occurs at the degeneracy condition $\mu_{\mathbf{r}} = nU$, which for a spherically symmetric potential happens at the radius

$$R_{c,n} = a \sqrt{\Omega_n / \Omega}, \quad (4.6)$$

where $\Omega_n = 2(\mu - nU)$. The relation $\mu_{\mathbf{r}} = nU$ determines the shape and size of the boundary between the n and $n+1$ shells. For instance, in the case of the anisotropic potential of Eq. 4.2 the same condition leads to ellipsoidal shells

$$\left(\frac{\rho}{a_\rho} \right)^2 + \left(\frac{z}{a_z} \right)^2 = 1 \quad (4.7)$$

with principal axes $a_\rho = a \sqrt{\Omega_n / \Omega_\rho}$, and $a_z = a \sqrt{\Omega_n / \Omega_z}$. However, near this region of degeneracy, fluctuations due to hopping introduce superfluid shells, as discussed next.

4.3.1 Continuum approximation

In this section, we show how the hopping term in Eq. (4.3) affects the ground state energy of the system. Qualitatively one can see that the kinetic energy controlled by t lifts the degeneracy of the system at $\mu_{\mathbf{r}} = nU$ and in the process introduces a superfluid order parameter in a region of finite width depending on parameters n, t, Ω and U .

To obtain analytical insight into the emergence of superfluid shells, we make first a continuum approximation through the Taylor expansion

$$\psi(\mathbf{r} + \mathbf{a}) = \psi(\mathbf{r}) + a_i \partial_i \psi(\mathbf{r}) + \frac{1}{2} a_i a_j \partial_i \partial_j \psi(\mathbf{r}), \quad (4.8)$$

where repeated indices indicate summation, $\delta_i = \partial/\partial r_i$, and $i = \{1, 2, 3\}$ with $r_1 = x$, $r_2 = y$, and $r_3 = z$. This should be true in the limit where the order parameter is smoothly varying at a length scale much greater than the unit lattice spacing a . Under this approximation the effective local Hamiltonian becomes

$$H_{\mathbf{r}}^{\text{eff}} = H_{0,n}(\mathbf{r}) - c_{\mathbf{r}} \Delta^*(\mathbf{r}) - c_{\mathbf{r}}^\dagger \Delta(\mathbf{r}) + \Lambda(\mathbf{r}) \quad (4.9)$$

where $\Delta(\mathbf{r}) = zt\psi(\mathbf{r}) + ta^2\nabla^2\psi(\mathbf{r})$ reflects the amplitude for the creation of a single boson excitation at position \mathbf{r} , while the last term

$$\Lambda(\mathbf{r}) = \frac{1}{2} [\Delta(\mathbf{r})\psi^*(\mathbf{r}) + \Delta^*(\mathbf{r})\psi(\mathbf{r})] \quad (4.10)$$

reflects the local mean-field energy shift. $\Delta^*(\mathbf{r})$ is complex conjugate of $\Delta(\mathbf{r})$. Here $z = 2d$ is the number of nearest-neighbor sites (coordination number) depending on

the lattice dimension d . Within this approximation, a simple analytical treatment of the emergence of superfluid shells is possible, as discussed next.

4.3.2 Nearly degenerate perturbation theory

We focus our attention now on the Mott regions with integer boson filling n and $n + 1$ and the superfluid shell that emerges between them. In the limit where $U \gg t$ we can restrict our Hilbert space to number-basis states $|n\rangle$ and $|n + 1\rangle$ at each site. Any contribution of other states to the local energy will be of the order of t^2/U . The hopping term in Eq. (4.3) affects the ground state energy of the system by removing the local degeneracy of $E_{0,n+1}(\mathbf{r})$ and $E_{0,n}(\mathbf{r})$ at $\mu_{\mathbf{r}} = nU$. To illustrate this point, we use the continuum approximation described above and write the Hamiltonian in Eq. 4.9 in the matrix form

$$H_{\mathbf{r}}^{\text{eff}} = \begin{pmatrix} E_{0,n}(\mathbf{r}) + \Lambda(\mathbf{r}) & -\sqrt{n+1}\Delta(\mathbf{r}) \\ -\sqrt{n+1}\Delta^*(\mathbf{r}) & E_{0,n+1}(\mathbf{r}) + \Lambda(\mathbf{r}) \end{pmatrix}, \quad (4.11)$$

where $\Delta(\mathbf{r})$ and $\Lambda(\mathbf{r})$ is defined in Eq. 4.10. Notice that $t \neq 0$ has two effects. First, it changes the local energies $E_{0,n}(\mathbf{r})$ and $E_{0,n+1}(\mathbf{r})$ of the Mott shells n and $n + 1$ through $\Lambda(\mathbf{r})$. Second, it mixes the two Mott regions through the off-diagonal term $\sqrt{n+1}\Delta(\mathbf{r})$ and its hermitian conjugate. Thus, the physics near the boundary between the n and $n + 1$ Mott regions is described by an effective local two-level system with diagonal ($\Lambda(\mathbf{r})$) and off-diagonal ($\sqrt{n+1}\Delta(\mathbf{r})$) perturbations.

The eigenvalues of Eq. (4.11) are given by,

$$E_{\pm}(\mathbf{r}) = E_s(\mathbf{r}) \pm \sqrt{(E_d(\mathbf{r}))^2 + (n+1)|\Delta(\mathbf{r})|^2}, \quad (4.12)$$

where $E_s(\mathbf{r}) = [E_{0,n+1}(\mathbf{r}) + E_{0,n}(\mathbf{r})]/2 + \Lambda(\mathbf{r})$ is proportional to the sum of the diagonal terms, and $E_d(\mathbf{r}) = [E_{0,n+1}(\mathbf{r}) - E_{0,n}(\mathbf{r})]/2 = (nU - \mu_{\mathbf{r}})/2$ is proportional to their difference. These local eigenvalues are illustrated schematically in Fig. 4.2, where the local energies $E_{0,n}(\mathbf{r})$ and $E_{0,n+1}(\mathbf{r})$ are shown together with the eigenvalues $E_{\pm}(\mathbf{r})$. The radii $R_{n,\pm}$ indicated in the figure correspond to the locations where $\Delta(\mathbf{r}) = 0$.

Notice that $E_-(\mathbf{r})$ is the lowest local energy, leading to the ground state energy $E = \frac{1}{L^d} \int d\mathbf{r} E_-(\mathbf{r})$, where L is the characteristic linear dimension of the system.

The order parameter equation (OPE) is determined by minimization of E with respect to $\psi^*(\mathbf{r})$ leading to

$$\Delta(\mathbf{r}) - \frac{(n+1)t(z + a^2\nabla^2)\Delta(\mathbf{r})}{2\sqrt{|E_d(\mathbf{r})|^2 + (n+1)|\Delta(\mathbf{r})|^2}} = 0. \quad (4.13)$$

Notice that the OPE is not of the Gross-Pitaevskii (GP) type, since the superfluid regions emerge from local fluctuations between nearly degenerate neighboring Mott shells. This non-Gross-Pitaevskii equation arises from the non-analytic structure of the local energy $E_-(\mathbf{r})$, because of the spatial local degeneracy of Mott shells with filling factor n and $n+1$, from which the superfluid emerges. The present situation is thus quite distinct from the case of bosons in a lattice without trapping potentials [73] or trapped bosons without a lattice [74], where the Gross-Pitaevskii equation describes the order parameter $|\Psi(\mathbf{r})|^2$.

The zeroth order solution of this equation with $\Delta(\mathbf{r}) = zt\psi(\mathbf{r})$ leads to the spatially dependent order parameter

$$|\psi(\mathbf{r})|^2 = \frac{n+1}{4} - \frac{(nU - \mu_{\mathbf{r}})^2}{4z^2t^2(n+1)}. \quad (4.14)$$

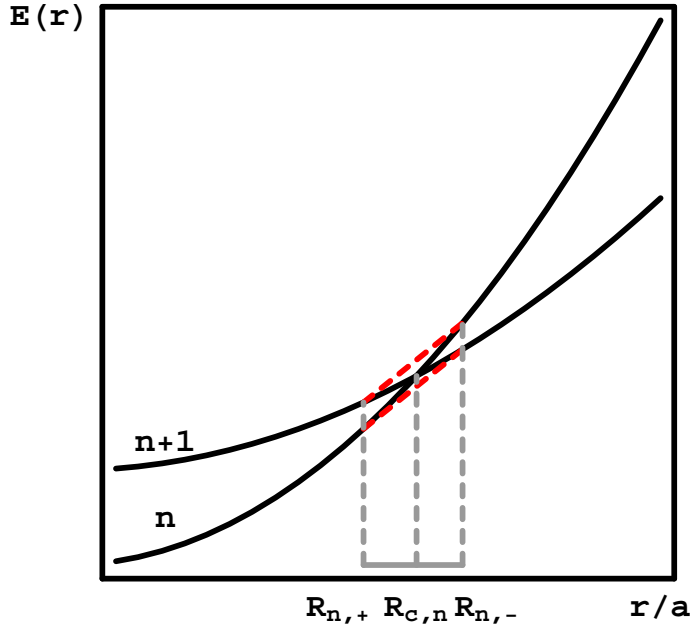


Figure 4.2: Schematic plot of local energies $E_{0,n}(\mathbf{r})$ and $E_{0,n+1}(\mathbf{r})$ showing the degenerate radius $R_{c,n}$. This local energy degeneracy is lifted by the presence of a finite hopping t , which leads to an avoided level crossing shown as dashed red curve, and to the emergence of a superfluid region with inner radius $R_{n,-}$ and outer radius $R_{n,+}$

Since $|\psi(\mathbf{r})|^2 \geq 0$, it implies that $|nU - \mu_{\mathbf{r}}| \leq (n + 1)zt$ in the superfluid region. Thus the inner radius $R_{n,-}$ and the outer radius $R_{n,+}$ of the superfluid shell between the n and $n + 1$ Mott regions is obtained by setting $|\psi(\mathbf{r})|^2 = 0$ leading to

$$R_{n,\pm} = R_{c,n} \sqrt{1 \pm \frac{2zt(n+1)}{\Omega} \frac{a^2}{R_{c,n}^2}}. \quad (4.15)$$

for a spherically symmetric harmonic potential $V(r) = \Omega(r/a)^2/2$, where $R_{c,n}$ is defined above. Our notation to describe the Mott-superfluid boundaries is illustrated in Fig. 4.3.

Equation 4.15 shows explicitly that t splits the spatial degeneracy of the n and $n + 1$ Mott shells at $r = R_{c,n}$ (or $\mu_{\mathbf{r}} = nU$) by introducing a superfluid region of thickness

$$\Delta R_n = R_{n,+} - R_{n,-}. \quad (4.16)$$

In the case of non-spherical harmonic potential $V(r) = \Omega_{\rho}(\rho/a)^2/2 + \Omega_z(z/a)^2/2$ the shell regions are ellipsoidal instead of spherical. Notice that ΔR_n depends strongly on filling fraction n , the ratio zt/Ω and the chemical potential μ through $R_{c,n}$.

In addition, the local filling fraction

$$n(\mathbf{r}) = -\frac{\partial E_-(\mathbf{r})}{\partial \mu} = n + \frac{1}{2} - \frac{nU - \mu_{\mathbf{r}}}{2zt(n+1)} \quad (4.17)$$

in the same region interpolates between $n + 1$ for $r \lesssim R_{n,-}$ and n for $r \gtrsim R_{n,+}$, while the chemical potential μ is fixed by the total number of particles $N = \int d\mathbf{r} n(\mathbf{r})$.

In Fig. 4.4, $n(\mathbf{r})$, $|\psi(\mathbf{r})|^2$, and $R_{n,\pm}$ are shown for the Mott and superfluid regions, for $t = 1.25 \times 10^{-2}U$, and $\Omega = 6 \times 10^{-6}U$, and $\mu = 2.5U$. For these

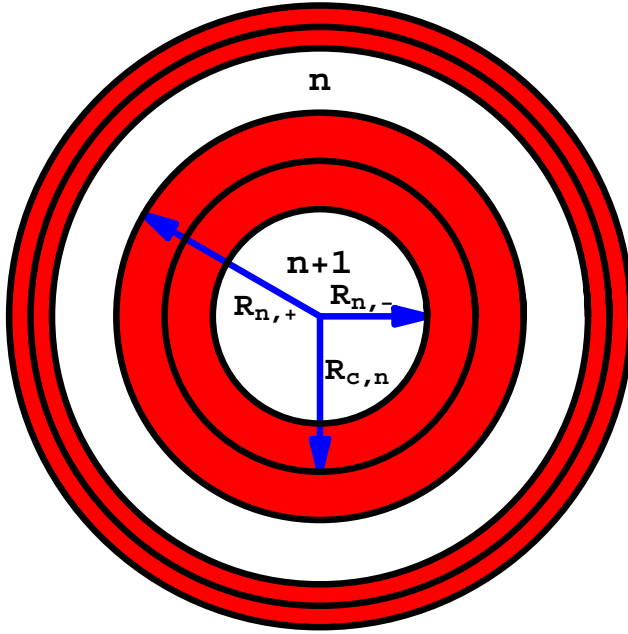


Figure 4.3: Schematic plot of superfluid regions, shown in red, and the Mott regions, shown in white. The radius $R_{c,n}$ separates Mott shells with filling factor n and $n + 1$ for $t = 0$. The superfluid regions have inner radius $R_{n,-}$ and outer radius $R_{n,+}$ and emerge between Mott shells n and $n + 1$ for non-zero t .

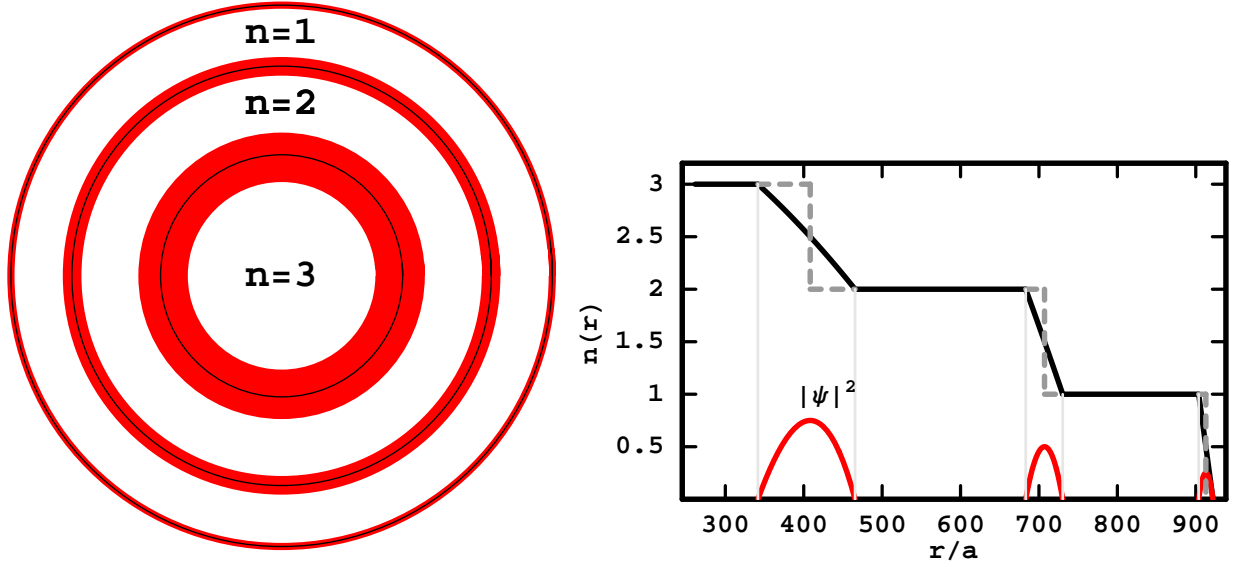


Figure 4.4: a) Shell structure of Mott and superfluids regions in a 2D square optical lattice with harmonic envelope as a function of radius r/a for $t \neq 0$. The superfluid regions are shown in red whereas the Mott regions are shown in white. The black circles indicate the Mott boundaries $R_{c,n}$ at $t = 0$. b) The local filling factor $n(\mathbf{r})$ is shown in solid lines for $t \neq 0$ and in dashed lined for ($t = 0$). The red curve shows the local superfluid order parameter $|\psi(\mathbf{r})|^2$. The parameters are $\Omega = 6 \times 10^{-6}U$, $t = 1.25 \times 10^{-2}U$ and $\mu = 2.5U$.

parameters, three Mott and three superfluid shells emerge. It is very important to emphasize that in the superfluid regions the order parameter $|\psi(\mathbf{r})|^2$ is not identical to $n(\mathbf{r})$ since the OPE equation is not of the Gross-Pitaevskii type. While the order parameter $\psi(\mathbf{r})$ vanishes at the boundaries $R_{n,\pm}$ between the superfluid and Mott shells, and reaches the maximum value $|\psi(\mathbf{r})|_{max}^2 = (n+1)/4$, when $\mu_{\mathbf{r}} = nU$, the average particle density $n(\mathbf{r})$ interpolates harmonically between Mott shells $n+1$ and n , having the average value of $n+1/2$ when $\mu_{\mathbf{r}} = nU$. Furthermore, we show in Fig. 4.5 that when $t = 1.25 \times 10^{-2}U$, and $\Omega = 6 \times 10^{-6}U$, and $\mu = 2.2U$ the central shell is superfluid, and the order parameter has a local minimum at the origin of the harmonic trap. As μ increases, this minimum is reduced to zero at a critical value, and the $n=3$ Mott shell emerges. This property of the emergence of a Mott shell from the center of the trap by suppressing the superfluid order parameter at that region is a generic feature, and can be inferred directly from the phase diagram of Fig. 4.1 via the substitution $\mu \rightarrow \mu_{\mathbf{r}}$.

The local compressibility

$$\kappa(\mathbf{r}) = \frac{\partial n(\mathbf{r})}{\partial \mu} = \frac{1}{2zt(n+1)} \quad (4.18)$$

of the superfluid shells is non-zero, in contrast to the incompressible ($\kappa = 0$) n and $n+1$ Mott shells for $r < R_{n,-}$ and $r > R_{n,+}$, respectively. The local compressibility indicates the presence of large (small) excitation energies in the Mott (superfluid) regions, as discussed later.

We note that only near the edges of the superfluid region (where $r \approx R_{n,\pm}$ and $\psi(\mathbf{r}) \approx 0$) a direct expansion of the OPE (Eq. 4.13) leads to the effective

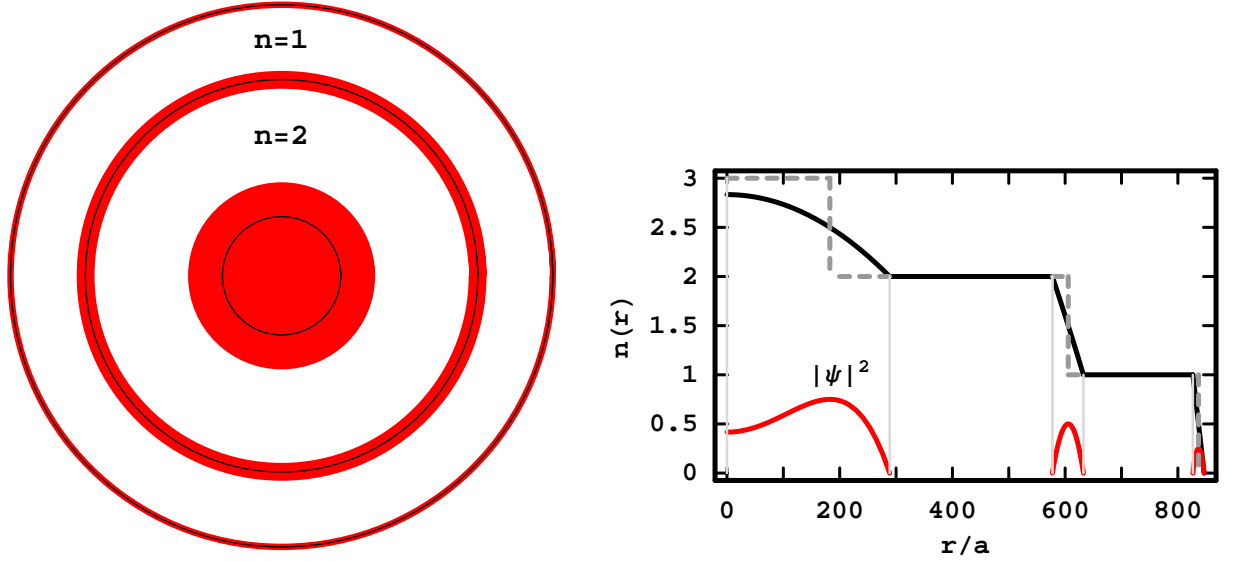


Figure 4.5: a) Shell structure of Mott and superfluids regions in a 2D square optical lattice with harmonic envelope as a function of radius r/a for $t \neq 0$. The superfluid regions are shown in red whereas the Mott regions are shown in white. The black circles indicate the Mott boundaries $R_{c,n}$ at $t = 0$. b) The local filling factor $n(\mathbf{r})$ is shown in solid lines for $t \neq 0$ and in dashed lined for ($t = 0$). The red curve shows the local superfluid order parameter $|\psi(\mathbf{r})|^2$. The parameters are $\Omega = 6 \times 10^{-6}U$, $t = 1.25 \times 10^{-2}U$ and $\mu = 2.2U$.

Gross-Pitaevskii equation

$$\left(-\frac{1}{2m_{\text{eff}}}\nabla^2 + V_{\text{eff}}(\mathbf{r}) + g_{\text{eff}} |\psi(\mathbf{r})|^2 \right) \psi(\mathbf{r}) = 0. \quad (4.19)$$

Here, $\hbar = 1$, $m_{\text{eff}} = 1/2a^2t$ is exactly the boson band mass due to the optical lattice, $V_{\text{eff}}(\mathbf{r}) = |nU - \mu_{\mathbf{r}}|/(n+1) - zt$ is the effective potential, and $g_{\text{eff}} = 2zt/(n+1)$ is the effective interaction. Notice that $V_{\text{eff}}(\mathbf{r}) \leq 0$ and vanishes at the boundaries $R_{n,\pm}$ of the superfluid region since $|nU - \mu_{\mathbf{r}}| = zt(n+1)$ there. Furthermore, $g_{\text{eff}} = zt/(n+1)$ is small in comparison to U , indicating that the superfluid near the edges is weakly interacting, and more so as the Mott index n increases. When $t \rightarrow 0$ ($m_{\text{eff}} \rightarrow \infty$) then $|\psi(\mathbf{r})|^2 = -V_{\text{eff}}/g_{\text{eff}}$ leading to the correct limiting behavior of Eq. 4.13 near $r \approx R_{n,\pm}$.

As discussed above, our nearly-degenerate perturbation theory method provides a good description of the emergence of superfluid shells. This method is a generalization of the perturbation theory developed in [73, 77] for the uniform case, which was believed not to be extendable to describe the emergence of superfluid in harmonically confined optical lattices [79]. To clarify when the standard theory developed in [73, 77] breaks down, we compare next the results from our nearly-degenerate perturbation theory with the non-degenerate case when applied to emergence of superfluid regions between Mott shells with fillings n and $n + 1$.

4.3.3 Non-degenerate perturbation theory

When the local energies for Mott phase with n bosons per site with energy $E_{0,n}(\mathbf{r}) = Un(n-1)/2 - \mu_{\mathbf{r}}n$, and Mott phase with $n + 1$ bosons per site with energy

$E_{0,n+1}(\mathbf{r}) = U(n+1)n/2 - \mu_{\mathbf{r}}(n+1)$, are away from the degeneracy region $\mu_{\mathbf{r}} = nU$, then the correction to the local energy $E_{0,n}$ is

$$E_n^{(2)} = \sum_{m \neq n} \frac{|\langle n|V|m\rangle|^2}{E_{0,n} - E_{0,m}}, \quad (4.20)$$

where $|m\rangle$ denotes the unperturbed wave function of the excited state with eigenvalue $E_{0,m}$. Here, $V = -c_{\mathbf{r}}\Delta^*(\mathbf{r}) - c_{\mathbf{r}}^\dagger\Delta(\mathbf{r})$ couples only to states with one more or one less atom than in the ground-state, and represents the perturbation to the Hamiltonian $H_{0,n}(\mathbf{r})$ defined in Eq. 4.4. The, fourth order correction can also be calculated using higher-order perturbation theory [73], and leads to the Ginzburg-Landau energy

$$E_n = a_0 + \Lambda(\mathbf{r}) + a_2|\Delta(\mathbf{r})|^2 + a_4|\Delta(\mathbf{r})|^4, \quad (4.21)$$

The coefficients a_0 , a_2 and a_4 are all functions of parameters $n, U, \mu_{\mathbf{r}}$, and t . The term a_0 corresponds to the unperturbed energy $E_{0,n}(\mathbf{r})$ described in Eq. 4.5 and associated with the unperturbed Hamiltonian $H_{0,n}$ defined in Eq. 4.4, while $\Lambda(\mathbf{r})$ is the energy shift shown in Eqs. 4.9 and 4.10, which contains spatial derivatives of the order parameter field $\psi(\mathbf{r})$.

The second order coefficient

$$a_2 = \frac{n}{U(n-1) - \mu_{\mathbf{r}}} + \frac{n+1}{\mu_{\mathbf{r}} - Un} + \frac{1}{zt}, \quad (4.22)$$

determines the existence of superfluid regions, when $a_2 < 0$, while the fourth order

coefficient

$$\begin{aligned}
a_4 &= \frac{n(n-1)}{[U(n-1) - \mu_{\mathbf{r}}]^2 [U(2n-3) - 2\mu_{\mathbf{r}}]} \\
&+ \frac{(n_{\mathbf{r}}+1)(n+2)}{[\mu - Un]^2 [2\mu_{\mathbf{r}} - U(2(n+1))]} \\
&- \left(\frac{n}{U(n-1) - \mu_{\mathbf{r}}} + \frac{n+1}{\mu_{\mathbf{r}} - Un} \right) \\
&\times \left(\frac{n}{(U(n-1) - \mu_{\mathbf{r}})^2} + \frac{n+1}{(\mu_{\mathbf{r}} - Un)^2} \right) \tag{4.23}
\end{aligned}$$

is always positive and is essentially identical to the homogeneous non-degenerate limit [73] except for the replacement of $\mu \rightarrow \mu_{\mathbf{r}}$. However, the inherent inhomogeneity of the trap potential manifests itself in the local energy for the superfluid regions (Eq. 4.21) through the spatial dependence of the coefficients a_0 , a_2 , and a_n and through the spatial derivatives of $\psi(\mathbf{r})$ contained in $\Lambda(\mathbf{r})$. Thus, we define the local Ginzburg-Landau energy difference $\Delta E_n = E_n - a_0$, which, in terms of the order parameter ψ , becomes

$$\Delta E_n = -ta^2\psi^*\nabla^2\psi + a_2z^2t^2|\psi(\mathbf{r})|^2 + a_4z^4t^4|\psi(\mathbf{r})|^4. \tag{4.24}$$

Here, we retained only terms up fourth order in ψ , and up to second order in derivatives of ψ .

Minimizing ΔE_n to zeroth order in the spatial derivatives of ψ , leads to

$$|\psi(\mathbf{r})|^2 = -\frac{a_2}{2a_4z^2t^2}, \tag{4.25}$$

and setting $|\psi(\mathbf{r})| = 0$ (or $a_2 = 0$) leads to the local chemical potential

$$2\mu_{\mathbf{r}}^{\pm} = U(2n-1) - zt \pm \sqrt{U^2 - 2U(2n+1)zt + z^2t^2}, \tag{4.26}$$

which determines the inner and outer radii of the Mott shell with filling n , where the order parameter $|\psi(\mathbf{r})|^2 = 0$ vanishes. Solving Eq. 4.26 gives the smaller radius of the Mott shell with filling n ,

$$R_{n,+} = R_{c,n} \sqrt{1 + \frac{2zt(n+1)}{\Omega} \frac{a^2}{R_{c,n}^2}}, \quad (4.27)$$

and the larger radius

$$R_{n-1,-} = R_{c,n-1} \sqrt{1 - \frac{2ztn}{\Omega} \frac{a^2}{R_{c,n-1}^2}}, \quad (4.28)$$

calculated to order t^2/U . Here, $R_{n,+} > R_{c,n}$, and $R_{n-1,-} < R_{c,n-1}$, where $R_{c,n}$ radius of the Mott shell with filling n when $t = 0$, as defined in Eq. 4.6. Notice that the size of the Mott region $\Delta R_{n,Mott} = R_{n-1,-} - R_{n,+}$ always decreases with increasing t from its value $R_{c,n-1} - R_{c,n}$ at $t = 0$, showing that superfluid regions emerge at the expense of shrinking the Mott insulator shells.

The corresponding radii defining the superfluid region between the Mott shells with filling factors n and $n + 1$ are precisely $R_{n,+}$ and $R_{n,-}$, where $R_{n,\pm}$ are defined in Eq. 4.15. Thus, to order t^2/U^2 , the thickness of the superfluid shells ΔR_n is again given by Eq. 4.16, and we recover the results obtained from our nearly-degenerate perturbation theory.

Furthermore, minimization of ΔE_n (Eq. 4.24) with respect to ψ reduces to the same Gross-Pitaevskii equation described in Eq. 4.19 near the boundaries $R_{n,+}$ and $R_{n,-}$, where the order parameter $\psi(\mathbf{r})$ vanishes. The mapping near the boundaries is $a^2 t \rightarrow 1/2m_{\text{eff}}$, $a_2 z^2 t^2 \rightarrow V_{\text{eff}}(\mathbf{r})$, and $a_4 z^4 t^4 \rightarrow g_{\text{eff}}$.

In Fig. 4.6 we compare the results of the non-degenerate perturbation theory with that of our nearly-degenerate perturbation theory for small values of t/U . The

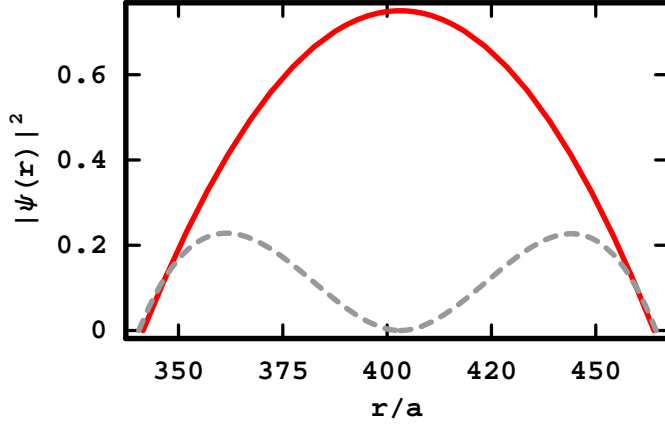


Figure 4.6: The squared amplitude of the superfluid order parameter $|\psi(\mathbf{r})|^2$ is shown as a solid line (red) for the nearly degenerate case, and as a dashed line (gray) for the non-degenerate case. Notice that near the boundaries where $\psi(\mathbf{r}) \approx 0$, both methods agree and describe the superfluid accurately. However, at the center of the superfluid shell, the non-degenerate method breaks down. The parameters are same as in Fig. 4.4, and we show the order parameter for the inner most superfluid shell, between $n = 2$ and $n = 3$ Mott shells.

parameters used are the same as in Fig. 4.4 and we show the results only for the innermost superfluid shell, between $n = 2$ and $n = 3$ Mott shells. Notice that the non-degenerate perturbation theory is correct only very close to the boundaries between the superfluid and Mott regions where $\psi(\mathbf{r})$ is small, but fails to describe the superfluid phase at the center of the superfluid shell corresponding to the degeneracy region.

Having, discussed the non-degenerate perturbation approach and its breakdown, we analyze next the excitation spectrum in the Mott and superfluids regions.

4.4 Excitations in Mott and superfluid regions

In this section, we discuss relevant excitations in the Mott and superfluid regions, and we use the method of functional integrals to obtain quasiparticle and quasihole excitations in the Mott shells and sound and vortex excitations in the superfluid shells. Eventhough, we are mostly interested in excitations of the superfluid regions, for completeness, we also present excitations in the Mott shells to be discussed next.

4.4.1 Quasiparticle and quasihole excitations

in the Mott regions

The excitation spectrum in the Mott shells can be obtained using the functional integration method for the action [73] ($\hbar = k_B = 1$, $\beta = 1/T$)

$$S[c^\dagger, c] = \int_0^\beta d\tau \sum_{\mathbf{r}} [c_{\mathbf{r},\tau}^\dagger \partial_\tau c_{\mathbf{r},\tau} + H]$$

leading to the partition function $Z = \int \mathcal{D}c^\dagger \mathcal{D}c \exp(-S[c^\dagger, c])$. Here \mathcal{D} indicates functional differential. In each Mott shell we introduce a Hubbard-Stratonovich field Ψ to take into account fluctuations due to the presence of finite hopping, and integrate out the bosons (c^\dagger, c) leading to an effective action

$$S_{\text{eff}}[\Psi^\dagger, \Psi] = \int d\mathbf{r} \sum_{i\omega, \mathbf{k}, \mathbf{k}'} \Psi_{i\omega, \mathbf{k}} \Psi_{i\omega, \mathbf{k}'}^* e^{i(\mathbf{k}-\mathbf{k}') \cdot \mathbf{r}} G_{\mathbf{k}\mathbf{k}'}^{-1}(i\omega, \mathbf{r})$$

to quadratic order in Ψ^\dagger and Ψ , where \mathbf{k}, \mathbf{k}' are momentum labels, ω are Matsubara frequencies [73], and

$$G_{\mathbf{k}\mathbf{k}'}^{-1}(i\omega, \mathbf{r}) = \epsilon_{\mathbf{k}'} \left[1 + \epsilon_{\mathbf{k}} \left(\frac{n+1}{i\omega - E_1(\mathbf{r})} - \frac{n}{i\omega - E_2(\mathbf{r})} \right) \right],$$

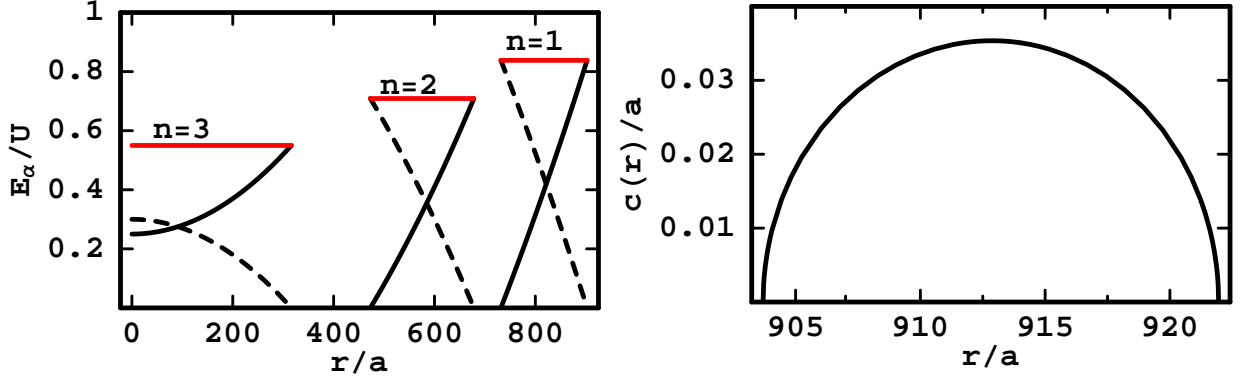


Figure 4.7: a) Quasiparticle E_{qp} (solid line), quasihole E_{qh} (dashed line), and Mott gap E_g (red) energies for $\mathbf{k} = 0$ versus r/a . b) Sound velocity for the outermost superfluid ring versus r/a . Same parameters as in Fig. 4.4

with $E_1(\mathbf{r}) = nU - \mu_{\mathbf{r}}$, $E_2(\mathbf{r}) = (n - 1)U - \mu_{\mathbf{r}}$, and The poles of $G_{\mathbf{k}\mathbf{k}'}(i\omega, \mathbf{r})$ are found upon the analytical continuation $i\omega = \omega + i\delta$, leading to the local excitation energies

$$\omega_{\pm} = -\mu_{\mathbf{r}} + \frac{U}{2}(2n - 1) - \frac{\epsilon_{\mathbf{k}}}{2} \pm \frac{1}{2}\sqrt{\epsilon_{\mathbf{k}}^2 - (4n + 2)\epsilon_{\mathbf{k}}U + U^2}$$

where the $+$ ($-$) sign labels quasiparticle (quasihole) excitations. The energy to add a quasiparticle is $E_{qp} = \omega_+$, while the energy to add a quasihole is $E_{qh} = -\omega_-$.

Figure 4.7a shows the quasiparticle and quasihole energies of the Mott phase as a function of position \mathbf{r} . The energy cost to create a quasiparticle (quasihole) is minimum (maximum) at the trap center and increases (decreases) radially, while the Mott-Hubbard gap $E_g = \min_{\mathbf{k}}(E_{qp} + E_{qh})$ is large and independent of \mathbf{r} . Thus, $E_g = \min_{\mathbf{k}}\sqrt{\epsilon_{\mathbf{k}}^2 - 4(n + 2)\epsilon_{\mathbf{k}}U + U^2}$, which leads to the final result $E_g = \sqrt{(zt)^2 - 4(n + 2)ztU + U^2}$. This expression indicates that it is easier to cre-

ate a quasiparticle-quasihole excitation inside higher n Mott shells. The horizontal solid (red) line in Fig. 4.7a also shows this tendency. Since this gap is reduced with increasing n the Mott-insulator gets weaker and thus more susceptible to superfluid fluctuations. Notice that E_g vanishes when $zt/U = (2n + 1) \pm 2\sqrt{n(n + 1)}$, but the physical solution for the critical value of zt/U corresponds to the largest value, and thus the plus (+) sign.

It should be noted that excitations within an individual Mott shell are related to the results obtained by non-degenerate perturbation theory for the case without a harmonic trap [73] via the substitution of the chemical potential by the local chemical potential, which includes the trap. However, the luxury of using degenerate perturbation theory with a local chemical potential does not apply to the superfluid shells between Mott regions n and $n + 1$, as discussed next.

4.4.2 Excitations in superfluid regions

While non-degenerate perturbation theory is sufficient to describe approximately excitations in the Mott regions with fixed filling n , it fails to describe approximately excitations in the superfluid shells, which emerge between locally degenerate Mott shells with filling n and $n + 1$, and depend strongly on the correct order parameter obtained from the nearly-degenerate perturbation theory. Even though the creation of quasiparticle-quasihole excitations in the Mott regions can be energetically costly, the creation of single quasiparticle excitations, sound waves and vortex excitations in the superfluid shells are more easily accessible, as we shall

discuss next.

Single quasiparticle excitations: The single quasiparticle excitation energy can be read off from Eq. 4.12, since the first excited state of $H_{\mathbf{r}}^{\text{eff}}$ is $E_+(\mathbf{r})$, and the ground state is $E_-(\mathbf{r})$. The local energy difference is $\Delta E = E_+(\mathbf{r}) - E_-(\mathbf{r})$ is independent of \mathbf{r} . This can be seen from the expression $\Delta E = 2\sqrt{|E_d(\mathbf{r})|^2 + (n+1)|\Delta(\mathbf{r})|^2}$, when the approximate result $\Delta(\mathbf{r}) \approx tz\psi(\mathbf{r})$ is used in combination with Eq. 4.14 and with the definition $E_d(\mathbf{r}) = [E_{0,n+1}(\mathbf{r}) - E_{0,n}(\mathbf{r})]/2 = (nU - \mu_{\mathbf{r}})/2$. The final answer is $\Delta E \approx (n+1)tz$, which indicates that energy cost of adding a quasiparticle in the superfluid shell is small in comparison to the cost of adding a quasiparticle in the Mott region.

It is also interesting to analyze the eigenvectors of the local Hamiltonian defined in Eq. 4.12. The eigenvector corresponding to E_+ is

$$|E_+\rangle = \begin{pmatrix} \frac{-E_d + \Delta E/2}{\sqrt{n+1}\Delta^*(r)} \\ 1 \end{pmatrix} \quad (4.29)$$

and reduces to the vector $(0, 1)^T$ corresponding to the energy E_n of the Mott phase with filling n , when $\Delta \rightarrow 0$. The eigenvector corresponding to E_- is

$$|E_-\rangle = \begin{pmatrix} 1 \\ \frac{\sqrt{n+1}\Delta^*(r)}{-E_d - \Delta E/2} \end{pmatrix} \quad (4.30)$$

and reduces to the vector $(1, 0)^{T1}$ corresponding to the energy E_{n+1} of the Mott phase with filling $n+1$, when $\Delta \rightarrow 0$.

However, the most interesting excitations in the superfluid regions are collective in nature. We will discuss next the collective sound excitations and later the

¹ T is transpose of the matrix

appearance of vortices.

Sound velocity: The excitation spectrum of collective modes in the superfluid region can also be calculated using the functional integral method. First we introduce the Hubbard-Stratonovich field ψ which now corresponds to the order parameter in the superfluid region. Second we use an amplitude-phase representation $\psi(\mathbf{r}, \tau) = |\psi(\mathbf{r}, \tau)| \exp[i\varphi(\mathbf{r}, \tau)]$ and apply the nearly degenerate perturbation theory described earlier to integrate out the boson fields c^\dagger and c . Thus, we obtain the phase-only effective action

$$S_{\text{eff}} = \frac{1}{2L^d} \int d\mathbf{r}d\tau [\kappa(\partial_\tau\varphi)^2 + \rho_{ij}\partial_i\varphi\partial_j\varphi] \quad (4.31)$$

to quadratic order in the phase variable for the superfluid region between the n and $n + 1$ Mott shells. Here, we assumed that $|\psi(\mathbf{r}, \tau)|$ is τ -independent at the saddle point. The coefficient κ is the compressibility of the superfluid described in Eq. 4.18, and the local superfluid density tensor

$$\rho_{ij} = \frac{(n+1)ta^2}{2} \frac{F(|\psi|, n, t)}{G(|\psi|, n, t)} - 2ta^2 |\psi|^2 \delta_{ij}, \quad (4.32)$$

where the numerator of the first term is

$$F(|\psi|, n, t) = t (4z|\psi|^2\delta_{ij} + 4|\psi|\nabla^2|\psi|\delta_{ij} - 2\partial_i|\psi|\partial_j|\psi|)$$

and the denominator of the first term is

$$G(|\psi|, n, t) = \sqrt{(nU - \mu_{\mathbf{r}})^2/4 + (n+1)t^2\Gamma(|\psi|)},$$

with the function

$$\Gamma(|\psi|) = z^2|\psi|^2 + 2|\psi|\nabla|\psi| + (\nabla^2|\psi|)^2.$$

The complex structure of the superfluid density tensor is a direct consequence of the non-Gross-Pitaevskii nature of the order parameter equation (Eq. 4.13).

Insight can be gained into the structure of the local superfluid density tensor by neglecting the gradient terms involving $|\psi|$, which in combination with Eq. 4.14 produces a local superfluid density tensor

$$\rho_s(\mathbf{r}) = \rho_{ii} = 2ta^2|\psi(\mathbf{r})|^2, \quad (4.33)$$

which vanishes at the Mott boundaries $R_{n,\pm}$. This local superfluid density tensor has been described previously in Refs. [72] and [79], however the more general expression shown in Eq. 4.32 goes beyond the mean field approximation presented in the pseudo-spin description [79]. In the present approximation, the resulting wave equation has the form

$$\partial_\tau^2 \varphi - \partial_i \left[\frac{\rho_s(\mathbf{r})}{\kappa} \partial_i \varphi \right] = 0, \quad (4.34)$$

leading to a local sound velocity $c(\mathbf{r}) = \sqrt{\rho_s(\mathbf{r})/\kappa}$, which in terms of the order parameter reads $c(\mathbf{r}) = 2\sqrt{(n+1)zta}|\psi(\mathbf{r})|$. The local speed of sound has its maximal value at $|\psi(\mathbf{r})|_{max} = (\sqrt{n+1})/2$, and the superfluid region behaves as a medium of continuous index of refraction

$$\chi(\mathbf{r}) = \frac{c_{max}}{c(\mathbf{r})} = \frac{\sqrt{n+1}}{2|\psi(\mathbf{r})|}. \quad (4.35)$$

Notice that $\chi(\mathbf{r}) \rightarrow \infty$ at the Mott boundaries where $|\psi(\mathbf{r})| = 0$, indicating that the sound waves of the superfluid do not propagate into the Mott regions. A plot of the local sound velocity is shown in Fig. 4.7b for the superfluid region between the $n = 1$ and $n = 0$ Mott shells. From the phase-only effective action for the superfluid region, we can also investigate the vortex excitations, which are discussed next.

Vortices and antivortices: Next, we explore vortex solutions in two cases where spontaneous vortex-antivortex pairs can appear as indicators of the Berezinski-Kosterlitz-Thouless (BKT) transition [75, 76]. Case I corresponds to a 3D system, where the superfluid regions are very thin $\Delta R_n \ll R_{c,n}$, leading to essentially a two-dimensional superfluid in curved space. Case II corresponds to a 2D system, where the superfluid regions are thick rings $\Delta R_n \sim R_{c,n}$, leading to essentially a two-dimensional superfluid subject to boundary conditions.

In a flat space two-dimensional system stationary vortex solutions must satisfy $\oint \nabla\varphi \cdot d\mathbf{l} = 2\pi m$, where $m = \pm 1, \pm 2, \dots$ is the vorticity (topological charge) and $\nabla\varphi$ is the superfluid velocity. The standard vortex solution in cylindrical coordinates is $\nabla\varphi = m\hat{\theta}/r$, and the corresponding free energy per unit volume is

$$\mathcal{F} = \frac{1}{2L^d} \int d\mathbf{r} \rho_s(\mathbf{r}) (\nabla\varphi)^2. \quad (4.36)$$

This situation is analogous to a two-dimensional linear dielectric material where the displacement field is

$$\mathbf{D} = \nabla\varphi \times \hat{z} = \epsilon(\mathbf{r})\mathbf{E}, \quad (4.37)$$

with dielectric function $\epsilon(\mathbf{r}) = 1/[2\pi\rho(\mathbf{r})]$. Notice that the dielectric function diverges at the superfluid boundaries, since $\rho_s(\mathbf{r}) \rightarrow 0$ in those regions. In this language \mathcal{F} is identical to the electrostatic energy per unit volume

$$U_{\text{el}} = \frac{1}{2L^d} \int d\mathbf{r} \mathbf{D} \cdot \mathbf{E}. \quad (4.38)$$

In general the solutions for several vortices (antivortices) can be obtained from

$$\nabla \wedge \nabla\varphi = 2\pi\hat{z} \sum_i m_i \delta(\mathbf{r} - \mathbf{r}_i), \quad (4.39)$$

where \mathbf{r}_i is the location of the vortex (or antivortex) of vorticity m_i .

In case I the superfluid state appears below $T_{BKT} \approx \pi \tilde{\rho}_s(\mathbf{r} = \mathbf{R}_{c,n})/2$, where $\tilde{\rho}_s = \rho_s/a^2$ has dimensions of energy. In this limit $\tilde{\rho}_s(\mathbf{r} = \mathbf{R}_{c,n}) = (n+1)t/2$ and the critical temperature of the superfluid shell between the n and $n+1$ Mott regions depends on the index n . Notice, however that such estimate is reasonable only when the radius of the shells are sufficiently large. The solution for a vortex-antivortex (VA) pair in curved two-dimensional space is

$$\varphi(r = R_{c,n}, \theta, \phi) = \arctan \left(\frac{4bR_{c,n} \tan \left(\frac{\pi-\theta}{2} \right) \sin(\phi)}{b^2 - 4R_{c,n}^2 \tan^2 \left(\frac{\pi-\theta}{2} \right)} \right)$$

where $R_{c,n} = a\sqrt{2(\mu - nU)/\Omega}$ is the radius of the superfluid shell, and b is the VA size. A three-dimensional view of the velocity field $\nabla\varphi(\theta, \phi)$ is shown in Fig. 4.8. When the superfluid shell has a small thickness ΔR_n then $T_{BKT} \approx \pi t(n+1)\Delta R_n/6a$, while the vortex-antivortex pair has an approximate solution of the same form as above which interpolates between $\varphi(r = R_{n,-}, \theta, \phi)$ and $\varphi(r = R_{n,+}, \theta, \phi)$.

In case II the superfluid regions are rings bounded by $R_{n,-}$ and $R_{n,+}$, and one can use the Coulomb gas analogy described above, conformal mapping techniques and proper boundary conditions to obtain vortex-antivortex solutions. The creation of vortex-antivortex pairs are energetically quite costly when $\Delta R_n \ll R_{c,n}$, due to strong confinement effects of the boundaries, thus we do not expect a BKT-type superfluid transition to occur until ΔR_n is substantially large ($\sim R_{c,n}$). Only in this limit, we expect a BKT transition with $T_{BKT} \approx \pi \langle \tilde{\rho}_s \rangle / 2$, where $\langle \tilde{\rho}_s \rangle / 2$ is the surface area average of $\tilde{\rho}_s(\mathbf{r})$.

Having analyzed the excitation spectra in the insulator and superfluid regions,

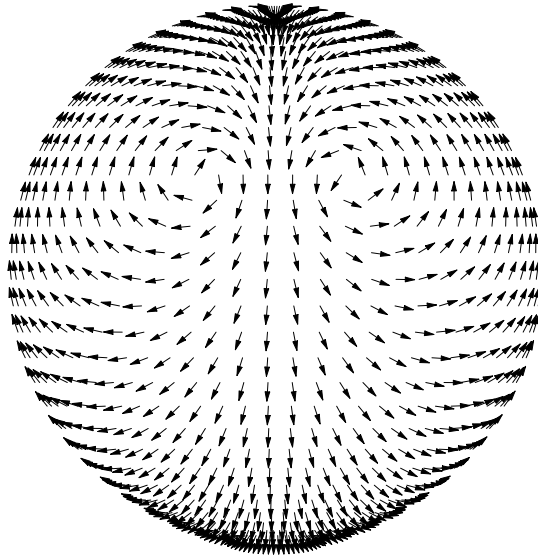


Figure 4.8: Three-dimensional view of a vortex-antivortex pair in 2D superfluid shell separating two 3D Mott regions.

we discuss next some possible experimental detection schemes for the superfluid shells.

4.5 Detection of superfluid shells

Eventhough the use of tomographic microwave techniques has allowed the detection of several Mott regions [68, 69], it has been quite challenging to detect superfluid shells. In this section, we propose a possible experiment for the detection of superfluid shells through the use of Laguerre-Gaussian and Gaussian beams followed by Bragg spectroscopy. The idea is that Laguerre-Gaussian and Gaussian beams can transfer angular momentum to the atoms in the superfluid phase without transferring linear momentum, while the Mott insulator regions do not absorb the angular momentum due to the presence of a large gap in their excitation spectrum. In this

situation, we can use Bragg spectroscopy to detect the existence of the superfluid since the technique is sensitive to the velocity of the atoms in the superfluid phase. When the frequencies of the beams used in Bragg spectroscopy are correctly chosen some of the rotating atoms in the superfluid regions acquire extra momentum, are kicked out of their shells and can be imaged.

The Laguerre-Gaussian technique has been successfully used to rotate superfluid sodium atoms ^{23}Na in a *mexican hat* potential [80, 81]. The technique used was a two step process, where initially a Laguerre-Gaussian beam transferred both linear and angular momentum to atoms, and a second Gaussian beam canceled the linear momentum transfer leaving each trapped atom with exactly one unit of angular momentum. In this manner, the atoms participating in superfluidity rotate without dissipation, and when the trap is released, the superfluid region expands, but does not fill the center of the cloud, thus maintaining a toroidal structure throughout time of flight. Furthermore, Bragg spectroscopy was used to detect the sense of rotation of vortices within a vortex lattice of sodium BEC [82] and to observe the persistent flow of Bose-condensed Sodium atoms in toroidal traps [83].

The Laguerre-Gaussian technique and Bragg spectroscopy may also be used to detect superfluid shells of bosons in harmonically confined optical lattices. However, the situation here is slightly different because of the existence of Mott shells and multiple superfluid regions. To illustrate this, we discuss the simpler case of a nearly two-dimensional configuration, where the harmonic trap is very tight along the z-direction, loose along the x- and y- directions and only two superfluid shells are present. Upon application of the Laguerre-Gaussian technique along the z-direction,

angular momentum transfer occurs essentially to the atoms in the superfluid phase, imposing a rotating superfluid current with a well defined superfluid velocity profile, while the Mott regions remain unchanged due to their large gap in the excitation spectrum. The angular momentum transfer is chosen to occur along the z direction generating superfluid currents in the x-y plane, and the amount of angular momentum transfer is assumed to be \hbar for each atom that absorbed a Laguerre-Gaussian photon with $l = 1$. Next, we use Bragg spectroscopy with counter-propagating beams along the x-direction to detect the sense of rotation and determine the regions of superfluid rings with well defined velocities. If there is sufficient optical resolution and signal-to-noise ratio, then the experiment may be performed *in situ*, otherwise Bragg spectroscopy measurements can be performed in time-of-flight.

A schematic plot of the detection of superfluid shells using Bragg spectroscopy can be found in Fig. 4.9, which shows two superfluid shells rotating counter-clockwise and two counter propagating beams applied along the x direction. As can be seen in Fig. 4.9 the right(left)-going beam has frequency $\omega(\omega')$ and linear momentum $\mathbf{k}(\mathbf{k}')$. The bose atoms undergo a transition from the internal state with energy ϵ_i to the internal state ϵ_f . In the following analysis, we retain \hbar , instead of setting $\hbar = 1$. Applying momentum conservation, we can easily obtain that the final linear momentum of the atoms in the superfluid region is $\mathbf{p}_f = \mathbf{p}_i + \hbar(k + k')\hat{\mathbf{x}}$, in terms of the initial linear momentum of the photons $\hbar k\hat{\mathbf{x}}$ and $-\hbar k'\hat{\mathbf{x}}$. Thus, the Bragg beams transfer a net linear momentum $\hbar(k + k')\mathbf{x}$ to the atoms which satisfy the energy

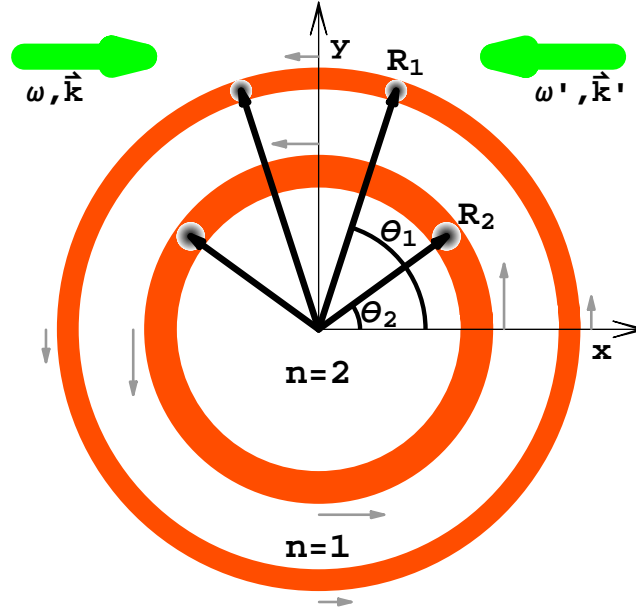


Figure 4.9: Schematic plot for the detection of superfluid shells using Bragg spectroscopy. The angles θ_1 and θ_2 indicate the locations of strongest momentum transfer from the Bragg beams (large green arrows) to the rotating superfluid shells of radii R_1 and R_2 . The gray arrows indicate the sense of rotation of the superfluid shells.

conservation condition

$$\hbar(\omega - \omega') = \epsilon_f - \epsilon_i - v_x \hbar(k + k') + \frac{\hbar^2(k + k')^2}{2m} \quad (4.40)$$

In the equation above v_x is the component of the velocity $\mathbf{v}_i = \mathbf{p}_i/m$ along the x direction. Notice that v_x can also be written as $v_x = v_i \sin \theta$ where θ is the angle between the Bragg beams and the velocity \mathbf{v}_i of the atoms in the superfluid shell and $v_i = p_i/m$ is the magnitude of \mathbf{v}_i . For an atom carrying one unit of angular momentum, the superfluid velocity is $\mathbf{v}_i = \hbar \hat{\theta} / mr$. Therefore, within a superfluid shell at position $r = R$ atoms get a linear momentum kick of $\hbar(k + k') \hat{\mathbf{x}}$ when the velocity $v_x = \hbar \sin \theta / mR$ satisfies the condition given in Eq. 4.40. This leads to

two Bragg angles $\theta = -\sin^{-1}(mRv_x/\hbar)$, and $\pi - \theta$ for each superfluid shell. As can be seen in Fig. 4.9 the Bragg angles are θ_1 and $\pi - \theta_1$ for the outer superfluid shell labelled by R_1 , and are θ_2 and $\pi - \theta_2$ for the inner superfluid shell labelled by R_2 . The regions with same velocity v_x are identified by the condition $\sin \theta_1/R_1 = \sin \theta_2/R_2 = mv_x/\hbar$. Once these atoms are kicked out of their respective superfluid shells, they form two small clouds, which can be detected by direct imaging. Thus, if there is sufficient optical resolution and signal-to-noise ratio, the experiment may be performed *in situ*, otherwise Bragg spectroscopy measurements can be performed in time-of-flight. These clouds also carry the information about the sense of rotation of the superfluid shells and their velocity profile, and one can in principle extract this information from the resulting images.

Having discussed our proposal for the experimental detection of superfluid shells in harmonically confined optical lattices, we present next our conclusions.

4.6 Conclusions

I studied 2D and 3D optical lattices of atomic or molecular bosons in harmonically confining potentials, and showed that between the Mott regions of filling fraction n and $n + 1$, superfluid shells emerge as a result of fluctuations due to finite hopping. I showed that standard non-degenerate perturbation theory can not be used to describe the superfluid shells that emerge between Mott regions of filling fraction n and $n + 1$, since these Mott shells are locally degenerate at their boundaries when the hopping is zero. I found that the presence of finite hopping breaks

the local energy degeneracy of neighboring Mott shells, determines the size of the superfluid regions as shown in Fig 4.4, and is responsible for quasiparticles, sound and vortex excitations in the superfluid regions.

In addition, because superfluid shells emerge between two locally degenerate insulating regions, the local energy is non-analytic in the hopping (or order parameter), and the equation of motion for the superfluid is not of the Gross-Pitaevskii type. The superfluid state analyzed here is then distinct from that obtained within non-degenerate perturbation theory in the context of lattices without a harmonic potential [73], or trapped bosons without a lattice [74], where the superfluid can be described by a Gross-Pitaevskii equation, since it emerges from a non-degenerate insulating or normal ground state, respectively.

Within my nearly-degenerate perturbation theory approach I obtained the quasiparticle, sound and vortex excitations in the superfluid regions. I showed that the sound excitations have a spatially dependent sound velocity, which vanishes between the superfluid and Mott shells. Furthermore, I obtained bound vortex-antivortex solutions (as shown in Fig 4.8 below the Berezinski-Kosterlitz-Thouless (BKT) transition when superfluid regions are thin (nearly 2D) spherical (or ellipsoidal) shells. Finally, I discussed that the emergence of these superfluid regions should be detectable using a combination of Laguerre-Gaussian and Bragg spectroscopy techniques.

Chapter 5

Superfluid and Fermi liquid phases of Bose-Fermi mixtures in optical lattices

5.1 Introduction

Fermi and Bose degenerate quantum gases and liquids display several remarkable macroscopic quantum phenomena. For instance, superfluidity is known to exist in neutral liquids such as ^4He (boson) and in ^3He (fermion), as well as in a variety of electronic materials that exhibit superconductivity. The role of quantum statistics and interactions is of fundamental importance to understand the phases emerging from purely bosonic or purely fermionic systems, and a substantial amount of understanding of these individual Bose or Fermi systems can be found in the atomic and condensed matter physics literature. However, new frontiers can be explored when mixtures of bosons and fermions are produced in harmonic traps or optical lattices.

An important example of the richness of quantum degenerate Bose-Fermi mixtures was revealed in ^4He - ^3He mixtures where for fixed ^4He concentration the critical temperature for superfluidity is reduced as the ^3He concentration is increased, and below the critical temperature a tricritical point phase separation appears [84]. In this Bose-Fermi mixture, essentially the only control parameter of interest is the

ratio between the concentration of ^4He and ^3He .

In atomic physics, a spectacular degree of control has been achieved in Bose-Fermi mixtures, where not only the ratio between the concentration of bosons and fermions can be adjusted, but also the interactions between fermions and bosons can be controlled through the use of Feshbach resonances [85], as demonstrated in mixtures of harmonically trapped Bose-Fermi mixtures of ^{40}K and ^{87}Rb . Furthermore, these same atoms have been successfully loaded into optical lattices [86] and have produced a system that has no counterpart in standard condensed matter systems. By controlling the depths of optical lattices we can change not only the interactions between boson and fermions, but also their hopping from site to site, thus allowing the exploration of a very rich phase space, where supersolid and phase separated states have been suggested [87]. The list of Bose-Fermi mixtures in atomic physics is growing, and include systems where the masses are close like ^6Li and ^7Li , ^{39}K and ^{40}K , or ^{172}Yb and ^{173}Yb ; or systems where the masses are quite different like ^6Li and ^{40}K , ^7Li and ^{39}K , ^6Li and ^{23}Na , ^6Li and ^{87}Rb , ^{40}K and ^{23}Na , or ^{40}K and ^{87}Rb . This suggests a wide possibility of regimes that can be reached by tuning interactions, concentration and geometry, which is not possible in ordinary condensed matter physics.

A few studies of quantum phases of Bose-Fermi mixtures have focused on homogeneous three dimensional systems with [89, 90], and without optical lattices [88]. However, only one effort focused on harmonically confined optical lattices [92]. Most of the descriptions of Bose-Fermi mixtures in optical lattices have relied on numerical methods using either Gutzwiller projection [89, 92] or quantum Monte Carlo [90]

techniques. In this chapter, I present a fully analytical theory of boson and spin polarized fermion mixtures in harmonically confined optical lattices by using degenerate perturbation theory for finite hopping in conjunction with the local density approximation. This chapter provides insight into the phase diagram of Bose-Fermi mixtures, and into the detection of superfluid and Fermi liquid shells at low temperatures. It is a longer version of the work presented in Ref. [91].

In this chapter I will analyse in detail the regime where the hopping parameters of bosons and fermions are comparable and the repulsion between bosons and fermions is a substantial fraction of the boson-boson repulsion. In this case, the system presents regions of (I) coexisting Bose-Mott and Fermi-band insulator, (II) coexisting Bose-Mott insulator and Fermi liquid, (III) Bose-Mott insulator, and (IV) Bose superfluid, as shown in Fig. 5.1. I will compute analytically the boundaries between various phases, and obtain the spatially dependent boson and fermions filling fractions in each region. Although one can envisage other situations where, for example, one can have coexistence of superfluid and Fermi band insulator, I confine my discussion to the situations above for the sake of simplicity. Finally, I propose a detection method of the shell structure of Bose-Fermi mixtures by using Laguerre-Gaussian beams [93] and Bragg spectroscopy [82], where angular momentum is transferred only to regions with extended states such as the superfluid and Fermi-liquid shells.

5.2 Bose-Fermi Hubbard Hamiltonian

To describe Bose-Fermi mixtures in harmonically confined square (2D) or cubic (3D) optical lattices we start with the Hamiltonian

$$\begin{aligned}\hat{H} &= K_B + K_F - \sum_{\mathbf{r}} \mu_B(\mathbf{r}) \hat{n}_B(\mathbf{r}) - \sum_{\mathbf{r}} \mu_F(\mathbf{r}) \hat{n}_F(\mathbf{r}) \\ &+ \frac{U_{BB}}{2} \sum_{\mathbf{r}} \hat{n}_B(\mathbf{r}) [\hat{n}_B(\mathbf{r}) - 1] + U_{BF} \sum_{\mathbf{r}} \hat{n}_B(\mathbf{r}) \hat{n}_F(\mathbf{r}),\end{aligned}$$

where $K_B = -t_B \sum_{\langle \mathbf{r}, \mathbf{r}' \rangle} b_{\mathbf{r}}^{\dagger} b_{\mathbf{r}'}$ and $K_F = -t_F \sum_{\langle \mathbf{r}, \mathbf{r}' \rangle} f_{\mathbf{r}}^{\dagger} f_{\mathbf{r}'}$ are the kinetic energies of boson and fermions with nearest-neighbor hoppings t_B and t_F , and $b_{\mathbf{r}}^{\dagger}$ and $f_{\mathbf{r}}^{\dagger}$ are the bosonic and fermionic creation operators at site \mathbf{r} . Here, the lattice sites for bosons and fermions are assumed to be the same, but the hopping parameters can be different. The number operators are $\hat{n}_B(\mathbf{r}) = b_{\mathbf{r}}^{\dagger} b_{\mathbf{r}}$ and $\hat{n}_F(\mathbf{r}) = f_{\mathbf{r}}^{\dagger} f_{\mathbf{r}}$, and the corresponding local chemical potentials are $\mu_F(\mathbf{r}) = \mu_F - V_F(\mathbf{r})$ and $\mu_B(\mathbf{r}) = \mu_B - V_B(\mathbf{r})$, where $V_F(\mathbf{r}) = \Omega_F(r/a)^2/2$ and $V_B(\mathbf{r}) = \Omega_B(r/a)^2/2$ are the harmonically confining potentials and μ_F and μ_B are the chemical potentials for fermions and bosons. The origin of the lattice with spacing a is chosen to be at the minimum of the harmonically confining potential. The terms containing U_{BB} (U_{BF}) represent the boson-boson (boson-fermion) interaction. Note that the fermions have zero onsite interaction energy (within the Bose-Hubbard model) due to Pauli's exclusion principle, and only have exchange interaction.

When $t_B = t_F = 0$, the Hamiltonian $\hat{H} = \hat{H}_0$ is a sum of single-site contributions, and the eigenstates are tensor products of number states with state vectors $|\psi\rangle = |n_{B,0}, n_{B,1}, \dots\rangle |n_{F,0}, n_{F,1}, \dots\rangle$, with $n_{B,\mathbf{r}} = 0, 1, 2, \dots$ and $n_{F,\mathbf{r}} = 0, 1$ representing the occupation number of bosons and fermions at site \mathbf{r} , respectively. At site \mathbf{r}

the local energy is $E_{n_B, n_F}(\mathbf{r}) = U_{BB}n_B(n_B - 1)/2 + U_{BF}n_Bn_F - \mu_B(\mathbf{r})n_B - \mu_F(\mathbf{r})n_F$. For the ground state wavefunction the number of bosons at site \mathbf{r} is determined by $\max(0, \lfloor (U_{BB} + \mu_B(\mathbf{r}))/2U_{BB} \rfloor)$ if $E_{n_B, 0}(\mathbf{r}) < E_{n_B, 1}(\mathbf{r})$ and $\max(0, \lfloor (U_{BB} + \mu_B(\mathbf{r}) - U_{BF})/2U_{BB} \rfloor)$ otherwise. Similarly, the number of fermions per site is zero if $E_{n_B, 0}(\mathbf{r}) < E_{n_B, 1}(\mathbf{r})$ and one otherwise. The symbol $\lfloor \cdot \cdot \rfloor$ is the floor function.¹

In the ground state solution shells (n_B, n_F) with n_B bosons and n_F fermions are formed by those lattice sites \mathbf{r} for which the local energy is the same. For our harmonic traps these shells are nearly spherically symmetric. The boundary between shells (n_B, n_F) and $(n_B + 1, n_F)$ is determined by $E_{n_B, n_F}(\mathbf{r}) = E_{n_B + 1, n_F}(\mathbf{r})$, leading to the radius $R_{B, n_B, n_F} = a\sqrt{\Omega_{n_B, n_F}/\Omega_B}$, where $\Omega_{n_B, n_F} = 2(\mu_B - n_B U_{BB} - n_F U_{BF})$. Similarly, the boundary between shells with occupation numbers $(n_B, 0)$ and $(n_B, 1)$ is determined by equating the local energies $E_{n_B, n_F}(\mathbf{r})$ and $E_{n_B, n_F + 1}(\mathbf{r})$, leading to the radius $R_{F, n_B} = a\sqrt{2(\mu_F - n_B U_{BF})/\Omega_F}$. We consider the number of particles to be sufficiently large such that the radii of the boundaries are much larger than the lattice spacing a .

5.3 Finite hopping: perturbative treatment

Next, we begin our discussion of finite hoppings by taking first $t_B \neq 0$, with $t_F = 0$. The Bose superfluid region emerges due to kinetic fluctuations at the boundaries between the (n_B, n_F) and $(n_B + 1, n_F)$ shells. At this boundary the local energy $E_{n_B + 1, n_F}(\mathbf{r})$ is degenerate with $E_{n_B, n_F}(\mathbf{r})$. To describe the emergence of

¹floor(x) = $\lfloor x \rfloor$ is the largest integer not greater than x.

superfluid regions, we introduce the order parameter for superfluidity $\psi_{B,j}$ via the transformation $b_i^\dagger b_j \rightarrow \psi_{B,i}^* b_j + b_i^\dagger \psi_{B,j} - \psi_{B,i}^* \psi_{B,j}$, and then for analytical convenience make the continuum approximation $\psi(\mathbf{r} + a) = \psi(\mathbf{r}) + a_i \partial_i \psi(\mathbf{r}) + (1/2) a_i a_j \partial_i \partial_j \psi(\mathbf{r})$.

In the limit of $U_{BB} \gg t_B$, we can restrict our Hilbert space to the number basis states $|n_B, n_F\rangle$ and $|n_B + 1, n_F\rangle$, as any contribution from other basis states to the local energy is of order t_B^2/U_{BB} . The hopping term t_B affects the energies $E_{n_B+1, n_F}(\mathbf{r})$ and $E_{n_B, n_F}(\mathbf{r})$ by removing their degeneracy, thus creating finite-width superfluid regions between shells $(n_B + 1, n_F)$ and (n_B, n_F) . The effective local Hamiltonian then becomes,

$$H_{\mathbf{r}}^{\text{eff}} = \begin{pmatrix} E_{n_B, n_F}(\mathbf{r}) + \Lambda(\mathbf{r}) & -\sqrt{n_B + 1} \Delta(\mathbf{r}) \\ -\sqrt{n_B + 1} \Delta^*(\mathbf{r}) & E_{n_B+1, n_F}(\mathbf{r}) + \Lambda(\mathbf{r}) \end{pmatrix}, \quad (5.1)$$

where $\Lambda(\mathbf{r}) = \frac{1}{2}(\Delta(\mathbf{r})\psi^*(\mathbf{r}) + cc)$ and $\Delta(\mathbf{r}) = t_B(z\psi(\mathbf{r}) + a^2\nabla^2\psi(\mathbf{r}))$. Here, z is the coordination number which depends on the lattice dimension d .

The eigenvalues of Eq. (5.1) are given by,

$$E_{\pm}(\mathbf{r}) = E_s(\mathbf{r}) \pm \sqrt{[E_d(\mathbf{r})]^2 + (n_B + 1) |\Delta(\mathbf{r})|^2},$$

where $E_s(\mathbf{r}) = [E_{n_B+1, n_F}(\mathbf{r}) + E_{n_B, n_F}(\mathbf{r})] / 2 + \Lambda(\mathbf{r})$ is proportional to the sum of the diagonal terms, and $E_d(\mathbf{r}) = [E_{n_B+1, n_F}(\mathbf{r}) - E_{n_B, n_F}(\mathbf{r})] / 2 = (n_B U_{BB} + n_F U_{BF} - \mu_B(\mathbf{r})) / 2$ is proportional to their difference. Notice that $E_-(\mathbf{r})$ is the lowest local energy leading to the total ground state energy $\mathbf{E} = \frac{1}{L^d} \int d\mathbf{r} E_-(\mathbf{r})$.

5.4 Order parameter and compressibility

The order parameter equation (OPE) is determined by minimization of \mathbf{E} with respect to $\psi^*(\mathbf{r})$ leading to

$$\Delta(\mathbf{r}) - \frac{(n_B + 1)t_B(z + a^2\nabla^2)\Delta(\mathbf{r})}{2\sqrt{|E_d(\mathbf{r})|^2 + (n_B + 1)|\Delta(\mathbf{r})|^2}} = 0. \quad (5.2)$$

Notice that the OPE is not of the Gross-Pitaevskii (GP) type, since the superfluid regions emerge from local fluctuations between neighboring Mott shells. Ignoring the spatial derivatives of ψ in Eq. (5.2) leads to the spatially dependent order parameter

$$|\psi(\mathbf{r})|^2 = \frac{n_B + 1}{4} - \frac{(n_B U_{BB} + n_F U_{BF} - \mu_B(\mathbf{r}))^2}{4z^2 t_B^2 (n_B + 1)}. \quad (5.3)$$

Since $|\psi(\mathbf{r})|^2 \geq 0$, hence $|n_B U_{BB} + n_F U_{BF} - \mu_B(\mathbf{r})| \leq (n_B + 1)zt_B$, and the inner $R_{n_B, n_F, -}$ and outer $R_{n_B, n_F, +}$ radii for the superfluid shell between the (n_B, n_F) and $(n_B + 1, n_F)$ Mott regions are obtained by setting $|\psi(\mathbf{r})|^2 = 0$ leading to

$$R_{n_B, n_F, \pm} = R_{B, n_B, n_F} \sqrt{1 \pm \frac{2zt_B(n_B + 1)}{\Omega_B} \frac{a^2}{R_{B, n_B, n_F}^2}}.$$

This relation shows explicitly that t_B splits the spatial degeneracy of the (n_B, n_F) and $(n_B + 1, n_F)$ insulating shells at $r = R_{c, n_B, n_F}$ or $\mu_B(\mathbf{r}) = n_B U_{BB} + n_F U_{BF}$ by introducing a superfluid region of width $\Delta R_{n_B, n_F} = R_{n_B, n_F, +} - R_{n_B, n_F, -}$. (See Fig. 5.1 for characteristic widths).

In addition, the local bosonic filling fraction

$$n_B(\mathbf{r}) = -\frac{\partial E_-(\mathbf{r})}{\partial \mu_B} = n_B + \frac{1}{2} - \frac{n_B U_{BB} + n_F U_{BF} - \mu_B(\mathbf{r})}{2zt_B(n_B + 1)}$$

in the same region interpolates between $n_B + 1$ for $r \lesssim R_{n_B, n_F, -}$ and n for $r \gtrsim R_{n_B, n_F, +}$, while the chemical potential μ_B is fixed by the total number of bosons

$N_B = \int d\mathbf{r} n(\mathbf{r})$. The local bosonic compressibility $\kappa_B(\mathbf{r}) = \partial n_B(\mathbf{r})/\partial \mu_B = 1/2zt_B(n_B + 1)$ of the superfluid shells is non-zero, in contrast to the incompressible ($\kappa_B = 0$) (n_B, n_F) and $(n_B + 1, n_F)$ insulating shells for $r < R_{n_B, n_F, -}$ and $r > R_{n_B, n_F, +}$, respectively.

Now, we consider finite t_F . In order to have a tractable theory we assume that the shell boundaries of the bosons and fermions are well separated. This allows us to investigate the Fermi liquid near the shell boundary of the fermions in the presence of a Bose-Mott insulator with n_B bosons per site. Furthermore, if we assume that the local density of the Fermi gas is smoothly varying then the local number of fermions is

$$n_F(\mathbf{r}) = \int_{\epsilon_{\min}}^{\epsilon_{\max}} d\epsilon \mathcal{D}(\epsilon) f[\epsilon - \mu_F^{\text{eff}}(\mathbf{r})] \quad (5.4)$$

where $f[x]$ is the Fermi function at temperature T , and $\mathcal{D}(\epsilon) = \sum_{\mathbf{k}} \delta(\epsilon - \epsilon_{\mathbf{k}})$ is the density of fermion states with energy dispersion $\epsilon_{\mathbf{k}} = -2t_F \sum_{\ell}^d \cos(k_{\ell} a)$. The effective chemical potential $\mu_F^{\text{eff}}(\mathbf{r}) = \mu_F(\mathbf{r}) - n_B U_{BF}$ accounts for the effect of the bosons. The band minimum and maximum of $\epsilon_{\mathbf{k}}$ are $\epsilon_{\min} = -2dt_F$ and $\epsilon_{\max} = 2dt_F$, respectively. Thus, the Fermi liquid region is limited by the boundaries $\epsilon_{\min} \leq \mu_F(\mathbf{r}) \leq \epsilon_{\max}$, leading to $R_{F, \pm} = R_{F, n_B} \sqrt{1 \pm 2zt_F a^2 / \Omega_F R_{F, n_B}^2}$ for the inner $R_{F, -}$ and outer $R_{F, +}$ radius of the FL shell. The width of the FL region is $\Delta R_{F, n_B} = R_{F, +} - R_{F, -}$. (See Fig. 5.1 for characteristic widths). The isothermal compressibility of the FL region is $\kappa_F(\mathbf{r}) = \partial n_F(\mathbf{r})/\partial \mu_F$, which leads at zero temperature to $\kappa_F(\mathbf{r}) = 0$ outside the FL shell, indicating the presence of insulating regions and $\kappa_F(\mathbf{r}) = \mathcal{D}[\mu_F(\mathbf{r})]$ inside the FL shell, indicating the presence of conducting regions. The

superfluid and FL shells for finite t_B and t_F , and their density profiles are shown in Fig. 5.1 for the two-dimensional case.

5.5 Detection of superfluid and Fermi liquid shells

Next, we propose an experiment to detect superfluid and Fermi liquid shells in Bose-Fermi mixtures using a combination of Gaussian and Laguerre-Gaussian beams followed by Bragg spectroscopy. To illustrate the idea, we discuss the simpler case of a nearly two-dimensional configuration, where the harmonic trap is very tight along the z-direction, loose along the x- and y- directions. Upon application of Gaussian and Laguerre-Gaussian beams along the z-direction, only angular momentum is transferred to the atoms in the conducting phases (superfluid or Fermi liquid), imposing a rotating current with a well defined velocity profile, while the insulating regions do not absorb angular momentum due to their large gap in the excitation spectrum.

To probe the rotating superfluid and Fermi liquid phases we propose the use of two counter-propagating Bragg beams applied in the xy plane along the x direction, as indicated in Fig. 5.2.

The Bragg beams transfer a net linear momentum $\hbar(k + k')\mathbf{x}$ to the atoms of mass m which satisfy the energy conservation condition

$$\hbar(\omega - \omega') = \epsilon_f - \epsilon_i - v_x \hbar(k + k') + \frac{\hbar^2(k + k')^2}{2m}, \quad (5.5)$$

where v_x is the component of the velocity $\mathbf{v}(\mathbf{r}) = \mathbf{p}(\mathbf{r})/m$ along the x direction and ϵ_i and ϵ_f are the experimentally accessible energies of the initial and final internal

states atom. For an atom carrying one unit of angular momentum, the velocity is $\mathbf{v}_i = \hbar\hat{\theta}/mr$. Therefore, within a conducting shell with radius $r = R$ atoms get a linear momentum kick of $\hbar(k + k')\hat{\mathbf{x}}$ when the velocity $v_x = \hbar \sin \theta/mR$ satisfies the condition given in Eq. (5.5). This leads to two Bragg angles $\theta = -\sin^{-1}(mRv_x/\hbar)$, and $\pi - \theta$ for each conducting shell. As can be seen in Fig. 5.2, the Bragg angles are θ_1 and $\pi - \theta_1$ for the outer superfluid shell labelled by R_1 , and are θ_2 and $\pi - \theta_2$ for the fermi liquid shell labelled by R_2 . Once these atoms are kicked out of the conducting shells, they form two small expanding clouds, which can be detected by direct absorption imaging.

Next, we discuss the time scales over which the rotation in the conducting regions persist and can be detected experimentally. In the case of the superfluid region we use the Landau criterion to show that the velocity imposed to the superfluid through the angular momentum transfer is much smaller than the local sound velocity $c(\mathbf{r}) = \sqrt{\rho_s(\mathbf{r})/\kappa}$, where $\rho_s(\mathbf{r}) = 2t_B a^2 |\psi(\mathbf{r})|^2$ is the local superfluid density, and κ is the compressibility. Thus, $c(\mathbf{r}) = 2\sqrt{(n_B + 1)zta}|\psi(\mathbf{r})|$ vanishes at the insulator boundaries where $|\psi(\mathbf{r})| = 0$, and only close to the edge of the superfluid regions the local rotational speed $v(\mathbf{r}) = \hbar/mr$ exceeds $c(\mathbf{r})$, which means that essentially all the superfluid region can be detected and the angular momentum transferred does not decay over time scales of at least seconds, limited by the lifetime of the trapped system.

In the case of the Fermi liquid region, the time scale over which the flow of the fermions persist in presence of the Bose-Mott insulator background can be calculated

from the imaginary part of the fermionic self-energy

$$\Sigma_F(k) = U_{BF}^2 T^2 \sum_{q_1, q_2} G_B(q_1) G_B(q_2) G_F(k + q_1 - q_2),$$

where $k = (\mathbf{k}, i\omega)$ and $q_i = (\mathbf{q}_i, i\nu_i)$, with ω (ν_i) are fermionic (bosonic) Matsubara frequencies and T is temperature. The bare inverse bosonic propagator in the Bose-Mott phase is

$$G_B^{-1}(q, \mathbf{r}) = \epsilon_{\mathbf{q}} \left[1 + \epsilon_{\mathbf{q}} \left(\frac{n_B + 1}{i\hbar\omega - E_1(\mathbf{r})} - \frac{n_B}{i\hbar\omega - E_2(\mathbf{r})} \right) \right],$$

where $E_1(\mathbf{r}) = (n_B - 1)U_{BB} - \mu_B(\mathbf{r})$, $E_2(\mathbf{r}) = (n_B - 2)U_{BB} - \mu_B(\mathbf{r})$ and $\epsilon_{\mathbf{q}} = -2t_B \sum_{\ell}^d \cos(k_{\ell}a)$. The bare inverse fermionic propagator in the Fermi liquid phase is $G_F^{-1}(k, \mathbf{r}) = i\hbar\omega - \epsilon_F(\mathbf{k}, \mathbf{r})$, where $\epsilon_F(\mathbf{k}, \mathbf{r}) = \epsilon_F(\mathbf{k}) - \mu_F(\mathbf{r})$. For $n_B = 1$ and $T = 0$, the imaginary part of the fermionic self-energy is

$$\text{Im}\Sigma_F(k, \mathbf{r}) = -\pi U_{BF}^2 [F(\hbar\omega) + F(-\hbar\omega)], \quad (5.6)$$

where $F(\hbar\omega) = \Theta(\hbar\omega)\Theta(-\hbar\omega + \mu_B(\mathbf{r}))\mathcal{D}(\hbar\omega + \mu_F(\mathbf{r}))$, Θ is the Heaviside step function, and $\mathcal{D}(\epsilon)$ is the fermion density of states. For a two-dimensional Fermi liquid shell, there is a Van Hove singularity in $\mathcal{D}(\epsilon)$ at half filling. The expression in Eq. (5.6) is independent of momentum, since the dominant excitations in the Bose-Mott region are number-conserving and low-momentum particle-hole excitations, but strongly dependent on position through $\mu_B(\mathbf{r})$ and $\mu_F(\mathbf{r})$, leading to a characteristic decay time $\tau_{\mathbf{r}} = -h/\text{Im}\Sigma(k, \mathbf{r})$. For the parameters used in Fig. 5.1, (with $U_{BF}/h = 1$ kHz) the time scale for the persistence of the flow near the edges (away from the Van Hove singularity) is $\tau_{\mathbf{r}} \approx 13$ ms. However, near the center of the Fermi liquid region (close to the Van Hove singularity) $\tau_{\mathbf{r}}$ is extremely short, indicating

that it is much easier to detect fermions at the edge than at the center of Fermi liquid shells.

5.6 Conclusions

I have discussed the phase diagram of Bose-Fermi mixtures in harmonically confined optical lattices in the regime where the hopping parameters of bosons and fermions are comparable and the repulsion between bosons and fermions is a substantial fraction of the boson-boson repulsion. I showed that the system exhibits regions of (I) coexisting Bose-Mott and Fermi-band insulator, (II) coexisting Bose-Mott insulator and Fermi liquid, (III) Bose-Mott insulator, and (IV) Bose-superfluid. I have calculated analytically the boundaries between these phases and obtained the spatially dependent filling fraction for each region. Finally, I proposed a detection method of the superfluid and Fermi liquid shells of Bose-Fermi mixtures by using Gaussian and Laguerre-Gaussian beams followed by Bragg spectroscopy.

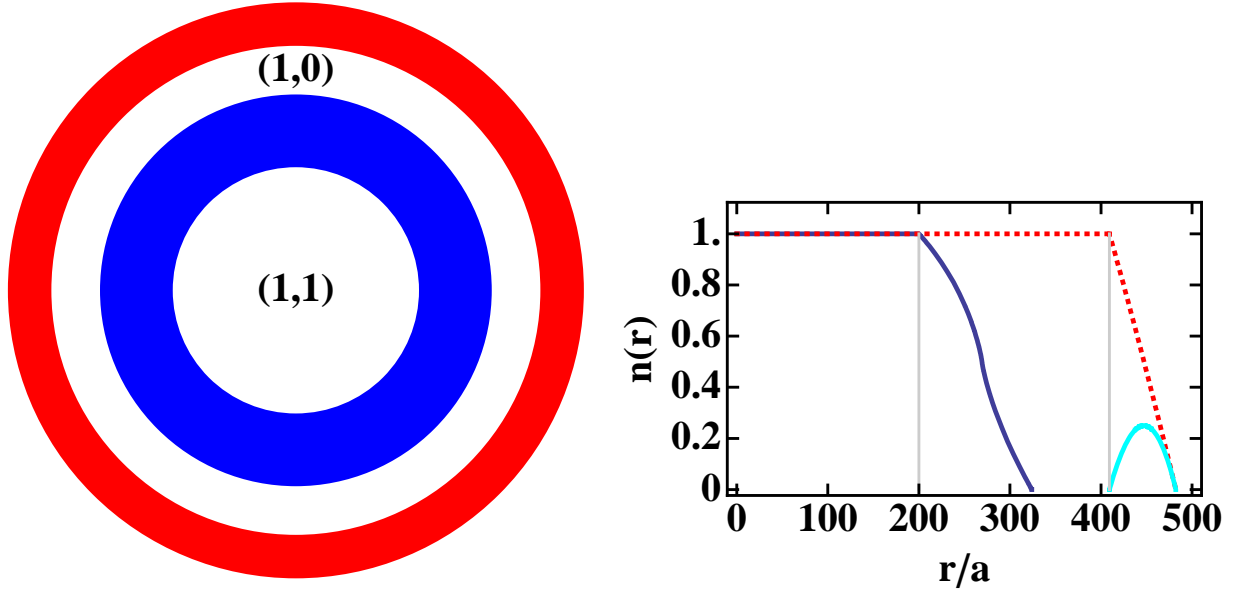


Figure 5.1: (a) Shell structure of Bose-Fermi mixtures in harmonically confined optical lattices showing a coexisting Bose-Mott and Fermi-band insulator region at the center ($n_B = 1, n_F = 1$), a coexisting Bose-Mott insulator and Fermi liquid region (in blue), a Bose-Mott insulator region ($n_B = 1, n_F = 0$), and Bose-Superfluid region at the edge (in red). (b) filling factors for fermions shown as the solid dark blue curve and for bosons shown as the dashed red curve. The solid parabolic curve in light blue shows the order parameter in the superfluid region. The parameters used are $t_F = t_B = 0.0325U_{BB}$, $U_{BF} = 0.1U_{BB}$, $\mu_B = 0.8U_{BB}$, $\mu_F = 0.4U_{BB}$ and $\Omega_F = \Omega_B = 8 \times 10^{-6}U_{BB}$, which are representative of Bose-Fermi mixtures with nearly the same mass such as ${}^6\text{Li}$ and ${}^7\text{Li}$, ${}^{39}\text{K}$ and ${}^{40}\text{K}$, or ${}^{172}\text{Yb}$ and ${}^{173}\text{Yb}$. For the parameters chosen, the widths of the superfluid and FL shells are several times larger than the lattice spacing a .

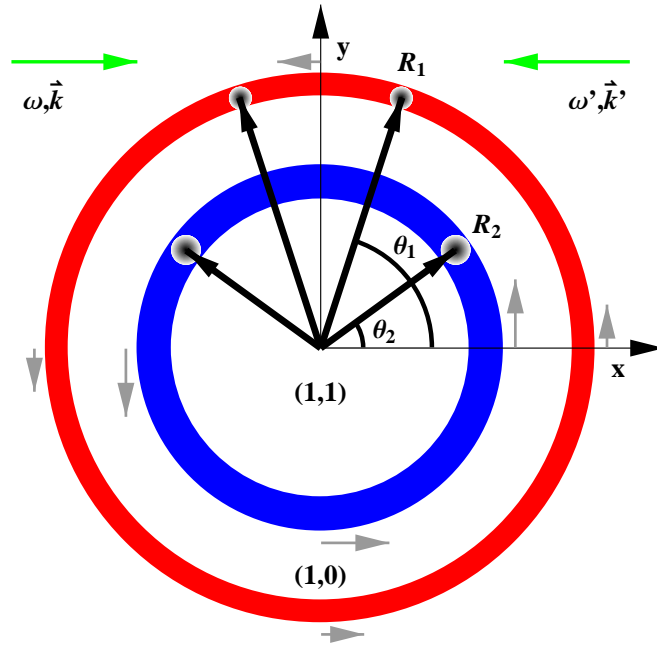


Figure 5.2: Schematic plot for the detection of outer red superfluid and inner blue Fermi liquid shells using Bragg spectroscopy. The angles θ_1 and θ_2 indicate the locations of strongest momentum transfer from the Bragg beams (large green arrows) to the rotating superfluid and Fermi liquid shells of radii R_1 and R_2 . The gray arrows indicate the sense of rotation of the conducting shells.

Chapter 6

Hexatic, Wigner crystal, and superfluid phases of dipolar bosons

6.1 Introduction

One of the next frontiers in ultracold atomic and molecular physics is the study of ultracold heteronuclear molecules such as KRb [94, 95], RbCs [96], and NaCs [97], which can be produced using Feshbach resonances observed in mixtures of two types of alkali atoms [98, 99, 100]. Thus, ultracold heteronuclear molecules consisting of Bose-Bose, Bose-Fermi, or Fermi-Fermi atom pairs offer many new opportunities because of their internal degrees of freedom [101, 102, 103, 104, 105] such as their permanent electric dipole moments.

The dipolar interaction between heteronuclear molecules is highly anisotropic in three dimensions having attractive and repulsive contributions. This makes it generally quite difficult to identify stable phases with good accuracy. In the particular case of bosonic heteronuclear molecules (Bose-Bose or Fermi-Fermi) the attractive part of the dipolar interaction may lead to undesired instabilities of the dipolar gas. However, the situation in two dimensions (2D) can be quite different, and arguably more interesting, as the dipolar interaction can be made to be purely repulsive by the application of suitable static electric or microwave fields. In the case of bosonic dipolar molecules, several stable and metastable many body phases of 2D systems may be found.

In this chapter, I will obtain the finite and zero-temperature phase diagram of bosons interacting via short-range repulsive interactions U and long-ranged dipolar interactions E_D in two dimensions. For weakly repulsive values of U , and small values of E_D , I find a dipolar superfluid phase (DSF) of the Berezinskii-Kosterlitz-Thouless (BKT) type, which upon increasing values of E_D becomes a dipolar Wigner crystal (DWC) forming a triangular lattice. Numerical evidence for the existence of the DWC phase was obtained recently in Quantum Monte Carlo simulations of dipolar boson systems at zero temperature [106, 107, 108]. Here, however, I develop an analytical variational theory that accounts not only for the superfluid to DWC phase transition at zero temperature, but also for the finite temperature melting of the DWC into a dipolar hexatic fluid (DHF) [109, 112], where crystalline translational order is destroyed but hexagonal orientational order is preserved. Further temperature increase leads to the melting of the hexatic phase into a dipolar normal fluid (DNF). I also find that the dipolar supersolid phase (DSS), exhibiting both superfluid and crystalline order, always has higher energy than the DWC, but is at least metastable, thus being accessible using thermal quenching. Lastly, I show that measurements of optical Bragg scattering can identify the DWC and DHF phases. This chapter is a longer version of the work presented in Ref. [110].

6.2 Hamiltonian

To describe the phases of interacting dipolar bosons in 2D, we start with the continuum Hamiltonian

$$H = -\frac{\hbar^2}{2m} \sum_i \nabla_i^2 + \frac{1}{2} \sum_{\langle i,j \rangle} \frac{D}{|\mathbf{x}_i - \mathbf{x}_j|^3} + V_{loc} \quad (6.1)$$

where $V_{loc} = \frac{1}{2} \sum_{\langle i,j \rangle} U \delta(\mathbf{x}_i - \mathbf{x}_j)$, and the sum over $\langle i,j \rangle$ indicates the sum over all pairs of molecules. The first term of H corresponds to the kinetic energy, the second to dipolar interactions, and the third (V_{loc}) to the local (short-range) interaction.

6.2.1 Dipolar Wigner crystal phase

We begin our discussion of different ground states by analyzing first the dipolar Wigner crystal (DWC) phase. In this phase the dipolar interactions are dominant in comparison to the kinetic energy and local energy terms, such that the system crystallizes into a triangular lattice in two dimensions (2D). Thus, our variational wavefunction can be chosen to be

$$\Psi_{\text{wc}}(\mathbf{x}_1, \mathbf{x}_2, \dots) = \frac{1}{\sqrt{A}} \sum_{p(\mathbf{a})} \prod_i G_{\mathbf{x}_i}^{\mathbf{a}_i} \quad (6.2)$$

where $\{\mathbf{a}_i\}$ forms a triangular lattice in 2D, and A is the normalization constant. The $\sum_{p(\mathbf{a}_i)}$ is a sum over all possible permutations P of $\{\mathbf{a}\}$ and the function $G_{\mathbf{x}_i}^{\mathbf{a}_i} = e^{-(\mathbf{x}_i - \mathbf{a}_i)^2 / 2\sigma^2} / \sqrt{\pi}\sigma$ is a normalized Gaussian centered at the lattice site \mathbf{a}_i and variance σ^2 . We define the separation between neighboring lattice sites to be a , and express the boson density as $\rho = 2/(\sqrt{3}a^2)$. In addition, we introduce the dimensionless parameters $r_D = 2mD\rho^{1/2}/\hbar^2$ ($r_U = 2mU/\hbar^2$) as the ratio of the char-

characteristic dipolar energy $E_D = D\rho^{3/2}$ (local energy $E_U = U\rho$) and kinetic energy $K = \hbar^2\rho/2m$.

The variational wavefunction described in Eq. (6.2) is expected to be good for $r_D \gg 1$, where the dipole-dipole interaction is much larger than the kinetic energy, and can be used to compute analytically the average kinetic, local and dipolar energies in terms of the variational parameter $\alpha = \sigma/a$, where σ is the Gaussian width and a is the lattice spacing.

Let us first calculate the norm of this wave function.

$$\langle\psi|\psi\rangle = N! \sum_{p(\tilde{\mathbf{a}})} \prod_i [G_{\mathbf{x}_i}^{\mathbf{a}_i} G_{\mathbf{x}_i}^{\tilde{\mathbf{a}}_i}], \quad (6.3)$$

where,

$$[G_{\mathbf{x}_i}^{\mathbf{a}_i} G_{\mathbf{x}_i}^{\tilde{\mathbf{a}}_i}] = \int d^2x_i \left(\frac{1}{\pi\sigma^2} e^{-(\mathbf{x}_i - \mathbf{a}_i)^2/2\sigma^2} e^{-(\mathbf{x}_i - \tilde{\mathbf{a}}_i)^2/2\sigma^2} \right). \quad (6.4)$$

Here $\{\tilde{\mathbf{a}}_i\}$ denotes a set of all lattice sites, and N is the number of atoms. Thus,

$$\langle\psi|\psi\rangle = N! \sum_{p(\tilde{\mathbf{a}})} \prod_i G^{(\mathbf{a}_i - \tilde{\mathbf{a}}_i)/\sqrt{2}}, \quad (6.5)$$

with $G^{\mathbf{a}} = e^{-\mathbf{a}^2/2\sigma^2}$. We can now compute the kinetic energy,

$$\langle\psi|T|\psi\rangle = -N! \frac{\hbar^2}{2m} \sum_{p(\tilde{\mathbf{a}})} \sum_i \prod_{k \neq i} [G_{\mathbf{x}_i}^{\mathbf{a}_i} \nabla_i^2 G_{\mathbf{x}_i}^{\tilde{\mathbf{a}}_i}] [G_{\mathbf{x}_k}^{\mathbf{a}_k} G_{\mathbf{x}_k}^{\tilde{\mathbf{a}}_k}] \quad (6.6)$$

$$= \frac{N\hbar^2}{2m\sigma^2} \langle\psi|\psi\rangle. \quad (6.7)$$

The local potential energy is given by,

$$\langle\psi|V_{local}|\psi\rangle = N! \frac{U}{2} \sum_{p(\tilde{\mathbf{a}})} \sum_{\langle i,j \rangle} \prod_{k \neq i,j} [G_{\mathbf{x}_k}^{\mathbf{a}_k} G_{\mathbf{x}_k}^{\tilde{\mathbf{a}}_k}] \left[G_{\mathbf{x}_i}^{\mathbf{a}_i} G_{\mathbf{x}_j}^{\mathbf{a}_j} G_{\mathbf{x}_i}^{\tilde{\mathbf{a}}_i} G_{\mathbf{x}_j}^{\tilde{\mathbf{a}}_j} \delta^2|\mathbf{x}_i - \mathbf{x}_j| \right] \quad (6.8)$$

Similarly the dipole interaction energy is,

$$\langle\psi|V_{dipole}|\psi\rangle = N! \frac{D}{2} \sum_{p(\tilde{\mathbf{a}})} \sum_{\langle i,j \rangle} \prod_{k \neq i,j} [G_{\mathbf{x}_k}^{\mathbf{a}_k} G_{\mathbf{x}_k}^{\tilde{\mathbf{a}}_k}] \left[\frac{G_{\mathbf{x}_i}^{\mathbf{a}_i} G_{\mathbf{x}_j}^{\mathbf{a}_j} G_{\mathbf{x}_i}^{\tilde{\mathbf{a}}_i} G_{\mathbf{x}_j}^{\tilde{\mathbf{a}}_j}}{|\mathbf{x}_i - \mathbf{x}_j|^3} \right] \quad (6.9)$$

Now to evaluate the integrals in Eq. (6.8) and in Eq. (6.9) we will consider only the following permutations which will have leading order contribution to the potential energy.

$$\begin{aligned}
P0 : & \quad P_{1234\dots\dots N} \rightarrow P_{1234\dots\dots N} \text{ etc. (no permutation)} \\
P1 : & \quad P_{1234\dots\dots N} \rightarrow P_{2134\dots\dots N} \text{ etc. (one exchange)} \\
P2 : & \quad P_{1234\dots\dots N} \rightarrow P_{2143\dots\dots N} \text{ etc. (two exchanges)}.
\end{aligned} \tag{6.10}$$

We will now derive explicit expressions for Eqs. (6.5), (6.8) and (6.9) using the permutations above. From the equation for the norm given in Eq. (6.5), and using permutations P0, P1, P2 described in Eq. (6.10) we get,

$$\langle \psi | \psi \rangle = N! \left(1 + \sum_{\langle i,j \rangle} G^{(\mathbf{a}_i - \mathbf{a}_j)\sqrt{2}} + \sum_{\langle i,j \rangle, \langle m,n \rangle} G^{(\mathbf{a}_i - \mathbf{a}_j)/\sqrt{2}} G^{(\mathbf{a}_m - \mathbf{a}_n)\sqrt{2}} + \dots \right) \tag{6.11}$$

The local potential energy term is derived as follows. Let us first go back to Eq. (6.8). We will only consider terms with no exchanges or one exchange in the potential energy integral in the right hand side of Eq. (6.8) and all possible

exchanges in the other integrals. Thus,

$$\begin{aligned}
\langle \psi | V_{local} | \psi \rangle &= N! \frac{U}{2} \sum_{p(\tilde{\mathbf{a}})} \sum_{\langle i,j \rangle} \prod_{k \neq i,j} [G_{\mathbf{x}_k}^{\mathbf{a}_k} G_{\mathbf{x}_k}^{\tilde{\mathbf{a}}_k}] \left[G_{\mathbf{x}_i}^{\mathbf{a}_i} G_{\mathbf{x}_j}^{\mathbf{a}_j} G_{\mathbf{x}_i}^{\tilde{\mathbf{a}}_i} G_{\mathbf{x}_j}^{\tilde{\mathbf{a}}_j} \delta^2 |\mathbf{x}_i - \mathbf{x}_j| \right] \\
&\approx N! \frac{U}{2} \sum_{p'(\tilde{\mathbf{a}})} \sum_{\langle i,j \rangle} \prod_{k \neq i,j} [G_{\mathbf{x}_k}^{\mathbf{a}_k} G_{\mathbf{x}_k}^{\tilde{\mathbf{a}}_k}] \times \\
&\quad \left(\left[G_{\mathbf{x}_i}^{\mathbf{a}_i} G_{\mathbf{x}_j}^{\mathbf{a}_j} G_{\mathbf{x}_i}^{\tilde{\mathbf{a}}_i} G_{\mathbf{x}_j}^{\tilde{\mathbf{a}}_j} \delta^2 |\mathbf{x}_i - \mathbf{x}_j| \right] + \left[G_{\mathbf{x}_i}^{\tilde{\mathbf{a}}_i} G_{\mathbf{x}_j}^{\tilde{\mathbf{a}}_j} G_{\mathbf{x}_i}^{\mathbf{a}_i} G_{\mathbf{x}_j}^{\mathbf{a}_j} \delta^2 |\mathbf{x}_i - \mathbf{x}_j| \right] \right) \\
&= N! \frac{U}{2} \sum_{p'(\tilde{\mathbf{a}})} \sum_{\langle i,j \rangle} \prod_{k \neq i,j} [G_{\mathbf{x}_k}^{\mathbf{a}_k} G_{\mathbf{x}_k}^{\tilde{\mathbf{a}}_k}] \left(\frac{1}{2\pi\sigma^2} G^{(\mathbf{a}_i - \mathbf{a}_j)} + \frac{1}{2\pi\sigma^2} G^{(\mathbf{a}_i - \mathbf{a}_j)} \right) \\
&= N! \frac{U}{2} \frac{1}{\pi\sigma^2} \sum_{\langle i,j \rangle} G^{(\mathbf{a}_i - \mathbf{a}_j)} \left(1 + \sum_{(m,n)} G^{(\mathbf{a}_m - \mathbf{a}_n)/\sqrt{2}} + \dots \right) \\
&= N! \frac{U}{2} \frac{1}{\pi\sigma^2} \sum_{\langle i,j \rangle} G^{(\mathbf{a}_i - \mathbf{a}_j)} \langle \psi | \psi \rangle \tag{6.12}
\end{aligned}$$

Similarly the dipole interaction energy is given by,

$$\begin{aligned}
\langle \psi | V_{dipole} | \psi \rangle &= N! \frac{D}{2} \sum_{p(\tilde{\mathbf{a}})} \sum_{\langle i,j \rangle} \prod_{k \neq i,j} [G_{\mathbf{x}_k}^{\mathbf{a}_k} G_{\mathbf{x}_k}^{\tilde{\mathbf{a}}_k}] \left[G_{\mathbf{x}_i}^{\mathbf{a}_i} G_{\mathbf{x}_j}^{\mathbf{a}_j} G_{\mathbf{x}_i}^{\tilde{\mathbf{a}}_i} G_{\mathbf{x}_j}^{\tilde{\mathbf{a}}_j} \frac{1}{(|\mathbf{x}_i - \mathbf{x}_j|)^3} \right] \\
&\approx N! \frac{D}{2} \sum_{p'(\tilde{\mathbf{a}})} \sum_{\langle i,j \rangle} \prod_{k \neq i,j} [G_{\mathbf{x}_k}^{\mathbf{a}_k} G_{\mathbf{x}_k}^{\tilde{\mathbf{a}}_k}] \times \\
&\quad \left(\left[G_{\mathbf{x}_i}^{\mathbf{a}_i} G_{\mathbf{x}_j}^{\mathbf{a}_j} G_{\mathbf{x}_i}^{\tilde{\mathbf{a}}_i} G_{\mathbf{x}_j}^{\tilde{\mathbf{a}}_j} \frac{1}{(|\mathbf{x}_i - \mathbf{x}_j|)^3} \right] + \left[G_{\mathbf{x}_i}^{\tilde{\mathbf{a}}_i} G_{\mathbf{x}_j}^{\tilde{\mathbf{a}}_j} G_{\mathbf{x}_i}^{\mathbf{a}_i} G_{\mathbf{x}_j}^{\mathbf{a}_j} \frac{1}{(|\mathbf{x}_i - \mathbf{x}_j|)^3} \right] \right) \\
&= N! \frac{D}{2} \sum_{p'(\tilde{\mathbf{a}})} \sum_{\langle i,j \rangle} \prod_{k \neq i,j} [G_{\mathbf{x}_k}^{\mathbf{a}_k} G_{\mathbf{x}_k}^{\tilde{\mathbf{a}}_k}] \times \\
&\quad \left(\frac{1}{2\pi\sigma^2} \int \frac{e^{-r^2/2\sigma^2}}{(r + \mathbf{a}_i - \mathbf{a}_j)^3} d^2r + G^{\mathbf{a}_i - \mathbf{a}_j} \left(\frac{1}{2\pi\sigma^2} \int \frac{e^{-r^2/2\sigma^2}}{r^3} d^2r \right) \right). \tag{6.13}
\end{aligned}$$

One can easily see that the integrals in the last line of Eq. (6.13) are divergent.

However assuming that the Gaussian wavefunctions are further suppressed around the region of overlap by additional corrections, we will only consider the integrals

around $r = a, 2a$ etc, up to 4 nearest neighbors. This gives,

$$\frac{1}{2\pi\sigma^2} \int \frac{e^{-r^2/2\sigma^2}}{(r + \mathbf{a}_i - \mathbf{a}_j)^3} d^2r = \frac{1}{a^3} \left(1 + \frac{1}{\sqrt{3}^3} + \frac{1}{2^3} + \frac{2}{\sqrt{7}^3} + \frac{1}{3^3} \right) \times \left(1 + \frac{9\alpha^2}{2} + \frac{225\alpha^4}{8} + \frac{3675\alpha^6}{16} \right) \quad (6.14)$$

with $\sigma = \alpha a$ and

$$\frac{1}{2\pi\sigma^2} \int \frac{e^{-r^2/2\sigma^2}}{r^3} d^2r = \left(1 + \frac{1}{\sqrt{3}^3} + \frac{1}{2^3} + \frac{2}{\sqrt{7}^3} + \frac{1}{3^3} \right) \frac{1}{a^3}. \quad (6.15)$$

Thus the dipole energy can be approximated as

$$\langle \psi | V_{dipole} | \psi \rangle = \frac{D}{2} \frac{A}{a^3} \langle \psi | \psi \rangle \left(\sum_{\langle i,j \rangle} G^{(\mathbf{a}_i - \mathbf{a}_j)} + F(\alpha) \right) \quad (6.16)$$

where $A = 1 + \frac{1}{\sqrt{3}^3} + \frac{1}{2^3} + \frac{2}{\sqrt{7}^3} + \frac{1}{3^3} + \dots = 1.8393$ and $F(\alpha) = 6\left(1 + \frac{9\alpha^2}{2} + \frac{225\alpha^4}{8} + \frac{3675\alpha^6}{16}\right)$.

We will now evaluate the Gaussian summations taking into account up to three nearest neighbor terms. Using this approximation, we get, for an infinite and homogeneous triangular lattice,

$$\sum_{\langle i,j \rangle} G^{(\mathbf{a}_i - \mathbf{a}_j)/\sqrt{2}} \approx 6N \left(e^{-a^2/4\sigma^2} + e^{-3a^2/4\sigma^2} + e^{-4a^2/4\sigma^2} \right) \quad (6.17)$$

$$\sum_{\langle i,j \rangle} G^{(\mathbf{a}_i - \mathbf{a}_j)} \approx 6N \left(e^{-a^2/2\sigma^2} + e^{-3a^2/2\sigma^2} + e^{-4a^2/2\sigma^2} \right) \quad (6.18)$$

The dipolar Wigner crystal is only expected for $0 < \alpha < 1$. We will hereafter consider the thermodynamic limit where $N \rightarrow \infty$, $V \rightarrow \infty$, and $N/V = \rho$. The square of the lattice spacing $a^2 = 2/\sqrt{3}\rho$ and $\sigma = \alpha a$. In this thermodynamic limit, the average kinetic energy is

$$\langle \Psi | K | \Psi \rangle_{\text{DWC}} = N\sqrt{3} \frac{\hbar^2 \rho}{4m\alpha^2}, \quad (6.19)$$

where N is the total number of particles. The average local energy is

$$\langle \Psi | V_{loc} | \Psi \rangle_{\text{DWC}} = N3\sqrt{3}U\rho P(\alpha)/(2\pi\alpha^2) \quad (6.20)$$

where $P(\alpha) = \left(e^{-1/2\alpha^2} + e^{-3/2\alpha^2} + e^{-2/\alpha^2} \right)$ and the average dipolar energy is

$$\langle \Psi | V_{dip} | \Psi \rangle_{\text{DWC}} = N3A \left(\sqrt{3}/2 \right)^{3/2} D\rho^{3/2} [P(\alpha) + F(\alpha)] \quad (6.21)$$

where $F(\alpha) = (1 + 9\alpha^2/2 + 225\alpha^4/8 + 3675\alpha^6/16)$, and $A = 1.8393$ is a numerical constant. In general, $P(\alpha)$ and $F(\alpha)$ are represented by an infinite series in the variational parameter α , but the series is rapidly convergent for $0 < \alpha < 1$, such that the first few terms are sufficient for the discussion of the total average energy $E_{\text{DWC}} = \langle \Psi | H | \Psi \rangle_{\text{DWC}}$. The minimization of E_{DWC} with respect to α leads to the minima illustrated in Fig. 6.1, for $r_U = 0$ and a few values of r_D . For small values of r_U the transition is shifted towards lower values of r_D (not shown in Fig. 6.1).

6.2.2 Superfluid phase

The superfluid phase is more easily described by writing our original Hamiltonian in Eq. (6.1) in second quantized notation, $\mathcal{H} = \mathcal{K} + \mathcal{V}$, with the kinetic energy

$$\mathcal{K} = -\frac{\hbar^2}{2m} \int d\mathbf{x} \Phi^\dagger(\mathbf{x}) \nabla^2 \Phi(\mathbf{x}) \quad (6.22)$$

and potential energy

$$\mathcal{V} = \frac{1}{2} \int d\mathbf{x} d\mathbf{x}' \Phi^\dagger(\mathbf{x}) \Phi^\dagger(\mathbf{x}') V(\mathbf{x}, \mathbf{x}') \Phi(\mathbf{x}) \Phi(\mathbf{x}'), \quad (6.23)$$

where

$$V(\mathbf{x}, \mathbf{x}') = \frac{D}{|\mathbf{x} - \mathbf{x}'|^3} + U\delta(\mathbf{x} - \mathbf{x}') \quad (6.24)$$

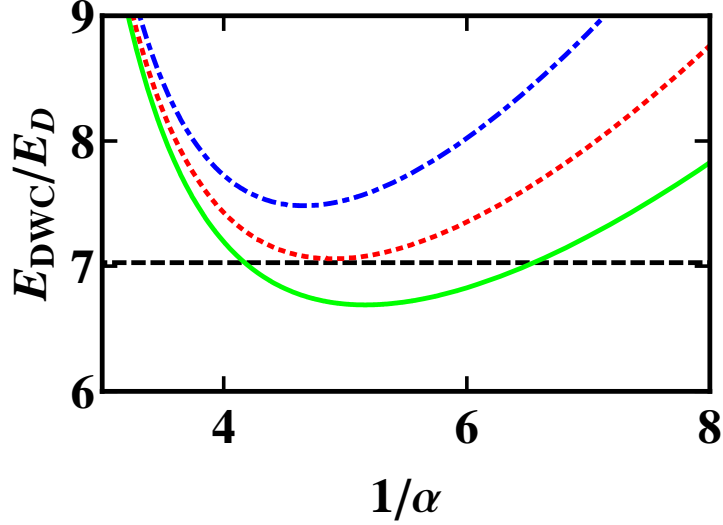


Figure 6.1: Plots of the dipolar Wigner crystal energy E_{DWC} in units of the dipolar energy E_D versus the inverse of the variational parameter α for $r_D = 10$ (blue dot-dashed line), $r_D = 13.1$ (red dotted line), $r_D = 17$ (green solid line). The horizontal (black dot-dashed line) is the energy E_{DSF} for a uniform superfluid.

and $\Phi^\dagger(\mathbf{x})$ is the bosonic field operator which creates a dipolar molecule at position \mathbf{x} . Describing the superfluid phase by the average $\langle \Phi^\dagger(\mathbf{x}) \rangle = \langle \Phi(\mathbf{x}) \rangle = \sqrt{\rho}$ leads to the ground state energy

$$E_{\text{DSF}} = N \left[\frac{3\pi\rho D}{2r_0} + \frac{U\rho}{2} \right], \quad (6.25)$$

by assuming that the dipolar potential $V_{\text{dip}}(r) = D/r^3$ is unscreened for length scales $r \geq r_0$, and screened to $V_{\text{dip}}(r) = D/r_0^3$ for length scales $r < r_0$, where $r_0 \approx 0.62a$. This choice of r_0 gives the zero temperature quantum phase transition from DWC phase to DSF phase at $r_D = 13.1$ which is obtained from the finite temperature calculations.

In Fig. 6.1, the energy of the DSF phase is shown and compared with that of

the DWC phase. In absence of any long range dipolar interaction, the BKT transition temperature from superfluid to normal phase is given by $T_{BKT}^0 = \pi\hbar^2/2ma^2$. In presence of long range dipolar interaction, the BKT transition temperature is modified to [114] $T = T_{BKT}^0 (\sqrt{\alpha^2 + 1} - \alpha)$ where $T_{BKT}^0 = \pi\hbar^2/2ma^2$ is the BKT temperature for a weakly interacting Bose gas, $\alpha = 2mD/(4\pi^{3/2}\hbar^2a_0)$, and a_0 is the size of the dipolar molecules. In the high density limit we assume $\rho^{1/2}a_0 \approx 1$.

Next, we discuss the melting of the Wigner crystal phase, which occurs in two stages. First the dipolar Wigner crystal melts into a hexatic fluid, which does not have translational order, but preserves rotational order. The melting occurs via the Kosterlitz-Thouless-Nelson-Halperin-Young (KTNHY) dislocation proliferation mechanism [112, 113]. Second, the dipolar hexatic fluid transforms itself into the dipolar normal fluid by losing its rotational order at a higher temperature.

6.3 Melting from Wigner crystal to hexatic phase

To study the melting of the DWC phase, we need to calculate its elastic energy. This calculation can be performed by using a semiclassical approximation to the quantum-mechanical method for the calculation of elastic energies [115]. The essential idea is to stretch the many-body wavefunction $\Psi(\mathbf{x}_1, \mathbf{x}_2, \dots)$ on each particle coordinate as $x_{i,\alpha} \rightarrow x_{i,\alpha} + \epsilon_{\alpha\beta}x_{i\beta}$ (where repeated indices indicate summation and $\alpha = \{x, y\}$ and $\beta = \{x, y\}$), and expand up to second order in the strain tensor $\epsilon_{\alpha\beta}$. Under this transformation the wave function becomes

$$\psi_\epsilon(\mathbf{x}) = \det(\mathbf{I} + \epsilon)^{-1/2} \psi((\mathbf{I} + \epsilon)^{-1}\mathbf{x}) \quad (6.26)$$

where ϵ is the matrix with elements $\epsilon_{\alpha\beta}$, and the prefactor preserves the normalization of ψ_ϵ . The expectation value of H with respect to ψ_ϵ involves an integral over all coordinates \mathbf{x} , which by the variable substitution $\mathbf{x} \rightarrow (\mathbf{I} + \epsilon)\mathbf{x}$ becomes,

$$\begin{aligned} \langle \psi_\epsilon | H | \psi_\epsilon \rangle &= \int \psi^*(\mathbf{x}) \sum_i \frac{1}{2m_i} \left[p_i^2 - 2 \sum_{\alpha,\beta} \epsilon_{\alpha\beta} p_{i\alpha} p_{i\beta} + \sum_{\alpha,\beta,\gamma} \epsilon_{\alpha\beta} \epsilon_{\alpha\gamma} p_{i\beta} p_{i\gamma} \right] \psi(\mathbf{x}) d\mathbf{x} + \\ &\int \psi^*(\mathbf{x}) V((1 + \epsilon)\mathbf{x}) \psi(\mathbf{x}) d\mathbf{x} \end{aligned} \quad (6.27)$$

where ψ_ϵ has been replaced by ψ using Eq. (6.26). The variational principle requires that $\langle \psi_\epsilon | H | \psi_\epsilon \rangle$ differs from $\langle \psi | H | \psi \rangle$ only in second order of $\epsilon_{\alpha\beta}$, which implies

$$\left[\frac{\partial \langle \psi_\epsilon | H | \psi_\epsilon \rangle}{\partial \epsilon_{\alpha\beta}} \right]_{\epsilon_{\alpha\beta}=0} = \sum_i \left\langle \psi \left| \frac{p_{i\alpha} p_{i\beta}}{m_i} - x_{i\beta} \nabla_{i\alpha} V \right| \psi \right\rangle = 0. \quad (6.28)$$

Thus the total elastic energy will be given by

$$E_{el} = \frac{1}{2} \frac{\partial^2 \langle \psi_\epsilon | H | \psi_\epsilon \rangle}{\partial \epsilon_{\delta\gamma} \partial \epsilon_{\alpha\beta}} \epsilon_{\delta\gamma} \epsilon_{\alpha\beta} = \frac{1}{2} \sum_i \left(\langle \psi | x_{i\gamma} x_{i\beta} \nabla_{i\delta} V \nabla_{i\alpha} V | \psi \rangle + \delta_{\alpha\delta} p_{i\beta} p_{i\gamma} \right) \epsilon_{\delta\gamma} \epsilon_{\alpha\beta} \quad (6.29)$$

Since we are working with central potentials a convenient way of writing the total elastic energy is,

$$\begin{aligned} E_{el} &= \frac{1}{2} \sum_{\langle i \rangle} \langle \delta_{\alpha\delta} p_{i\beta} p_{i\gamma} \rangle \epsilon_{\delta\gamma} \epsilon_{\alpha\beta} \\ &+ \frac{1}{2} \sum_{\langle i,j \rangle} \left\langle \frac{(\mathbf{x}_i - \mathbf{x}_j)_\alpha (\mathbf{x}_i - \mathbf{x}_j)_\beta (\mathbf{x}_i - \mathbf{x}_j)_\gamma (\mathbf{x}_i - \mathbf{x}_j)_\delta}{|\mathbf{x}_i - \mathbf{x}_j|^2} V''_{ij} \right\rangle \epsilon_{\delta\gamma} \epsilon_{\alpha\beta} \\ &- \frac{1}{2} \sum_{\langle i,j \rangle} \left\langle \frac{(\mathbf{x}_i - \mathbf{x}_j)_\alpha (\mathbf{x}_i - \mathbf{x}_j)_\beta (\mathbf{x}_i - \mathbf{x}_j)_\gamma (\mathbf{x}_i - \mathbf{x}_j)_\delta}{|\mathbf{x}_i - \mathbf{x}_j|^2} V'_{ij} \right\rangle \epsilon_{\delta\gamma} \epsilon_{\alpha\beta} \end{aligned} \quad (6.30)$$

where $V'(\mathbf{x}, \mathbf{x}') = \nabla_x V$, and $i = \{x, y\}$ and $j = \{x, y\}$ and $\langle \dots \rangle = \langle \psi | \dots | \psi \rangle$. Here we have omitted the explicit reference to ψ . This form is symmetric i.e., torque free, and is manifestly dependent only upon the relative position of particles.

The resulting elastic energy is

$$E_{\text{el}} = \frac{1}{2} \int d\mathbf{x} [2\mu\epsilon_{\alpha\beta}^2 + \lambda\epsilon_{\alpha\alpha}^2], \quad (6.31)$$

where $\mu = 15\sqrt{3}D/4a^5$ and $\lambda = 3\mu$ are the unrenormalized Lamé coefficients, and the symmetric (rotation-free) strain tensor is $\epsilon_{\alpha\beta}(\mathbf{x}) = \frac{1}{2} \left[\frac{\partial u_\alpha(\mathbf{x})}{\partial \mathbf{x}_\beta} + \frac{\partial u_\beta(\mathbf{x})}{\partial \mathbf{x}_\alpha} \right]$, with $u_\alpha(\mathbf{x})$ being the displacement from equilibrium position.

We follow Ref. [112], and decompose the strain tensor $\epsilon_{\alpha\beta}(\mathbf{x})$ into a regular (smoothly varying) $\phi_{\alpha\beta}(\mathbf{x})$ and a singular (dislocation) $d_{\alpha\beta}(\mathbf{x})$ contribution. Using $k_B = 1$, the Hamiltonian for the smooth part can be written as

$$\frac{H_{\text{reg}}}{T} = \frac{1}{2} \int \frac{d\mathbf{x}}{a^2} [2\bar{\mu}\phi_{\alpha\beta}^2 + \bar{\lambda}\phi_{\alpha\alpha}^2], \quad (6.32)$$

where $\bar{\mu} = \mu a^2/T$ and $\bar{\lambda} = \lambda a^2/T$. Additionally the Hamiltonian for the singular part can be written as

$$\frac{H_{\text{dis}}}{T} = -\frac{K}{8\pi} \sum_{\mathbf{x} \neq \mathbf{x}'} b_\alpha(\mathbf{x}) \Gamma_{\alpha\beta} b_\beta(\mathbf{x}') + \frac{E_c}{T} \sum_{\mathbf{x}} |\mathbf{b}(\mathbf{x})|^2, \quad (6.33)$$

where b_α is the alpha-component of the Burger's vector \mathbf{b} defined by the contour integral of the displacement field \mathbf{u} around the dislocation: $\int d\mathbf{u} = a\mathbf{b}(\mathbf{x})$. Also, the coefficient $K = K_0 a^2/T$, is related to the unrenormalized Lamé constants through $K_0 = 4\mu(\mu + \lambda)/(2\mu + \lambda)$, and $E_c = (\eta + 1)KT/8\pi$ is the core energy associated with a dislocation of core diameter ηa , while the interaction coefficient is

$$\Gamma_{\alpha\beta} = \delta_{\alpha\beta} \ln \left[\frac{|\mathbf{x} - \mathbf{x}'|}{a} \right] - \frac{[\mathbf{x} - \mathbf{x}']_\alpha [\mathbf{x} - \mathbf{x}']_\beta}{|\mathbf{x} - \mathbf{x}'|^2} \quad (6.34)$$

To obtain the critical temperature for the melting T_h of the dipolar Wigner

crystal we solve the renormalization flow equations for the elastic parameters

$$\begin{aligned}\frac{d\bar{\mu}^{-1}}{dl} &= 3\pi y^2(l)e^{K(l)/8\pi} \\ \frac{d[\bar{\mu}(l) + \bar{\lambda}(l)]^{-1}}{dl} &= 3\pi y^2(l)e^{K(l)/8\pi} (F_0(l) + F_1(l)),\end{aligned}$$

of the Hamiltonian H_{reg} , where $F_n(l) = I_n(K(l)/8\pi)$, with $I_n(x)$ being the modified Bessel function of order n . These equations need to be solved self-consistently with the flow equations for the parameters

$$\begin{aligned}\frac{dy(l)}{dl} &= \left(2 - \frac{K(l)}{8\pi}\right) y(l) + 2\pi y^2(l)e^{K(l)/16\pi} F_0(l) \\ \frac{dK^{-1}}{dl} &= \frac{3}{2}\pi y^2(l)e^{K(l)/8\pi} F_0(l) - \frac{3}{4}\pi y^2(l)e^{K(l)/8\pi} F_1(l),\end{aligned}$$

of the dislocation Hamiltonian H_{dis} . All flow equations are accurate to order y^3 , where $y = e^{-E_c/T}$ plays the role of the fugacity. The critical temperature T_h is reached when

$$K(T_h) = \frac{4\bar{\mu}(T_h) [\bar{\mu}(T_h) + \bar{\lambda}(T_h)]}{2\bar{\mu}(T_h) + \bar{\lambda}(T_h)} = 16\pi \quad (6.35)$$

6.4 Transition from hexatic to normal phase

As the dipolar Wigner crystal melts at T_h , translational order disappears but orientational order is preserved, with the emergence of the hexatic order parameter $\Psi_6(\mathbf{x}) = e^{6i\theta(\mathbf{x})}$. The bond-angle field $\theta(\mathbf{x})$ between the location of the center of masses of the dipolar bosons (heteronuclear molecules) is related to the displacement field $u(\mathbf{x})$ by $\theta(\mathbf{x}) = [\partial_x u_y(\mathbf{x}) - \partial_y u_x(\mathbf{x})]/2$. The elastic energy for such a situation can be also obtained using a semiclassical approximation to the method of Ref. [115], where each particle coordinate in the many-body wavefunction $\Psi(\mathbf{x}_1, \mathbf{x}_2, \dots)$ is locally

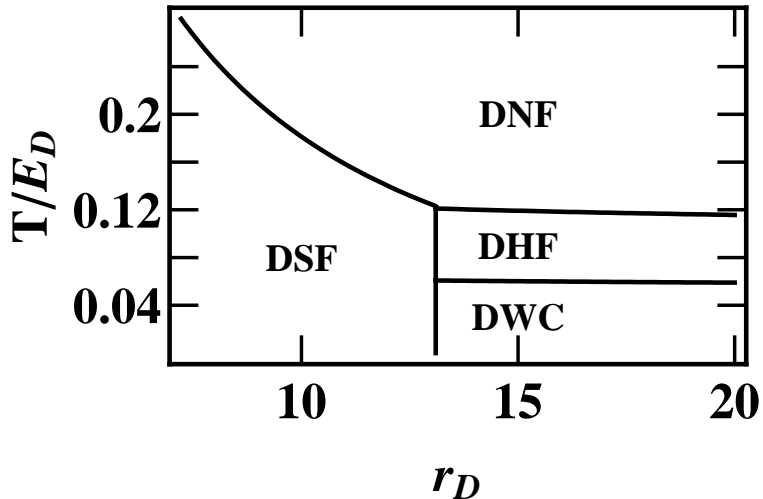


Figure 6.2: Finite temperature phase diagram of T/E_D versus r_D showing the dipolar superfluid (DSS), dipolar Wigner crystal (DWC), dipolar hexatic (DHF) and dipolar normal fluid (DNF) phases.

rotated $r_{i,\alpha} \rightarrow M_{\alpha\beta} r_{i,\beta}$, where $M_{\alpha\beta}$ is a local rotation matrix (tensor). For the triangular lattice considered here the elastic energy becomes

$$E_{\text{he}} = \frac{\Gamma_6}{2} \int \frac{d\mathbf{r}}{a^2} |\nabla\theta(\mathbf{x})|^2, \quad (6.36)$$

where $\Gamma_6 \approx 2E_c$ is the phase stiffness of the hexatic phase, which is directly related to the dislocation core energy $E_c = 1.1KT/8\pi$. The critical temperature for the disappearance of hexatic order and the emergence of the normal phase T_n is then determined by the RG flow of the 2D-XY model [116], which leads to the condition $\Gamma_6(T_n) = 72T_n/\pi$. The algebraic decay of orientational order is then destroyed at temperature T_n by the dissociation of pairs of $\pm\pi/3$ disclinations, which play the role of vortices and anti-vortices of the standard 2D-XY model.

6.5 The phase diagram

In Fig. 6.2 we show the melting temperature T_h separating the DWC and DHF phases and the melting temperature T_n separating the DHF and DNF phases as a function of r_D . When $r_D \rightarrow \infty$, we obtain $T_h \rightarrow 0.06E_D$, and $T_n \rightarrow 0.11E_D$. With decrease in r_D , T_h and T_n increases due to delocalization of the wave function of the dipoles which results in higher energy of the phases. We also show the BKT transition temperature between DSF and DNF phases. The point of intersection between the BKT curve and the T_n curve gives the value of $r_D = r_{QM} = 13.1$ at which the zero temperature phase transition between DSF and DWC occurs. This is because any other scenario would entail a phase transition between DSF and DHF (or DWC) on increase of temperature which is thermodynamically unfavorable. Existing Monte Carlo results give $r_{QM} \approx 30$ [106, 107, 108], $T_h \approx 0.077E_D$, and $T_n \approx 0.081E_D$ [111].

6.6 Supersolid phase

Starting from the Hamiltonian defined in the superfluid section we seek a variational solution

$$\langle \Phi(\mathbf{x}) \rangle_{\text{ss}} = \tilde{\Phi}_{\text{ss}}(\mathbf{x}) = \sqrt{\rho_{\text{sf}}} + \sqrt{\rho_{\text{ss}}} \sum_i G_{\mathbf{a}_i, \sigma_{\text{ss}}}(\mathbf{x}), \quad (6.37)$$

for the supersolid phase, where the Gaussian functions $G_{\mathbf{a}_i, \sigma_{\text{ss}}}(\mathbf{x})$ form a triangular lattice of side a_{ss} . The normalization condition is $\int d\mathbf{x} |\tilde{\Phi}_{\text{ss}}(\mathbf{x})|^2 / V = \rho$, while $\sigma_{\text{ss}} = \beta a_{\text{ss}}$ is the gaussian width and β is the corresponding variational parameter. The supersolid order parameter $\tilde{\Phi}_{\text{ss}}(\mathbf{x})$ describes a non-uniform superfluid

with both off-diagonal long-range order due to broken $U(1)$ symmetry and diagonal long-range order due to the discrete lattice symmetry. When $\rho_{\text{sf}} \gg \rho_{\text{ss}}$, the energy is essentially that of a superfluid, and when $\rho_{\text{sf}} \ll \rho_{\text{ss}}$, the average kinetic energy is $K_{\text{dss}} = N\sqrt{3}\hbar^2\rho/(4m\beta^2)$, while the total potential energy is $V_{\text{dss}} = V_1 + V_2$, where $V_1 = N3\sqrt{3}U\rho P(\beta)/(2\pi\beta^2) + N\sqrt{3}U\rho/8\pi\beta^2$ is the local potential energy and $V_2 = N3AD\rho^{3/2}(\sqrt{3}/2)^{3/2}[P(\beta) + F(\beta)] + N(\sqrt{3}/2)D\rho/(2r_0)$ is the dipolar energy.

We find that the total energy $E_{\text{dss}} = K_{\text{dss}} + V_{\text{dss}}$ of the dipolar supersolid (DSS) phase is always higher than the total energy E_{DWC} of the dipolar Wigner crystal for the same values of parameters. Thus, the transition from the superfluid to the supersolid phase does not occur within our variational ansatz, even if we include additional correlations via Jastrow factors [107]. Additionally, we find that the supersolid phase is at least metastable, since E_{ss} has a minimum that could be reached upon thermal quenching. Results in [108] indicate that the zero temperature ground state itself might be supersolid close to the DSF-DWC transition, although no conclusive evidence was found.

6.7 Experimental characterization of various phases

The various phases proposed here can be characterized by the measurement of their density-density correlations [108, 117], as reflected in the structure factor $S(\mathbf{q}) = \langle n(\mathbf{q})n(-\mathbf{q}) \rangle$, where $n(\mathbf{q})$ is the Fourier transform of the density operator $n(\mathbf{x})$, and the symbol $\langle \dots \rangle$ corresponds to both quantum mechanical and thermal

averaging.

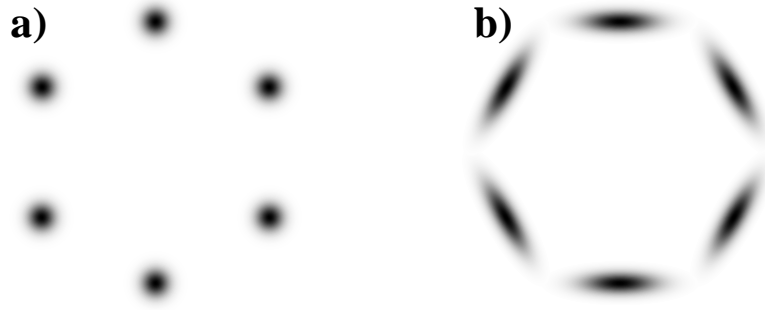


Figure 6.3: Bragg scattering patterns near the first reciprocal vectors for a) the dipolar Wigner crystal phase and for b) the dipolar hexatic fluid phase.

The most dramatic effects in the structure factor are found in dipolar Wigner crystal phase where $S(\mathbf{q}) \sim |\mathbf{q} - \mathbf{G}|^{-2+\nu(\mathbf{G},T)}$ revealing the power law behavior characteristic of two dimensions in the vicinity of the reciprocal lattice (Bragg) vectors \mathbf{G} . The first Bragg vector has magnitude $|\mathbf{G}_1| = 4\pi/\sqrt{3}a$, and the Bragg scattering pattern then exhibits 6-fold symmetry below the melting temperature T_m as shown in Fig. 6.3a. The exponent $\nu(\mathbf{G}, T) = (|\mathbf{G}_1|/4\pi)(T/\mu_*)(3\mu_* + \lambda_*)/(2\mu_* + \lambda_*)$ is related to the renormalized Lamé coefficients μ_* and λ_* . This reflects the power law decay of the correlation function $C(\mathbf{G}, \mathbf{R}) \sim |\mathbf{R}|^{-\nu(\mathbf{G},T)}$, which is the Fourier transform of $S(\mathbf{q})$. The profile of $S(\mathbf{q})$ for the dipolar hexatic phase corresponding to a melted dipolar Wigner crystal with orientational order is characterized by the hexagonal pattern shown in Fig. 6.3b.

6.8 Conclusions

I described some of the possible phases of dipolar bosons in two dimensions, including superfluid, supersolid, Wigner crystal, hexatic and normal fluids. Within my variational approach I concluded that the supersolid has always higher free energy than the Wigner crystal or hexatic fluid in the same region. However, the supersolid phase is at least metastable, and thus may be reached via thermal quenching, and probed via Bragg scattering. Furthermore, I showed that dipolar Wigner crystal does not melt directly into a normal fluid, but presents a two-stage melting first into a hexatic phase which preserves orientational order, and then into a normal fluid upon further increase in temperature. Finally, I indicated the experimental signatures of stable phases with translational or orientational order in a Bragg spectroscopy measurement that detect the static structure factor.

Chapter 7

Quantum fluctuations, entropy removal and non-equilibrium cooling of bosons in harmonically confined optical lattices

7.1 Introduction

Storing ultracold quantum gases in optical lattices has opened innovative manipulation and control possibilities, in many cases creating structures far beyond those currently achievable in typical condensed-matter physics systems. Amazingly, strong correlation effects can be observed in dilute atomic gases despite the densities of the particles in the trapping potentials being more than five orders of magnitude less than that of the air surrounding us! Ultracold quantum gases in optical lattices can in fact be considered as quantum simulators, as Feynman originally conceived for a quantum computer: a powerful simulator in which a highly controllable quantum system can be used to simulate the dynamical behavior of another complex quantum system. As a simulator, an optical lattice offers remarkably clean access to a particular Hamiltonian and thereby serves as a model system for testing fundamental theoretical concepts, at times providing textbook examples of quantum many-body effects.

Typically, experiments are performed in the regime where the quantum gas is in a tight binding band. A necessary condition for reaching the strongly correlated

regime is that the lattice gas must achieve quantum degeneracy in this narrow band. This can be very challenging, as the temperature for quantum degeneracy can be several orders of magnitude lower than that in the bulk [118].

As shown in [71] bosons in harmonically confined optical lattices exhibit alternating superfluid and Mott insulating regions and can be described very well using the Bose-Hubbard model. This model has three parameters of interest, *viz.* the on-site interaction term U , the tunneling t , and the temperature T . The total number of atoms N and the harmonic trap frequency Ω determine the phase boundaries and the nature of the Mott and superfluid shells. In current experiments typically $t \ll T \ll U$, whereas the critical temperature T_c of the superfluid regions is expected to be $\lesssim t$.

In this chapter I extend the work presented in chapter 4 to a finite temperature theory. Here I will calculate the finite temperature order parameter and the critical temperature of the superfluid regions, as well as the local entropy (within the local density approximation) for the entire system using two different approaches. First, I will use a mean field local density approximation [119] where the superfluid regions are considered as a two level system. Next, I will use a more accurate slave fermion method [120]. The results of the later indicate that the mean-field local density approximation alone overestimates the critical temperature for superfluidity, and that when quantum fluctuations are included, the critical temperature drops typically by a factor of three. Thus, to study the superfluid regions, it becomes necessary to reduce the temperature much further than originally thought within the mean-field local density approximation [119].

In current experiments on bosons, one typically starts with a magnetic trap and then turns on a lattice adiabatically to bring the system into the Mott regime. The adiabatic turning-on of the optical lattice leads to compression of the Bose gas which causes heating and an increase of temperature [119]. However, essentially all the entropy of the Bose gas is now confined to the regions between the Mott shells which for temperatures $t \ll T \ll U$ are normal (non-superfluid) [119]. To reduce the temperature to values $T < t$ in order to access the superfluid regions, this entropy must be either removed or rearranged as in an adiabatic expansion process [119]. The disadvantage of the adiabatic expansion process is that the confining potential of the Hamiltonian must be changed to produce the desired reduction of temperature, which means that the new system is different from the original. I will describe a cooling method using entropy removal, in which the system remains the same after rethermalization, but the number of particles is reduced. While the adiabatic expansion is a thermodynamic procedure, entropy removal method is done via a non-equilibrium process followed by rethermalization to a lower temperature.

The rest of this chapter is organized as follows. In Sec. 7.2 I will derive the thermodynamic potential using a mean field local density approximation (LDA) approach. Using this thermodynamic potential I will calculate the entropy, order parameter equation, compressibility, number density, and the critical temperature. In Sec 7.3 I will introduce the slave fermion method, and calculate the thermodynamic potential using this method. In Sec. 7.3.1 I will describe the slave fermion method. In Sec. 7.3.2 I will describe the Hubbard-Stratonovich method to decouple the tunneling term in the Bose-Hubbard Hamiltonian. In Sec. 7.3.3 I will use the

mean field approximation within the slave fermion technique to derive the thermodynamic potential. In Sec 7.3.4 I will calculate the thermodynamic potential beyond the mean field approximation by including quasiparticle excitations perturbatively. In Sec 7.3.5 I will describe under what limit the thermodynamic potential derived using slave fermion and mean field LDA methods are equivalent. In Sec. 7.4 I will discuss my results and the figures. In Sec 7.5 I will describe a non-equilibrium cooling method to reduce the temperature of these systems. Finally I will state my conclusions in Sec. 7.6.

7.2 Mean-field local density approximation

Harmonically confined bosons can be described by the Hamiltonian

$$H = -t \sum_{\langle i,j \rangle} a_i^\dagger a_j - \sum_i \mu_i a_i^\dagger a_i + \frac{U}{2} \sum_i a_i^\dagger a_i^\dagger a_i a_i, \quad (7.1)$$

where $\langle i, j \rangle$ denotes the sum over nearest neighbors, t_{ij} are the hopping parameters, $\mu_i = \mu - V_i$ is the local chemical potential with μ being the global chemical potential and V_i is the harmonically confining trap potential.

Within the local density approximation (LDA) in the limit of $t \ll U$ the local grand-canonical partition function describing superfluid regions between two Mott shells [71] with p and $p + 1$ atoms per site is

$$\mathcal{Z}_{TL}(\mathbf{r}) = e^{-\beta E_+(\mathbf{r})} + e^{-\beta E_-(\mathbf{r})}, \quad (7.2)$$

where $E_\pm(\mathbf{r}) = E_s(\mathbf{r}) \pm \sqrt{[E_d(\mathbf{r})]^2 + (p+1)|\Delta(\mathbf{r})|^2}$ correspond to the local energies describing the superfluid region between the p -th and $(p+1)$ -th Mott phase, where

$\Delta(\mathbf{r}) \neq 0$. The term $E_s(\mathbf{r}) = [E_{p+1}(\mathbf{r}) + E_p(\mathbf{r})]/2 + \Lambda(\mathbf{r})$ where $E_p(\mathbf{r}) = Up(p - 1)/2 - \mu_{\mathbf{r}}p$ and Λ and Δ are functions of the order parameter [71]. The corresponding local thermodynamic potential is $\Omega_{TL}(\mathbf{r}) = -T \ln \mathcal{Z}_{TL}(\mathbf{r})$. Using Eq.(7.2), we get

$$\Omega_{TL} = E_s(\mathbf{r}) - T \log \left[2 \cosh \frac{\alpha(\mathbf{r})}{T} \right] \quad (7.3)$$

and using entropy $S_{TL} = -(\partial\Omega_{TL}/\partial T)_{V,\mu}$ we get,

$$S_{TL} = \left(\frac{\partial E_s(\mathbf{r})}{\partial T} \right)_{V,\mu} + \ln \left[2 \cosh \frac{\alpha(\mathbf{r})}{T} \right] + \tanh \left[\frac{\alpha(\mathbf{r})}{T} \right] \left\{ \left(\frac{\partial \alpha(\mathbf{r})}{\partial T} \right)_{V,\mu} - \frac{\alpha(\mathbf{r})}{T} \right\} \quad (7.4)$$

where $\alpha(\mathbf{r}) = \sqrt{[E_d(\mathbf{r})]^2 + (p+1)|\Delta(\mathbf{r})|^2}$. The number density $n(\mathbf{r}) = -(\partial\Omega_{TL}/\partial\mu)_{V,T}$ gives ,

$$n(\mathbf{r}) = - \left(\frac{\partial E_s(\mathbf{r})}{\partial \mu} \right)_{V,T} + \tanh \left[\frac{\alpha(\mathbf{r})}{T} \right] \left(\frac{\partial \alpha(\mathbf{r})}{\partial \mu} \right)_{V,T} \quad (7.5)$$

Similarly, the compressibility $\chi(\mathbf{r}) = (\partial n(\mathbf{r})/\partial\mu)_{V,T}$ is,

$$\chi(\mathbf{r}) = - \left(\frac{\partial^2 E_s(\mathbf{r})}{\partial \mu^2} \right)_{V,T} + \tanh \left[\frac{\alpha(\mathbf{r})}{T} \right] \left(\frac{\partial^2 \alpha(\mathbf{r})}{\partial \mu^2} \right)_{V,T} + \text{sech}^2 \left[\frac{\alpha(\mathbf{r})}{T} \right] \left[\left(\frac{\partial \alpha(\mathbf{r})}{\partial \mu} \right)_{V,T} \right]^2 \frac{1}{T} \quad (7.6)$$

Note that the expressions for the number density and the compressibility ignores the contribution from the collective modes and hence should be valid only near or above critical temperature when $\psi \approx 0$.

We will now consider two different temperature regimes *viz.* $T > T_c(\mathbf{r})$ and $T \lesssim T_c$ where $T_c(\mathbf{r})$ is the spatially dependent critical temperature of the superfluid shells.

Case 1: $T > T_c(\mathbf{r})$ In this regime, $\psi = 0$ which implies

$$\alpha(\mathbf{r}) = |E_d(\mathbf{r})| = \frac{|pU - \mu_{\mathbf{r}}|}{2}, \quad (7.7)$$

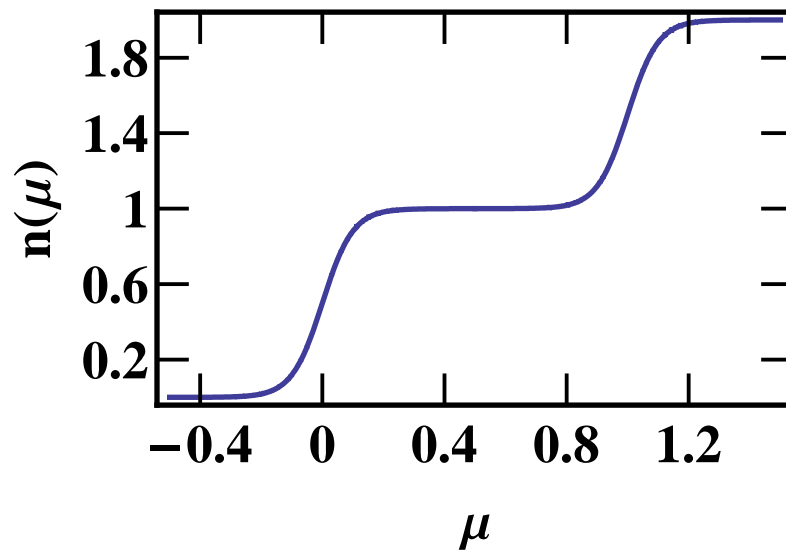


Figure 7.1: The number density of atoms per site in 2D between $n = 2$ and $n = 0$ Mott states. The parameters used are $t = 0.0125U$, $U = 1$, and temperature $T = 0.05U$ much higher than the critical temperature.

and

$$E_s(\mathbf{r}) = \frac{U}{2}n^2 - \mu_{\mathbf{r}} \left(p + \frac{1}{2} \right) \quad (7.8)$$

This leads to entropy

$$S(\mathbf{r}) = \ln \left[2 \cosh \frac{pU - \mu_{\mathbf{r}}}{2T} \right] - \tanh \left[\frac{(pU - \mu_{\mathbf{r}})}{2T} \right] \left(\frac{(pU - \mu_{\mathbf{r}})}{2T} \right), \quad (7.9)$$

number density

$$n(\mathbf{r}) = p + \frac{1}{2} \left[1 - \tanh \left(\frac{pU - \mu_{\mathbf{r}}}{2T} \right) \right] = p + f(pU - \mu_{\mathbf{r}}), \quad (7.10)$$

and compressibility

$$\chi(\mathbf{r}) = \frac{1}{4T} \text{sech}^2 \left(\frac{pU - \mu_{\mathbf{r}}}{2T} \right). \quad (7.11)$$

Case 2: $T \lesssim T_c(\mathbf{r})$. In this regime the order parameter ψ is small which implies that we can still ignore the contribution of the thermally excited collective modes to the thermodynamic potential, which can be assumed to be heavily damped. We will begin by calculating the order parameter equation. This can be obtained by minimizing Ω_{TL} with respect to $\psi^*(\mathbf{r})$. Before we do that we will make the approximation of ignoring the spatial derivatives of ψ such that $\Delta(\mathbf{r}) = zt\psi(\mathbf{r})$. This leads to $(\partial E_s(\mathbf{r})/\partial \psi^*(\mathbf{r}))_{\mu, V, T} = zt\psi(\mathbf{r})$ and $(\partial \alpha(\mathbf{r})/\partial \psi^*(\mathbf{r}))_{\mu, V, T} = (p+1)z^2t^2\psi(\mathbf{r})/2\alpha(\mathbf{r})$.

This leads to the order parameter equation

$$\frac{1}{\alpha(\mathbf{r})} \tanh \left[\frac{\alpha(\mathbf{r})}{T} \right] = \frac{2}{(p+1)zt}. \quad (7.12)$$

Now at the critical temperature $\alpha(\mathbf{r}) = (pU - \mu_{\mathbf{r}})/2$ which leads to

$$T_c = \frac{pU - \mu_{\mathbf{r}}}{2 \tanh^{-1} \frac{pU - \mu_{\mathbf{r}}}{(p+1)zt}}. \quad (7.13)$$

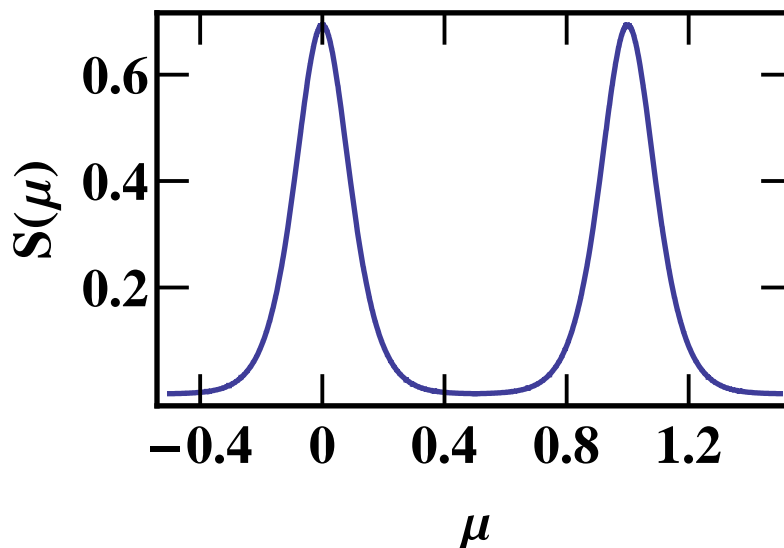


Figure 7.2: The local entropy in 2D between $n = 2$ and $n = 0$ Mott states. The parameters used are the same as in Fig. 7.1.

The finite temperature order parameter equation (7.12) can be solved numerically to find $\alpha(\mathbf{r})$ which can be plugged in Eqs.(7.5) and (7.6) to calculate the number density and compressibility respectively.

7.3 Functional integral approach

The big problem with the standard LDA approach is that quantum and thermal fluctuation effects are not easy to implement, and the standard theory tends to over-estimate the critical temperature for superfluidity and the entropy at low temperatures. Thus any attempt to use the standard theory as a guide for thermometry will lead to inaccurate and misleading results. In order to improve on the standard results when $t \ll U$ and to develop a regular perturbation theory around this limit

we will use a functional integral approach [121].

Let us first summarize the main challenges we have to face in this process. First, as one can easily see, the Hamiltonian can be divided into the local part which involves the onsite interaction and the chemical potential and the non local term which involves the tunneling. In the limit where $t = 0$, the local term can be solved exactly as it is diagonal in local number basis. However if we want to use coherent state functional integral technique with only the local part of the Hamiltonian contributing to the bare action, we have to figure out a way to deal with the term which is quartic in the creation and annihilation operators. This is done using the well known slave particle technique [122]. I will briefly summarize below how the slave particle technique works. Slave particles can either be bosonic or fermionic. I will explain why, in our problem, it is more appropriate to use the slave fermion method rather than the slave boson. To deal with the hopping term we will use the Hubbard-Stratonovich transformation [121]. With these two mathematical steps we can derive the action for the system.

7.3.1 Slave - fermion technique

Consider a single site of our lattice. If the creation and annihilation operators for the bosons are denoted by \hat{a}_i^\dagger and \hat{a}_i , respectively, we can form the number operator $\hat{N}_i = \hat{a}_i^\dagger \hat{a}_i$ which counts the number of bosons at the site i . In the slave particle formalism, for any occupation number a pair of annihilation and creation operators is introduced that create and annihilate the state with precisely that

given integer number of particles. The original occupation number state $|n_i\rangle$ are now decomposed as $|n_i^0, n_i^1, \dots\rangle$ where n_i^α is the eigenvalue of the number operator $\hat{n}_i^\alpha \equiv (\hat{a}_i^\alpha)^\dagger \hat{a}_i^\alpha$ formed by the pair of creation $(\hat{a}_i^\alpha)^\dagger$ and annihilation \hat{a}_i^α operators that create and annihilate bosons of type α at the site i . The operator $(\hat{a}_i^\alpha)^\dagger$ may be either a (slave) boson operator $(\hat{b}_i^\alpha)^\dagger$ with $[(\hat{b}_i^\alpha)^\dagger, (\hat{b}_j^\beta)^\dagger] = \delta_{\alpha,\beta} \delta_{i,j}$ or the (slave) fermion operator $(\hat{f}_i^\alpha)^\dagger$, with $\{(\hat{f}_i^\alpha)^\dagger, (\hat{f}_j^\beta)^\dagger\} = \delta_{\alpha,\beta} \delta_{i,j}$.

As it stands, this decomposition is certainly not unique for slave bosons. For example, the original state $|2\rangle$ could be written as $|0, 0, 1, 0, \dots\rangle$ or as $|0, 2, 0, \dots\rangle$. Such a state is prohibited by construction in slave fermions because of Pauli's exclusion principle. Also, states like $|0, 1, 1, 0, \dots\rangle$ where two of the slaves particles states are simultaneously occupied are prohibited both in slave fermions and slave bosons. Our Hilbert space thus greatly increases. To make sure that every occupation occurs only once we have to introduce an additional constraint, namely

$$\sum_{\alpha} \hat{n}_j^{\alpha} = 1 \tag{7.14}$$

for every site j . This constraint thus makes sure that there is always just one slave particle per site. Because in the positive U Bose-Hubbard model bosons on the same site repel each other, high on-site occupation numbers are disfavored.

Since we are interested in Mott regions with p particles per site and superfluid regions that emerge between p and $p + 1$ Mott shells, slave fermions are more appropriate. So henceforth, we will only consider the slave operators to be fermionic.

Using our slave-particle operators we now rewrite Eq. (7.1) into the form

$$\begin{aligned} \hat{H} = & - \sum_{\langle i,j \rangle} \sum_{\alpha,\beta} \sqrt{\alpha+1} \sqrt{\beta+1} (\hat{a}_i^{\alpha+1})^\dagger \hat{a}_i^\alpha t_{ij} \hat{a}_j^{\beta+1} (\hat{a}_j^\beta)^\dagger - \sum_i \mu_i \sum_\alpha \alpha \hat{n}_i^\alpha \\ & + \frac{U}{2} \sum_i \sum_\alpha \alpha(\alpha-1) \hat{n}_i^\alpha, \end{aligned} \quad (7.15)$$

with the additional constraint given by Eq. (7.14). We see that the quartic term in the original Bose-Hubbard Hamiltonian has been replaced by one that is quadratic in the slave-particle creation and annihilation operators, which is the essential motivation behind the introduction of slave particles.

Next we will perform the two-level approximation under which we will confine our Hilbert space to that of the slave fermions $|n_p^i\rangle$ and $|n_{p+1}^i\rangle$. This is appropriate when we are looking at only the superfluid region that emerges between two Mott regions with occupation number p and $p+1$. Using the condition $\hat{n}^p + \hat{n}^{p+1} = 1$, we get

$$\begin{aligned} \hat{H} = & - \sum_{\langle i,j \rangle} (p+1) (\hat{a}_i^{p+1})^\dagger \hat{a}_i^p t_{ij} \hat{a}_j^{p+1} (\hat{a}_j^p)^\dagger - \sum_i \mu_i (1 + p - \hat{n}_i^p) \\ & + U \sum_i \left(\frac{p(p+1)}{2} - \hat{n}_i^p \right). \end{aligned} \quad (7.16)$$

Note that in the slave fermion formalism, the tunneling term automatically satisfies the constraint $\hat{n}^p + \hat{n}^{p+1} = 1$.

Now that we have introduced the slave-fermion method and derived its representation of the Bose-Hubbard model, we want to turn the Hamiltonian into an

action for the imaginary time evolution. Using the standard recipe [121] we find

$$\begin{aligned}
S[(a^p)^*, a^p, (a^{p+1})^*, a^{p+1}] &= \int_0^{\hbar\beta} d\tau \left\{ \sum_i ((a_i^p)^* (\hbar\partial/\partial\tau - pU + \mu_i) a_i^p + E_{p+1}^i) \right\} \\
&- \int_0^{\hbar\beta} d\tau \left\{ \sum_{\langle i,j \rangle} (p+1) (a_i^{p+1})^* a_i^p t_{ij} a_j^{p+1} (a_j^p)^* \right\}, \quad (7.17)
\end{aligned}$$

where $E_{p+1}^i = Up(p+1)/2 - \mu_i(p+1)$ and $\beta = 1/k_B T$ is the inverse thermal energy.

7.3.2 Hubbard-Stratonovich transformation

Although we have simplified the interaction term, the hopping term has become more complicated. By performing a Hubbard-Stratonovich transformation on the above action we can decouple the hopping term in a similar manner. This introduces a field Φ into the action which, as we will see, may be identified with the superfluid order parameter. The Hubbard-Stratonovich transformation basically consists of adding a complete square to the action, i.e., adding

$$\int_0^{\hbar\beta} d\tau \sum_{i,j} \left(\Phi_i^* - \sum_p \sqrt{p+1} (a_i^{p+1})^* a_i^p \right) t_{ij} \left(\Phi_j - \sum_p \sqrt{p+1} a_i^{p+1} (a_i^p)^* \right). \quad (7.18)$$

Since a complete square can be added to the action without changing the physics we see that this procedure allows us to decouple the hopping term.

We now perform a Fourier transform on all fields,

$$a_i^p(\tau) = (1/\sqrt{N_s \hbar\beta}) \sum_{\mathbf{k}, n} a_{\mathbf{k}, n}^p e^{i(\mathbf{k}\cdot\mathbf{x}_i - \omega_n \tau)}, \quad (7.19)$$

and so on. Here N_s is the number of lattice sites. If we also carry out the remaining

integrals and sums we find

$$\begin{aligned}
S[\Phi^*, \Phi, ((a^p)^*, a^p, (a^{p+1})^*, a^{p+1})] &= \sum_{\mathbf{k}, n} \epsilon_{\mathbf{k}} |\Phi_{\mathbf{k}, n}|^2 + \frac{1}{\sqrt{N_s \hbar \beta}} \sum_{\mathbf{k}, \mathbf{q}} \sum_{n, n'} \mu_{\mathbf{q}, n'} p (a_{\mathbf{k}, n}^p)^* a_{\mathbf{k}+\mathbf{q}, n+n'}^p \\
&+ i N_s \hbar \beta \left(U \frac{p(p+1)}{2} - \frac{\mu_{\mathbf{0}, 0}(p+1)}{\sqrt{N_s \hbar \beta}} \right) + \sum_{\mathbf{k}, n} (a_{\mathbf{k}, n}^p)^* (-i \hbar \omega_n - pU) a_{\mathbf{k}, n}^p - \\
&\sum_{\mathbf{k}, \mathbf{k}', n, n'} \frac{\epsilon_{\mathbf{k}'}}{\sqrt{N_s \hbar \beta}} \left\{ \left(\sqrt{p+1} (a_{\mathbf{k}+\mathbf{k}', n+n'}^{p+1})^* a_{\mathbf{k}, n}^p \right) \Phi_{\mathbf{k}', n'} \right. \\
&\left. + \Phi_{\mathbf{k}', n'}^* \left(\sqrt{p+1} a_{\mathbf{k}+\mathbf{k}', n+n'}^{p+1} (a_{\mathbf{k}, n}^p)^* \right) \right\}. \tag{7.20}
\end{aligned}$$

The expression $\epsilon_{\mathbf{k}} = 2t \sum_{j=1}^d \cos(k_j a)$, where a is the lattice constant of the square lattice with N_s lattice sites. The partition function becomes

$$\begin{aligned}
\mathcal{Z} &= \frac{1}{\hbar \beta} \int \left(\prod_{\mathbf{k}, n} D[(a_{\mathbf{k}, n}^p)^*] D[a_{\mathbf{k}, n}^p] D[(a_{\mathbf{k}, n}^{p+1})^*] D[a_{\mathbf{k}, n}^{p+1}] D[(\phi_{\mathbf{k}, n})^*] D[\phi_{\mathbf{k}, n}] \right) \times \\
&e^{-S[\Phi^*, \Phi, (a^p)^*, a^p, (a^{p+1})^*, a^{p+1}]/\hbar}. \tag{7.21}
\end{aligned}$$

We will now make a local density approximation which allows the replacement of $\mu_{\mathbf{q}, n}/\sqrt{N_s \hbar \beta}$ with $\mu_i \delta_{\mathbf{k}, \mathbf{q}} \delta_{n, n'}$. This approximation is valid as long as the change in the harmonic trap potential between adjacent sites is very small compared to any other energy scale (t , U , or μ), of the problem.

This reduces the action to

$$\begin{aligned}
S[\Phi^*, \Phi, a^{p*}, a^p, a^{p+1*}, a^{p+1}] &= \sum_{\mathbf{k}, n} \epsilon_{\mathbf{k}} |\Phi_{\mathbf{k}, n}|^2 + i N_s \hbar \beta \left(U \frac{p(p+1)}{2} - \mu_i (p+1) \right) \\
&+ \sum_{\mathbf{k}, \mathbf{k}', n, n'} \left((a_{\mathbf{k}, n}^p)^* (a_{\mathbf{k}', n+n'}^{p+1})^* \right) \times \\
&\begin{pmatrix} \tilde{M}_i^{p,p}(i\omega_n) & \sqrt{p+1} \frac{\epsilon_{\mathbf{k}-\mathbf{k}'}}{\sqrt{N_s \hbar \beta}} \Phi_{\mathbf{k}-\mathbf{k}', n'-n}^* \\ \sqrt{p+1} \frac{\epsilon_{\mathbf{k}-\mathbf{k}'}}{\sqrt{N_s \hbar \beta}} \Phi_{\mathbf{k}-\mathbf{k}', n'-n} & 0 \end{pmatrix} \begin{pmatrix} a_{\mathbf{k}, n}^p \\ a_{\mathbf{k}', n'}^{p+1} \end{pmatrix}. \tag{7.22}
\end{aligned}$$

Now, since $a_{\mathbf{k},n}^p$ and $a_{\mathbf{k},n}^{p+1}$ are quadratic we can integrate them out, which gives us

$$S[\Phi^*, \Phi] = \sum_{\mathbf{q},n} \epsilon_{\mathbf{q}} |\Phi_{\mathbf{q},n}|^2 + iN_s \hbar \beta \left(\frac{Up(p+1)}{2} - \mu_i(p+1) \right) - \sum_{\mathbf{q},n,n'} \text{Tr} \left[\ln \begin{bmatrix} -pU + \mu_i & \sqrt{p+1} \frac{\epsilon_{\mathbf{k}}}{\sqrt{N_s \hbar \beta}} \Phi_{\mathbf{q},n'-n}^* \\ \sqrt{p+1} \frac{\epsilon_{\mathbf{k}}}{\sqrt{N_s \hbar \beta}} \Phi_{\mathbf{q},n'-n} & 0 \end{bmatrix} \right]. \quad (7.23)$$

The action derived above is accurate so long as the approximations above hold (for a superfluid region between two Mott shells with p and $p+1$ particles per site) with Φ being the Hubbard-Stratonovitch Bose field. The partition function is thus given by,

$$\mathcal{Z} = \frac{1}{\beta} \int D[\Phi] D[\Phi^*] e^{-S[\Phi^*, \Phi]/\hbar} \quad (7.24)$$

7.3.3 Mean field theory

In this section we will make the mean field approximation

$\phi_{\mathbf{q},n'-n}/\sqrt{N_s \hbar \beta} = \psi \delta_{\mathbf{q}\mathbf{0}} \delta_{nn'}$ and derive within that approximation the thermodynamic potential. We will show how within this approximation, the action given by Eq (7.23) gives us the results obtained from the mean field theory derived in Sec. 7.2 in the limit $t = 0$ where the problem is exactly solvable. We first rewrite the action

$$S_0[\psi, \psi^*] = N_s \hbar \beta z t |\psi|^2 + N_s \hbar \beta \left(U \frac{p(p+1)}{2} - \mu_i(p+1) \right) - N_s \sum_n \{ \ln [E'_+ - i\hbar\omega_n] + \ln [E'_- - i\hbar\omega_n] \}. \quad (7.25)$$

The factor $E'_\pm = \frac{-pU + \mu}{2} \pm \sqrt{((pU - \mu_i)/2)^2 + (\alpha + 1)z^2t^2|\psi|^2}$. The thermodynamic potential is thus defined as

$$\begin{aligned} \Omega[\psi, \psi^*] &= N_s z t |\psi|^2 + N_s \left(U \frac{p(p+1)}{2} - \mu_i(p+1) \right) \\ &\quad - \frac{N_s}{\hbar\beta} \sum_n \{ \ln [E'_+ - i\hbar\omega_n] + \ln [E'_- - i\hbar\omega_n] \} \end{aligned} \quad (7.26)$$

After performing the Matsubara summation, one gets,

$$\begin{aligned} \Omega[\psi, \psi^*] &= N_s z t |\psi|^2 + N_s \left(U \frac{p(p+1)}{2} - \mu_i(p+1) \right) \\ &\quad - \frac{N_s}{\beta} \left\{ \ln [1 + e^{-\beta E'_+}] + \ln [1 + e^{-\beta E'_-}] \right\} \end{aligned} \quad (7.27)$$

One can easily check that in the limit of $t = 0$ (or equivalently at a temperature much higher than the critical temperature where $\psi = 0$) one gets a thermodynamic potential same as in Eq. (7.3) (upto a constant term $-T \log 2$), as should be the case.

7.3.4 Beyond mean field theory

We will now compute the Bogoliubov dispersion relation for the superfluid phase. If we add fluctuation in $\phi_{\mathbf{q},n'-n} = \psi \delta_{\mathbf{q}\mathbf{0}} \delta_{nn'} + \delta\phi_{\mathbf{q},n} + \delta\phi_{-\mathbf{q},-n}$, to the order parameter, then the action is described by,

$$S[\phi_{\mathbf{q},n}, \phi_{\mathbf{q},n}^*] = S_0[\psi, \psi^*] + \frac{\hbar}{2} \sum_{\mathbf{q},n} \begin{pmatrix} \phi_{\mathbf{q},n} & \phi_{\mathbf{q},n}^* \end{pmatrix} \mathcal{G}^{-1}(\mathbf{q}, i\omega_n) \begin{pmatrix} \phi_{\mathbf{q},n}^* \\ \phi_{\mathbf{q},n} \end{pmatrix} \quad (7.28)$$

The inverse Green's function

$$\mathcal{G}^{-1}(\mathbf{q}, i\omega_n) = \begin{pmatrix} -G^{-1}(\mathbf{q}, i\omega_n) + 4\Lambda|\psi|^2 & 2\Lambda|\psi|^2 \\ 2\Lambda|\psi|^2 & -G^{-1}(\mathbf{q}, i\omega_n) + 4\Lambda|\psi|^2 \end{pmatrix} \quad (7.29)$$

where,

$$-\hbar G^{-1}(\mathbf{q}, i\omega_n) = \epsilon_q + \epsilon_q^2(p+1) \frac{n'_+ - n'_-}{4\Gamma^{1/2} - i\hbar\omega_n} \quad (7.30)$$

which is also the dispersion relation, and

$$\Lambda = -\frac{z^4 t^4}{2N_s \hbar^2 \beta} \left\{ \frac{(p+1)^2 \beta}{4\Gamma} [n'_-(1-n'_-) + n'_+(1-n'_+)] + \frac{(p+1)^2}{4\Gamma^{3/2}} (n'_+ - n'_-) \right\} \quad (7.31)$$

where $\Gamma = ((pU - \mu_i)/2)^2 + (p+1)z^2 t^2 |\psi|^2$. The Fermi functions $n'_\pm = (1 + e^{\beta E'_\pm})^{-1}$.

Thus, after including the fourth order *gaussian* correction to the order parameter,

the thermodynamic potential is given by,

$$\begin{aligned} \Omega[\psi, \psi^*] = & N_s z t |\psi|^2 + N_s \left(\frac{p(p+1)}{2} - \mu_i(p+1) \right) \\ & - \frac{N_s}{\beta} \left(\ln(1 + \exp^{-\beta E'_+}) + \ln(1 + \exp^{-\beta E'_-}) \right) \\ & + \frac{1}{\beta} \sum_{\mathbf{q} \neq \mathbf{0}, \omega_n \neq 0} \text{Tr} \ln \hbar \beta \mathcal{G}(\mathbf{q}, i\omega_n). \end{aligned} \quad (7.32)$$

7.3.5 Equivalence with mean field LDA approach

The thermodynamic potential given by Eq. (7.27) derived using the slave fermion method is equivalent to that derived using the mean field LDA method given by Eq. (7.3) only in the limit $t = 0$ and/or $\psi = 0$. Under what limit is the slave fermion method equivalent to the mean field LDA method? In this section we will show that:

1. If one takes into account the constraint $\hat{n}_i^p + \hat{n}_i^{p+1} = 1$ not exactly but only in the mean field sense and

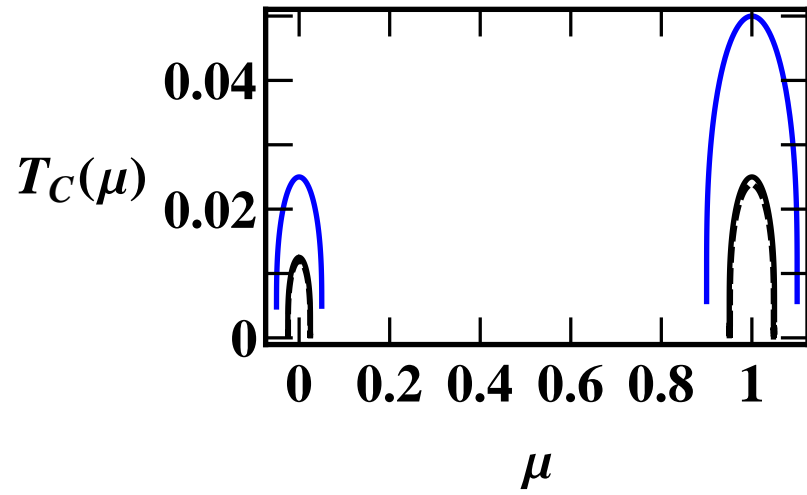


Figure 7.3: The local critical temperature in 2D between $n = 2$ and $n = 0$ Mott shells calculated using slave fermion (black solid), slave fermion with gaussian fluctuations (black dashed), and mean field LDA method (blue). The parameters used are $t = 0.0125U$ and $U = 1$.

2. if one takes the high temperature limit where the Fermi function is replaced by the Boltzmann function

the two methods are equivalent. This indicates that the slave fermion method is more accurate than the mean field LDA method. An implicit way to take into account the constraint would be to introduce a real valued field λ in the action through,

$$\prod_i \delta\left(\sum_{\alpha} n_i^{\alpha} - 1\right) = \int d[\lambda] e^{\frac{i}{\hbar} \int_0^{\hbar\beta} \sum_i \lambda_i(\tau) (\sum_{\alpha} n_i^{\alpha} - 1) d\tau}. \quad (7.33)$$

After taking the Fourier transform of the action, we get

$$\begin{aligned} S[\Phi^*, \Phi, (a^{\alpha})^*, a^{\alpha}, \lambda] &= \sum_{\mathbf{k}, n} \epsilon_{\mathbf{k}} |\Phi_{\mathbf{k}, n}|^2 - \frac{1}{\sqrt{N_s \hbar \beta}} \sum_{\mathbf{k}, \mathbf{q}} \sum_{n, n'} \mu_{\mathbf{q}, n'} \alpha (a_{\mathbf{k}, n}^{\alpha})^* a_{\mathbf{k}+\mathbf{q}, n+n'}^{\alpha} \\ &- i \frac{1}{\sqrt{N_s \hbar \beta}} \sum_{\mathbf{k}, \mathbf{q}} \sum_{n, n'} \lambda_{\mathbf{q}, n'} (a_{\mathbf{k}, n}^{\alpha})^* a_{\mathbf{k}+\mathbf{q}, n+n'}^{\alpha} + i N_s \hbar \beta \lambda \\ &+ \sum_{\mathbf{k}, n} (a_{\mathbf{k}, n}^{\alpha})^* M^{\alpha\beta} (i\omega_n) a_{\mathbf{k}, n}^{\beta} - \sum_{\mathbf{k}, \mathbf{k}', n, n'} \frac{\epsilon_{\mathbf{k}'}}{\sqrt{N_s \hbar \beta}} \left\{ \left(\sum_{\alpha} \sqrt{\alpha+1} (a_{\mathbf{k}+\mathbf{k}', n+n'}^{\alpha+1})^* a_{\mathbf{k}, n}^{\alpha} \right) \Phi_{\mathbf{k}', n'} \right. \\ &\left. + \Phi_{\mathbf{k}', n'}^* \left(\sum_{\alpha} \sqrt{\alpha+1} a_{\mathbf{k}+\mathbf{k}', n+n'}^{\alpha+1} (a_{\mathbf{k}, n}^{\alpha})^* \right) \right\}, \end{aligned} \quad (7.34)$$

where the matrix $M(i\omega_n)$ is Fourier transform of the matrix $M = \hbar\partial/\partial\tau - \mu_i + pU$. Furthermore, $\lambda = (\lambda_{\mathbf{0}, 0}/\sqrt{N_s \hbar \beta})$, $\epsilon_{\mathbf{k}} = 2t \sum_{j=1}^d \cos(k_j a)$, where a is the lattice constant of the square lattice with N_s lattice sites. For completeness we point out that the partition function becomes

$$\mathcal{Z} = \frac{1}{\hbar\beta} \int \left(\prod_{\mathbf{k}, n} D[(a_{\mathbf{k}, n}^{\alpha})^*] D[a_{\mathbf{k}, n}^{\alpha}] D[(\phi_{\mathbf{k}, n})^*] D[\phi_{\mathbf{k}, n}] D[\lambda_{\mathbf{k}, n}] \right) e^{-S[\Phi^*, \Phi, (a^{\alpha})^*, a^{\alpha}, \lambda]/\hbar}. \quad (7.35)$$

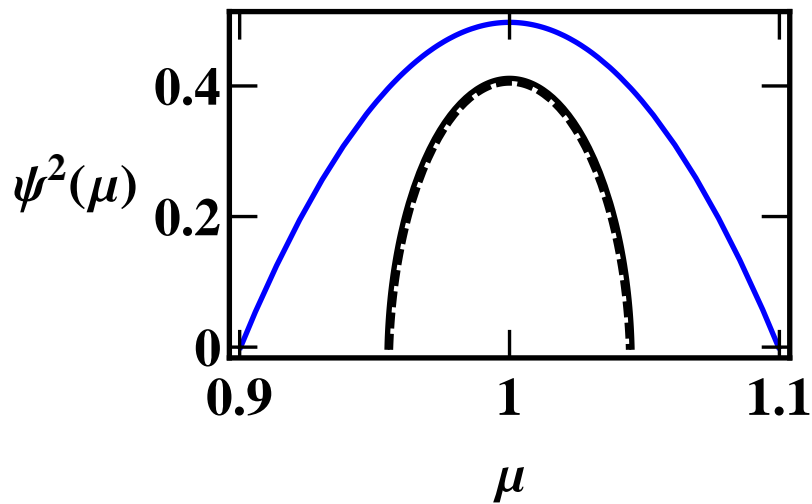


Figure 7.4: The order parameter in 2D between $n = 2$ and $n = 1$ Mott shells. The parameters used are $t = 0.0125U$, $U = 1$, and temperature $T = 0.015U$. The black solid curve is calculated using slave fermionic theory, the black dashed curve using slave fermion with gaussian fluctuations, and blue curve using mean field LDA theory.

We will now make the approximation that the λ field is time and position independent. This softens the constraint by replacing the general constraint field $\lambda_i(\tau)$ with a time and position independent field λ . By neglecting the position dependence we enforce the constraint only on the sum of all lattice sites. Doing this we are only left with the $\lambda_{\mathbf{0},0}$ contribution in Eq. (7.34), which can then be added to the matrix M . The path-integral over the constraint field then reduces to an ordinary integral. After making the two-level approximation, the action reduces to,

$$\begin{aligned}
S[\Phi^*, \Phi, a^{p*}, a^p, a^{p+1*}, a^{p+1}, \lambda] &= \sum_{\mathbf{k}, n} \epsilon_{\mathbf{k}} |\Phi_{\mathbf{k}, n}|^2 + iN_s \hbar \beta \lambda \\
&+ \sum_{\mathbf{k}, \mathbf{k}', n, n'} \left((a_{\mathbf{k}, n}^p)^* (a_{\mathbf{k}', n+n'}^{p+1})^* \right) \times \\
&\left(\begin{array}{cc} \tilde{M}_i^{p,p}(i\omega_n) & \sqrt{p+1} \frac{\epsilon_{\mathbf{k}-\mathbf{k}'}}{\sqrt{N_s \hbar \beta}} \Phi_{\mathbf{k}-\mathbf{k}', n'-n}^* \\ \sqrt{p+1} \frac{\epsilon_{\mathbf{k}-\mathbf{k}'}}{\sqrt{N_s \hbar \beta}} \Phi_{\mathbf{k}-\mathbf{k}', n'-n} & \tilde{M}_i^{p+1, p+1}(i\omega_{n'}) \end{array} \right) \begin{pmatrix} a_{\mathbf{k}, n}^p \\ a_{\mathbf{k}', n'}^{p+1} \end{pmatrix} \quad (7.36)
\end{aligned}$$

Now, since $a_{\mathbf{k}, n}^p$ and $a_{\mathbf{k}, n}^{p+1}$ are quadratic we can integrate it out, which gives us,

$$\begin{aligned}
S[\Phi^*, \Phi, \lambda] &= \sum_{\mathbf{q}, n} \epsilon_{\mathbf{q}} |\Phi_{\mathbf{q}, n}|^2 + iN_s \hbar \beta \lambda \\
&- \sum_{\mathbf{q}, n, n'} \text{Tr} \left[\ln \left[\begin{array}{cc} \tilde{M}_i^{p,p}(i\omega_n) & \sqrt{p+1} \frac{\epsilon_{\mathbf{q}}}{\sqrt{N_s \hbar \beta}} \Phi_{\mathbf{q}, n'-n}^* \\ \sqrt{p+1} \frac{\epsilon_{\mathbf{q}}}{\sqrt{N_s \hbar \beta}} \Phi_{\mathbf{q}, n'-n} & \tilde{M}_i^{p+1, p+1}(i\omega_{n'}) \end{array} \right] \right] \quad (7.37)
\end{aligned}$$

The partition function is thus given by,

$$\mathcal{Z} = \frac{1}{\beta} \int D[\Phi] D[\Phi^*] D[\lambda] e^{-S[\Phi^*, \Phi, \lambda]/\hbar} \quad (7.38)$$

We will now show how in the mean field and high temperature limit, the action derived above gives us the results obtained from the mean field LDA method. Within the approximation, $\phi_{\mathbf{q}, n'-n}/\sqrt{N_s \hbar \beta} = \psi \delta_{\mathbf{q} \mathbf{0}} \delta_{nn'}$, the action becomes:

$$\begin{aligned}
S_0[\psi, \psi^*, \lambda] &= N_s z t |\psi|^2 + iN_s \hbar \beta \lambda \\
&- N_s \sum_n \{ \ln [E_+ - i\lambda - i\hbar \omega_n] + \ln [E_- - i\lambda - i\hbar \omega_n] \} \quad (7.39)
\end{aligned}$$

The factor $E_{\pm} = -(2p+1)/2\mu + p^2/2U \pm \sqrt{((pU - \mu_i)/2)^2 + (p+1)z^2 t^2 |\psi|^2}$ is same as that in Eq. (7.2). The thermodynamic potential is thus defined as

$$\begin{aligned}
\Omega[\psi, \psi^*, \lambda] &= N_s z t |\psi|^2 + iN_s \lambda \\
&- \frac{N_s}{\beta} \{ \ln [1 + e^{-\beta(E_- - i\lambda)}] + \ln [1 + e^{-\beta(E_+ - i\lambda)}] \} \quad (7.40)
\end{aligned}$$

Now, we should have

$$\frac{d\Omega}{d\lambda} = 0 = iN_s - iN_s \left\{ \frac{1}{[e^{\beta(E_+ - i\lambda)} + 1]} + \frac{1}{[e^{\beta(E_- - i\lambda)} + 1]} \right\} \quad (7.41)$$

We will choose $-i\beta\lambda$ such that

$$\frac{d\Omega}{d\lambda} = 0 \equiv 1 - (n_- + n_+) \quad (7.42)$$

where we have defined $n_+ = f(E_+ - i\lambda)$ which is the occupation of the n^{p+1} slave fermions and $n_- = f(E_- + i\lambda)$ which is the occupation of the n^p slave fermions. $f(\cdot)$ is the Fermi function.

If we are in the high temperature limit, we replace the Fermi function by Boltzmann function, which gives $n_+ = e^{-(E_+ - i\lambda)\beta}$ and $n_- = e^{-(E_- - i\lambda)\beta}$. Since $n_+ + n_- = 1$, we get $e^{-i\lambda} = e^{-\beta E_+} + e^{-\beta E_-}$. In this limit,

$$\begin{aligned} \Omega[\psi, \psi^*, \lambda] &= N_s z t |\psi|^2 + iN_s \lambda \\ &\quad - \frac{N_s}{\beta} \{-\beta(E_- - i\lambda) - \beta(E_+ - i\lambda)\} \end{aligned} \quad (7.43)$$

Putting $e^{-i\lambda} = e^{-\beta E_+} + e^{-\beta E_-}$, we get $\Omega = -T \log \mathcal{Z}_{TL}$ same as Eq. (7.3).

7.4 Analytical results

Given the thermodynamic potential as in Eq. 7.32, one can calculate the entropy $S = -\partial\Omega/\partial T$ (with volume V and chemical potential μ kept fixed), the number density $n(\mathbf{r}) = -\partial\Omega_{TL}/\partial\mu$, the order parameter equation by minimizing Ω_{TL} with respect to $\psi^*(\mathbf{r})$, and the critical temperature by putting $\psi = 0$ in the order parameter equation and solving for T . We will now discuss our results for the

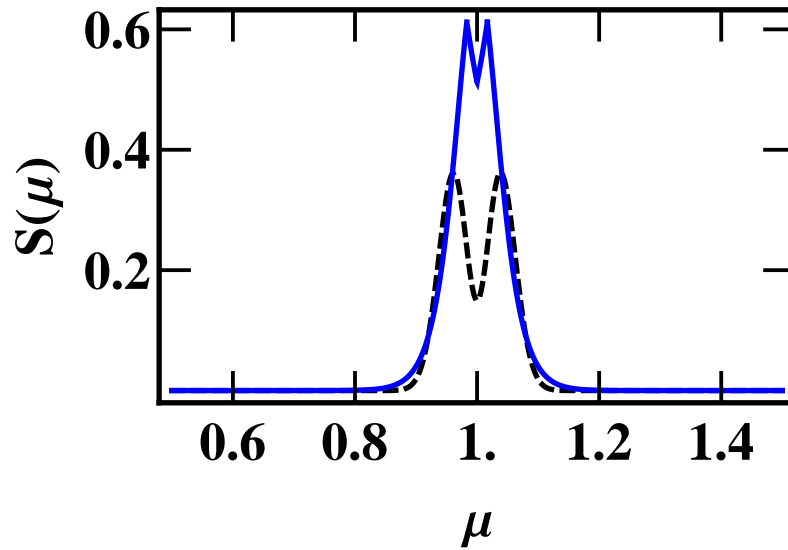


Figure 7.5: The local entropy in 2D between $n = 2$ and $n = 1$ Mott state using the slave fermion approach upto fourth order gaussian correction in $\phi_{\mathbf{q}}$ (dashed) and spin wave spectrum (solid). The parameters used are $t = 0.0125U$, $U = 1$, and temperature $T = 0.02U$.

entropy, order parameter, critical temperature, and the critical density of the system. In Fig. 7.1 we show the number density of atoms per site in 2D between $n = 2$ and $n = 0$ Mott states as a function of the chemical potential (instead of position). The parameters used are $t = 0.0125U$, $U = 1$, and temperature $T = 0.05U$ much above the critical temperature. At this temperature the order parameter $\psi = 0$, and the system exhibits Mott shells with normal (fluid) interlayers. The normal regions are given by non-integer number density per site. Note that at this temperature, the mean field LDA method and the slave fermion method are equivalent. The width of the normal regions increase with increase in temperature. In Fig. 7.2 we show the local entropy of the system as a function of the chemical potential. The parameters used are same as in Fig. 7.1. As expected, most of the entropy contribution comes from the normal regions, whereas the Mott regions almost have zero entropy. In Fig. 7.3 we show the critical temperature of the superfluid regions using three different methods: the slave fermion (black solid), slave fermion with gaussian fluctuations (black dashed), and mean field LDA method in blue/gray. The parameters used are $U = 1$ and $t = 0.0125U$. The mean field LDA overestimates the critical temperature. Taking into account quantum fluctuations by the slave fermion method reduces the estimated critical temperature by a factor of two (at the center of the superfluid regions). We see only a slight decrease in critical temperature if the gaussian fluctuations are included on top of the slave fermion method, indicating that the method is quite good at the mean field level. As expected the critical temperature $T_c \lesssim t$. In Fig. 7.4 we show the order parameter in 2D of the superfluid shell between $n = 2$ and $n = 1$ Mott states. The parameters used are $t = 0.0125U$,

$U = 1$, and temperature $T = 0.015U$. The black solid curve is calculated using slave fermionic theory, the black dashed curve using slave fermion with gaussian fluctuations, and the blue/gray using classical theory. As expected the order parameter is suppressed when we take quantum fluctuations into account. In Fig. 7.5 we show the local entropy in 2D between $n = 2$ and $n = 1$ Mott state using the slave fermion approach upto fourth order correction in q (blue) and spin wave spectrum [119]. The parameters used are $t = 0.0125U$, $U = 1$, and temperature $T = 0.02U$. Here we take into account contribution to entropy due to quasiparticle excitations. The double peak structure indicates that it is easier to generate quasiparticles near the edges rather than at the center of the superfluid shells [119].

7.5 Non-equilibrium cooling

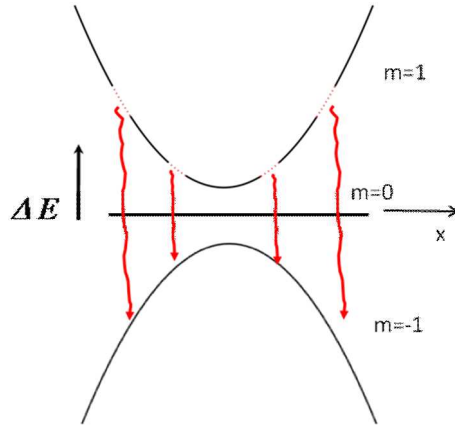
As indicated by Fig. 7.2, since the boson number fluctuates in the normal shells between the Mott shells, they have much higher entropy density than the Mott shells at temperature $T < U$, and are the sources of entropy at low temperature. Therefore, a much lower temperature can be achieved by getting rid of the atoms in these conducting shells, and letting the remaining atoms to rethermalize. Below we propose a scheme for getting rid of the atoms in these conducting shells and show that this leads to final temperature $T \lesssim t$. In current experiments $t \ll T \ll U$, whereas the critical temperature of the superfluid shells are $T_c \lesssim t$. Thus our method will enable experimentalists to observe the superfluid shells between the Mott shells [71].

In current experiments, the optical lattices are constructed from red detuned lasers where atoms are sitting in the region where the laser intensity is high. The lattice is switched on adiabatically in a magnetic trap $V_m(\mathbf{r}) = M\omega_0^2 r^2/2$, with frequency ω_0 . However, due to the Gaussian profile of the laser beam, the laser itself will also produce a confining harmonic potential. When these two potentials are properly aligned, the frequency ω of the total harmonic trap ($V(\mathbf{r}) = M\omega^2 r^2/2$) exceeds ω_0 , and is given by

$$\omega^2 = \omega_0^2 + 8V_0/(Mw^2), \quad (7.44)$$

where w is the waist of the laser beam.

We will first discuss the cooling scheme in three dimensions. Our strategy is to trap the atoms in a given positive m state, and subsequently getting rid of the normal atoms using the RF-knife technique used in evaporation cooling, which excites the normal atoms to the antitrapped negative m state. For this the overall trap should be mostly magnetic with a very weak optical component to it. For example if one has a strong magnetic field such that $\omega_0 = 2\pi \times 90Hz$ and we choose a blue detuned lasers with waist $w = 65\mu m$ and $V_0 = 12E_R$, $E_R = h \times 3.2kHz$, the optical trap would be repulsive and 15 times weaker than the magnetic trap. Note that even though the optical trap is weak and repulsive, $V_0 = 12E_R$ gives a hopping term $t \approx 0.01U$. Since the trap is magnetic, it selectively traps the positive m states. Hence, using a RF knife of frequencies in resonance with that of the atoms in the normal regions (estimated theoretically as discussed above) we can excite the atoms to the negative m state. This is illustrated in Fig. 7.6. The excited atoms see a



77

Figure 7.6: The energy levels of the $F = 1$ trapped atoms for different m levels as a function of site index. The cooling technique employs RF knives that selectively takes the atoms in normal phase, shown as dashed (red) curve, to antitrapped $m = -1$ state.

repulsive magnetic field and gets thrown out of the system. As it gets out of the system it will scatter with the stationary Mott atoms. However, the Mott atoms are in an insulator state with a large gap energy $U \approx 1kHz$ and remains unaffected by the atoms getting out of the trap. In two dimensions one has to be more careful in using the technique described above. This is because in current experiments, the 2D layers of atoms are achieved by switching on an optical lattice on a 3D trapped atoms along the z axis. Hence, the atoms are strongly confined optically along the z - axis and one has to employ the RF-knife along the $x - y$ plane.

Once the normal atoms gets thrown out, the remaining atoms then rethermalize to a lower temperature. The new temperature can be calculated as follows. Suppose we started with a temperature T and with N number of atoms. From this and using the values of U and t one can calculate the average energy $\langle E \rangle$. Just

after getting rid of the atoms in the conducting phase we know the new number of atoms \bar{N} and new average energy $\langle \bar{E} \rangle$. Using the rules of microcanonical statistical mechanics, one can calculate the new configuration of the system that will maximize the local entropy $\langle \bar{S} \rangle$. One can then calculate the new temperature using $1/\bar{T} = \partial S / \partial \langle E \rangle$. In Fig. 7.7 we show the number density of atoms per site in 3D between $n = 2$ and $n = 0$ Mott states using the slave fermion approach upto fourth order correction in $\phi_{\mathbf{q}}$. The parameters used are $t = 0.0125U$, and $U = 1$. The temperature $T = 0.1U$ and $\mu = 1.4$ for dashed curve. After entropy removal which kicks out atoms in the normal phase between $n = 0.8$ and $n = 0.2$ and atoms between $n = 1.2$ and $n = 1.8$, the new temperature is $T = 0.03U$ and $\mu = 1.23$ and the new density distribution shown in solid.

7.6 Conclusions

To conclude, I developed a finite temperature theory for superfluid bosons in harmonically confined optical lattices, that emerge in between the Mott insulating shells. Using this method I calculated various thermodynamic quantities like the entropy, number density, order parameter equation, etc. for this system. I showed that the mean-field local density approximation alone overestimates the critical temperature for superfluidity of harmonically confined bosons in optical lattices, and that when quantum fluctuations are included, the critical temperature drops typically by a factor of three. In current experiments $t \ll T \ll U$ where as the critical temperature $T_c \lesssim t$. Thus, to study the superfluid regions, it becomes necessary to reduce

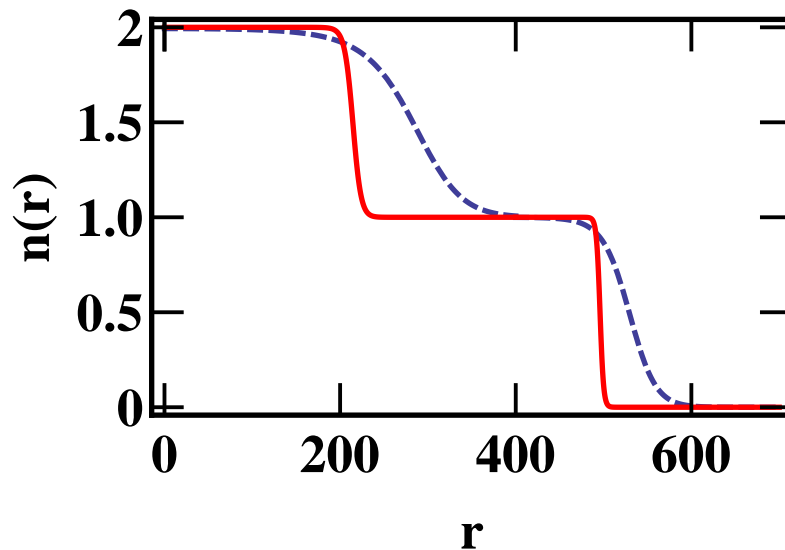


Figure 7.7: The number density of atoms per site in 3D between $n = 2$ and $n = 0$ Mott states using the slave fermion approach with Gaussian corrections. The parameters used are $t = 0.0125U$, and $U = 1$. The harmonic trap potential is $1/2\Omega r^2$ where $\Omega = 10^{-5}U$. The temperature $T = 0.1U$ and $\mu = 1.4$ for dashed curve. After entropy removal which kicks out atoms in the normal phase between $n = 0.8$ and $n = 0.2$ and atoms between $n = 1.2$ and $n = 1.8$, the new temperature is $T = 0.03U$ and $\mu = 1.23$. The new density distribution is shown in red.

the temperature much further than originally thought within the mean-field local density approximation. Essentially all the entropy of the Bose gas is confined to the regions between the Mott shells which for temperatures $U \ll T \ll t$ are normal (non-superfluid). To reduce the temperature to values $T < t$ in order to access the superfluid regions, this entropy must be either removed or rearranged as in an adiabatic expansion process. I discussed a non-equilibrium cooling method employing entropy removal, under which the system rethermalizes to a lower temperature.

Chapter 8

Summary and future directions

In this thesis I have presented my research in two different areas of quantum physics. My first area is the study of theoretical models of ultracold atoms which are relevant to condensed matter systems. Second is the study of quantum decoherence in superconducting qubits.

8.1 Superconducting qubits

Recent developments in the field of superconducting qubits include demonstration of high coherence time of the order of a few microseconds, non-dispersive readout [123], and circuit quantum electrodynamics(QED) [27]. In chapter 2 I analyzed the resonant properties and decoherence behavior of dc SQUID phase qubits, in which one junction acts as a phase qubit and the rest of the device provides isolation from dissipation and noise in the bias lead. This chapter is an extended version of the work presented in Ref. [54]. Ignoring dissipation, I found the two-dimensional Hamiltonian of the system and used numerical methods and a cubic approximation [44] to solve Schrödinger's equation for the eigenstates, energy levels, tunneling rates, and expectation value of the currents in the junctions. Using these results, I investigated how well this design provides isolation while preserving the characteristics of a phase qubit.

Typically qubit states in phase qubits are detected by tunneling it to the voltage state [22]. Although this can provide a fast, high-fidelity readout, it is a highly intrusive measurement that not only causes the qubit state to leave the computational basis, but also causes the dissipation of relatively large amounts of energy at the junction. I have proposed an alternate non-destructive readout mechanism which relies on the difference in the magnetic flux through the SQUID loop due to state of the qubit.

I would like to better understand the nature of the switching measurement in superconducting phase qubits. What is the measurement operator when one detects by switching the qubit to the voltage state? This question has not been carefully answered in the literature. How to understand the junction bifurcation amplifier (JBA) method for measurement in phase qubits in a fully quantum mechanical sense as opposed to treating the resonator classically [43]? Also, since in real experiments one either ramps the bias current continuously or sends a sudden pulse of bias current, is it okay to perform a time independent analysis, as has always been done in the past [44]?

In chapter 3 I studied decoherence effects in a dc SQUID phase qubit caused by the isolation circuit. This chapter is an extended version of the work presented in Ref. [50, 53]. The coupling between the SQUID phase qubit and its environment was modeled via the Caldeira-Leggett formulation [124] of quantum dissipation/decoherence, where the spectral density of the environment is related to the admittance of the isolation circuit. When the frequency of the qubit is at least two times larger than the resonance frequency of the isolation circuit, I found that the

decoherence time of the qubit is two orders of magnitude larger than in the typical ohmic regime, where the frequency of the qubit is much smaller than the resonance frequency of the isolation circuit. Aspects of this can be extended to other similar superconducting quantum devices and have been applied to experiments from the group at the University of Maryland [38, 61, 125].

In chapter 3 I have theoretically predicted vacuum Rabi oscillations, analogous to circuit-QED [27], in dc SQUID phase qubits. The result obtained gives an exact analytical expression for the Rabi oscillation of the qubit due to the coupling with the resonator (the isolation junction). This work can be extended to similar experiments in the field of circuit-QED [27, 126].

A natural extension of this work would be to understand the quantum mechanical nature of the two level systems that have been observed experimentally as a prime source of decoherence [127]. Can it be understood under the Caldeira-Leggett formalism? How can one formulate a Hamiltonian to explain $1/f$ noise [128]? The vacuum Rabi oscillations that we have demonstrated are analogous to circuit QED. Can we achieve a strong coupling between the resonator (*photon*) and the qubit (*atom*) such that the bare coupling is stronger than the fine structure constant? If yes, one can study QED in a strong coupling regime never studied before in experiments.

8.2 Ultracold atoms

Due to recent experimental breakthroughs, we can now study many body systems of interacting bosonic and fermionic atoms and molecules where the interaction strengths can be experimentally tuned. Such systems have been previously considered as models for condensed matter systems, and thus the field of ultracold atoms has helped to merge atomic-molecular-optical and condensed matter physics [129].

One such merger is the recent experimental discovery of Bose-Mott insulating phases in optical lattices. These Bose-Mott insulators have exhibited a quantum phase transition to a superfluid phase as the potential depth of the lattice is decreased [65]. Lattices are produced optically by the interference of counter-propagating laser beams, which creates a spatially periodic intensity pattern. This quantum phase transition of interacting bosons in lattice was first proposed by Fisher *et al.* in 1989 [77]. However, as in most condensed matter models, the model studied consisted of a homogeneous lattice.

One of my focus areas has been the physics of bosons in harmonically confined optical lattices. My research in this area is described in chapters 4 and 7. These chapters are an extended version of the work presented in Ref. [71]. Bosons in harmonically confined optical lattices system exhibits a ‘wedding cake structure’ of alternating Mott shells with different number of bosons per site [70]. In regions between the Mott shells, a superfluid phase emerges at low temperatures which at higher temperatures becomes a normal Bose liquid. Using finite temperature quantum field theoretic techniques, I calculated analytically the properties of the super-

fluid, Bose liquid, and Mott insulating regions. These calculations include the finite temperature order parameter equation for the superfluid phase, excitation spectrum, Berezinskii-Kosterlitz-Thouless transition temperature and vortex-antivortex pair formation in the two dimensional case, finite temperature compressibility and density - density correlation function. In current experiments, the temperature is much higher than the critical temperature of the superfluid shells.

In chapter 7 I proposed a cooling technique that can be used to achieve much lower temperatures in such systems. This technique relies on the RF knife method used currently for evaporation cooling which removes high entropy atoms from the system.

There are several questions that remain unanswered. We showed that the superfluid shells in between the Mott shells do not follow the Gross-Pitaevskii equation, and the free energy cannot be expressed in terms of the order parameter in the Gross-Pitaevskii form. This leads to the question, what is the nature of the phase transition? How can one formulate the quantum critical field theory for such systems?

In recent experiments tomographic microwave techniques have allowed the detection of several Mott regions for trapped ^{87}Rb atoms in optical lattice [68]. However, it has been quite challenging to detect the superfluid shells. In chapter 4, I proposed a possible experiment for the detection of superfluid shells through the use of Gauss-Laguerre and Gaussian beams followed by Bragg spectroscopy. The idea is that Gauss-Laguerre and Gaussian beams can transfer angular momentum to the atoms in superfluid phase without transferring linear momentum, and that

Bragg spectroscopy can detect their existence since the technique is only sensitive to the velocity of the atoms in the superfluid phase.

Another interesting development in the field of ultracold atoms are experiments involving mixture of bosons and fermions loaded into optical lattices [85, 86]. Such a system has no counterpart in standard condensed matter systems. A spectacular degree of control has been achieved, where not only the ratio between concentrations of bosons and fermions can be adjusted, but also the interactions between fermions and bosons can be controlled through the use of Feshbach resonances. In chapter 5 I studied interacting mixtures of ultracold bosonic and fermionic atoms in harmonically confined optical lattices. This chapter is an extended version of the work presented in Ref. [91]. For a suitable choice of parameters I found emergence of superfluid and Fermi liquid (non-insulating) regions out of Bose-Mott and Fermi-band insulators, due to finite boson and fermion hopping.

In chapter 5 I have carefully avoided the situation where the Fermi liquid and the superfluid regions overlap. A natural extension to this problem would be to understand what happens when they do overlap? Do new phases of matter emerge? How can they be detected?

Another frontier in ultracold atomic and molecular physics is the study of ultracold heteronuclear molecules such as KRb [94, 95], RbCs [96], and NaCs [97]. These molecules, consisting of Bose-Bose, Bose-Fermi, or Fermi-Fermi atom pairs, offer many new opportunities because of their internal degrees of freedom such as their permanent electric dipole moment. In chapter 6 I obtained the finite and zero-temperature phase diagram of bosons interacting via short range repulsive in-

teractions and long-ranged isotropic dipolar interactions in two-dimensions. This chapter is an extended version of the work presented in Ref. [110]. The dipolar interaction can be made to be purely repulsive and isotropic in two dimensions by the application of suitable static electric or microwave fields. I built an analytical model for such systems that describes a first order quantum phase transition at zero temperature from a triangular crystalline phase (analogous to Wigner crystal phase of electrons [130]) to superfluid phase. At finite temperature the crystalline phase melts, due to topological defects, to a hexatic phase where translational order is destroyed but hexagonal orientational order is preserved. Further temperature increase leads to the melting of the hexatic phase into a normal dipolar Bose liquid.

An important question that I did not address is what is the nature of the zero temperature phase transition from dipolar Wigner crystal to dipolar superfluid. It is an interesting phase transition because it goes from one broken symmetry state (diagonal long range order) to another (off-diagonal long range order). How can one explain this phase transition phenomenologically in the Ginzburg-Landau sense [131]? Can one prove that the phase transition is first order? Why do not we have a situation where both orders coexists and one has a supersolid phase? Will longer range interactions lead to a supersolid phase?

Bibliography

- [1] M. H. Anderson, J. R. Ensher, M. R. Matthews, C. E. Wieman, and E. A. Cornell, *Science*, **269**, 198.
- [2] K. B. Davis, M. -O. Mewes, M. R. Andrews, N. J. van Druten, D. S. Durfee, D. M. Kurn, and W. Ketterle, *Phys. Rev. Lett.* **75**, 3969 (1995).
- [3] Y. Nakamura, Yu. A. Pashkin, and J. S. Tsai, *Nature* **398**, 786 (1999).
- [4] Michael A. Nielsen and Isaac L. Chuang, *Quantum computation and quantum information*, Cambridge University Press (2000).
- [5] M. Brune, E. Hagley, J. Dreyer, X. Matre, A. Maali, C. Wunderlich, J. M. Raimond, and S. Haroche, *Phys. Rev. Letters* **77**, 4887 (1996).
- [6] S Gider, DD Awschalom, T Douglas, S Mann, and M Chaparala, *Science* **268**, 77 (1995).
- [7] A. Hikata and C. Elbaum: Tunneling of Dislocation Kinks and the Effect of Dissipation (1985) , *Phys. Rev. Letters* **54**, 2418.
- [8] J. R. Friedman, V. Patel, W. Chen, S. K. Tolpygo and J. E. Lukens, *Nature* **406**, 43 (2000).
- [9] J. E. Mooij, T. P. Orlando, L. Levitov, L. Tian, C. H. van der Wal, and S. Lloyd, *Science* **285**, 1036 (1999).
- [10] A Leggett, Quantum mechanics at the macroscopic level (1986), in *Chance and Matter*, J. Souletie, J. Vannimenus, and R. Stora, ed., North-Holland, Amsterdam, pp. 395-507.
- [11] Erich Joos, H. Dieter Zeh, Claus Kiefer, Domenico J. W. Giulini, Joachim Kupsch, Ion-Olimpiu Stamatescu, *Decoherence and the Appearance of a Classical World in Quantum Theory*, Springer (2003).
- [12] A. Einstein, *S. B. Preuss. Akad. Wiss. phys.-math. Klasse* **13**, 3 (1925).
- [13] L. P. Pitaevskii and S. Stringari, *BoseEinstein Condensation*, Clarendon Press (2003).
- [14] O. Penrose and L. Onsager, *Phys. Rev.* **104**, 576584 (1956).

- [15] B. D. Josephson, Phys. Lett **1**, 251 (1962).
- [16] Alexander L. Fetter and John Dirk Walecka, *Quantum Theory of Many-Particle Systems*, Dover Publications (2003).
- [17] M. R. Andrews, C. G. Townsend, H.-J. Miesner, D. S. Durfee, D. M. Kurn, W. Ketterle, Science **275**, 637 (1997).
- [18] G. J. Milburn and J. Corney, Phys. Rev. A **55**, 4318 (1997).
- [19] A P Tonel, J Links, and A Foerster, Journal of Physics A **38**, 1235 (2005).
- [20] R Gati and M K Oberthaler, J. Phys. B: At. Mol. Opt. Phys. **40**, R61 (2007).
- [21] R. C. Ramos, M. A. Gubrud, A. J. Berkley, J. R. Anderson, C. J. Lobb, and F. C. Wellstood, IEEE Trans. Appl. Supercond. **11**, 998 (2001).
- [22] J. M. Martinis, S. Nam, J. Aumentado, and C. Urbina, Phys. Rev. Lett. **89**, 117901 (2002).
- [23] V. Bouchiat, D. Vion, P. Joyez, D. Esteve and M.H. Devoret, Physica Scripta **T76** 165, (1998).
- [24] D. Vion, A. Aassime, A. Cottet, P. Joyez, H. Pothier, C. Urbina, D. Esteve, M. H. Devoret, Science **296**, 886 (2002).
- [25] I. Chiorescu, Y. Nakamura, C. J. P. M. Harmans, and J. E. Mooij, Science **299**, 1869 (2003).
- [26] T. Duty, D. Gunnarsson, K. Bladh, and P. Delsing, Phys. Rev. B **69**, 140503(R) (2004).
- [27] A. Wallraff, D. I. Schuster, A. Blais, L. Frunzio, R.-S. Huang, J. Majer, S. Kumar, S. M Girvin and R. J. Schoelkopf, Nature **431**, 162 (2004).
- [28] V.T. Petrashov, K.G. Chua, K.M.Marshall, R. Sh. Shaikhaidarov and J. T. Nicholls, Phys. Rev. Lett. **95**, 147001 (2005).
- [29] J. M. Martinis, S. Nam, J. Aumentado, K. M. Lang, and C. Urbina, Phys Rev. B **67**, 094510 (2003).

- [30] H. Xu, A. J. Berkley, R. C. Ramos, M. A. Gubrud, P. R. Johnson, F. W. Strauch, A. J. Dragt, J. R. Anderson, C. J. Lobb, and F. C. Wellstood, *Phys. Rev. B* **71**, 064512 (2005).
- [31] See for example: C. D. Tesche and J. Clarke, *J. Low Temp. Phys.* **37**, 405 (1979).
- [32] M. Tinkham, *Introduction to Superconductivity: Second Edition*, Cityplace-Dover Books on Physics, (1996).
- [33] R. H. Koch, D. J. Harlingen, and J. C. Clarke, *Appl. Phys. Lett.*, **38**, 380 (1981)
- [34] Y. C. Chen, *J. Low Temp. Phys.* **65**, 133 (1986).
- [35] John M. Martinis, K. B. Cooper, R. McDermott, Matthias Steffen, Markus Ansmann, K. D. Osborn, K. Cicak, Seongshik Oh, D. P. Pappas, R. W. Simmonds, and Clare C. Yu, *Phys. Rev. Lett.*, **95**, 210503 (2005)
- [36] Jeans Koch, Terri M. Yu, Jay Gambetta, A. A. Houck, D. I. Schuster, J. Majer, Alexandre Blais, M. H. Devoret, S. M. Girvin, and R. J. Schoelkopf, *Phys. Rev. A* **76**, 042319 (2007).
- [37] T. Van Duzer and C. W. Turner, *Principles of Superconductive Devices and Circuits* (Elseiver, New York, 1981).
- [38] T. A. Palomaki, S. K. Dutta, H. Paik, H. Xu, J. Matthews, R. M. Lewis, R. C. Ramos, K. Mitra, P. R. Johnson, F. W. Strauch, A. J. Dragt, C. J. Lobb, J. R. Anderson, and F. C. Wellstood, *Phys. Rev. B* **73**, 014520 (2006).
- [39] V. Lefevre-Seguin, E. Turlot, C. Urbina, D. Esteve, and M. H. Devoret, *Phys. Rev. B* **46**, 5507 (1992).
- [40] N. Moiseyev, *Phys. Rep.* **302**, 211 (1998).
- [41] Mohsen Razavy, *Quantum Theory of Tunneling*, World Scientific Publishing Company (2003).
- [42] Coherence in dc SQUID phase qubits, Hanhee Paik, PhD thesis, University of Maryland (2007) (Web Address: <https://drum.umd.edu/dspace/handle/1903/7469>).
- [43] M. N. Boulant, G. Ithier, P. Meeson, F. Nguyen, D. Vion, D. Esteve, I. Siddiqi, R. Vijay, C. Rigetti, F. Pierre, and M. Devoret, *Phys. Rev. B* **76**, 014525 (2007).

- [44] Theory of superconducting phase qubits, F. W. Strauch, PhD thesis, University of Maryland (2005) (Web Address: <https://drum.umd.edu/dspace/handle/1903/2063>).
- [45] C. Monroe, D. M. Meekhof, B. E. King, W. M. Itano, and D. J. Wineland, Phys. Rev. Lett. **75**, 4714 (1995).
- [46] G. K. Brennen, C. M. Caves, P. S. Jessen, and I. H. Deutsch, Phys. Rev. Lett **82**, 1060 (1999).
- [47] R. Hanson, B. Witkamp, L. M. K. Vandersypen, L. H. Willems van Beveren, J. M. Elzerman, and L. P. Kouwenhoven, Phys. Rev. Lett **91**, 196802 (2003).
- [48] T. Hayashi, T. Fujisawa, H. D. Cheong, Y. H. Jeong, and Y. Hirayama, Phys. Rev. Lett **91**, 226804 (2003).
- [49] A. Shnirman, G. Schon, and Z. Hermon, Phys. Rev. Lett **79**, 2371 (1997).
- [50] Kaushik Mitra, C. J. Lobb, and C. A. R. Sá de Melo, Phys. Rev. B **79**, 132507 (2009).
- [51] C. H. van der wal, F. K. Wilhelm, C. J. P. M. Harmans, J. E. Mooij, Eur. Phys. J. B **31**, 111 (2003).
- [52] Kaushik Mitra, C. J. Lobb, and C. A. R. Sá de Melo Phys. Rev. B **79**, 132507 (2009).
- [53] Kaushik Mitra, C. J. Lobb, and C. A. R. Sá de Melo, arXiv:1001.1701.
- [54] Kaushik Mitra, F. W. Strauch, C. J. Lobb, J. R. Anderson, F. C. Wellstood, and Eite Tiesinga, Phys. Rev. B **77**, 214512(2008).
- [55] U. Weiss, *Quantum Dissipative Systems*, World Scientific (1999).
- [56] Lin Tian, Seth Lloyd, and T.P. Orlando, Phys. Rev. B **65**, 144516 (2002).
- [57] Alexandre Blais, Ren-Shou Huang, Andreas Wallraff, S. M. Girvin, R. J. Schoelkopf, Phys. Rev. A **69**, 062320 (2004).
- [58] A. J. Leggett, S. Chakravarty, A. T. Dorsey, Matthew P. A. Fisher, Anupam Garg, and W. Zwerger, Rev. Mod. Phys. **59**, 1 (1987).

- [59] F. K. Wilhelm, M. J. Storcz, U. Hartmann, and M. R. Geller, NATO-ASI proceedings: Mathematics, Physics and Chemistry **244**, 195 (2007).
- [60] F. K. Wilhelm, S. Kleff, and J. von Delft, Chemical Physics **296**, 345, (2003).
- [61] Hanhee Paik, S. K. Dutta, R. M. Lewis, T. A. Palomaki, B. K. Cooper, R. C. Ramos, H. Xu, A. J. Dragt, J. R. Anderson, C. J. Lobb, and F. C. Wellstood, Phys. Rev. B **77**, 214510 (2008).
- [62] I. Chiooescu, P. Bertet, K. Semba, Y. Nakamura, C. J. P. M. Harmans, and J. E. Mooij, Nature **431**, 159 (2004).
- [63] Mike A. Sillanp, Jae I. Park, and Raymond W. Simmonds, Nature **449**, 438 (2007).
- [64] Immanuel Bloch, Nature Phys. **1**, 23 (2005).
- [65] Markus Greiner, Olaf Mandel, Tilman Esslinger, Theodor W. Hänsch, and Immanuel Bloch, Nature (London) **415**, 39 (2002).
- [66] Thilo Stöferle, Henning Moritz, Christian Schori, Michael Köhl, and Tilman Esslinger, Phys. Rev. Lett. **92**, 130403 (2004).
- [67] I. B. Spielman, W. D. Phillips, and J. V. Porto, Phys. Rev. Lett. **98**, 080404 (2007).
- [68] Gretchen K. Campbell, Jongchul Mun, Micah Boyd, Patrick Medley, Aaron E. Leanhardt, Luis G. Marcassa, David E. Pritchard, and Wolfgang Ketterle, Science **313** 649 (2006).
- [69] Simon Fölling, Artur Widera, Torben Mller, Fabrice Gerbier, and Immanuel Bloch, Phys. Rev. Lett. **97**, 060403 (2006).
- [70] D. Jaksch, C. Bruder, J. I. Cirac, C. W. Gardiner, and P. Zoller, Phys. Rev. Lett. **81**, 3108 (1998).
- [71] Kaushik Mitra, C. J. Williams, and C. A. R. Sá de Melo, Phys. Rev. A **77**, 033607 (2008).
- [72] Kaushik Mitra, C. J. Williams, and C. A. R. Sá de Melo, cond-mat/0702156 (2007).

- [73] D. van Oosten, P. van der Straten, and H. T. C. Stoof, Phys. Rev. A, **63**, 053601 (2001).
- [74] L. Pitaevskii, and S. Stringari, “Bose-Einstein Condensation”, Clarendon Press, Oxford (2003).
- [75] V. L Berezinskii, Sov. Phys. JETP **32**, 493 (1971).
- [76] J. M. Kosterlitz, and D. Thouless, J. Phys. C **5**, L124 (1972).
- [77] Matthew P. A. Fisher, Peter B. Weichman, G. Grinstein, and Daniel S. Fisher, Phys. Rev. B **40**, 546 (1989).
- [78] N. F. Mott, Proc. Phys. Soc., London, Sect. A **62**, 416 (1949).
- [79] R. A. Barankov, C. Lannert, S. Vishveshwara, Phys. Rev. A **75**, 063622 (2007).
- [80] M. F. Andersen, C. Ryu, Pierre Cladé, Vasant Natarajan, A. Vaziri, K. Helmerson, and W. D. Phillips, Phys. Rev. Lett. **97**, 170406 (2006).
- [81] C. Ryu, M. F. Andersen, P. Cladé, Vasant Natarajan, K. Helmerson, W. D. Phillips, cond-mat/0709.0012v1.
- [82] S. R. Muniz, D. S. Naik, and C. Raman, Phys. Rev. A **73** 041605(R) (2006).
- [83] K. Helmerson, *private communication*.
- [84] E. H. Graf, D. M. Lee, and J. D. Reppy, Phys. Rev. Lett. **19**, 417 (1967).
- [85] S. Ospelkaus, C. Ospelkaus, L. Humbert, P. Ernst, K. Sengstock, and K. Bongs, Phys. Rev. Lett. **97**, 120403 (2006).
- [86] K. Günter, T. Stöferle, H. Moritz, M. Köhl, and T. Esslinger, Phys. Rev. Lett. **96** 180402 (2006).
- [87] H. P. Büchler and G. Blatter, Phys. Rev. Lett. **91**, 130404 (2003).
- [88] L. Viverit, C. J. Pethick, and H. Smith, Phys. Rev. A **A**, 053605 (2000).
- [89] M. Lewenstein, L. Santos, M. A. Baranov, and H. Fehrmann, Phys. Rev. Lett. **92**, 050401 (2004).

- [90] F. Hébert, F. Haudin, L. Pollet, and G. G. Batrouni, Phys. Rev. A **76**, 043619 (2007).
- [91] Kaushik Mitra, C. J. Williams, and C. A. R. Sá de Melo, Phys. Rev. A **79**, 055601 (2009)
- [92] M. Cramer, J. Eisert, and F. Illuminati, Phys. Rev. Lett. **93**, 190405 (2004).
- [93] C. Ryu, C. Ryu, M. F. Andersen, P. Cladé, V. Natarajan, K. Helmerson, W. D. Phillips, Phys. Rev. Lett. **99**, 260401 (2007).
- [94] Jeremy M. Sage, Sunil Sainis, Thomas Bergeman, and David DeMille, Phys. Rev. Lett. **94**, 203001 (2005).
- [95] D. Wang, J. Qi, M. F. Stone, O. Nikolayeva, H. Wang, B. Hattaway, S. D. Gensemer, P. L. Gould, E. E. Eyler, and W. C. Stwalley, Phys. Rev. Lett. **93**, 243005 (2004).
- [96] A. J. Kerman, Jeremy M. Sage, Sunil Sainis, Thomas Bergeman, and David DeMille, Phys. Rev. Lett. **92**, 153001 (2004).
- [97] C. Haimberger, J. Kleinert, M. Bhattacharya, and N. P. Bigelow, Phys. Rev. A **70**, 021402(R) (2004).
- [98] C. A. Stan, M. W. Zwierlein, C. H. Schunck, S. M. F. Raupach, and W. Ketterle, Phys. Rev. Lett. **93**, 143001 (2004).
- [99] S. Inouye, J. Goldwin, M. L. Olsen, C. Ticknor, J. L. Bohn, and D. S. Jin, Phys. Rev. Lett. **93**, 183201 (2004).
- [100] F. Ferlaino, Chiara D'Errico, Giacomo Roati, Matteo Zaccanti, Massimo Inguscio, and Giovanni Modugno, Phys. Rev. A **73**, 040702(R) (2006).
- [101] K. Goral, Kazimierz Rzazewski, and Tilman Pfau, Phys. Rev. A **61**, 051601(R) (2000).
- [102] L. Santos, G. V. Shlyapnikov, P. Zoller, and M. Lewenstein, Phys. Rev. Lett. **85**, 1791 (2000).
- [103] M. A. Baranov, M. S. Marenko, Val. S. Rychkov, and G. V. Shlyapnikov, Phys. Rev. A **66**, 013606 (2002).

- [104] T. Rieger, T. Junglen, S. A. Rangwala, P. W. H. Pinkse, and G. Rempe, *Phys. Rev. Lett.* **95**, 173002 (2005).
- [105] M. Iskin, C. A. R. Sá de Melo, *Phys. Rev. Lett.* **99**, 110402 (2007).
- [106] H. P. Büchler, E. Demler, M. Lukin, A. Micheli, N. Prokofev, G. Pupillo, and P. Zoller, *Phys. Rev. Lett.* **98**, 060404 (2007).
- [107] G. E. Astrakharchik, J. Boronat, I. L. Kurbakov, and Yu. E. Lozovik, *Phys. Rev. Lett.* **98**, 060405 (2007).
- [108] C. Mora, O. Parcollet, and X. Waintal, *Phys. Rev. B* **76**, 064511 (2007).
- [109] Amnon Aharony, R. J. Birgeneau, J. D. Brock, and J. D. Litster, *Phys. Rev. Lett.* **57**, 1012 (1986).
- [110] Kaushik Mitra and C. A. R. Sá de Melo, arXiv:0903.4655.
- [111] S. Z. Lin, B. Zheng, and S. Trimper, *Phys. Rev. E* **73**, 066106 (2006).
- [112] David R. Nelson and B. I. Halperin, *Phys. Rev. B* **19**, 2457 (1979).
- [113] A. P. Young, *Phys. Rev. B* **19**, 1855 (1979).
- [114] T. Lahaye, J. Metz, T. Koch, B. Frhlich, A. Griesmaier, T. Pfau, *Pushing the frontiers of atomic physics*, Proceedings of the XXI International Conference on Atomic Physics (2009).
- [115] O. H. Nielsen, and R. M. Martin, *Phys. Rev. B* **32**, 3780 (1985).
- [116] J. M. Kosterlitz, *J. Phys. C* **7**, 1046 (1974).
- [117] A. Ghazali and J.-C. S. Levy, *Europhys. Lett.* **74**, 355 (2006).
- [118] Roberto B. Diener, Qi Zhou, Hui Zhai, Tin-Lun Ho, *Physical Review Letters*, **98**, 180404 (2007).
- [119] Tin-Lun Ho and Qi Zhou, *Phys. Rev. Lett.* **99**, 120404 (2007).
- [120] Xiancong Lu, Jinbin Li, and Yue Yu, *Phys. Rev. A* **73**, 043607 (2006).
- [121] J. W. Negele and Henri Orland, *Quantum Many-Particle Systems (Frontiers in Physics)*, Westview Press (1998).

- [122] G. Kotliar and A. E. Ruckenstein, Phys. Rev. Lett. **57**, 1362 (1986)
- [123] R. Vijay, M. H. Devoret, I. Siddiqi, Review of Scientific Instruments **80**, 111101 (2009).
- [124] A. O. Caldeira and A. J. Leggett, Phys. Rev. Lett. **46**, 211 (1981).
- [125] S. K. Dutta, Frederick W. Strauch, R. M. Lewis, Kaushik Mitra, Hanhee Paik, T. A. Palomaki, Eite Tiesinga, J. R. Anderson, Alex J. Dragt, C. J. Lobb, and F. C. Wellstood, Phys. Rev. B **78**, 104510 (2008).
- [126] D. I. Schuster, A. Wallraff, A. Blais, L. Frunzio, R.-S. Huang, J. Majer, S. M. Girvin, and R. J. Schoelkopf, Physical Review Letters **94**, 123602 (2005).
- [127] T. A. Palomaki, S. K. Dutta, R. M. Lewis, A. J. Przybysz, Hanhee Paik, B. K. Cooper, H. Kwon, J. R. Anderson, C. J. Lobb, F. C. Wellstood, and E. Tiesinga Phys. Rev. B **81**, 144503 (2010).
- [128] Radoslaw C. Bialczak, R. McDermott, M. Ansmann, M. Hofheinz, N. Katz, Erik Lucero, Matthew Neeley, A. D. OConnell, H. Wang, A. N. Cleland, and John M. Martinis, Phys. Rev. Lett. **99**, 187006 (2007).
- [129] Immanuel Bloch, Jean Dalibard, and Wilhelm Zwerger, Rev. Mod. Phys. **80**, 885 (2008).
- [130] E. P. Wigner, Phys. Rev. **46**, 10021011 (1934).
- [131] V.L. Ginzburg and L.D. Landau, Zh. Eksp. Teor. Fiz. **20**, 1064 (1950).